Pertanika Journal of

SCIENCE & TECHNOLOGY

JST

VOL. 33 (S1) 2025

A Special Issue devoted to

Global Food and Agriculture Recovery in the Post-Pandemic World

Guest Editors

Hazreen Haizi Harith & Nazmi Mat Nawi

PERTANIKA JOURNALS

A scientific journal published by Universiti Putra Malaysia Press

Pertanika Journal of Science & Technology
Pertanika Journal of Science & Technology

PERTANIKA JOURNAL OF SCIENCE & TECHNOLOGY

About the Journal

Overview

Pertanika Journal of Science & Technology is an official journal of Universiti Putra Malaysia. It is an open-access online scientific journal. It publishes original scientific outputs. It neither accepts nor commissions third party content.

Recognised internationally as the leading peer-reviewed interdisciplinary journal devoted to the publication of original papers, it serves as a forum for practical approaches to improve quality on issues pertaining to science and engineering and its related fields.

Pertanika Journal of Science & Technology currently publishes 6 issues a year (*January, March, April*, *July, August,* and *October*). It is considered for publication of original articles as per its scope. The journal publishes in **English** and it is open for submission by authors from all over the world.

The journal is available world-wide.

Aims and scope

Pertanika Journal of Science & Technology aims to provide a forum for high quality research related to science and engineering research. Areas relevant to the scope of the journal include: bioinformatics, bioscience, biotechnology and bio-molecular sciences, chemistry, computer science, ecology, engineering, engineering design, environmental control and management, mathematics and statistics, medicine and health sciences, nanotechnology, physics, safety and emergency management, and related fields of study.

History

Pertanika Journal of Science & Technology was founded in 1993 and focuses on research in science and engineering and its related fields.

Vision

To publish a journal of international repute.

Mission

Our goal is to bring the highest quality research to the widest possible audience.

Quality

We aim for excellence, sustained by a responsible and professional approach to journal publishing. Submissions can expect to receive a decision within 90 days. The elapsed time from submission to publication for the articles averages 180 days. We are working towards decreasing the processing time with the help of our editors and the reviewers.

Abstracting and indexing of Pertanika

Pertanika Journal of Science & Technology is now over 32 years old; this accumulated knowledge and experience has resulted the journal being abstracted and indexed in SCOPUS (Elsevier), Journal Citation Reports (JCR-Clarivate), EBSCO, ASEAN CITATION INDEX, Microsoft Academic, Google Scholar, and MyCite.

Citing journal articles

The abbreviation for Pertanika Journal of Science & Technology is *Pertanika J. Sci. & Technol.*

Publication policy

Pertanika policy prohibits an author from submitting the same manuscript for concurrent consideration by two or more publications. It prohibits as well publication of any manuscript that has already been published either in whole or substantial part elsewhere. It also does not permit publication of manuscript that has been published in full in proceedings.

Code of Ethics

The *Pertanika* journals and Universiti Putra Malaysia take seriously the responsibility of all of its journal publications to reflect the highest in publication ethics. Thus, all journals and journal editors are expected to abide by the journal's codes of ethics. Refer to *Pertanika*'s **Code of Ethics** for full details, or visit the journal's web link at http://www.pertanika.upm.edu.my/code_of_ethics.php

Originality

The author must ensure that when a manuscript is submitted to *Pertanika*, the manuscript must be an original work. The author should check the manuscript for any possible plagiarism using any program such as Turn-It-In or any other software before submitting the manuscripts to the *Pertanika* Editorial Office, Journal Division.

All submitted manuscripts must be in the journal's acceptable similarity index range:

≤ 20% – PASS; > 20% – REJECT.

International Standard Serial Number (ISSN)

An ISSN is an 8-digit code used to identify periodicals such as journals of all kinds and on all media–print and electronic.

Pertanika Journal of Science & Technology: e-ISSN 2231-8526 (Online).

Lag time

A decision on acceptance or rejection of a manuscript is reached in 90 days (average). The elapsed time from submission to publication for the articles averages 180 days.

Authorship

Authors are not permitted to add or remove any names from the authorship provided at the time of initial submission without the consent of the journal's Chief Executive Editor.

Manuscript preparation

For manuscript preparation, authors may refer to Pertanika's **INSTRUCTION TO AUTHORS**, available on the official website of *Pertanika*.

Editorial process

Authors who complete any submission are notified with an acknowledgement containing a manuscript ID on receipt of a manuscript, and upon the editorial decision regarding publication.

Pertanika follows a **double-blind peer-review** process. Manuscripts deemed suitable for publication are sent to reviewers. Authors are encouraged to suggest names of at least 3 potential reviewers at the time of submission of their manuscripts to *Pertanika*, but the editors will make the final selection and are not, however, bound by these suggestions.

Notification of the editorial decision is usually provided within 90 days from the receipt of manuscript. Publication of solicited manuscripts is not guaranteed. In most cases, manuscripts are accepted conditionally, pending an author's revision of the material.

The journal's peer review

In the peer-review process, 2 to 3 referees independently evaluate the scientific quality of the submitted manuscripts. At least 2 referee reports are required to help make a decision.

Peer reviewers are experts chosen by journal editors to provide written assessment of the **strengths** and **weaknesses** of written research, with the aim of improving the reporting of research and identifying the most appropriate and highest quality material for the journal.

Operating and review process

What happens to a manuscript once it is submitted to *Pertanika*? Typically, there are 7 steps to the editorial review process:

1. The journal's Chief Executive Editor and the Editor-in-Chief examine the paper to determine whether it is relevance to journal needs in terms of novelty, impact, design, procedure, language as well as presentation and allow it to proceed to the reviewing process. If not appropriate, the manuscript is rejected outright and the author is informed.

2. The Chief Executive Editor sends the article-identifying information having been removed, to 2 to 3 reviewers. They are specialists in the subject matter of the article. The Chief Executive Editor requests that they complete the review within 3 weeks.

   Comments to authors are about the appropriateness and adequacy of the theoretical or conceptual framework, literature review, method, results and discussion, and conclusions. Reviewers often include suggestions for strengthening of the manuscript. Comments to the editor are in the nature of the significance of the work and its potential contribution to the research field.

Pertanika Journal of Science & Technology
Pertanika Journal of Science & Technology

Pertanika Journal of Science & Technology
Pertanika Journal of Science & Technology

3. The Editor-in-Chief examines the review reports and decides whether to accept or reject the manuscript, invite the authors to revise and resubmit the manuscript, or seek additional review reports. In rare instances, the manuscript is accepted with almost no revision. Almost without exception, reviewers' comments (to the authors) are forwarded to the authors. If a revision is indicated, the editor provides guidelines for attending to the reviewers' suggestions and perhaps additional advice about revising the manuscript.

4. The authors decide whether and how to address the reviewers' comments and criticisms and the editor's concerns. The authors return a revised version of the paper to the Chief Executive Editor along with specific information describing how they have addressed' the concerns of the reviewers and the editor, usually in a tabular form. The authors may also submit a rebuttal if there is a need especially when the authors disagree with certain comments provided by reviewers.

5. The Chief Executive Editor sends the revised manuscript out for re-review. Typically, at least 1 of the original reviewers will be asked to examine the article.

6. When the reviewers have completed their work, the Editor-in-Chief examines their comments and decides whether the manuscript is ready to be published, needs another round of revisions, or should be rejected. If the decision is to accept, the Chief Executive Editor is notified.

7. The Chief Executive Editor reserves the final right to accept or reject any material for publication, if the processing of a particular manuscript is deemed not to be in compliance with the S.O.P. of *Pertanika*. An acceptance letter is sent to all the authors.

   The editorial office ensures that the manuscript adheres to the correct style (in-text citations, the reference list, and tables are typical areas of concern, clarity, and grammar). The authors are asked to respond to any minor queries by the editorial office. Following these corrections, page proofs are mailed to the corresponding authors for their final approval. At this point, **only essential changes are accepted**. Finally, the manuscript appears in the pages of the journal and is posted on-line.

Pertanika Journal of

SCIENCE & TECHNOLOGY

A Special Issue devoted to
Global Food and Agriculture Recovery in the Post-Pandemic World

Vol. 33 (S1) 2025

Guest Editors
Hazreen Haizi Harith & Nazmi Mat Nawi

PERTANIKA JOURNALS

A scientific journal published by Universiti Putra Malaysia Press

PJST
Pertanika Journal of Science & Technology
AN INTERNATIONAL PEER-REVIEWED JOURNAL

EDITORIAL OFFICE
JOURNAL DIVISION
Putra Science Park
1st Floor, IDEA Tower II
UPM-MTDC Technology Centre
Universiti Putra Malaysia
43400 Serdang, Selangor Malaysia.

General Enquiry
Tel. No: +603 9769 1622 | 1616
E-mail:
executive_editor.pertanika@upm.edu.my
URL: www.journals-jd.upm.edu.my

PUBLISHER
UPM Press
Universiti Putra Malaysia
43400 UPM, Serdang, Selangor, Malaysia.
Tel: +603 9769 8851
E-mail: penerbit@putra.upm.edu.my
URL: http://penerbit.upm.edu.my

ABSTRACTING AND INDEXING OF PERTANIKA JOURNALS

Pertanika Journal of Science & Technology is indexed in Journal Citation Reports (JCR-Clarivate), SCOPUS (Elsevier), EBSCO, ASEAN Citation Index, Microsoft Academic, Google Scholar and MyCite.

Pertanika Journal of Science & Technology
Vol. 33 (S1) 2025

Contents

Preface

It is with great pride that we present this special issue of Pertanika Journal of Science and Technology, featuring selected peer-reviewed articles from the International Conference on Agricultural and Food Engineering 2023 (CAFE*i* 2023). Themed *"Global Food and Agriculture Recovery in the Post-Pandemic World,"* this conference provided a platform for researchers, practitioners, and policymakers to explore innovative strategies to rebuild and strengthen the global agricultural and food systems in the wake of the COVID-19 pandemic.

This special issue reflects the interdisciplinary spirit of the conference, capturing diverse research aimed at addressing critical challenges in agriculture, food processing, and biosystems resource management. The featured articles exemplify the dedication of the research community in the South East Asia region in advancing sustainable and resilient solutions. Collectively, they demonstrate the conference's emphasis on sustainability, innovation, and resilience in agricultural and food systems.

Highlights of this issue include:

- **Innovations in agricultural processing,** such as drying optimization of desiccated coconut and the development of pectin-pineapple juice films for sustainable food packaging.
- **Improvements in agricultural mechanization and labor ergonomics**, including the evaluation of harvesting baskets for male pineapple harvesters in Johor, Malaysia.
- **Advancements in sustainable construction materials**, as demonstrated by studies on chemical treatments on porous rice husk ash-based geopolymer foam to improve its strength.
- **Water resource management and irrigation system analyses**, exemplified by evaluations of the Taguibo River Irrigation System Diversion Dam and the water yield assessments in the Taguibo River Watershed Forest Reserve in the Philippines.
- **Development of practical engineering solutions**, such as the development of a testing rig for ram pump systems, which highlight the importance of accessible and efficient water management technologies for agricultural applications.

The collective efforts of the authors, reviewers, the journal's administrative team and the conference organizers have made this special issue possible and enriched the field of agricultural and food engineering. We hope this special issue will be a resource for researchers, practitioners, and policymakers alike, and inspire further innovation and collaboration to build a resilient and sustainable future for global agriculture and food systems.

Guest Editors
Hazreen Haizi Harith (Dr.)
Nazmi Mat Nawi (Assoc. Prof. Dr.)

Pertanika J. Sci. & Technol. 33 (S1): 1 - 22 (2025)

PERTANIKA JOURNALS

SCIENCE & TECHNOLOGY

Journal homepage: http://www.pertanika.upm.edu.my/

Enhancing the Efficiency of Infrared Drying of Desiccated Coconut Through Process Optimization and Validation

Yahya Sahari[1,2], Mohd Shamsul Anuar[1], Mohd Zuhair Mohd Nor[1]* and Nur Hamizah Abdul Ghani[1]

[1]Department of Food and Process Engineering, Faculty of Engineering, Universiti Putra Malaysia, 43400 Serdang, Selangor, Malaysia
[2]Engineering Research Centre, Malaysian Agricultural Research and Development Institute, 43400 Serdang, Selangor, Malaysia

ABSTRACT

Drying desiccated coconut is always challenging due to its sensitivity to heat, which can reduce its color quality. The main goal of this study is to optimize infrared drying (IR) efficiency without affecting the final color quality of desiccated coconut. Single-mode infrared drying was optimized using Response Surface Methodology (RSM) with a central composite rotatable design (CCRD). Using a radiation output of 600 Watts and a fixed distance of 15 cm from the emitter, a single layer of fresh shredded coconut with a wet basis of approximately 51.35±4.0% was dried to less than 3% (w.b). Drying temperature and air velocity were taken into consideration as independent parameters. The selected optimal drying conditions, with the desirability value (D = 0.812), were 61°C drying temperature and 2.2 m/s air velocity. The response of optimal values for drying time, specific energy consumption (SEC), color changes, and whiteness index were 36.826 minutes, 19.821 kWh/kg, 3.431, and 71.762, respectively. Models for predicting these response values had R^2 values of more than 0.90. All responses were shown to be significantly impacted by drying temperature and air velocity ($p<0.05$), with drying temperature having a larger effect than air velocity. The optimal drying parameters were validated with a less than 2% deviation.

Keywords: Color quality, desiccated coconut, infrared drying, optimization, specific energy consumption

ARTICLE INFO

Article history:
Received: 08 November 2023
Accepted: 05 November 2024
Published: 31 January 2025

DOI: https://doi.org/10.47836/pjst.33.S1.01

E-mail addresses:
yayasaha82@gmail.com.my (Yahya Sahari)
mshamsul@upm.edu.my (Mohd Shamsul Anuar)
zuhair@upm.edu.my (Mohd Zuhair Mohd Nor)
nurhamizah@upm.edu.my (Nur Hamizah Abdul Ghani)
* Corresponding author

INTRODUCTION

Coconut is undoubtedly the world's most significant tree crop, providing food and shelter to millions in the tropical region. Coconut (*Cocos nucifera L.)* has long been popular in Southeast Asia. People in over 110 nations worldwide use coconut palm,

ISSN: 0128-7680
e-ISSN: 2231-8526

which is farmed on around 12.25 million hectares in over 90 countries. The economic impact of coconuts is estimated to be approximately USD 13.18 billion as export value in 2022 (Alouw, 2023).

In Malaysia, coconuts are grown for both fresh produce and downstream products. Since the demand for products made from coconut increases yearly, Malaysia still needs to import coconut from Indonesia and the Philippines (Nor et al., 2020). Between 2016 and 2020, the average import of fresh coconut was 217 thousand metric tonnes per year in Malaysia (Zainol et al., 2023). The edible part, which is coconut kernel meat, makes up 33% of the coconut, and it has long been a staple of many people's diets for its protein, fat, and carbohydrate sources (Patil et al., 2017; Wynn, 2017). On the other hand, the composition of coconut kernel is predominantly influenced by variety, nut maturity, geographic location, and cultural behaviors (Adoyo et al., 2021). However, according to Ngampeerapong and Chavasit (2019), coconut kernels' macronutrients and bioactive components differed slightly in three distinct nations (Thailand, Indonesia, and Vietnam). After removing the husk and paring the coconut, the edible section of the coconut kernel is obtained by removing the shell and draining the water. The coconut meat/kernel is manually scrapped and grated to make various items. From the nuts' harvesting to drying and storing, a lack of understanding and genuine abilities in coconut postharvest technology has resulted in severe losses. Like many other agricultural products, coconut kernel is also subject to spoilage and quality deterioration due to the presence of important constituents such as high fat, sugar, and moisture content (Lamdande et al., 2018). As a result, many food products would rather be marketed in their dried forms since they are more appealing than their fresh counterparts.

Today, there are a variety of ways to reduce postharvest losses. Drying or dehydration is the most practical and innovative process for increasing shelf life and maintaining long-term product quality. Many researchers have conducted studies on coconut kernel products using artificial dryers in the laboratory or on a pilot scale (Abidin et al., 2014; Aggary & Arowanti, 2012; Jongyingcharoen et al., 2019; Madamba, 2003; Madhiyanon et al., 2009; Niamnuy & Devahastin, 2005; Pestaño, 2015; Yahya et al., 2020). Air is used in most artificial dryers to convey heat to food, and vaporized water is transported to air via convection. Nevertheless, the hot-air drying process has drawbacks, including low energy efficiency, degradation in quality, and prolonged drying times during the falling rate stage (Kipcak et al., 2019). Traditional methods such as sun drying and kiln drying might produce poor dried product quality, such as discoloration, case hardening, and shrinkage of food, resulting in the loss of phenolic components in the final product (Sarkar et al., 2020).

As technology advances, infrared drying is becoming increasingly popular as an effective way of drying food and agricultural products, thereby reducing and complementing the drawbacks of artificial drying. This non-conventional infrared drying technology offers superior energy efficiency, fast heat transfer rates, and uniform heating of products

(Kian-Pour, 2020). Infrared radiation modifies the product's molecule's vibrational state at between 60,000 and 150,000 MHz, providing intermolecular friction and rapid internal heating (Sakare et al., 2020). Studies show that infrared has a more effective moisture diffusivity and a higher thermal sensitivity than hot air drying (Wu et al., 2019). Unlike hot air drying, no medium is needed to transmit infrared radiation energy from the emitter to the product (Adak et al., 2017). Ceramic emitters are one of the most common electrically heated infrared sources for processing agricultural products (Delfiya et al., 2021; Pan, 2021; Sakare et al., 2020). In addition to that, the short drying period makes it ideal for heat-sensitive products like fruits and vegetables (Delfiya et al., 2021; Riadh et al., 2015; Sakare et al., 2020). Moreover, this type of drying has a unique advantage over conventional drying, including effective product heating, outstanding energy efficiency, and high-quality dried products since it prevents the loss of the product's chemical and organoleptic properties (Sossa et al., 2021). Since its huge potential in food drying was discovered, various agricultural and food products have been investigated using either single-mode infrared drying, combination with others or infrared-assisted mode.

Single-mode infrared drying has been successfully studied by Isik et al. (2019) on bee pollen, saffron by Torki-Harchegani et al. (2017), cherry tomatoes by Kipcak and Doymaz (2020), green bean by Doymaz et al. (2015); apple slices by Salehi and Satorabi (2021); stevia leaves by Huang et al. (2021); eggplant slices by Jafari et al. (2020); turmeric by Fernando et al. (2021)—those mentioned studies covered mostly from drying kinetics to optimization and quality evaluation of products. Despite the fact that Shingare and Thorat (2012) looked at the drying kinetics of infrared drying of desiccated coconut, the study lacked optimization and quality assessment. Other research on desiccated coconut using microwave drying was also reported by Moses et al. (2013), whereby changes in the final product's color were minimal at lower power levels. Choosing the best and optimal drying conditions in food processing is crucial for system effectiveness, creating high-quality dried products, and reducing energy usage. One of the most modern statistical and mathematical techniques, called response surface methodology (RSM), is widely used to design, improve, and optimize a range of processes where a specific response is influenced by multiple variables (Šumić et al., 2016). Several studies have successfully used RSM to optimize drying parameters, producing acceptable results (Koca et al., 2018; Majdi et al., 2019; Omolola et al., 2015; Sharma et al., 2020; Tajudin et al., 2021). Unfortunately, no previous research has looked into the possibility of infrared drying on desiccated coconut, with optimization studies in particular.

This study used an infrared drying approach to examine the effects of drying factors (drying temperature and air velocity) on the desiccated coconut's drying performance and color quality. At the end of this study, an optimal drying condition for desiccated coconut using single-mode infrared drying will be validated and suggested.

MATERIALS AND METHODS

The newly harvested local variety of de-husked coconuts was obtained from a wet market in Senawang, Negeri Sembilan, Malaysia. Only intact and matured coconut (10-12 months) was chosen for this experiment, and sprouted coconut was eliminated to maintain product consistency throughout the drying process. The coconuts were processed daily to ensure the freshness of the coconut kernels. Before being transformed into shredded coconut, the de-husked coconut must first go through a number of steps. The coconut was manually broken open to remove the shell before being cut open with a sharp knife. The brown skin, or so-called testa, was then scraped off the de-shelled coconut using a specialized scraper. The white peeled coconut kernel balls were meticulously cleaned and washed with filtered tap water after the coconut water had been removed from them. Following cleaning, a 1.5 horsepower mechanical shredder (Brand: Anson, Malaysia) was used to grind or shred the white coconut kernels into uniform coconut shreds measuring around 4.06±0.89 mm.

Experimental Apparatus

A picture of the infrared dryer and a schematic diagram are illustrated in Figures 1(a) and (b). The drying chamber was made of stainless steel and well-insulated to prevent heat loss. On the top inner surface of the drying chamber, a ceramic infrared heater with a radiation power of 600 W was installed. Electrical IR emitters were chosen because they are more versatile in power distribution and have a greater conversion efficiency of 78 to 85 percent (Yadav et al., 2020). The control panel attached to the dryer can adjust the output power and infrared drying temperature. With a set distance of 150 mm, a round sample tray of 140 mm in diameter made of woven wire mesh was placed beneath the infrared heater. The Shinko Denshi AJ 820E, Japan underhook weighing scale (820 ±0.01 g) was configured to monitor and display the mass loss of the sample throughout the drying process. A blower was installed to generate and adjust air velocity to increase

(a)

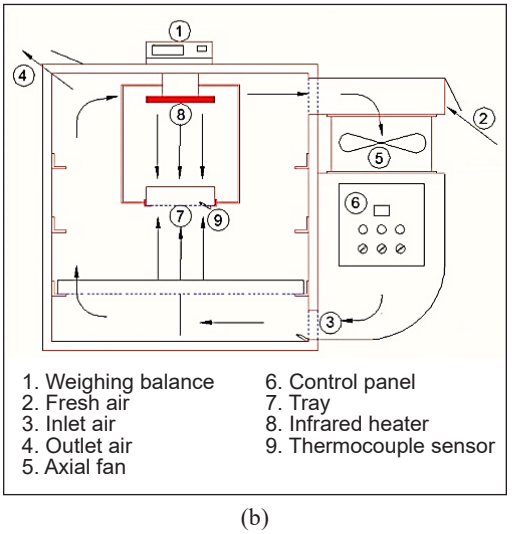

(b)

Figure 1. Single-mode infrared dryer: (a) Picture; and (b) schematic diagram

air circulation during infrared drying. A Vane Anemometer (TESTO 416, Germany) was used to measure the input air velocity, and the reading accuracy was 0.2 m/s ±1.5 percent. A Watt-hour meter was also used to calculate the overall energy used by the blower and infrared emitter.

Experimental Procedures

A layer of white coconut shreds sample weighing about 40 g was placed on a sample tray, and infrared radiation was applied. The infrared drying process was set at 600 W or 3.90 W/cm^2 for each experiment run. This study used a ceramic type of infrared emitter (Model: white ceramic emitter; Brand: Infrapara, China) with dimension (L×W×H: 24.5×6.0×3.1 cm) which is considered a far-infrared drying as the peak-wavelength was in the range of (8.25–9.05 µm). Most ceramic emitters used in drying processes have an emission of up to 3 µm (Aboud et al., 2019). It is important to ensure the drying temperature reaches the steady state condition beforehand. As the drying started, moisture content reduction from the sample was continuously recorded, and the experiment ended when it fell below 3% moisture content (w.b). The intended final moisture content was referred to the standard set by (International Coconut Community, 2009), also reported by (Madhiyanon et al., 2009; Niamnuy & Devahastin, 2005; Yahya et al., 2020). The final moisture content of white shredded coconut was determined by hot air oven drying at 105±2°C (Model: 500/1081, Memmert GmbH + Co.KG, Germany) for 24 h (AOAC, 2005). After being allowed to cool for approximately ten minutes at room temperature, the dried samples were packed into aluminum foil bags for further analysis. After the drying procedure was completed, the drying time for each run was recorded.

Design of Experiments and Statistical Analysis

Two numerical independent variables, temperature (50°C, 60°C, and 70°C) and air velocity (1.5, 2.3, and 3.0 m/s), were used in this central composite rotatable design (CCRD). The measured responses were drying time, specific energy consumption (SEC), color changes (ΔE), and whiteness index (WI). Table 1 shows all the factors involved with their levels. Response surface methodology (RSM) of Statistical Software Design Expert 12 (Stat Ease, Inc., Minneapolis, USA) was used to examine the responses to the collected data. Fitting the experimental data was done using the second-order polynomial of Equation 1 (Wang et al., 2019):

$$y = \beta_o + \sum_{i=1}^{k} \beta_i x_i + \sum_{i=1}^{k} \beta_{ii} x_i^2 + \sum \sum_{i<j=1}^{k} \beta_{ij} x_i x_j \quad [1]$$

Where y values are measured responses (drying time, SEC, ΔE, and WI); β_o, β_i, β_{ii}, and β_{ij} are constant regression coefficients of intercept, linear, quadratic, and interaction terms,

respectively; x_i and x_j are the coded independent variables. The analysis of variance (ANOVA) was employed to statistically test the experimental data at the significance level of $p = 0.05$. The p-value and coefficient of determination (R^2) were also used to assess the model's suitability.

Table 1
Levels of factors

Factors	Type	Unit	-α (1.414)	low (-1)	mid (0)	high (+1)	+α (1.414)
IR Temperature (A)	Numerical	°C	46	50	60	70	74
Air velocity (B)	Numerical	m/s	1.2	1.5	2.3	3.0	3.3

When different industrial processes are optimized, several responses are often adjusted to define the performance and quality attributes. While others must be maximized, some of these response factors must be minimized. These variables may be antagonistic, meaning that when modifying one response, the opposite effect can result in another, complicating matters. The problem can typically be solved in three different ways, whereby the most typical approach to problem-solving is using the desirability function (Erbay & Icier, 2009; Sharma et al., 2020; Tajudin et al., 2019). The desirability function is the summation of all responses into a single measurement in the following Equation 2 (Majdi et al., 2019; Manohar et al., 2013):

$$D(X) = d_1 \times d_2 \times \ldots\ldots {d_n}^{1/n} = [\prod_{i-1}^{n} di(Yi)]^{1/n} \quad [2]$$

Where *Yi (i* = 1, 2 *... n)* are the dependent parameters while *n* is the total number of responses measured in the optimization study, the *di* represents the desirability index for each response variable, which varies from 0 to 1. The desire function, or "D," expresses the degree of desirability of the dependent parameters at a selected level of independent variables.

Validation of Models

The suitability of the second-order polynomial model for predicting the optimum condition values was confirmed by conducting experiments under the suggested optimal parameters and predicted values. Response data from the obtained experimental and predicted values were compared to evaluate the model's veracity. The percentage error (*PE*) between the experimental and predicted values was determined by using the formula given in Equation 3:

$$PE(\%) = \frac{M_{ev} - M_{pv}}{M_{ev}} \times 100 \quad [3]$$

Where M_{ev} is the experimental value, and M_{pv} is the predicted value. According to Nordin et al. (2019), a less than 10% error indicates a good fit between experimental and predicted values.

Specific Energy Consumption (SEC)

Equations 4 and 5 were deployed to determine the total energy used by the dryer at particular infrared drying parameters (Kaveh et al., 2021; Sahari et al., 2023):

$$E_T = \left(E_{IR+fan}\right).t \quad [4]$$

$$SEC = \frac{E_T}{m_w} \quad [5]$$

Where E_T is the overall energy consumption (kWh), SEC is the specific energy consumption (kWh/kg), m_w reflects the water evaporation weight loss (kg), E_{IR+fan} is the total IR emitter and fan power (Watt), and t is the time (hour).

Color Changes (ΔE)

Color is an important consideration for consumers when making food product purchases. It also holds for the desiccated coconut's color quality. A chroma meter (Minolta Co., Osaka, Japan) model CR-400/410 was utilized to evaluate the color of the dried coconuts and fresh coconut shreds. Prior to use, the color analyzer was calibrated to guarantee the accuracy of the results. Three color parameters were identified: L^* (lightness), a^* (red/green), and b^* (yellow/blue). Both fresh and dried samples were filled in a standard transparent petri dish during the measuring process. The color difference (ΔE) was then calculated by Equation 6:

$$\Delta E = \sqrt{[(L^* - L_o^*)^2 + (a^* - a_o^*)^2 + (b^* - b_0^*)^2]} \quad [6]$$

Where ΔE is the color difference between fresh and dried samples (desiccated coconut). L^*_o, a^*_o and b^*_o are the values for fresh coconut shreds, while L^*, a^* and b^* are the values for desiccated coconut. Each color measurement was taken thrice at three sample locations to determine the average color change (Sahari et al., 2023).

Whiteness Index (WI)

Besides the color change attribute, the whiteness index (WI) can also describe color quality. Pathare et al. (2013) state that the whiteness index is a measure of whiteness that incorporates yellow-blue and brightness into a single term. The Whiteness index was also applied to products derived from coconut residue, according to Jongyingcharoen et al. (2019). The WI can be calculated by the following Equation 7 (Nurkhoeriyati et al., 2021):

$$WI = 100 - \sqrt{(100 - L^*)^2 + a^{*2} + b^{*2}} \quad [7]$$

RESULTS AND DISCUSSION

For two factors and four responses, 13 experiments were designed (Table 2). Temperature and air velocity, two independent variables, were combined in the tests with response values from experimental results. It should be noted that using CCRD, the center point from the combination of temperature and air velocity of every pre-treatment was repeated 5 times, in this case (60°C and 2.3m/s). Since it was rotatable CCD, the minimum and maximum temperature and air velocity factor parameters were also extended to 46°C and 74°C and 1.2 and 3.3 m/s, respectively. Ultimately, the optimization aimed to find minimum drying time, SEC, and color changes while targeting the maximum value of the whiteness index of desiccated coconut.

Table 2
Results for two factors and four measured responses

Factor				Response			
Std	**Run**	**Temperature (°C)**	**Air velocity (m/s)**	**Drying time (min)**	**SEC (kWh/kg)**	**ΔE**	**WI**
1	1	50	1.5	61.79	33.90	4.37±0.179	70.88±0.152
6	2	74	2.3	25.85	17.67	9.42±1.311	66.50±1.272
12	3	60	2.3	36.85	19.91	3.51±0.488	71.63±0.486
4	4	70	3.0	39.85	22.21	5.62±0.724	69.89±0.693
7	5	60	1.2	37.98	20.90	5.86±0.903	69.42±0.873
13	6	60	2.3	46.41	25.07	3.02±1.181	72.14±1.184
3	7	50	3.0	77.95	43.95	3.55±1.127	71.70±1.131
2	8	70	1.5	35.38	16.61	7.69±0.985	67.98±1.124
10	9	60	2.3	42.53	22.27	2.19±0.098	73.00±0.110
5	10	46	2.3	65.18	38.71	4.44±0.727	70.80±0.708
8	11	60	3.3	63.20	38.10	4.21±0.246	71.01±0.243
11	12	60	2.3	31.38	17.86	4.17±0.919	70.99±0.890
9	13	60	2.3	40.46	22.45	2.71±0.833	72.45±0.848

Effect of Infrared Drying Parameters on Drying Time

Figure 2 depicts how drying variables affect the drying time of desiccated coconut. By referring to the 3D surface of Figure 2, the increment of drying temperature decreased the drying time significantly. Higher drying temperatures may increase thermal flux from the drying medium, raising the temperature differential between the drying medium and the drying product and enhancing the heat transfer rate (Zeng et al., 2019). A comparable result was also reported in the optimization of the infrared drying process of pumpkin (Sadeghi et al., 2020) and garlic slices (Zhou et al., 2017).

Conversely, an increase in air velocity increases in drying time. It could be due to the cooling effect on the product being dried at higher air velocity, reducing heat and mass

transfer rate in most infrared drying processes (Sadeghi et al., 2020; Srinivas et al., 2018). According to Muga et al. (2021), the cooling effect of the drying air on the IR emitter as a result of convective heat losses is responsible for the IR emitter's temperature decrease with increased drying air velocity.

In other words, individual factors (drying temperature and air velocity) played a significant role in determining the drying behavior of desiccated coconut. It can be proven by the (p-value <0.05) of both factors in Table 3. Nevertheless, drying temperature had a greater effect on drying time compared to air velocity. It was evident from the data in Table 2 that the shortest drying time of 25.85 minutes was recorded at the highest drying temperature of 74°C and a medium air velocity of 2.3 m/s. Park et al. (2015) also mentioned the phenomenon when the drying rate of slice radishes was predominantly influenced by infrared drying temperature rather than air velocity.

The declining trend of drying time was obvious at elevated drying temperature or infrared power during infrared drying, as reported by Bhat et al. (2020) and Doymaz et al. (2015). On the other hand, the longest drying time of 77.95 minutes was observed at a lower drying temperature of 50°C and a

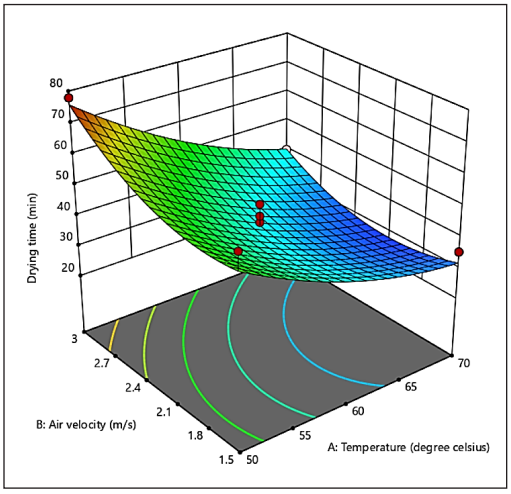

Figure 2. 3D surface of drying time against temperature and air velocity

Table 3
ANOVA results for drying time response

Term	Sum of squares	df	Mean square	F-value	p-value
Model	2656.16	5	531.23	15.79	0.0011 (significant)
A-Temperature	1779.01	1	1779.01	52.90	0.0002
B-Air velocity	389.98	1	389.98	11.60	0.0114
AB	32.51	1	32.51	0.9665	0.3583
A^2	139.76	1	139.76	4.16	0.0809
B^2	366.39	1	366.39	10.89	0.0131
Residual	235.42	7	33.63		
Lack of Fit	104.62	3	34.87	1.07	0.4569 (not significant)
Pure Error	130.80	4	32.70		
Cor Total	2891.59	12			
R^2: 0.9186		Adjusted R^2: 0.8604			Predicted R^2: 0.6616

p-value less than 0.05 is significant at $\alpha = 0.05$
Lack of fit is not significant at a p-value of more than 0.05

higher air velocity of 3.0 m/s. From the statistical analysis, the effect of drying temperature (A) was superior to air velocity (B) with the larger value of coefficient estimate (β_i) and *F*-value. The coefficient estimate was -15, indicating that the mean drying time would decrease by 15 points for every increment of degrees Celsius.

Meanwhile, the interaction between the drying temperature and the air velocity was insignificant ($p>0.05$) concerning drying time. Although both linear terms for the drying temperature and air velocity happened to be significant, only a quadratic term of air velocity showed a relatively large effect ($p<0.05$) on drying time. Therefore, the interaction term of AB and the quadratic term of drying temperature were excluded from the model equation. Equation 8 of the optimized model was recommended for predicting drying time with *p*-value <0.05, 0.8590 of *R*-squared and insignificant lack of fit. Notably, the residuals in Figure 3 follow approximately a straight line, indicating a normal distribution for the residuals.

$$Drying\ time = 42.09 - 15.10A + 6.98B + 6.84B^2 \quad [8]$$

Effect of Infrared Drying Parameters on Specific Energy Consumption (SEC)

Table 4 illustrates that the model's F-value is 26.72, indicating its suitability and significance. It is also proven by the *p*-value, which is less than 0.05. Figure 4 illustrates the 3D surface graph of SEC, which has a pattern quite similar to that of the 3D surface of drying time. While drying temperature and air velocity remain significant factors ($p<0.05$), the effect of drying temperature was more pronounced when compared with air velocity based on its *p*-value of less than 0.0001 and higher *F*-value. Another study employing infrared drying

Table 4
ANOVA results for specific energy consumption (SEC) response

Term	Sum of squares	df	Mean square	F-value	p-value
Model	970.65	5	194.13	26.72	0.0002 (significant)
A-Temperature	586.83	1	586.83	80.78	<0.0001
B-Air velocity	198.83	1	198.83	27.37	0.0012
AB	4.24	1	4.24	0.58	0.4698
A^2	82.72	1	82.72	11.39	0.0118
B^2	126.81	1	126.81	17.46	0.0041
Residual	50.85	7	7.26		
Lack of Fit	20.83	3	6.94	0.9254	0.5055 (not significant)
Pure Error	30.02	4	7.50		
Cor Total	1021.50	12			
R^2: 0.9052		Adjusted R^2: 0.9147			Predicted R^2: 0.8079

p-value less than 0.05 is significant at $\alpha = 0.05$
Lack of fit is not significant at a *p*-value of more than 0.05

on white mulberries (Golpour et al., 2020) and garlic slices (Younis et al., 2018) also found that the infrared power factor was more effective at lowering drying time than air velocity.

It is noteworthy that only the quadratic term of air velocity was significant in the drying time response. However, the quadratic terms of temperature (A^2) and air velocity (B^2) were significant at $p<0.05$ in the SEC response. Therefore, changing the drying temperature and air velocity will significantly affect SEC, hence the cost of energy consumption. The longest drying time at 50°C and 3.0 m/s also contributed to the highest SEC, indicating that drying time response was somehow related to SEC. When the interaction between drying temperature and air velocity (AB) was insignificant in the drying time response, the same trend was observed in the SEC response. The removal of AB interaction from the model equation has increased the value of adjusted R^2 and predicted R^2 from 0.9147 to 0.9191 and 0.8079 to 0.8474, respectively. Based on the value of R^2 (0.9461), a quadratic model (Equation 9) to predict SEC was suggested in the infrared drying of desiccated coconut. There was a normal distribution of residual, which reflects the accuracy of prediction in the SEC response data as the plots lie along a straight line (Figure 5).

$$SEC = 21.16 - 8.65A + 5.01B + 3.50A^2 + 4.35B^2 \quad [9]$$

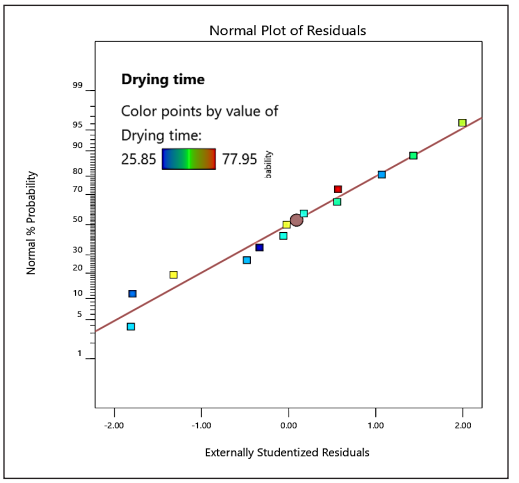

Figure 3. Normal plot of residuals for drying time

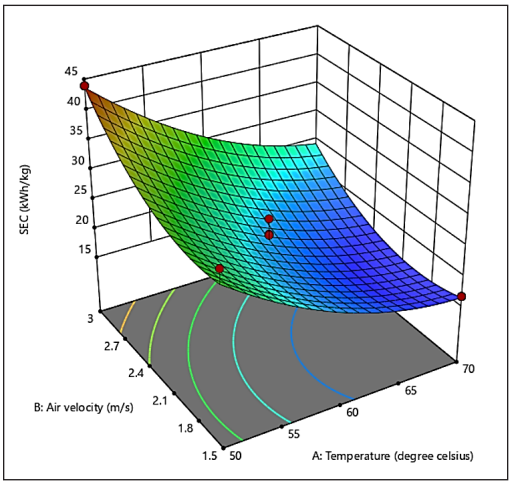

Figure 4. 3D plot of specific energy consumption against temperature and air velocity

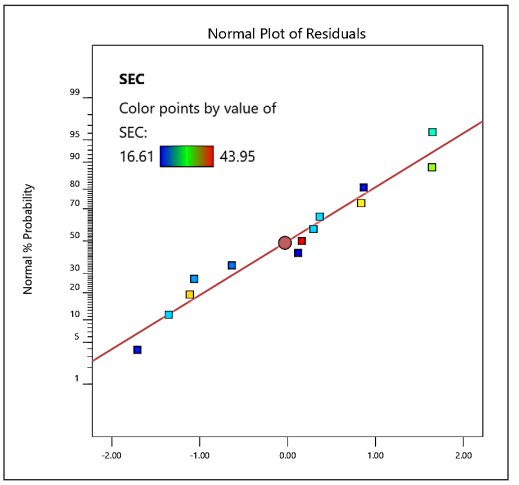

Figure 5. The normal plot of residuals for SEC

Effect of Infrared Drying Parameters on Color Changes (ΔE)

In order to compare the color changes, the color of fresh shredded coconut was first measured beforehand, and the measured values of L*, a*, and b* were 76.46±0.30, -5.59±0.08 and 6.14±0.20 respectively. When it came to color change response, drying temperature and air velocity were both significant, although drying temperature's effect was discovered to be more pronounced than air velocities. It is evident by the higher *F*-value (35.47) and the coefficient estimate value, β_i (1.56). Jafari et al. (2020) also reported similar results, observing that air velocity significantly affected the color changes of eggplant during infrared drying. Drying temperature contributed in a different way to color changes compared to other earlier responses. Since higher drying temperatures resulted in a positive effect of reducing drying time for desiccated coconuts, the effect on color changes was totally inversed. Again, the drying temperature was a dominant factor in determining the color changes of desiccated coconut, followed by air velocity. Nevertheless, in this case, the quadratic term of drying temperature had the highest *F*-value and the least *p*-value among all terms, as seen in Table 5. Unlike drying temperature in model responses drying time and SEC, the drying temperature factor in color changes had a positive sign, which reflects that an increment of 1.56 points of color changes would happen in every degree Celsius increases.

On the other hand, air velocity exhibits the ability to reduce color changes with a negative linear effect of coefficient estimate (-0.6505). In other words, a higher drying temperature, especially at 74°C, may have an advantage in reducing drying time but not preserving the desiccated coconut's color. Figure 6 illustrates that the minimum ΔE of desiccated coconut (2.19) was in the middle range of air velocity and drying temperature

Table 5
ANOVA results for color changes (ΔE) response

Term	Sum of squares	df	Mean square	F-value	p-value
Model	46.07	5	9.21	16.77	0.0009 (significant)
A-Temperature	19.50	1	19.50	35.47	0.0006
B-Air velocity	3.35	1	3.35	6.10	0.0429
AB	0.3551	1	0.3551	0.6461	0.4480
A^2	20.67	1	20.67	37.60	0.0005
B^2	3.90	1	3.90	7.09	0.0323
Residual	3.85	7	0.5496		
Lack of Fit	1.55	3	0.5166	0.8994	0.5153 (not significant)
Pure Error	2.30	4	0.5744		
Cor Total	49.92	12			
R^2: 0.9229		Adjusted R^2: 0.8679			Predicted R^2: 0.7096

p-value less than 0.05 is significant at $\alpha = 0.05$
Lack of fit is not significant at a *p*-value of more than 0.05

(60°C and 2.3 m/s). In terms of the model, the coefficient determination (R^2), Adj-R^2, and Pred-R^2 values were 0.9229, 0.8679, and 0.7096, respectively, as shown in Table 5. Besides the higher R^2 value, the difference between Adj-R^2 and Pred-R^2 values was also less than 0.2, which reflects a reasonable agreement. On top of that, it is clearly seen from Table 5 that the model for color change response was significant at $p<0.05$ with a non-significant lack of fit of ($p>0.05$). Since the interaction term (AB) was insignificant, the term was removed; hence, the model of equation 10 was suggested with higher adjusted and predicted R^2 values (0.8737 and 0.7624), respectively. All these values and findings indicated that model equation 10 can be suggested to predict the response for given levels of each factor on the color changes of desiccated coconut. It was also supported by the residual data in Figure 7, which found no outliers.

$$Color\ changes = 3.17 + 1.56A - 0.6505B + 1.75A^2 + 0.7620B^2 \quad [10]$$

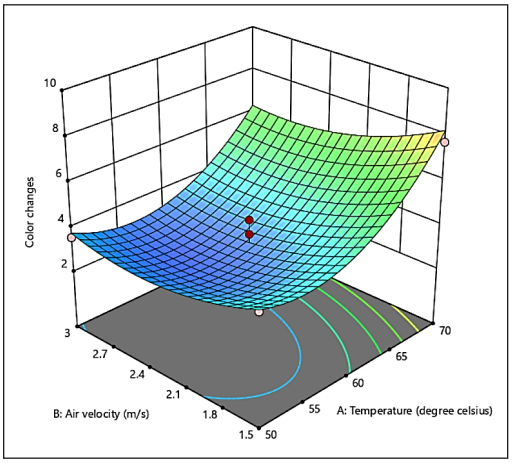

Figure 6. 3D plot of color changes against temperature and air velocity

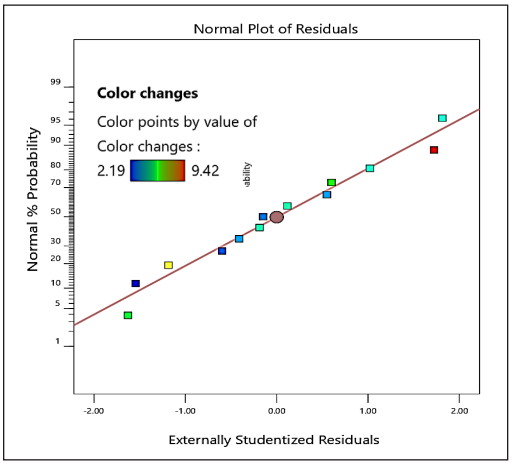

Figure 7. Normal plot of residuals for color changes

Effect of Infrared Drying Parameters on Whiteness Index (WI)

Table 6 shows that both linear (A, B) and quadratic terms (A^2, B^2) of drying temperature and air velocity substantially affected the whiteness index of desiccated coconut. In view of this, drying temperature (linear and quadratic terms) remains the main factor for WI response, and this can be proven by the *p*-value of less than 0.05 with higher *F*-values of 27.17 and 29.49, respectively, compared to air velocity. Overall, the whiteness index of desiccated coconut varies from 66.50±1.272 to 73.00±0.110 for all conditions of variables (temperature and air velocity) during infrared drying. It's noteworthy to note in Figure 8 that the curvature of the 3D surface of WI was somewhat different from that of the 3D surface of color changes.

Table 6
ANOVA results for whiteness index (WI) response

Term	Sum of squares	df	Mean square	F-value	p-value
Model	36.02	5	7.20	13.33	0.0018
A-Temperature	14.69	1	14.69	27.17	0.0012
B-Air velocity	3.04	1	3.04	5.63	0.0495
AB	0.2712	1	0.2712	0.5017	0.5017
A^2	15.94	1	15.94	29.49	0.0010
B^2	3.46	1	3.46	6.41	0.0392
Residual	3.78	7	0.5406		
Lack of Fit	1.41	3	0.4713	1.74	0.5570 (not significant)
Pure Error	2.37	4	0.5926		
Cor Total	39.81	12			
R^2: 0.9049		Adjusted R^2: 0.8370			Predicted R^2: 0.6567

p-value less than 0.05 is significant at $\alpha = 0.05$
Lack of fit is not significant at a *p*-value of more than 0.05

The minimum value of color changes (2.19±0.098), for example, indicates the highest value of the whiteness index (73.00±0.110) when desiccated coconut is dried using infrared drying at (60°C and 2.3 m/s). Nevertheless, the whiteness index was at its lowest at (74°C and 2.3 m/s). In other words, the lower the color changes, the higher the whiteness index of desiccated coconut. This result may have been caused by the destruction of some temperature-sensitive color-attributing pigments at higher temperatures, which would increase color variance and lower the whiteness index (Bhat et al., 2020). Therefore, it can be said that the WI of desiccated coconut was inversely related to the color changes that occurred during infrared drying.

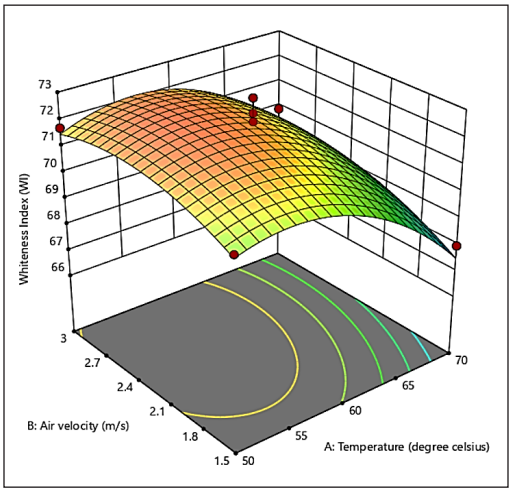

Figure 8. 3D plot of whiteness index against temperature and air velocity

Using hot air drying, Jongyingcharoen et al. (2019) also conducted another study and found that the drying duration also affected the dried coconut's whiteness index (WI), with shorter drying times producing whiter dried coconut. The longer drying times with lower drying temperatures probably led to the enzymatic browning of desiccated coconut. This phenomenon could also be seen at the lowest drying temperature and air velocity during infrared drying. Nevertheless, the non-enzymatic browning of desiccated

coconut caused by the radiation of higher temperatures was more impactful to the whiteness index. Meanwhile, the optimized model in equation 11 was introduced after removing the insignificant interaction term (AB). The probability plot of whiteness index residuals in Figure 9 further verified the model's suitability.

$$\textit{Whiteness Index (WI)} = 72.0 - 1.35A + 0.6197B - 1.54A^2 - 0.7184B^2 \quad [11]$$

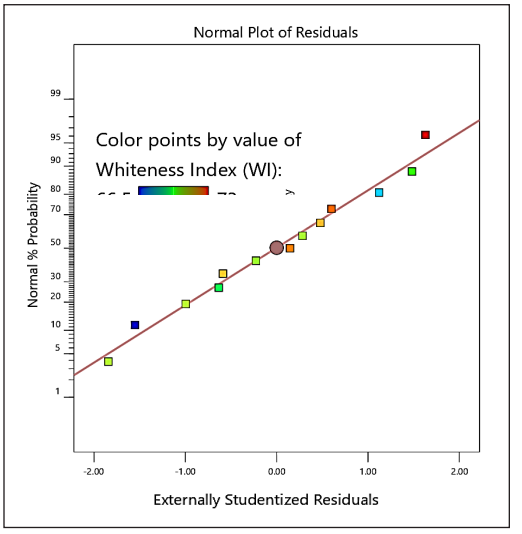

Figure 9. Normal plot of residuals for whiteness index

Optimization of Infrared Drying Process Parameter and Validation of Model

The optimization aimed to maximize the desiccated coconut's whiteness index while minimizing the drying time, SEC, and color changes. Solution 1 in Table 7 was chosen as the optimum condition for infrared drying of desiccated coconut. The optimum IR temperature and air velocity for drying desiccated coconut in an infrared dryer were 61°C and 2.2 m/s, respectively. These independent variables led to the following dependent variables: drying time of 36.826 minutes, SEC of 19.821 kWh/kg, color changes (ΔE) of 3.431, and whiteness index (WI) of 71.762, with desirability of 0.827. Tables 8 and 9 compare the results between experiments and predicted under the optimum conditions.

Table 7
Result and solutions of optimization by desirability value of RSM

Number	Temperature (°C)	Air velocity (m/s)	Drying time (min)	SEC (kWh/kg)	ΔE	WI	Desirability
1	61.059	2.172	36.826	19.821	3.431	71.762	0.827 (Selected)
2	61.096	2.180	36.833	19.836	3.429	71.764	0.827

Table 8
The predicted and measured experimental values for four responses at optimum drying condition

Run	Drying time (min)	SEC (kWh/kg)	Color changes (ΔE)	Whiteness Index (WI)
Experiment 1	36.930	19.960	3.286	71.890
Experiment 2	36.100	19.511	3.636	71.576
Experiment 3	37.020	20.008	3.565	71.618
Predicted value	36.826	19.821	3.431	71.762

Table 9
Validation of optimum infrared drying conditions for desiccated coconut

Response	Selected range	Predicted value	Experimental values[1]	Relative Difference[2]	% error[3]
Drying time (min)	Minimum	36.826	36.683±0.507	0.017	0.39
SEC (kWh/kg)	Minimum	19.821	19.826±0.274	-0.076	0.03
ΔE	Minimum	3.431	3.496±0.185	-0.063	1.86
WI	Maximum	71.762	71.695±0.170	0.285	0.09

[1]Experimental values were expressed as mean ± standard deviation
[2](Predicted-Experimental)
[3]The % error $= \left[\left|M_{ev} - M_{pv}\right|/M_{ev}\right] \times 100$

Verification experiments under optimum conditions show the percentage error values of less than 2%, demonstrating the appropriateness of the developed models. According to (Nordin et al., 2019; Sadeghi et al., 2019; Tajudin et al., 2021), a percentage error of less than 10% was considered acceptable. Therefore, the optimum process parameters of discovered infrared drying can be recommended for producing high-quality desiccated coconut in which the drying time and SEC were decreased while maintaining the final product's color quality. The optimal conditions for validation are shown in Figure 10, where there is no discernible color difference between fresh shredded coconut and desiccated coconut. It unquestionably shows that the color of desiccated coconut could be conserved and retained under ideal infrared drying conditions.

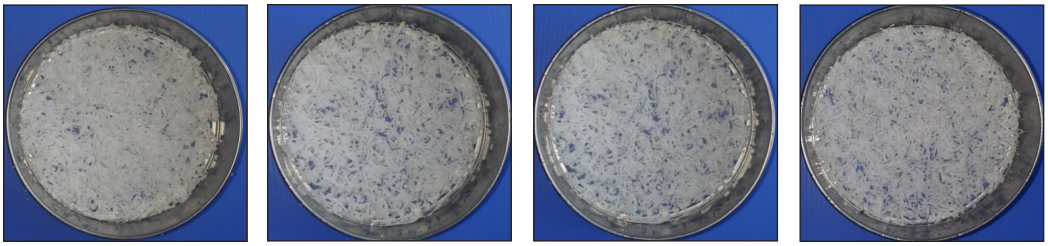

(a) (b) (c) (d)

Figure 10. Pictures of fresh sample (a) and dried samples at optimal infrared drying conditions (b, c and d) for validation

CONCLUSION

This study demonstrated the effects of infrared drying conditions with a fixed power intensity of 600 Watts and an emitter distance of 15 cm from the thin layer desiccated coconut sample. The drying temperature, followed by air velocity, was the most significant factor affecting all responses. Nevertheless, the interaction factor was insignificant in every response with $p>0.05$. Aside from a quicker drying period at a higher temperature of 74°C, it appeared to have a detrimental impact on color changes in comparison to

freshly shredded coconut. On the other hand, higher air velocity prolonged the drying time and increased the SEC. The drying time response was closely related to the SEC response, as the results and the 3D surface plot had almost the same pattern. In contrast, minimum color changes would determine the desiccated coconut's maximum whiteness index value. Although higher air velocity had no advantage in reducing drying time and SEC, it plays a vital role in achieving the product's final quality by retaining the whiteness index of desiccated coconut. The optimal experimental conditions for infrared drying of desiccated coconut were 61°C (drying temperature) and 2.2 m/s (air velocity) with minimum drying time, SEC, ΔE, and maximum WI. Suggested models for each response were well accepted with (p<0.05), insignificant lack of fit, and higher value of coefficient determination. The variance between predicted and experimental results was (<10.0%) within the acceptable range, providing strong validation for the optimization models. These optimized models could be used as a reference for the commercial application of infrared drying on desiccated coconut.

ACKNOWLEDGEMENTS

The Malaysian Agricultural Research and Development Institute (MARDI) and Universiti Putra Malaysia (UPM) provided funding and advice for this research project. The authors also thank Universiti Putra Malaysia for funding their research with the Inisiatif Putra Siswazah Research Grant (GP-IPS/2022/9722300) and VOT number 972230.

REFERENCES

Abidin, M. H. Z., Sabudin, S., Zakaria, J. H., & Batcha, M. F. M. (2014). Thin layer modeling of grated coconut drying. *Applied Mechanics and Materials*, *660*, 367–372. https://doi.org/10.4028/www.scientific.net/AMM.660.367

Aboud, S. A., Altemimi, A. B., Al-hiiphy, A. R. S., Yi-chen, L., & Cacciola, F. (2019). A comprehensive review on infrared heating. *Molecules*, *24*(22), Article 4125. https://doi.org/10.3390/molecules24224125

Adak, N., Heybeli, N., & Ertekin, C. (2017). Infrared drying of strawberry. *Food Chemistry*, *219*, 109–116. https://doi.org/10.1016/j.foodchem.2016.09.103

Adoyo, G. O., Sila, D. N., & Onyango, A. N. (2021). Physico-chemical properties of kernel from coconut (Cocos nucifera L.) varieties grown at the Kenyan Coast. *African Journal of Food Science*, *15*(8), 313–321. https://doi.org/10.5897/ajfs2021.2116

Aggary, S., & Arowanti, O. (2012). Modelling the drying characteristics of osmosised coconut strips at constant air temperature. *Journal of Food Processing & Technology*, *3*(4), Article 1000151. https://doi.org/10.4172/2157-7110.1000151

Alouw, J. C. (2023). *Towards the 2023 sustainable development goals summit*. International Coconut Commuity. https://www.unescap.org/sites/default/d8files/event-documents/ICC_Statement - International Coconut Community_AI3.pdf

AOAC. (2005). *In official methods of analysis* (18th ed.). Association of Officiating Analytical Chemists.

Bhat, M. I., Shahi, N. C., Singh, A., & Malik, S. (2020). Response surface optimization of quality parameters of turmeric slices in an innovative infrared assisted hybrid solar dryer. *International Journal of Chemical Studies*, *8*(3), 1958–1967. https://doi.org/10.22271/chemi.2020.v8.i3aa.9492

Delfiya, D. S. A., Prashob, K., Murali, S., Alfiya, P. V., Samuel, M. P., & Pandiselvam, R. (2021). Drying kinetics of food materials in infrared radiation drying: A review. *Journal of Food Process Engineering*, *45*(6), Article e13810. https://doi.org/10.1111/jfpe.13810

Doymaz, I., Kipcak, A. S., & Piskin, S. (2015). Characteristics of thin-layer infrared drying of green bean. *Czech Journal of Food Sciences*, *33*(1), 83–90. https://doi.org/10.17221/423/2014-CJFS

Erbay, Z., & Icier, F. (2009). Optimization of hot air drying of olive leaves using response surface methodology. *Journal of Food Engineering*, *91*(4), 533–541. https://doi.org/10.1016/j.jfoodeng.2008.10.004

Fernando, A. J., Gunathunga, C., Brumm, T., & Amaratunga, S. (2021). Drying turmeric (Curcuma longa L.) using far-Infrared radiation: Drying characteristics and process optimization. *Journal of Food Process Engineering*, *44*(9), Article e13780. https://doi.org/10.1111/jfpe.13780

Golpour, I., Kaveh, M., Amiri Chayjan, R., & Guiné, R. P. F. (2020). Optimization of infrared-convective drying of white mulberry fruit using response surface methodology and development of a predictive model through artificial neural network. *International Journal of Fruit Science*, *20*(2), S1015-S1035. https://doi.org/10.1080/15538362.2020.1774474

Huang, X., Li, W., Wang, Y., & Wan, F. (2021). Drying characteristics and quality of Stevia rebaudiana leaves by far-infrared radiation. *LWT-Food Science and Technology*, *140*, Article 110638. https://doi.org/10.1016/j.lwt.2020.110638

International Coconut Community. (2009). *APCC quality standard.* International Coconut Community. https://coconutcommunity.org/viewpdf/apcc_quality_standards_for_coconut_products/4

Isik, A., Ozdemir, M., & Doymaz, I. (2019). Infrared drying of bee pollen: Effects and impacts on food components. *Czech Journal of Food Sciences*, *37*(1), 69–74. https://doi.org/10.17221/410/2017-CJFS

Jafari, F., Movagharnejad, K., & Sadeghi, E. (2020, April 15-17). *Investigation of drying kinetics of eggplant slices using infrared.* [Paper presentation]. The 11th International Chemical Engineering Congress & Exhibition (IChEC 2020), Guilan, Iran.

Jongyingcharoen, J. S., Wuttigarn, P., & Assawarachan, R. (2019). Hot air drying of coconut residue: Shelf life, drying characteristics, and product quality. *IOP Conference Series: Earth and Environmental Science*, *301*(1), Article 012033. https://doi.org/10.1088/1755-1315/301/1/012033

Kaveh, M., Abbaspour-Gilandeh, Y., Fatemi, H., & Chen, G. (2021). Impact of different drying methods on the drying time, energy, and quality of green peas. *Journal of Food Processing and Preservation*, *45*(6), Article e15503. https://doi.org/10.1111/jfpp.15503

Kıan-pour, N. (2020). Fundamental drying techniques applied in food science and technology. *International Journal of Food Engineering Research, 6*(1), 35-63.

Kipcak, A. S., & Doymaz, İ. (2020). Microwave and infrared drying kinetics and energy consumption of cherry tomatoes. *Chemical Industry and Chemical Engineering Quarterly*, *26*(2), 203–212. https://doi.org/10.2298/CICEQ190916039K

Kipcak, A. S., Doymaz, İ., & Moroydor-Derun, E. (2019). Infrared drying kinetics of blue mussels and physical properties. *Chemical Industry and Chemical Engineering Quarterly, 25*(1), 1-10. https://doi.org/10.2298/CICEQ170808014K

Koca, I., Yilmaz, V. A., Odabas, I. H., & Tekguler, B. (2018). Optimization of drying parameters for chestnut fruits using central composite design. *Acta Horticulturae*, *1220*, 221–226. https://doi.org/10.17660/ActaHortic.2018.1220.31

Lamdande, A. G., Prakash, M., & Raghavarao, K. S. M. S. (2018). Storage study and quality evaluation of fresh coconut grating. *Journal of Food Processing and Preservation*, *42*(1), Article e13350. https://doi.org/10.1111/jfpp.13350

Madamba, P. S. (2003). Thin layer drying models for osmotically pre-dried young coconut. *Drying Technology*, *21*(9), 1759–1780. https://doi.org/10.1081/DRT-120025507

Madhiyanon, T., Phila, A., & Soponronnarit, S. (2009). Models of fluidized bed drying for thin-layer chopped coconut. *Applied Thermal Engineering*, *29*(14–15), 2849–2854. https://doi.org/10.1016/j.applthermaleng.2009.02.003

Majdi, H., Esfahani, J. A., & Mohebbi, M. (2019). Optimization of convective drying by response surface methodology. *Computers and Electronics in Agriculture*, *156*, 574–584. https://doi.org/10.1016/j.compag.2018.12.021

Manohar, M., Joseph, J., Selvaraj, T., & Sivakumar, D. (2013). Application of desirability-function and RSM to optimise the multi-objectives while turning Inconel 718 using coated carbide tools. *International Journal of Manufacturing Technology and Management*, *27*(4–6), 218–237. https://doi.org/10.1504/IJMTM.2013.058899

Moses, J. A. A., Paramasivan, K., Sinija, V. R. R., Alagusundaram, K., Brijesh kumar, T., Alugusundaram, K., & Kumar, B. (2013). Effect of microwave treatment on drying characteristics and quality parameters of thin layer drying of coconut Jeyan. *Asian Journal of Food and Agro-Industry*, *6*(2), 72–85.

Muga, F. C., Marenya, M. O., & Workneh, T. S. (2021). Modelling the Thin-layer drying kinetics of marinated beef during infrared-assisted hot air processing of biltong. *International Journal of Food Science*, *2021*(1), Article 8819780. https://doi.org/10.1155/2021/8819780

Ngampeerapong, C., & Chavasit, V. (2019). Nutritional and bioactive compounds in coconut meat of different sources: Thailand, Indonesia and Vietnam. *Chiang Mai University Journal of Natural Sciences*, *18*(4), 562–573. https://doi.org/10.12982/CMUJNS.2019.0037

Niamnuy, C., & Devahastin, S. (2005). Drying kinetics and quality of coconut dried in a fluidized bed dryer. *Journal of Food Engineering*, *66*(2), 267–271. https://doi.org/10.1016/j.jfoodeng.2004.03.017

Nor, N. A. A. M., Arif, E. E. E., Omar, N. R. N., Abidin, A. Z. Z., Muhammad, R. M., Rahim, H., Nazmi, M. S., & Sulaiman, N. H. (2020). Total productivity and technical efficiency of coconuts in Malaysia. *Economic and Technology Management Review*, *15*, 11–22.

Nordin, R., Rozalli, N. H. M., & Yang, T. A. (2019). Application of response surface methodology to optimize the drying conditions of black tea using a superheated steam dryer. *International Journal of Food Studies*, *8*(2), 81–92. https://doi.org/10.7455/ijfs/8.2.2019.a8

Nurkhoeriyati, T., Kulig, B., Sturm, B., & Hensel, O. (2021). The effect of pre-drying treatment and drying conditions on quality and energy consumption of hot air-dried celeriac slices: Optimisation. *Foods*, *10*(8), Article 1758. https://doi.org/10.3390/foods10081758

Omolola, A. O., Jideani, A. I. O., Kapila, P. F., & Jideani, V. A. (2015). Optimization of microwave drying conditions of two banana varieties using response surface methodology. *Food Science and Technology (Brazil)*, *35*(3), 438–444. https://doi.org/10.1590/1678-457X.6700

Pan, Z. (2021). Innovative infrared heating technologies for food and agricultural processing. *Technology & Innovation*, *21*(4), 1–16. https://doi.org/10.21300/21.4.2020.8

Park, B. S., Kang, T. H., Lee, J. H., Choi, J. M., & Han, C. S. (2015). Drying Characteristics of radishes using far infrared ray dryer. *Journal of Biosystems Engineering*, *40*(1), 61–66. https://doi.org/10.5307/jbe.2015.40.1.061

Patil, U., Benjakul, S., Prodpran, T., Senphan, T., & Cheetangdee, N. (2017). A comparative study of the physicochemical properties and emulsion stability of coconut milk at different maturity stages. *Italian Journal of Food Science*, *29*(1), 145–157. https://doi.org/10.14674/1120-1770/ijfs.v536

Pestaño, L. D. B. (2015, April 12). *Mathematical modeling of the drying process of coconut meat*. [Paper presentation]. Third International Conference on Advances in Applied Science and Environmental Engineering, London, United Kingdom. https://doi.org/10.15224/978-1-63248-055-2-80

Riadh, M. H., Ahmad, S. A. B., Marhaban, M. H., & Soh, A. C. (2015). Infrared heating in food drying: An overview. *Drying Technology*, *33*(3), 322–335. https://doi.org/10.1080/07373937.2014.951124

Sadeghi, E., Asl, A. H., & Movagharnejad, K. (2019). Mathematical modelling of infrared-dried kiwifruit slices under natural and forced convection. F*ood Science & Nutrition, 7*(11), 3589-3606. https://doi.org/10.1002/fsn3.1212

Sadeghi, E., Movagharnejad, K., & Asl, A. H. (2020). Parameters optimization and quality evaluation of mechanical properties of infrared radiation thin layer drying of pumpkin samples. *Journal of Food Process Engineering*, *43*(2), Article e13309. https://doi.org/10.1111/jfpe.13309

Sahari, Y., Anuar, M. S., Nor, M. Z. M., & Ghani, N. H. A. (2023). Characterization of single and hybrid mode drying of desiccated coconut. *Journal of Food Engineering*, *357*, Article 111628. https://doi.org/10.1016/j.jfoodeng.2023.111628

Sakare, P., Prasad, N., Thombare, N., Singh, R., & Sharma, S. C. (2020). Infrared drying of food materials: Recent advances. *Food Engineering Reviews*, *12*(3), 381–398. https://doi.org/10.1007/s12393-020-09237-w

Salehi, F., & Satorabi, M. (2021). Influence of infrared drying on drying kinetics of apple slices coated with basil seed and xanthan gums. *International Journal of Fruit Science, 21*(1), 519-527. https://doi.org/10.1080/15538362.2021.1908202

Sarkar, A., Ahmed, T., Alam, M., Rahman, S., & Pramanik, S. K. (2020). Influences of osmotic dehydration on drying behavior and product quality of coconut (Cocos nucifera). *Asian Food Science Journal*, *15*(3), 21–30. https://doi.org/10.9734/afsj/2020/v15i330153

Sharma, S., Vaidya, D., Kaushal, M., & Gupta, A. (2020). Optimization of process parameters for hybrid drying of apple. *International Journal of Fruit Science*, *9*(1), 1756–1760. https://doi.org/10.1080/15538362.2020.1812017

Shingare, S. P., & Thorat, B. N. (2012). Dehydration of coconut using an infrared dryer. *International Journal of Biotechnology, Chemical & Environmental Engineering*, *1*(3), 56–63.

Sossa, J. W. Z., Orozco, G. L., Murillo, L. M. G., Osorio, M. P., & Suarez, N. S. (2021). Infrared drying trends applied to fruit. *Frontiers in Sustainable Food Systems, 5*, Article 650690. https://doi.org/10.3389/fsufs.2021.650690

Srinivas, M. S., Champawat, P. S., & Jain, S. K. (2018). Effect of infrared radiation on the drying kinetics of osmosed papaya cubes. *International Journal of Chemical Studies*, *6*(3), 1696–1698.

Šumić, Z., Vakula, A., Tepić, A., Čakarević, J., Vitas, J., & Pavlić, B. (2016). Modeling and optimization of red currants vacuum drying process by response surface methodology (RSM). *Food Chemistry*, *203*, 465–475. https://doi.org/10.1016/j.foodchem.2016.02.109

Tajudin, N. H. A., Ang, W. L., Tasirin, S. M., & Rosli, M. I. (2021). Process variables optimization for heat pump drying of Roselle Calyx by using response surface methodology. *Jurnal Kejuruteraan*, *33*(4), 903–914. https://doi.org/10.17576/jkukm-2021-33(4)-13

Tajudin, N. H. A., Tasirin, S. M., Ang, W. L., Rosli, M. I., & Lim, L. C. (2019). Comparison of drying kinetics and product quality from convective heat pump and solar drying of Roselle calyx. *Food and Bioproducts Processing*, *118*, 40–49. https://doi.org/10.1016/j.fbp.2019.08.012

Torki-Harchegani, M., Ghanbarian, D., Maghsoodi, V., & Moheb, A. (2017). Infrared thin layer drying of saffron (Crocus sativus L.) stigmas: Mass transfer parameters and quality assessment. *Chinese Journal of Chemical Engineering, 25*(4), 426-432. https://doi.org/10.1016/j.cjche.2016.09.005

Wang, H., Liu, D., Yu, H., Wang, D., & Li, J. (2019). Optimization of microwave coupled hot air drying for chinese yam using response surface methodology. *Processes*, *7*(10), Article 745. https://doi.org/10.3390/pr7100745

Wu, X. F., Zhang, M., & Li, Z. (2019). Influence of infrared drying on the drying kinetics, bioactive compounds and flavor of Cordyceps militaris. *LWT-Food Science and Technology, 111*, 790-798. https://doi.org/10.1016/j.lwt.2019.05.108

Wynn, T. (2017). Nutrition studies on mature and immature coconut meat and coconut water. *Yadanabon University Research Journal*, *8*(1), 1-8.

Yadav, G., Gupta, N., Sood, M., & Anjum, N. (2020). Infrared heating and its application in food processing. *The Pharma Innovation Journal*, *9*(2), 142–151.

Yahya, S., Shahrir, A. M., Syariffudden, M. A. A. A., Shafie, A., Shukri, J. S., Zaimi, Z. A. A. M., & Redzuan, S. R. (2020). A study of drying parameters on drying time and colour quality of grated coconut using tumbling mechanism in convective dryer. *Food Research*, *4*(6), 64–69. https://doi.org/10.26656/fr.2017.4(S6).023

Younis, M., Abdelkarim, D., & Zein El-Abdein, A. (2018). Kinetics and mathematical modeling of infrared thin-layer drying of garlic slices. *Saudi Journal of Biological Sciences*, *25*(2), 332–338. https://doi.org/10.1016/j.sjbs.2017.06.011

Zainol, F. A., Arumugam, N., Daud, W. N. W., Suhaimi, N. A. M., Ishola, B. D., Ishak, A. Z., & Afthanorhan, A. (2023). Coconut value chain analysis: A systematic review. *Agriculture*, *13*(7), Article 1379. https://doi.org/10.3390/agriculture13071379

Zeng, Y., Liu, Y., Zhang, J., Xi, H., & Duan, X. (2019). Effects of far-infrared radiation temperature on drying characteristics, water status, microstructure and quality of kiwifruit slices. *Journal of Food Measurement and Characterization*, *13*(4), 3086–3096. https://doi.org/10.1007/s11694-019-00231-3

Zhou, L., Guo, X., Bi, J., Yi, J., Chen, Q., Wu, X., & Zhou, M. (2017). Drying of garlic slices (Allium sativum L.) and its effect on thiosulfinates, total phenolic compounds and antioxidant activity during infrared drying. *Journal of Food Processing and Preservation*, *41*(1), Article e12734. https://doi.org/10.1111/jfpp.12734

Pertanika J. Sci. & Technol. 33 (S1): 23 - 41 (2025)

PERTANIKA JOURNALS

SCIENCE & TECHNOLOGY

Journal homepage: http://www.pertanika.upm.edu.my/

Testing and Evaluation of Newly Developed Harvesting Basket Among Male Pineapple Harvesters in Johor, Malaysia

Siti Nur Alya Suhaimi[1], Emilia Zainal Abidin[1]*, Mohd Hasif Malik @ Malek[1], Sharifah Norkhadijah Syed Ismail[1], Irniza Rasdi[1], Karmegam Karuppiah[1], Mohd Shahrizal Dolah[2] and Noor Hassim Ismail[3]

[1]Department of Environmental and Occupational Health, Faculty of Medicine and Health Sciences, Universiti Putra Malaysia, UPM Serdang, 43400, Selangor, Malaysia
[2]Department of Industrial Design, Faculty of Design and Architecture, Universiti Putra Malaysia, UPM Serdang, 43400, Selangor, Malaysia
[3]Department of Public Health, Faculty of Medicine, Kompleks Pendidikan Perubatan Canselor Tuanku Ja'afar, Jalan Yaacob Latif, Bandar Tun Razak, 56000 Cheras, Kuala Lumpur, Malaysia

ABSTRACT

This study evaluates a newly developed harvesting basket used in manual pineapple harvesting work in Malaysia, specifically focusing on its impact on physiological workload, body part discomfort, perception of harvesters and risk level of musculoskeletal disorders (MSD). An experimental study was conducted among pineapple harvesters in Muar, Johor. Data from 25 harvesters were collected using questionnaires, including the Borg CR-10 Scale, to assess body part discomfort using traditional rattan and newly developed harvesting baskets. The physiological workload was measured to record heart rates and calculate the workload. The risk level of awkward posture during harvesting tasks was assessed using the Rapid Entire Body Assessment (REBA) tool for both baskets. Descriptive analysis was used to analyze respondents' perceptions, while statistical tests determined performance differences between the two baskets. The results revealed that workers experienced a significant reduction in physiological workload between the use of rattan (6.6 ± 0.9 kJ-min) and prototype baskets (5.0 ± 1.1 kJ-min). Harvesters experienced reduced discomfort when using new harvesting baskets. The postural analysis indicated a decrease in the risk level of awkward posture from high (rattan) to medium (prototype) when harvesting. Most harvesters perceived that the new harvesting basket fulfilled their needs. In conclusion, the newly developed harvesting basket demonstrated the potential to improve work posture, discomfort and physiological workload of pineapple harvesters, thereby

ARTICLE INFO

Article history:
Received: 08 November 2023
Accepted: 05 November 2024
Published: 31 January 2025

DOI: https://doi.org/10.47836/pjst.33.S1.02

E-mail addresses:
alyasuhaimi@gmail.com (Siti Nur Alya Suhaimi)
za_emilia@upm.edu.my (Emilia Zainal Abidin)
mhasif.malek@yahoo.com (Mohd Hasif Malik @ Malek)
norkhadijah@upm.edu.my (Sharifah Norkhadijah Syed Ismail)
irniza@upm.edu.my (Irniza Rasdi)
megam@upm.edu.my (Karmegam Karuppiah)
shahrizal@upm.edu.my (Mohd Shahrizal Dolah)
ramalbaru@gmail.com (Noor Hassim Ismail)
* Corresponding author

ISSN: 0128-7680
e-ISSN: 2231-8526

reducing the potential of obtaining MSD disease. Adopting ergonomically designed work tools aligns with the MyGAP policy and supports improving workers' health in pineapple harvesting operations.

Keywords: Awkward posture, discomfort, ergonomic tools, physiological workload, pineapple harvesting

INTRODUCTION

The pineapple industry plays a vital role in Malaysia's socio-economic development by improving the livelihoods of smallholder farmers through income generation. A recent study showed that the benefit-cost ratio for the profitability of pineapple farming among 191 smallholder farmers in Johor is 1.72, indicating that pineapple plantations are economically viable and generate profit (Suhaimi & Fatah, 2019). Additionally, it contributes to the overall economic development and supports related economic activities such as packaging, transportation and value-added income-generating opportunities, particularly in Johor. The state of Johor emerged and remained as the largest pineapple producer since 2011 up till today, with an estimated production quantity of 267,913 metric tons (MPIB, 2018) and a total hectare of 8112.06 hectares, followed by Sarawak and Sabah (Suhaimi & Fatah, 2019).

Work in pineapple plantations is characterized by its labor-intensive nature and high physical exertion. Tasks such as harvesting, cultivating, weeding and land preparation involve significant muscle strain and discomfort (Ya'acob et al., 2018). Pineapple plantation workers often encounter posture-related issues, primarily due to the demanding nature of the work and the absence of automation and ergonomic tools (Tamrin & Aumran, 2014). Consequently, these workers face an increased risk of developing musculoskeletal disorders (MSDs) from prolonged symptoms (Rani, Abidin et al., 2016). The prevalence of overall musculoskeletal symptoms (MSS) among pineapple plantation workers was 87.0% and was highest for the lower back (64.8%). The risk for MSDs for pineapple plantation workers may arise from awkward postures, forceful exertion and repetitive movements (Rani, Abidin et al., 2016).

There has been research and reports about mechanized harvesting of fruits to reduce labor intensity and improve harvesting efficiency, including in Malaysia. However, the current market still lacks options for ergonomically designed manual harvesting baskets specifically tailored for pineapple plantations on peat soil (Liu et al., 2022; Mezlan et al., 2019; Rani, Rashid et al., 2016; Yusoff et al., 2014). Rattan fruit harvesting baskets remain the primary equipment used in pineapple harvesting both in small- and large-scale plantations across Johor (Rani, Rashid et al., 2016). Many harvesters modify their rattan baskets to accommodate heavier loads, causing the full-load basket to exceed the safe limit of an ideal lifting load of 23 kg (Kamarudin et al., 2013). However, apart from carrying heavy loads, harvesters are also required to bend their bodies extensively forward during the pineapple unloading process. Specifically, workers need to bend at the waist at an angle of 60° (beyond the safe

limit of 45°) to tip the fruits out of the basket due to the basket's design limitations during unloading (Figure 1). The use of raffia rope as the basket strap exacerbates the situation, as it is non-adjustable and does not provide a secure fit, leading to high contact stress on the harvester's shoulder. The flawed design of the existing basket, including inadequate load capacity and a lack of consideration for the tasks at hand (Mezlan et al., 2019), exposes workers to ergonomic risks, especially MSDs, due to awkward postures and repetitive movements during the harvesting process (Rani, Rashid et al., 2016).

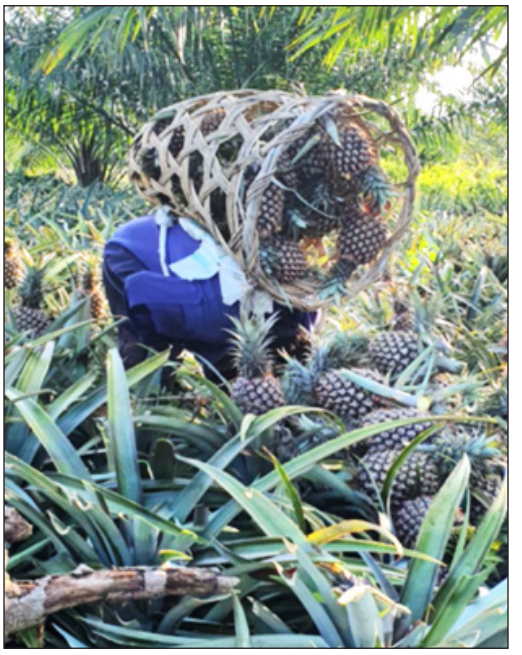

Figure 1. Unloading of pineapples onto the ground by a worker using a rattan pineapple harvesting basket

Given the prevalent challenges faced by pineapple plantation workers in Malaysia, the development of an ergonomically designed harvesting basket is essential to enhance their work conditions. The authors addressed this concern in previous research by creating a novel pineapple harvesting prototype basket (Mezlan et al., 2019). The primary objective of the newly developed basket was to alleviate issues associated with poor posture, contact stress and excessive load burden among workers, thereby reducing the occurrence of reported musculoskeletal symptoms (MSS) over an extended period. The design of the basket incorporated a latch opening into the front side of the rectangular fruit basket, enabling the latch to pivot outward when opened (Mezlan et al., 2019). Adjustable shoulder straps and foam padding were incorporated on one side of the basket, specifically where it comes into contact with the user's back. The new ergonomic basket also implemented a 30% reduction in size (Mansor, 2020). This subsequent study measured several indicators, including physiological parameters such as heart rate, while comparing the use of the rattan basket with the prototype basket, revealing the need for improvements in the basket design because results were not favorable to reduce the probability of workload (average heart rate: 104.9±14.8 beats/minute vs. 108.4±14.7 beats/minute; $p>0.05$) and exertion.

A newer version of the pineapple harvesting basket was developed with the updated findings from the study outcomes in Mansor (2020). There is a need to evaluate and test the newer prototype basket among harvesting workers to provide quantitative data to validate the present design. Perceived musculoskeletal discomfort has been used to indicate early signs of musculoskeletal pain using other studies as a reference (Galinsky et al., 2007;

McLean et al., 2001). Other signs that can predict musculoskeletal pain include bodily discomfort such as soreness, tension, fatigue or tremors (Reenen et al., 2008). Perceived discomfort can be an indicator of early signs of pain arising from short-term biomechanical load on the musculoskeletal system. These short-term effects, coupled with a lack of recovery time, in addition to being recurrent, can lead to musculoskeletal pain (Beek & Frings-Dresen, 1998).

As such, this study aims to evaluate and test a newly developed harvesting basket to assess the potential of its ergonomic design in reducing the discomfort, physiological workload and risk level of awkward posture during unloading tasks experienced by pineapple harvesters. Additionally, the study aims to examine the perceptions of harvesters regarding the new basket to ascertain opinions on satisfaction. The development of the new harvesting basket is expected to improve safety, health, and well-being among agricultural farmers and workers. By promoting the adoption of safe work methods and utilizing enhanced tools and techniques, the new basket is anticipated to facilitate long-term benefits for the workers in terms of their safety and overall welfare.

The academic contributions of this study lie in its comprehensive evaluation of the newly developed pineapple harvesting basket's impact on various critical aspects of manual pineapple harvesting work in Malaysia. This study offers empirical evidence of improvements from a newly developed tool, providing valuable insights into the potential ergonomic benefits of improving the work process. The investigation performed in this study delves into harvester perceptions, serving as an essential step toward understanding user acceptance and facilitating the adoption of ergonomically designed work tools in agricultural practices, which can have implications for improving workers' health and well-being.

MATERIALS AND METHODS

Study Design and Sample Size

This study adopts an experimental design. The research location was purposefully selected as Muar, a district and town in the state of Johor, in the southern part of Peninsular Malaysia, and is known for its pineapple plantation activities.

For the sample size calculation, a formula for sample size estimation with single group mean and standard deviation was used (Kang et al., 2008). Using the study by Mezlan et al. (2019), the means and standard deviations of heart rate measurements were referred to and used for calculations. Sample size estimation was calculated at 12 and with the addition of 10% non-response, a total of 14 sample sizes was required. However, to ensure minimal clinically important effects are observed, the sample size was raised to 25. It is supported by Žunkovič et al. (2023), where the recommended range of 19 to 300 subjects are required to show the minimal clinical effects for heart rate at standard deviations of more than 30%.

Newly Developed Harvesting Basket

The research team developed the new harvesting basket, incorporating ergonomic features to assist harvesters in harvesting tasks (MyIPO Copyright Registration AR2023W02635). It is an upgraded version of the harvesting basket modified from the previous work by the authors (Mezlan et al., 2019). Figure 2 illustrates the design of the new harvesting basket, which was tested in this study. Stainless steel was used as the material to reduce the weight of the basket. The opening latch installed at the bottom of the basket allows for easier unloading of pineapples onto the ground without excessive bending. A single-hand operation on the lever will open the bottom opening and release the fruits, and when the handle to the cable latch is pulled, this closes the bottom opening and locks it back into place. The back structure will evenly distribute the load of the basket on the body, and the adjustable shoulder strap and padded back will provide comfort and reduce contact stress.

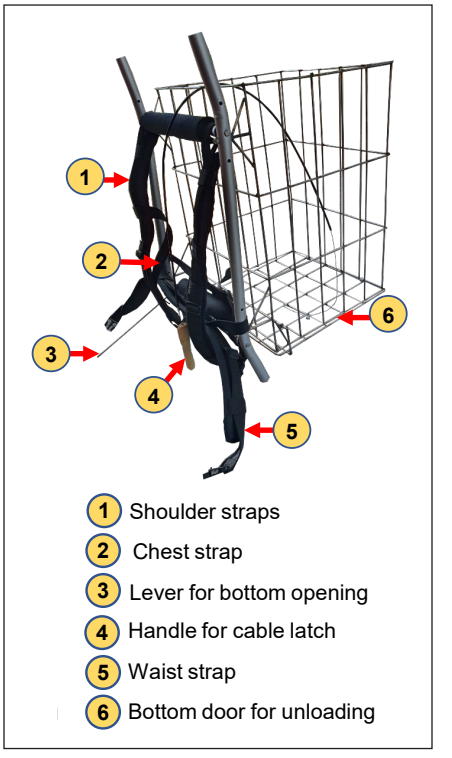

Figure 2. The ISO view of the newly designed pineapple harvesting basket

Approvals and Study Respondents

This experimental study was conducted in December 2021. This study has obtained approval from the Research Ethics Committee at Universiti Putra Malaysia (JKEUPM) with reference number UPM/TNCPI/RMC/JKEUPM/1.4.18.2 (JKEUPM). It has adhered to all necessary ethical guidelines throughout the research process. For this study, approval was obtained from the Malaysian Industrial Pineapple Board (MIPB), and the Muar office helped recruit harvesters registered under the MIPB in the Johor area. A total of 25 pineapple harvesters were recruited as respondents for this study through purposive sampling to conduct testing and evaluation of the traditional harvesting basket, as in Figure 1, while comparing it to the new harvesting basket in Figure 2. The respondents in this study were small-holding pineapple harvesters who were mostly Malaysians.

All harvesting simulation work in this study was carried out at a pineapple collection center in Johor under the MIPB. The area has laterite soil and provides a stable environment for the harvesting simulation exercises. The weather during the data collection period was clear, and the exercises were conducted from morning to before 12 pm only. Inclusion criteria for respondents included male harvesters aged between 18–60 years and engaged

in full-time harvesting. Respondents diagnosed with chronic diseases such as heart disease were excluded from the study.

Study Instrumentation and Methods

Questionnaire

A modified questionnaire was prepared in Malay and was administered by the researcher. The questionnaire comprised several sections and was initiated by items on personal, professional or working information and medical history. The last section of the questionnaire was items on perceptions of the new harvesting basket. However, this questionnaire section was provided to the respondents at the end of the loading and unloading simulation exercises.

Borg's CR-10 Scale

Borg's Category Ratio (CR)-10 scale (Borg, 1998) was used in conjunction with a body map from the Nordic questionnaire to enable respondents to visualize the location of the discomfort better to assess perceived discomfort (Kuorinka et al., 1987). Borg's CR-10 uses a rating from 0 for "nothing at all" to 10 for "excruciating" and is a verbally level-anchored ratio scaling.

The use of Borg's CR-10 for assessing perceived discomfort, such as in this study, has been used in other reported ergonomic-related studies elsewhere (Karuppiah et al., 2012; Waongenngarm et al., 2022; Yusof et al., 2022). The primary use of Borg's CR-10 is to determine exertion, chest pain and other kinds of pain, such as muscle pain, breathlessness, and fatigue. It has the advantage of being easier to use for laypersons.

Rapid Entire Body Assessment (REBA)

The Rapid Entire Body Assessment (REBA) tool was utilized. REBA was developed by Hignett and McAtamney (2000) and is a field tool for practitioners to assess changes in postures and movements. It provides a quantitative measure to compare pineapple unloading tasks while using rattan and a new harvesting basket. It is sensitive enough to capture unpredictable working postures in many industries (Cancela et al., 2014).

During the simulation exercise of loading and unloading pineapple fruits, a video of the activity was recorded for each of the respondents. When the authors returned to the laboratory, the video was viewed on a computer and still frames of unloading postures and movements were generated. These were then assessed using the scoring card provided with the tool. The final REBA score determined the risk level associated with the unloading tasks. In addition, a goniometer was used to measure movement angles where needed. REBA exercise represents the biomechanical aspect that is assessed in this study.

Physiological Workload

Physiological parameters used in this study are heart rate measurement and energy expenditure calculation. Heart rate is an indicator of cardiac stress due to physical workload (Bhattacharyya & Chakrabarti, 2012). Although these parameters are not strong indicators linking directly to MSDs, measurements of heart rate and calculation of energy expenditures are practical values to benchmark and compare the efforts to perform the tasks within a short time interval.

The respondents were provided and wore Fitbit Fitness Smartwatches to measure the average heart rate during the task performance of loading and unloading pineapple fruits using both baskets in two different sessions with a 10-minute break in between. Participants were asked to rest under a shaded area but were asked to refrain from smoking to minimize factors that might contribute to variation in heart rate reading. The recorded measurements were downloaded after the fieldwork and were used to calculate energy expenditure (expressed as kJ/min) using Equation 1 (Bhattacharyya & Chakrabarti, 2012; Varghese et al., 1994):

$$0.159 \times \text{Average Heart Rate (beats per minute)} - 8.72 \quad [1]$$

Flow of Data Collection

Prior to initiating the basket testing simulation, each participant donned a Fitbit Smartwatch to collect data for heart rates during the harvesting procedure. In a single simulation round, the harvesters collected 20 pineapple fruits using the traditional rattan basket while being video recorded. Following a 10-minute rest period, participants responded to the questions to gauge their discomfort levels linked to using the rattan basket.

The simulation process was then replicated utilizing the new harvesting basket, maintaining consistent conditions. In this phase, participants again harvested 20 pineapples using the new basket while video-recorded. Following the physical activity, questions on perceived discomfort were administered to the participants again to assess the use of the new harvesting basket.

Next, a supplementary set of questions pertaining to usage perceptions, which the authors formulated, was provided to the respondents. These supplementary perception items were designed to obtain feedback regarding the new basket's ease of use, comfort and overall practicality. The items in this part of the questionnaire were scored using a Likert scale ranging from 1 (Strongly Disagree) to 10 (Completely Agree) to provide a large enough option to enable differences to be clearly identified. In addition, several open-ended questions were also included to obtain their general perceptions of the design and material of the new basket.

Quality Control

To ensure the questionnaire's validity Borg's CR-10 was translated to Malay from English by a native speaker of Malay and back-translated to English by a Ph.D.-level academic officer who is fluent in Malay and English. The differences in both versions of the questionnaires were identified and only a few translations required amendments, which were then amended.

As evidence of the researchers' competencies, two research team members are recognized as Ergonomically Trained Persons under the Guidelines of Ergonomic Risk Assessment by the Department of Occupational Safety and Health (DOSH, 2017). The researchers trained other team members and cross-checked all assessments to ensure the risk assessments best represented the tasks recorded from video and photos.

The full questionnaire was validated during the pilot-testing phase before the actual data collection, which is intended to ensure respondents understand the questionnaire items and reduce issues with the choice of wording (Sekaran & Bougie, 2016; Stockemer, 2019). A sample of 10% of the total sample size, consisting of male respondents from an educational institution with a similar age range and gender to the intended participants of this study, received the questionnaires. Ambiguous terms identified during the pilot test were amended to ensure respondents clearly understood the questionnaire.

Cronbach's Alpha was employed to assess the questionnaire's reliability. The range of Cronbach's Alpha is from 0 to 1, where a value of 0 indicates no relation and a value of 1 signifies perfect correlation. An acceptable internal consistency is when the value is more than 0.7 (Taber, 2018). In this study, the obtained Cronbach's Alpha value was desirable at 0.78.

Data Analysis

Paired t-tests were conducted to compare the physiological workload and REBA score between the rattan harvesting basket and the new harvesting basket. Wilcoxon signed-rank tests were employed to compare the discomfort level of body parts when using the two different baskets during the harvesting task. The perception of the harvesters towards the new harvesting basket was re-categorized from the 1 to 10 Likert Scale into three groups of Low Agreement (1 to 4), Moderate (5 to 6) and High Agreement (7–10) and was then presented as descriptive analysis.

RESULTS AND DISCUSSION

Sociodemographic and Work Characteristics of Pineapple Harvesters

A total of 25 pineapple harvesters were included in the sample, consisting of Malaysian adult men and non-Malaysian adult men aged between 20 and 60 years, with an average

age of 43.45 ± 11.4 years. The majority of respondents were Malaysian (92%, n=23). Regarding education level, the majority had secondary education (52%, n=13), while 40% (n=10) had primary education. Table 1 presents the summary of the sociodemographic distribution of the pineapple harvesters.

Discomfort Level of Pineapple Harvesters Using Different Types of Baskets

Regarding the level of discomfort experienced by the pineapple harvesters using different types of baskets, the results of the Wilcoxon signed-rank test revealed a significant difference in discomfort for all body parts of the respondents. Waist, shoulder, lower back and lower leg areas exhibited significant differences in discomfort levels. Table 2 presents the median distribution of discomfort for the body parts of the respondents using the rattan harvesting basket and the new harvesting basket.

Table 1
Sociodemographic of pineapple harvesters in Muar, Johor (n=25)

Variables	Frequency (n)	%	Mean ± SD
Age (Years)			43.45 ± 11.4
<29	4	16	
30–49	10	40	
>50	11	44	
Education			
Informal education	2	8	
Primary education	10	40	
Secondary education	13	52	
Previous employment			
No	5	20	
Yes	20	80	
Working experiences			
1–10 years	12	48	
11–20 years	8	32	
21–30 years	3	12	
>30 years	2	8	
Working status			
Full time	25	100	
Harvesting Training No	25	100	

Table 2
Distribution of discomfort score for the body parts of the respondents using the rattan harvesting basket and the new harvesting basket

Variables	Rattan basket	New basket	z-value	p-value*
	Median (IQR)			
Discomfort of all body parts	0.5 (1.00)	0.204 (.00)	-3.760	<0.001*
Waist	0.5 (3.0)	0.00 (.00)	-3.815	<0.001*
Upper back	0.00 (.00)	0.00 (.00)	-1.089	0.276
Middle back	0.00 (.00)	0.00 (.00)	-1.414	0.157
Lower back	1.00 (2.50)	0.00 (.00)	-4.176	<0.001*
Shoulder	3.0 (2.00)	0.5 (0.5)	-4.223	<0.001*
Thighs	0.00(.00)	0.00 (.00)	-1.342	0.180
Lower leg	0.5 (0.50)	0.00 (.00)	-3.690	<0.001*

Significant at p<0.05 The Statistical test used was the Wilcoxon Signed Rank Test; Explanation: 0 indicates "nothing at all," and 10 indicates "excruciating"

The results showed a significant reduction in discomfort levels for various body parts, including the waist, lower back, shoulder and lower leg. The respondents reported less discomfort when using the new harvesting basket compared to the rattan basket. These findings are consistent with previous studies conducted by Mezlan et al. (2019) and Vanderwal et al. (2011), which found reduced discomfort reported by respondents using ergonomically designed tools compared to traditional tools. The most affected body parts while using the rattan basket were the shoulder, waist, and lower back area, which had to support the weight of the load. These results are supported by Mezlan et al. (2019), which showed that the lower back, upper back, and shoulder had the highest mean discomfort scores according to the Borg CR-10 scale.

The results also highlighted positive effects on the comfort of specific body parts with the usage of the new harvesting basket, particularly in the lower back and shoulder area. These improvements can be attributed to the design features of the new basket, such as the bottom opening for unloading, which is key and helps reduce poor posture and excessive bending. Additionally, the adjustable cushioned shoulder strap and padded back of the new basket contribute to both comfort and reduced contact stress on workers' backs (Mezlan et al., 2019).

Body Posture Assessment Comparison for Unloading of Pineapples Using Rattan and New Harvesting Basket

The results indicated that the average Rapid Entire Body Assessment (REBA) score for the rattan harvesting basket was 10.04 ± 0.79, indicating a high-risk level. Conversely, the average REBA score for the new harvesting basket was 4.12 ± 0.82, falling under the medium-risk level. Paired t-test analysis demonstrated significant differences in the REBA scores between the rattan and new harvesting basks, with $p<0.001$. Table 3 illustrates the mean difference in the REBA scores between the two types of baskets, while Table 4 shows sample calculation for the REBA assessment.

The Rapid Entire Body Assessment (REBA) was employed as an evaluation tool in this study to assess the postural risks associated with a specific work task, namely unloading pineapples onto the ground. The risk assessment results indicated that the unloading process using the existing rattan harvesting basket is classified as high risk (64%, n = 16) and very high risk (9%, n = 36). These findings are consistent with Rani, Rashid et al. (2016), who highlighted the hazardous nature of pineapple unloading due to the required work posture and the heavy load of pineapples weighing approximately 50–70 kg. The postural risk analysis reveals that the harvesting process is classified as a very high postural risk, with a REBA score of more than 10, emphasizing the need for improvements.

Comparatively, the risk level of the unloading process is reduced when using the new harvesting basket compared to the rattan basket. The risk level for unloading with the

Table 3
REBA score of awkward posture risk during the unloading process while using rattan basket and new basket (n=25)

Reba Score and Level	Ratan basket n (%)	New basket n (%)	Differences (95%CI)	t-statistics (df)	p-value*
1 (None)	-	-	-	-	-
2–3 (Low)	-	7 (28)	-	-	-
4–7 (Medium)	-	18 (72)	-	-	-
8–10 (High)	16 (64)	-	-	-	-
11+ (Very High)	9 (36)	-	-	-	-
Average REBA score	10.04 (0.79)	4.12 (0.82)	6.1 (5.6, 6.6)	25.47 (24)	<0.001*

Significant at p<0.05 The Statistic test used was a paired t-test for average REBA score only

Table 4
Sample calculation for REBA scoring for unloading of pineapples using rattan basket

Part A: Neck, Trunk and Leg Analysis							**Part B: Arm And Wrist Analysis**						**REBA Final Score**	**Risk Level**
Neck Score	Trunk Score	Leg Score	**POSTURE Score A**	Force / Load Score	**SCORE A**	Upper Arm Score	Lower Arm Score	Wrist Score	**POSTURE Score B**	Coupling Score	**SCORE B**	**SCORE C**	**Activity Score**	12	Very High Risk
2	5	2	7	2	9	4	2	3	7	1	8	11	1		

new harvesting basket is classified as low risk (28%, n=7) and medium risk (72%, n=17). Conversely, unloading using the rattan harvesting basket is associated with high and very high risk levels. This disparity can be attributed to the excessive forward bending at the waist angle of 60° required during unloading with the existing rattan harvesting basket (Rani, Rashid et al., 2016), as illustrated in Figure 1.

The new harvesting basket introduces a novel feature for the unloading process, thereby reducing or eliminating excessive bending during the task. This improvement is attributed to the ergonomic design of the new harvesting basket, which allows fruits to tip out and be unloaded while standing, which contributes to a reduced REBA score. Similar studies have reported comparable findings, where a comparison of postural risks using the Rapid Upper Limb Assessment (RULA) between new ergonomic design tools and existing tools revealed that the RULA score for the new ergonomic design tool was lower than that for the

existing tool. The new tool reduced awkward postures to a low-risk score of 3, compared to the existing chisel tool with a score of 7, classified as high risk (Yusoff et al., 2014).

The REBA assessment highlights that the design of the newly developed harvesting basket has the potential to mitigate awkward postures compared to the current harvesting basket (rattan), as suggested by Salleh and Sukadarin (2018). This emphasizes the importance of implementing ergonomic interventions such as tool mechanization to eliminate awkward postures among pineapple plantation workers.

Physiological Workload of Pineapple Harvesters Using Different Types of Baskets

The physiological workload of the respondents was assessed through average heart rate and energy expenditure. Heart rate can be used to indicate cardiac stress due to physical workload, expressed in the calculation using the formula for energy expenditure (Bhattacharyya & Chakrabarti, 2012). The energy expenditure formula is a simple and rapid method to measure occupational workload when performing manual activities. It was developed based on the association between physiological change and subjective feeling of exertion (Varghese et al., 1994). The average heart rate of the respondents using the rattan harvesting basket was 97±6 beats per minute. For the new harvesting basket, the average heart rate of the respondents was lower than that of the rattan basket, measuring 89±7 beats per minute. The average energy expenditure of the respondents while using the new harvesting basket (5.0±1.1 kJ/min) was lower than that of the rattan harvesting basket (6.6±0.9 kJ/min). Paired t-test results indicated a significant difference in heart rate and energy expenditure between respondents using the rattan harvesting basket and the new harvesting basket, with $p<0.001$. Table 5 displays the heart rate and energy expenditure of the harvesters while using the two different types of baskets during the harvesting task.

In this study, the simulation of the harvesting exercise can be considered light compared to the routine work from morning to afternoon. For energy expenditure, the averages obtained in this study denote lower physiological workload because a recent field study showed that energy expenditure for agricultural workers using hoe weeders for 20 minutes

Table 5
The physiological workload of the harvesters while using rattan basket and new harvesting basket (n=25)

Physiological workload	Rattan basket	New basket	Mean (95% CI)	t-test statistics value (df)	P value
	Mean (SD)				
Heart rate	97 (6)	89 (7)	7 (6,9)	10.93 (24)	<0.001*
Energy expenditure (kJ/min)	6.6 (0.9)	5.0 (1.1)	1.18 (0.86, 1.35)	9.32 (24)	<0.001*

Significant at $p<0.05$ The Statistical test used was a paired t-test. From the average values of heart rate (AHR), energy expenditure (EE) is calculated in the formula as the following EE (Kj-min) = 0.159 × AHR (beats per min.) – 8.72

on a 100 m^2 area ranged between 7.18 and 11.31 kJ/min among workers between the ages of 21 and 36 (Patel & Beg, 2024).

Nevertheless, this does not take away the fact that the use of the new harvesting basket does not eliminate physiological workload because it is still a manual instrument. Because manual harvesting is a selective harvesting approach, only ripe and mature fruit is collected while ensuring the quality of produce and value is retained; it is still often preferred by many small-scaled fruit farmers (Kaur et al., 2023). There are also other reasons for the use of a manual approach, such as to compensate for the peat soil surface, which is soft and uneven, in addition to being a sustainable method that can ensure the employment of local populations (Kaur et al., 2023; Mezlan et al., 2019).

The reduced workload and the reduced heart rate can be linked to the ergonomic features of the new harvesting basket. The new basket, with its features of a rear opening, eliminates excessive bending during unloading by incorporating an opening latch at the rear. It can be depicted in Figure 3, where a respondent unloaded the harvesting baskets. It reduces the ergonomic risks associated with bending, as supported by Mezlan et al. (2019). Additionally, Chung et al. (2001) found that when the trunk of the body was laterally bent and twisted, the average heart rate increased compared to when it was not bent and twisted. Therefore, the opening and unloading features of the newly developed harvesting basket can help reduce the physiological workload of the harvesters.

(a)

(b)

Figure 3. A respondent unloading the load from (a) a rattan harvesting basket while bending more than 45 degrees and (b) a new harvesting basket with a rear opening without bending

Perception of Harvesters Towards the New Harvesting Basket

According to the respondents' perception of the new basket, the majority (92%, n=23) agreed that it met their expectations, and 96% (n=24) believed that it fulfilled the harvesters' needs. A significant majority of respondents, 92% (n=23), expressed that the basket met their expectations. The respondents noted that the basket's lighter weight and comfort make harvesting easier. Table 6 presents the distribution of respondents' perceptions of the new basket.

Table 6
Perceptions of pineapple harvesters towards the new harvesting basket (n=25)

Perception of the new basket	Frequency (n)	(%)
Fulfils expectation		
Medium Agreement	2	8
High Agreement	23	92
Make harvesting easier		
Medium Agreement	1	4
High Agreement	24	96
Feels comfortable		
Medium Agreement	1	4
High Agreement	24	96
Does it fulfill harvester's need		
Medium Agreement	1	4
High Agreement	24	96
Willing to use the new basket?		
Medium Agreement	1	4
High Agreement	24	96
Will reduce harvesting time		
Medium Agreement	2	8
High Agreement	23	92

* Likert-scale re-categorization: Low agreement: 1–3, Medium agreement: 4–6, High agreement: 7–10

When asked about the most important features in a harvesting basket, 64% (n=16) of respondents identified weight and material as crucial factors they look for in a harvesting basket. On the other hand, the opening latch was considered the most interesting and favored feature of the new harvesting basket by 92% of respondents (n=23). It is attributed to the ergonomic design of the basket, which allows for unloading fruits while standing. In contrast, the design of the rattan harvesting basket lacked a bottom opening, requiring workers to bend excessively while unloading fruits onto the ground (Mezlan et al., 2019). Furthermore, the new harvesting basket is perceived as lighter than the rattan harvesting basket, weighing 3kg without a load compared to 5 kg for the rattan basket (Mezlan et al., 2019). Respondents also perceived that the newly added features, such as the adjustable shoulder strap and padded back, provide comfort to harvesters during the harvesting process, making the new basket suitable for extended periods of use (92%, n=23).

However, 60% of respondents believed that the new harvesting basket is incapable of carrying the same load as the rattan harvesting basket. This perception is related to the design and load capacity of the new basket. The new basket is 30% smaller in size compared to the previous rattan harvesting basket, aiming to lower the threshold weight to a safer limit and reduce the burden of heavy loads on the harvesting basket. The new harvesting

basket can handle up to 40 kg, but a fully loaded rattan harvesting basket weighs between 50 kg and 70 kg. Since employees carry approximately 500–600 kg daily, this load capacity is considered dangerous (Rani, Rashid et al., 2016).

CONCLUSION

The evaluation showed that the new harvesting basket is linked to the reduction of the physiological workload and discomfort experienced by harvesters compared to the rattan basket. Significant differences were observed in workload and discomfort levels, indicating the potential of the new design to improve posture during harvesting. Respondents expressed satisfaction with the new basket due to its lighter weight, increased comfort and improved usability. On the other hand, social acceptance of the new basket needs to be considered because the new basket is intentionally smaller to reduce the load carrying, which raises a high safety risk during harvesting work. When safety is to be considered to go against the perception of reduced productivity, it may be a barrier for a population of pineapple harvesters to accept and adapt to the use of the new harvesting basket. Further efforts to encourage the use of such harvesting baskets need to be based on existing theories of innovation diffusion (Weinstein et al., 2007).

This study needs to consider some limitations. In the study by Kaur et al. (2023), lower energy expenditures were mostly observed among younger workers, which raises the point about the respondents' age distribution within the present study. This analysis in this study did not differentiate the respondents' age distribution in the energy expenditure calculation. Because half of the workers were from an older age group, the age effects need to also be considered when considering the parameter of energy expenditure. One way to do so is by using the % of maximum heart rate instead of absolute heart rate value (Korshøj et al., 2021).

Generalizing the findings to other pineapple plantations is also not possible as the testing was simulated rather than conducted in real harvesting conditions. The simulated load may differ from actual field conditions in addition to peat soil conditions in Johor plantation areas. Further field testing is necessary to determine the effectiveness and suitability of the new ergonomic basket in actual pineapple plantations, specifically in Johor. In addition, the calculation of the efficiency rate needs to also be included in future research for benchmarking. For example, published literature reported that farmers performing manual harvesting practices for selected fruits can only cover an average of 7.50 ha/hour (Kaur et al., 2023).

The study's findings are valuable and contribute significantly to the scope of enhancing harvesting tools, promoting safety and health and reducing musculoskeletal disorders among agricultural workers in Malaysia. Implementing ergonomic interventions aligns with the Malaysian Good Agricultural Practices (myGAP) certification, which emphasizes seven elements consisting of worker welfare, safety and health apart from environmentally

friendly practices as established in the Malaysian Standard Crop Commodity guide (MS 1784:2005) (Department of Agriculture, 2023). This research guides future studies aiming to develop and improve ergonomic tools for agricultural workers. Future research should employ electromyography (EMG) instruments to assess muscle electrical activity, estimate muscle force and analyze muscle fatigue rates in relation to the new basket's design for a more comprehensive and objective assessment.

ACKNOWLEDGMENTS

This project was made possible with the funding provided by the Ministry of Higher Education Malaysia via the Prototype Research Grant Scheme (PRGS 2019-1) with the project number 13050 (reference number PRGS/1/2019/WAB01/UPM/02/2). The project title was "Identification and Evaluation of Design Specification for Prototype Development of Pineapple Harvesting Basket to Potentially Reduce Physiological Load, Musculo-skeletal Symptoms and Discomfort". The project also received support from the Yayasan Inovasi Malaysia and SME Corporation. The authors would also like to give gratitude to the Malaysian Pineapple Industrial Board, Johor for their invaluable support and significant contributions to this project.

REFERENCES

Beek, A. J. V. D., & Frings-Dresen, M. H. (1998) Assessment of mechanical exposure in ergonomic epidemiology. *Occupational Environmental Medicine, 55*(5), 291–299. https://doi.org/10.1136/oem.55.5.291

Bhattacharyya, N., & Chakrabarti, D. (2012). Ergonomic basket design to reduce cumulative trauma disorders in tea leaf plucking operation. *Work*, *41*(Supplement 1), 1234–1238. https://doi.org/10.3233/WOR-2012-0308-1234

Borg, G. (1998). *Borg's Perceived Exertion and Pain Scales*. Human Kinetics.

Cancela, J., Pastorino, M., Tzallas, A. T., Tsipouras, M. G., Rigas, G., Arredondo, M. T., & Fotiadis, D. I. (2014). Wearability assessment of a wearable system for parkinson's disease remote monitoring based on a body area network of sensors. *Sensors, 14*(9), 17235-17255. https://doi.org/10.3390/s140917235

Chung, M. K., Lee, I., & Yeo, Y. S. (2001). Physiological workload evaluation of screw driving tasks in automobile assembly jobs. *International Journal of Industrial Ergonomics, 28*(3), 181–188. https://doi.org/10.1016/S0169-8141(01)00031-2

Department of Agriculture. (2023). *Malaysian good agricultural practices certification scheme (myGAP)*. Department of Agriculture. http://www.doa.gov.my/index.php/pages/view/373

DOSH. (2017). *Guidelines on ergonomic risk assessment at workplace*. Department of Occupational, Safety and Health. https://www.dosh.gov.my/index.php/competent-person-form/occupational-health/regulation-2-1/guidelines/ergonomic/2621-01-guidelines-on-ergonomics-risk-assessment-at-workplace-2017?path=guidelines/ergonomic

Galinsky, T., Swanson, N., Sauter, S., Dunkin, R., Hurrell, J., & Schleifer, L. (2007). Supplementary breaks and stretching exercises for data entry operators: a follow-up field study. *American Journal of Industrial Medicine, 50*(7), 519–527. https://doi.org/10.1002/ajim.20472

Hignett, S., & McAtamney, L. (2000). Rapid entire body assessment (REBA). *Applied Ergonomics*, *31*(2), 201–205. https://doi.org/10.1016/S0003-6870(99)00039-3

Kamarudin, N. H., Ahmad, S. A., Hassan, M. K., Yusuff, R. M., & Dawal, S. Z. M. (2013). A review of the niosh lifting equation and ergonomics analysis. *Advanced Engineering Forum*, *10*, 214–219. https://doi.org/10.4028/www.scientific.net/aef.10.214

Kang, M., Ragan, B. G., & Park, J. H. (2008). Issues in outcomes research: An overview of randomization techniques for clinical trials. *Journal of Athletic Training, 43*(2), 215–21. https://doi.org/10.4085/1062-6050-43.2.215

Karuppiah, K., Salit, M. S., Ismail, M. Y., Ismail, N., & Tamrin, S. B. (2012). Evaluation of motorcyclist's discomfort during prolonged riding process with and without lumbar support. *Anaus da Acadenua Brasileira de Ciências, 84*(4), 1169-88. https://doi.org/10.1590/s0001-37652012000400031

Kaur, B., Dimri, M. S., Singh, J., Mishra, S., Chauhan, N., Kukreti, T., Sharma, B., Singh, S. P., Arora, S., Uniyal, D. Agrawal, Y., Akhtar, S., Ahmad Rather, M., Naik, B., Kumar, V., Gupta, A. K., Rustagi, S., & Preet, M. S. (2023). Insights into the harvesting tools and equipment's for horticultural crops: From then to now. *Journal of Agriculture and Food Research, 14*, Article 100814. https://doi.org/10.1016/j.jafr.2023.100814

Korshøj, M., Rasmussen, C. L., Sato, T. D. O., Holtermann, A., & Hallman, D. (2021). Heart rate during work and heart rate variability during the following night: A day-by-day investigation on the physical activity paradox among blue-collar workers. *Scandinavian Journal of Work Environment and Health, 47*(5), 387-394. https://doi.org/10.5271/sjweh.3965

Kuorinka, I., Jonsson, B., Kilbom, A., Vinterberg, H., Biering-Sørensen, F., Andersson, G., & Jørgensen, K. (1987). Standardised Nordic questionnaires for the analysis of musculoskeletal symptoms. *Applied Ergonomics, 18*(3), 233-237. https://doi.org/10.1016/0003-6870(87)90010-X

Liu, T., Liu, W., Zeng, T., Cheng, Y., Zheng, Y. & Qiu, J. (2022). A multi-flexible-fingered roller pineapple harvesting mechanism. *Agriculture, 12*(8), Article 1175. https://doi.org/10.3390/agriculture12081175

Mansor, F. S. (2020). *The assessment of anthropometric measurement and development of harvesting basket for harvesting at selected areas in Johor* [Unpublish doctoral thesis]. Universiti Putra Malaysia.

McLean, L., Tingley, M., Scott, R. N., & Rickards, J. (2001). Computer terminal work and the benefit of microbreaks. *Applied Ergonomic, 32*(3), 225–237. https://doi.org/10.1016/s0003-6870(00)00071-5

Mezlan, N. S., Abidin, E. Z., Karuppiah, K., Rasdi, I., Ismail, S. N. S., & Ismail, N. H. (2019). Development of smart fruit basket for pineapple harvesting. *Malaysian Journal of Medicine and Health Sciences*, *15*(SP4), 26–34.

MPIB. (2011). *Quantity of pineapple production*. Malaysian Pineapple Industry Board. http://mpib.gov.my/en/sejarah

Patel, N. K., & Beg, A. (2024). Effect of the physiological parameters of different age group workers on hoe weeder. *Journal of Experimental Agriculture International, 46*(5), 76-82. https://doi.org/10.9734/jeai/2024/v46i52359

Rani, N. H., Abidin, E. Z., Ya'acob, N. A., Karuppiah, K., & Rasdi, I. (2016). Musculoskeletal symptoms risk factors and postural risk analysis of pineapple plantation workers in Johor. *Journal of Occupational Safety and Health*, *13*(1), 17–26.

Rani, R. A., Rashid, K. F. A., & Joyo, M. (2016). Pakej teknologi mekanisasi ladang bagi pengeluaran nanas di tanah mineral [Package of farm mechanisation technologies for the production of pineapple at mineral soil]. *Buletin Teknologi MARDI*, *9*, 139–147

Reenen, H. H. H., Beek, A. J. V. D., Blatter, B. M., Grinten, M. P. V. D., Mechelen, W. V., & Bongers, P. M. (2008). Does musculoskeletal discomfort at work predict future musculoskeletal pain? *Ergonomics, 51*(5), 637-648. https://doi.org/10.1080/00140130701743433

Salleh, N. F. M., & Sukadarin, E. H. (2018, August 18-19). *Analyses of working postures among Malaysia pineapple plantation workers using ovako working posture analysis system*. [Paper presentation]. Proceedings Book: National Conference for Postgraduate Research, Pahang, Malaysia.

Sekaran, U. & Bougie, R. (2016) *Research Methods for Business: A Skill-building Approach*. (7th ed.). Wiley & Sons.

Stockemer, D. (2019) *Quantitative Methods for the Social Sciences*. Springer. https://doi.org/10.1007/978-3-319-99118-4

Suhaimi, N. H. M., & Fatah, F. A. (2019). Profitability of pineapple production (Ananas comosus) among smallholders in Malaysia. *International Journal of Recent Technology and Engineering*, *8*(4), 4202–4207.

Taber, K. S. (2018). The use of cronbachs'alpha when developing and reporting research instruments in science education. *Research in Science Education, 48*, 1273–1296. https://doi:10.1007/s11165-016-9602-2

Tamrin, S. B. M., & Aumran, N. (2014). A comparison of the hazards, the risks, and the types of control in three selected agricultural industries. In K. Saliman & B. M. Tamrin (Eds.) *Occupational Safety and Health in Commodity Agriculture: Case Studies from Malaysian Agriculture Perspective* (pp. 93–146). Universiti Putra Malaysia.

Vanderwal, L., Rautiainen, R., Kuye, R., Peek-Asa, C., Cook, T., Ramirez, M., Culp, K., & Donham, K. (2011). Evaluation of long- and short-handled hand hoes for land preparation, developed in a participatory manner among women vegetable farmers in the Gambia. *Applied Ergonomics*, *42*(5), 749–756. https://doi.org/10.1016/j.apergo.2010.12.002

Varghese, M. A., Saha, P. N., & Atreya, N. (1994). A rapid appraisal of occupational workload from a modified scale of perceived exertion. *Ergonomics*, *37*(3), 485–491. https://doi.org/10.1080/00140139408963665

Waongenngarm, P., Beek, A. J. V. D., Janwantanakul, P., Akkarakittichoke, N., & Coenen, P. (2022). Can the borg CR-10 scale for neck and low back discomfort predict future neck and low back pain among high-risk office workers? *International Archives of Occupational and Environmental Health, 95*(9), 1881-1889. http://doi: 10.1007/s00420-022-01883-3

Weinstein, M. G., Hecker, S. F., Hess, J. A., & Kincl, L. (2007). A roadmap to diffuse ergonomic innovations in the construction industry: There is nothing so practical as a good theory. *International Journal of Occupational and Environmental Health, 13*(1), 46-55. https://doi:10.1179/107735207800245054

Ya'acob, N. A., Abidin, E. Z., Rasdi, I., Rahman, A. A., & Ismail, S. (2018). Reducing work-related musculoskeletal symptoms through implementation of Kiken Yochi training intervention approach. *Work*, *60*(1), 143–152. https://doi.org/10.3233/WOR-182711

Yusof, N. A. D. M., Karuppiah, K., Jamil, P. A. S. M., Khalid, M. S., Tamrin, S. B. M., & Naeini, H. S. (2022). Development of a high-powered motorcycle seat discomfort survey (MSDS): Traffic police motorcycle. *International Journal of Industrial Ergonomics, 92,* Article 103374. https://doi.org/10.1016/j.ergon.2022.103374

Yusoff, I. S. M., Tamrin, S. B. M., Aini, M. A. T., Ng, Y. G., & Ippei, M. (2014). Oil palm workers: Designing ergonomics harvesting tool using user centered design approach to reducing awkward body posture by Catia simulation. *Iranian Journal of Public Health*, *43*(S3), 72–80.

Žunkovič, B., Kejžar, N., & Bajrović, F. F. (2023). Standard heart rate variability parameters—their within-session stability, reliability, and sample size required to detect the minimal clinically important effect. *Journal of Clinical Medicine*, *12*(9), Article 3118. https://doi.org/10.3390/jcm12093118

Pertanika J. Sci. & Technol. 33 (S1): 43 - 63 (2025)

PERTANIKA JOURNALS

SCIENCE & TECHNOLOGY

Journal homepage: http://www.pertanika.upm.edu.my/

Development of Pectin-Pineapple Juice Films Incorporated with Ginger Essential Oil Nanoemulsion for Food Packaging Application

Mazween Mohamad Mazlan[1], Nik Nur Syazwani Ab Ghani[1], Rosnita A. Talib[1]*, Rabitah Zakaria[1], Roseliza Kadir Basha[1], Intan Syafinaz Mohamed Amin Tawakkal[1] and Hayati Samsudin[2]

[1]Department of Process and Food Engineering, Faculty of Engineering, Universiti Putra Malaysia, 43400 Serdang, Selangor, Malaysia
[2]Food Technology Division, School of Industrial Technology, Universiti Sains Malaysia, 11800 Gelugor, Pulau Pinang, Malaysia

ABSTRACT

Edible films loaded with essential oil nanoemulsions dissolve quickly in water and are completely biodegradable and compostable, making them an appropriate and sustainable alternative to single-use food packaging. This study aims to develop pectin-pineapple juice (PPJ) films with varying loadings of ginger essential oil nanoemulsion (GEONe), ranging from 5% to 20%, with a PPJ film without GEONe serving as a control. The effect of incorporating GEONe on the films' physical, mechanical, colour, and thermal properties, including enthalpy and moisture loss, was evaluated. The thickness of the films significantly increased ($p \leq 0.05$) from 91.0 µm to 112.0 µm when the loading of GEONe increased. The PPJ films' moisture content (11.57% to 10.33%) was insignificantly affected ($p > 0.05$) by the presence of GEONe. The water solubility of the PPJ film with 20% GEONe (83.16%) was lower than that of the control PPJ film (93.77%). The control film yielded the highest lightness (L* value = 84.40) and intermediate yellowness (b* value = -1.08). As GEONe was incorporated into the PPJ films, the lightness decreased while the b value, yellowness index, and colour differences increased. The tensile strength and Young's modulus values significantly decreased ($p \leq 0.05$) from 15.97 MPa to 9.54 MPa and from 398.92 MPa to 186.91 MPa, respectively, with increasing GEONe loading. It indicates that the GEONe nano-size droplets have plasticising effects, increasing the elongation at break of the PPJ films from 8.71% to 16.49%. Additionally, the differential scanning calorimetric curves demonstrated that films incorporated with

ARTICLE INFO

Article history:
Received: 08 November 2023
Accepted: 05 November 2024
Published: 31 January 2025

DOI: https://doi.org/10.47836/pjst.33.S1.03

E-mail addresses:
mazween.5624@gmail.com (Mazween Mohamad Mazlan)
203722@student.upm.edu.my (Nik Nur Syazwani Ab Ghani)
rosnita@upm.edu.my (Rosnita A. Talib)
rabitah@upm.edu.my (Rabitah Zakaria)
roseliza@upm.edu.my (Roseliza Kadir Basha)
intanamin@upm.edu.my (Intan Syafinaz Mohamed Amin Tawakkal)
hayatis@usm.my (Hayati Samsudin)
* Corresponding author

ISSN: 0128-7680
e-ISSN: 2231-8526

increasing GEONe had a lower crystallisation enthalpy, improving the thermal stability of the PPJ-GEONe films. These findings revealed the potential of incorporating GEONe into pectin-based films, resulting in acceptable physical properties, flexibility, and thermal stability.

Keywords: Differential scanning calorimetry, ginger essential oil, nanoemulsion, pectin-based film, tensile properties

INTRODUCTION

Single-use plastics, including production, processing, distribution, and consumption, are widely used across the food chain system. This food packaging material is specifically designed for one-time use, without any reuse provisions, before being discarded or recycled (Foodprint, 2020). Malaysia is now ranked eighth among the world's top ten countries for the highest levels of mismanaged plastic waste (Zainal et al., 2023). In response, Malaysia introduced an ambitious roadmap in 2018 with the goal of eliminating single-use plastics by 2030 (Zainal et al., 2023). This initiative seeks to mitigate plastic mismanagement and promotes consumer education on reusable grocery bags, containers, and cutlery. Furthermore, there is a growing demand for food packaging manufacturers to develop biodegradable and compostable plastics as alternatives to single-use plastic food packaging. The biopolymer-based films, made from sustainable raw materials such as proteins, polysaccharides, and lipids, play a crucial role in facilitating this transition. These biopolymers are both environmentally friendly and edible and safe to consume along with packaged foods, offering a sustainable solution to the plastic waste problem.

Polysaccharides used to produce biodegradable and edible plastic films include starch, cellulose, chitosan, chitin, pullulan, and pectin. Industrially processed pectin obtained from apple pomace and citrus peels is also often used for this application (Dranca et al., 2021; Kute et al., 2020). Furthermore, sugar beet pulp and sunflower seed heads are sources with notable physicochemical qualities, characterised by their abundant pectin content and biomass availability (Adetunji et al., 2017). Pectin, a complex polysaccharide, comprises α-1,4-linked d-galacturonic acid units. The methylation of the carbonyl groups at the carbon-6 position within the pectin backbone is responsible for its gelling properties. Pectin can be categorised into two groups based on its degree of esterification (DE). High methoxyl pectin (HMP) is characterised by a methylation degree greater than 50%, whereas low methoxyl pectin (LMP) has a methylation degree of less than 50% (Blanco-Pérez et al., 2021; Marić et al., 2018). The DE might also differ based on the source of pectin. Pectin plays an important role in food manufacturing as a thickening agent, stabiliser, and emulsifier. Additionally, it is used to create edible coatings and films (Kumar et al., 2023). Pectin offers considerable potential as a bio-based packaging material due to its water solubility, excellent film-forming capability, and effective barrier against gases and aromatic compounds (Roy et al., 2023). However, films made from pectin are susceptible

to moisture due to the abundance of hydroxyl groups in their structure, leading to high permeability. They also exhibit limited thermal stability and are rigid and fragile. Combining pectin with other raw materials or subjecting it to modifications is a promising approach to overcome these drawbacks.

Different hydrophobic materials have been added to the pectin-based film as a food packaging material to improve its properties (e.g., physical, mechanical, and thermal). Essential oils (EO) are a a prominent type of plant extract used in pectin-based film (Nastasi et al., 2022). Ginger essential oil (GEO), formally known as *Zingiber officinale*, is a highly valued aromatic oil derived from the tuber of the ginger plant. GEO is extracted through steam distillation, which captures the concentrated essence of the ginger plant. Due to its benefits, ginger is frequently used in food applications as a condiment, flavouring ingredient, and natural preservative. According to Noori et al. (2018), GEO has remarkable antimicrobial, antifungal, and antioxidant properties, which make it an excellent choice for food packaging applications. Unfortunately, most raw EOs are unstable and prone to oxidation in the presence of light, oxygen, and high temperatures (Fasihi et al., 2023). Furthermore, the hydrophobic characteristics of EOs can result in inadequate compatibility and phase separation when directly integrated into a water-soluble biopolymeric film-forming dispersion (Almasi et al., 2020). Poor compatibility between hydrophobic EO and hydrophilic pectin results in the film's not uniform structure and overall decreases its mechanical properties (Chen et al., 2023).

One potential strategy for addressing the aforementioned issues is to incorporate EO in nanoemulsion form. Several studies, including those conducted by Almasi et al. (2020), Candido et al. (2022), Jahromi et al. (2022), Norcino et al. (2020), and Shaaban et al. (2016) have investigated the potential of utilising essential oils such as pracaxi, marjoram, cinnamon, copaiba, and clove in the formulation of pectin-based films. The pharmaceutical, cosmetic, and food industries use the lipid-based colloidal delivery system to encapsulate essential oils such as emulsions. Encapsulating essential oils by emulsification is a feasible method to form a colloidal delivery system to stabilise the lipophilic functional materials (Fernandes et al., 2016). The nanoemulsion, featuring droplets smaller than 200 nm in diameter, represents a dispersion of an immiscible liquid in which lipid-based hydrophobic materials are dispersed within the water phase. This nanoemulsion is typically a stabilised non-ionic emulsifier, which is produced through a combination of high-speed homogenisation and ultrasonic crushing techniques. Nanoemulsions have several advantages over coarse emulsions, which have larger droplets measured in micrometres, including high stability and a larger surface area. The small droplets can better sustain the original structural arrangement of the film microstructure, reducing negative effects on film performance (Zhang et al., 2022). In addition, liquid lipid carriers such as edible oil (virgin coconut oil, corn, sesame, sweet almond, and black seed oil) have been widely

used in the formulation of lipid-based nanoemulsion to overcome micelles different storage conditions (Bashiri et al., 2020; Rosli et al., 2022).

Edible films have been incorporated with fruit juices such as grape, jambolan, pear, and purees of mango and pineapple (Chambi et al., 2020; Pimiento et al., 2023; Susmitha et al., 2021; Yıldırım-Yalçın et al., 2021). These fruit juices comprise carbohydrates (such as fructose, glucose, sorbitol, and sucrose), organic acids, amino acids, phenolic compounds, vitamins, and minerals (Salehi, 2020). Incorporating fruit-based products into edible films can improve their appearance and physical and mechanical properties and enhance their nutritional value. Simple sugars in fruit juice are known to have a plasticising effect on edible films, impacting their tensile strength, elongation at break, and water vapour permeability (Azeredo et al., 2016). Nonetheless, the amount of fruit juice added to edible films needs to be optimised to achieve the desired quality (Yıldırım-Yalçın et al., 2021).

Pineapple, or *Ananas comosus*, is a well-liked tropical fruit distinguished by its distinct aroma and sweet flavour. Malaysia has expanded its pineapple production cultivation area in recent years. In 2022, 537,231 tonnes of pineapple were produced in Malaysia (DOA, 2022). Post-harvest processing operations are crucial for preserving the quality, safety, and shelf life of processed pineapple products because pineapple is highly perishable (Abraham et al., 2023). Pineapple has attracted significant interest for its potential as a functional food and for various products made from pineapple (Ali et al., 2020). Commonly seen pineapple-based products in the market include drinks, jam, dehydrated slices, canned pineapple slices, and beverages. Both unsweetened and sweetened pineapple juice drinks are widely consumed in Malaysia. The amount of vitamins, minerals, and sugars in pineapple juice varies based on the variety and ripeness of the fruit. It has an especially high concentration of 9.2 to 93.8 mg of vitamin C per 100 mL (Kabasakalis, 2000). Significant levels of minerals such as potassium, magnesium, phosphorus, iron, and manganese are also present in pineapple juice. According to Statista (2024), Malaysia's pineapple juice sales revenue is predicted to increase by 1.52% yearly between 2024 and 2028. Thus, adding pineapple juice to biopolymers could offer new opportunities to diversify pineapple-based products beyond just drinking it as a beverage.

This study aimed to develop pectin-pineapple juice (PPJ) films containing ginger essential oil nanoemulsion (GEONe) with enhanced flexibility and thermal stability. The ginger essential oil was selected because it is commercially available, and its nanoemulsion form is a promising strategy to enhance the targeted properties effectively. Virgin coconut oil, which contains the health benefits of medium-chain triglycerides (MCT), was selected as a carrier oil in the nanoemulsion formulation (Ghani, Channip et al., 2018). MCT oils have lower interfacial tension and viscosity than long-chain triglyceride oils (e.g., soybean oil, safflower oil), resulting in the formation of smaller droplet sizes during the emulsification

process (Sampaio et al., 2022; Walker et al., 2017). The objectives of this study were: (1) to evaluate the effects of adding virgin coconut oil to the GEONe formulation to achieve a stable and homogenous nanoemulsion with nano droplet size and (2) to evaluate the effects of incorporating varying GEONe loadings (5% to 20%) into the PPJ films on the thickness, moisture content, water solubility, visual appearance, colour, tensile strength (TS), Young's modulus (YM), elongation at break (EAB), and thermal stability of the film in comparison to control PPJ film (absence of GEONe).

MATERIALS AND METHODS

Materials

The highly concentrated ginger essential oil (GEO), which is 100% pure, was purchased from Now Foods, Illinois, United States of America. Extra virgin coconut oil (VCO) was obtained from Country Farms Sdn. Bhd., Selangor, Malaysia. Polysorbate 80 (Tween 80), an emulsifier, was purchased from EvaChem, Selangor, Malaysia. Cold-pressed pineapple juice (16.0 ± 0.1° Brix, pH 4.1 ± 0.1) of the MD2 variety was purchased from Cafe Nanas Montel in Selangor, Malaysia, and included no additional sugar. Rapid set high methoxyl (HM) pectin powder (Product code: 1121) with a degree of esterification (DE) of 75%, extracted from citrus fruit peels, was obtained from Modernist Pantry, Eliot, ME 03903, United States of America. Edible beeswax was acquired from American Soy Organics, United States of America, while glyceryl monostearate with 99% purity was obtained from Eastchem Inc., United States of America. In this research, pectin was applied as the film matrix, and glycerin was employed as a plasticiser. Glyceryl monostearate served as the emulsifier, while beeswax was added to the mixture as a hydrophobic agent to improve the film's moisture resistance. Distilled water was produced using a water distiller (Favorit W4L Water Stills) from PLT Scientific Sdn. Bhd., Malaysia.

Preparation of Ginger Essential Oil Nanoemulsion (GEONe)

In a beaker, 5 mL of ginger essential oil (GEO) was added to 95 mL of distilled water and stirred using a high-speed stirrer (HS-30D, WiseStir®HS-D, DAIHAN Scientific, Kangwon-do, South Korea) at 700 rpm. Subsequently, two levels of virgin coconut oil (VCO) (1 mL and 3 mL) were added to the mixture, followed by 1.5 mL of polysorbate 80. Next, the mixture was stirred at 1400 rpm for 10 min to obtain a coarse emulsion. The coarse emulsion was subjected to ultrasonic emulsification using a Branson 450 ultrasonic emulsifier (Branson Ultrasonics Corp., United States of America) at 50% amplitude for 9 min to achieve a nanometer-sized droplet emulsion. Then, the ginger essential oil nanoemulsion (GEONe) was transferred to an amber glass bottle and stored at room temperature (25 ± 2°C) for future use.

Characterisation of Ginger Essential Oil Nanoemulsion (GEONe)

Droplet Size, Size Distribution, and Stability Measurement

The GEONe nano-size droplet diameter was indicated by the z-average value and polydispersity index (PDI) values yielded from the diameter distribution curve. These values were obtained using dynamic light scattering with a Zetasizer Nano ZS (Malvern Instruments Inc., Worcestershire, U.K.). The first measurements were taken when the emulsification reached 24 hours, followed by a second measurement on day 7 to assess the stability of the nanoemulsion during storage. The mean diameter on each day was measured twice, and the average mean diameter was reported.

Preparation of Pectin-pineapple Juice-GEONe Films

Four grams of pectin were added to 100 mL of 70 ± 2°C distilled water. Next, 20% (w/w of pectin) glycerin, 1% (w/w of pectin) beeswax, and 0.2% (w/w of pectin) of glyceryl monostearate were added to the pectin solution. Then, the pectin-based solution's temperature was raised to 90 ± 2°C and was continuously stirred at 100 rpm using a hot plate stirrer (MSH-20D, Daihan Scientific Co., Ltd., Wonju, South Korea) for 30 min. Once all the materials were dissolved completely, the pectin-based solution was cooled down to below 10°C in a chiller before subsequently adding 4% (v/v of distilled water) of pineapple juice (PJ) to the pectin-based solution and continuously mixing with a magnetic stirrer at 100 rpm for another 10 min until thoroughly mixed. Next, the ginger essential oil nanoemulsion (GEONe) was added at different loadings of 5%, 10%, 15%, and 20% (v/v of distilled water) and mixed under the same settings until GEONe was dispersed evenly. The concentrations were chosen following a research work reported by Ghoshal (2022). Ultrasonic degassing was performed on the film-forming solution to eliminate any entrapped air bubbles using an ultrasonic probe (Branson 450, Branson Ultrasonics Corp., United States) at 50% amplitude for 10 minutes with a pulse mode (59 sec. 'ON', 10 sec. 'OFF'). The pectin-based film without GEONe acts as a control film. Approximately 22 mL of each film solution was cast onto glass petri dishes with a 140 mm diameter and then dried at room temperature (25 ± 2°C) for 24 hours. Finally, the dried films were peeled off and conditioned in a humidity-controlled cabinet (DB-90s, VAMOS, Selangor, Malaysia) at 50% relative humidity for 48 hours before testing.

Characterisation of Pectin-pineapple Juice-GEONe Films

Film Thickness Measurement

The film's thickness was measured using a digital micrometre (Mitutoyo Corp. Kawasaki, Japan). The mean value was obtained by measuring three random locations on each film.

Moisture Content Measurement

The MX-50 Moisture Analyzer (Mettler Toledo, Greifensee, Switzerland) was employed to determine the film's moisture content. Prior to measurement, 2 g of the film was heated to 105°C until a constant weight was reached, following the preparation procedure as in AOAC International (1995). Measurement was taken twice from a separate film, and the average moisture content was recorded.

Water Solubility Measurement

The film's dissolvability in water was assessed through a water solubility test following a method procedure by Tulamandi et al. (2016), with the soaking condition underwent a minor modification.. The PPJ-GEONe and PJJ films were cut into square samples measuring 40 mm × 40 mm each. These films were oven-dried (model 30-1060, Memmert GmbH + Co. KG., Schwabach, Germany) at 105°C for 24 hours. The weight of the dried films was measured, representing the initial dry weight of the film (W_o). Subsequently, the dried films were soaked in 50 mL of distilled water and shaken under constant agitation at 100 rpm for 24 hours at 26 ± 2°C using a water bath shaker (BS-21, Alirantek (M) Sdn. Bhd., Selangor, Malaysia). Next, filter papers (Whatman No. 541) were pre-dried at 105°C for 24 hours before use. Then, the film-dissolved solution was filtered through the filter paper, and the residue of water-insoluble matter was pre-dried at 105°C for 24 hours to remove moisture until a constant weight (W_1) was obtained. All tests were performed in triplicate to obtain the mean values. Finally, the percentage of the film's water solubility was calculated using the following formula:

$$Water\ solubility\ (\%) = \frac{W_o - W_1}{W_o} \times 100 \quad [1]$$

Colour Measurement

The colour parameters of the film samples L*, a*, and b* were measured using a portable calorimeter (FRU WR10, Shenzhen Wave Optoelectronics Technology Co., Ltd., China). The colour parameters were based on the CIELAB colour scale for L* = 0 (darkness) to L* = 100 (lightness), −a* (greenness) to +a* (redness), and −b* (blueness) to +b* (yellowness). The colour parameter readings were taken at five random locations on each film, and the mean of the five readings was recorded. Next, the L*, a*, and b* values were used to calculate the yellowness index (YI) and total colour difference (ΔE) of each film using Equations 2 and 3 (Ranjbaryan et al., 2019):

$$YI = \frac{142.86 \times b^*}{L^*} \quad [2]$$

$$\Delta E = \sqrt{(L^* - L_o^*)^2 + (a^* - a_o^*)^2 + (b^* - b_o^*)^2} \quad [3]$$

Tensile Test

The tensile main properties, including tensile strength (TS), Young's modulus (YM), and elongation at break (EAB), were obtained using a TA-XT_{plus} Texture Analyzer (Stable Micro Systems, Surrey, UK) following the ASTM standard method D882-18 (ASTM D882-18, 2018). The film samples were cut into 100 × 15 mm^2 rectangular strip dimensions. These film strips were securely mounted on the instrument's fixture grips with 50 mm between them. The tension of the film strip was carried out at a test speed of 0.5 mm/sec until a breaking point was reached. The tensile force (N) and the elongation distance (mm) were acquired to plot a graph of force against the deformation curve for data analysis. The mean value was taken from at least three replicates of separate films. The mean values for TS, YM, and EAB of the films were calculated using the following equations:

$$Tensile\ Strength\ (MPa) = \frac{F}{A} \quad [4]$$

where, F = The ultimate force at the failure point, N; A = Cross-sectional area of the film, mm^2

$$Young's\ modulus\ (MPa) = \frac{\sigma}{\varepsilon} \quad [5]$$

where, σ = Tensile stress, MPa; ε = Tensile strain

$$Elongation\ at\ break\ (\%) = \frac{L_f - L_o}{L_o} \times 100 \quad [6]$$

where, L_f = Final length of the film at specimen break; L_o = Initial length of the film

Differential Scanning Calorimetry Analysis (DSC)

The film's thermal properties, namely enthalpy (ΔH) and moisture loss (%), were analysed from the endothermic peak areas observed in the DSC curves acquired using a differential scanning calorimeter (DSC 3, Mettler Toledo, Greinfensee, Switzerland). Approximately 10 mg of each film sample was placed and hermetically sealed in a standard aluminium pan and subjected to a temperature increase from -25°C to 200°C at a constant heating rate of 20°C/min. The chamber was purged with nitrogen gas flowing at 50 cm^3/min. The acquired DSC curves were analysed using STARe Excellence software (Mettler Toledo, Greinfensee, Switzerland).

Statistical Analysis

The effect of VCO levels (0, 1, and 3 mL) and seven days of storage on droplet size and size distribution were assessed using a two-way analysis of variance (ANOVA). A one-way ANOVA was performed to evaluate the effect of five levels of GEONe addition (0%, 5%, 10%, 15%, and 20% GEONe) on PPJ films. The results were presented as mean values ± standard deviation. Tukey's multiple comparison test with a p-value of 0.05 was employed to determine significant differences between mean values. The experimental data's mean and standard deviation calculations were performed using Microsoft Excel 2021 (Microsoft Corporation, Albuquerque, NM, USA). The error bar included in the graph represents the one standard deviation of the mean values.

RESULTS AND DISCUSSION

Droplet Size, Size Distribution, and Stability of Ginger Essential Oil Nanoemulsion (GEONe)

The measurement of ginger essential oil nanoemulsion (GEONe) droplet size (z-average value) and size distribution (polydispersity index) is important to evaluate its stability and impact on the pectin-based films' properties. Figures 1(a) and 1(b) depict the mean droplet size and polydispersity index (PDI) values for GEONe with and without virgin coconut oil (VCO). On day one, GEONe droplets without VCO measured 47.05 ± 2.62 nm (Figure 1(a)). Noori et al. (2018) reported a droplet size of 57.4 ± 2.7 nm for a freshly produced ginger essential oil (GEO) nanoemulsion using polysorbate 80 and water without a carrier oil. The nanoemulsion was prepared via ultrasonic emulsification with different setting parameters than the present study, such as power at 200 W and time for 5 min. Nevertheless, the present study has investigated the influence of VCO as the carrier oil on the droplet size and stability of the nanoemulsion. For this reason, during the oil phase preparation, VCO was mixed with GEO (lipophilic bioactive agent). VCO, which is rich in medium-chain triglycerides (MCT), has been used as a carrier oil in emulsions due to its safety and availability compared to long-chain triglycerides (e.g., corn oil) and short-chain triglycerides (e.g., tributyrin) (Jiang & Charcosset, 2022; Man & Marina, 2006; Nguyen & Diep, 2022). Walker et al. (2017) and Sampaio et al. (2022) reported that MCT oils exhibit lower interfacial tension and viscosity than long-chain triglyceride oils, forming smaller droplet sizes during emulsification. Adding 3 mL of VCO reduced droplet diameter significantly ($p \leq 0.05$) from 47.05 ± 2.62 nm (GEONe without VCO) to 24.6 ± 0.78 nm. Previous research by Walker et al. (2017) and Sampaio et al. (2022) found that combining low-viscosity carrier oils with high-viscosity bioactive oils reduced droplet size and promoted stable nanoemulsion.

GEONe without VCO showed a significant increase in droplet size over 7 days (from 47.05 ± 2.62 nm to 62.5 ± 0.21 nm (Figure 1(a)), while GEONe with VCO did not show

significant changes. These results indicate that the emulsions containing VCO as a carrier oil are more stable in short-term storage (7 days) than GEONe without VCO. Regarding the polydispersity index (PDI), both the GEONe without VCO and GEONe with 1 mL VCO yielded values above 0.4 (Figure 1(b)). However, the GEONe formulation with 3 mL VCO has a lower PDI value of 0.21, indicating a good droplet size distribution in the emulsion than the former formulations. Regardless of the amount of VCO added in the formulation (1 mL and 3 mL), the GEONe with VCO demonstrated no significant change in the 7-day storage, indicating short-term stability. The GEONe formulation with 3 mL VCO was chosen to fabricate films with small droplet sizes and a stable emulsion. This GEONe formulation was then incorporated into pectin-pineapple juice (PPJ) films at 5%, 10%, 15%, and 20% loadings.

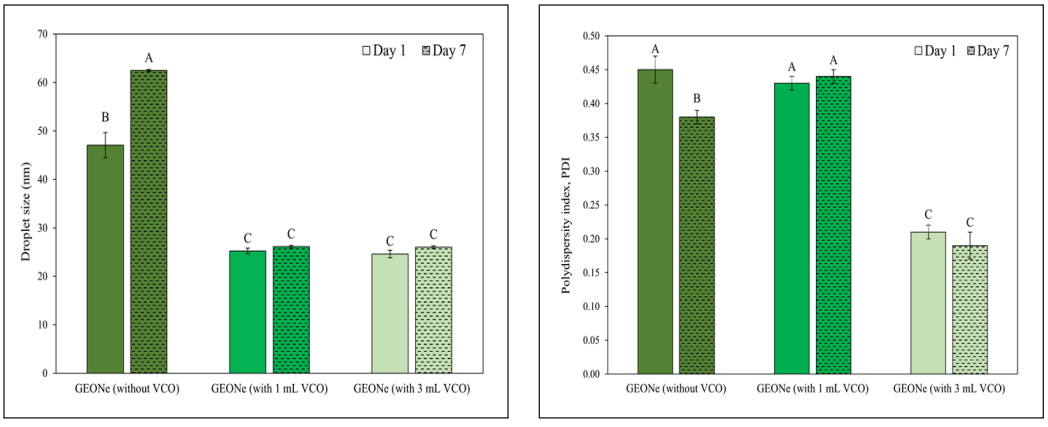

(a) (b)

Figure 1. Droplet size (a) and polydispersity index (PDI) (b) of GEONe with varying levels of VCO, measured on Day 1 and Day 7. Different letters (A, B, and C) indicate significant variations in mean values when considering the interaction of both factors ($p \leq 0.05$)

Characterisation of Pectin-pineapple Juice-GEONe Films

Thickness, Moisture Content, and Water Solubility

Table 1 presents the thickness, moisture content, and water solubility of the pectin-pineapple juice-GEONe films. The thickness of the pectin-pineapple juice (PPJ) film was 91.0 ± 6.9 µm, but the addition of GEONe significantly ($p \leq 0.05$) increased the film's thickness. A study by Li et al. (2021) reported that low thickness formed a compact and ordered network. Nevertheless, an increase in films' thickness from 102.0 ± 0.9 µm to 112.0 ± 2.3 µm was recorded as the GEONe loading increased from 5% to 20%. All of the films have a thickness that is less than the 250 µm maximum standard thickness for edible film set by the Japanese Industrial Standard (1975). A similar increasing trend (55 ± 5 µm to 121 ± 1 µm) was also reported by Jahromi et al. (2022) when emulsified clove essential oil was

added to pectin-based films. Adding essential oil might weaken the interaction between biopolymer molecules and develop a discontinuous and non-compact matrix, increasing the thickness (Li et al., 2022; Wu et al., 2017). When equal volumes of the film-forming solution are applied for casting, the differences in thickness can be attributed to variations in the concentration of total solids present in the film-forming suspensions (Ghani, Barzegar et al., 2018; Kong et al., 2022). Furthermore, the nanoemulsion comprises a lipid phase, water, and surfactant; thus, they can contribute to a thicker film.

Table 1 displays the films' moisture content. The moisture content of PJJ films without GEONe was approximately 11.57%, while the moisture content with various GEONe loadings demonstrated insignificant change ($p > 0.05$). This result can be explained by a considerably low range of GEONe added to the films' solution in the present study.

In addition, Table 1 presents the film's water solubility. The PJJ film was highly soluble in water (93.77% ± 1.07). However, adding 20% GEONe to the film significantly reduces water solubility ($p \leq 0.05$) to 83.16% ± 5.28, indicating a high water solubility. GEO's hydrophobic nature is expected to cause a decrease in water solubility. According to Nisar et al. (2018), cross-linking pectin with essential oils reduces the attraction between the polysaccharide polymer and water molecules. Consequently, the film has a low moisture content and is less water soluble.

Table 1
Thickness, moisture content, and water solubility of PPJ-GEONe films

Film samples	Thickness (µm)	Moisture content (%)	Solubility in water (%)
PPJ-0% GEONe (control)	91.0 ± 6.9^{c}	11.57 ± 1.13^{a}	93.77 ± 1.07^{a}
PPJ-5% GEONe	102.0 ± 0.9^{b}	11.49 ± 0.40^{a}	89.77 ± 0.66^{ab}
PPJ-10% GEONe	108.0 ± 0.6^{ab}	11.25 ± 2.67^{a}	86.27 ± 0.33^{ab}
PPJ-15% GEONe	108.0 ± 0.4^{ab}	10.98 ± 0.62^{a}	86.20 ± 0.49^{ab}
PPJ-20% GEONe	112.0 ± 2.3^{a}	10.33 ± 0.69^{a}	83.16 ± 5.28^{b}

[1]The data is shown as the mean ± standard deviation. Distinct letters within the same column signify statistically significant differences ($p < 0.05$)

Physical Appearance and Colour

Table 2 exhibits the photographic images of the films. All films were visually transparent and had a smooth surface. They were sufficiently flexible when peeling off by hand from petri dishes, indicating good strength and flexibility. Comparing the PPJ films containing various GEONe loadings to the PJJ films without GEONe, the former films exhibited better peel ability than the latter films. These findings are in line with a study by Jahromi et al. (2022), where adding clove essential oil emulsion to high methoxyl pectin-based films had improved peel ability and produced a smoother surface appearance than that of films without the clove essential oil emulsion. The films from the current study have a

mechanical peel ability comparable to the previous study, which makes them suitable for tensile testing (Figure 2(a) to (c)).

Table 2
Photographic images of PPJ-GEONe films

Film samples	PPJ-0% GEONe (control)	PPJ-5% GEONe	PPJ-10% GEONe	PPJ-15% GEONe	PPJ-20% GEONe
Images					

Table 3 presents the data acquired on the PPJ-GEONe films' surface colour parameters, including lightness (*L**), redness-green (*a**, blue-yellow *b**), total colour difference (ΔE), and yellowness index (YI). Adding different GEONe loadings to the films had a significant impact ($p \leq 0.05$) on all colour properties. The control film yields the highest lightness (84.40 ± 0.39) and intermediate yellowness (-1.08 ± 0.42) than the PPJ-GEONe films that were added with 15% and 20% GEONe nanoemulsions. The lightness and yellowness values of the PPJ-20% GEONe films were the lowest, with 81.14 ± 0.76 and 2.78 ± 0.97, respectively. The yellowness in the films was anticipated due to the inherent yellow colour in the pineapple juice. However, PPJ films with 0% to 10% GEONe demonstrated no significant difference ($p > 0.05$) in their yellowness. Adding 15% and 20% GEONe in the films significantly increased the yellowness. Thus, it is speculated that sufficient loading of ginger essential oil in the films influenced the increased yellowness. According to Atarés et al. (2010), variations in colour parameters were influenced by the natural amber-yellow colour of essential oils or lipids. Nisar et al. (2018) reported a similar change in colour parameters in citrus pectin films added with clove bud essential oil.

Table 3
Surface colour parameters (L, a*, b*), total colour difference (ΔE), and yellowness index (YI) values of PPJ-GEONe films*

Film samples	**L***	**a***	**b***	**YI**	**ΔE**
PPJ-0% GEONe (control)	84.40 ± 0.39^{a}	1.25 ± 0.04^{a}	-1.08 ± 0.42^{b}	-1.82 ± 0.63^{b}	-
PPJ-5% GEONe	83.07 ± 0.40^{b}	1.06 ± 0.07^{b}	-0.77 ± 0.46^{b}	-1.33 ± 0.80^{b}	1.43 ± 0.48^{b}
PPJ-10% GEONe	82.90 ± 0.71^{b}	1.03 ± 0.07^{b}	-0.64 ± 0.78^{b}	-1.09 ± 1.15^{b}	1.67 ± 0.78^{b}
PPJ-15% GEONe	81.75 ± 0.37^{c}	0.73 ± 0.03^{c}	1.29 ± 0.54^{a}	2.26 ± 0.96^{a}	3.61 ± 0.61^{a}
PPJ-20% GEONe	81.14 ± 0.76^{c}	0.69 ± 0.05^{c}	1.58 ± 0.54^{a}	2.78 ± 0.97^{a}	4.22 ± 0.87^{a}

[1]The data is shown as the mean ± standard deviation. Distinct letters within the same column signify statistically significant differences ($p < 0.05$)

Tensile Properties

Figure 2 shows the tensile strength (TS), Young's modulus (YM), and elongation at break (EAB) of the PPJ-GEONe films. These are critical mechanical properties to assess the film's strength and flexibility in response to the applied tension force (Shen et al., 2021). The control film (PPJ-0%GEONe) yields TS, YM, and EAB values of 15.98 ± 1.96 MPa, 398.92 ± 83.35 MPa, and 8.71 ± 1.88%, respectively. At the 20% GEONe loading in the PPJ film, the TS and the YM were significantly decreased ($p \leq 0.05$) to 9.54 ± 2.60 MPa (Figure 2 (a)) and 187 ± 38.58 -MPa (Figure 2 (b)), respectively. Conversely, the EAB of the PPJ-20%GEONe films did not change significantly ($p > 0.05$) when compared to the control film. JIS Z 1707 (1975) requires films used for food packaging to have a tensile strength of at least 0.39 MPa. The films produced in this study have tensile strengths that exceed the minimum requirement. However, according to JIS 1975, none of the films' EAB values meet the minimum elongation value requirement of 70%. Almasi et al. (2020) found that the incorporation of marjoram essential oil-loaded nanoemulsion (at 2.5% and 5% w/w of pectin) in the pectin-based films reduced TS from 3.95 ± 0.17 MPa to 1.87 ± 0.45 MPa, and YM from 648 ± 9.43 MPa to 619 ± 4.14 MPa, but had no significant effect on EAB. These findings can be attributed to the incorporation of an essential oil-loaded nanoemulsion, which reduces elasticity and increases plasticity. The ductility and flexibility of the PPJ-GEONe films are

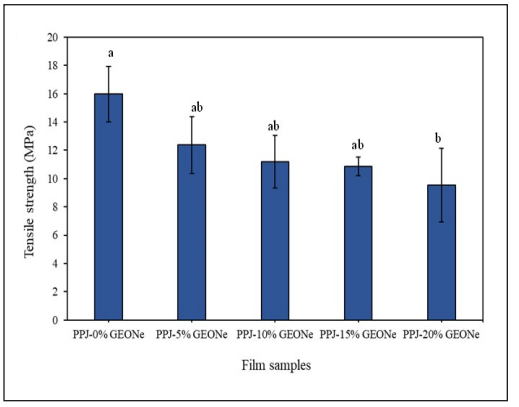

(a)

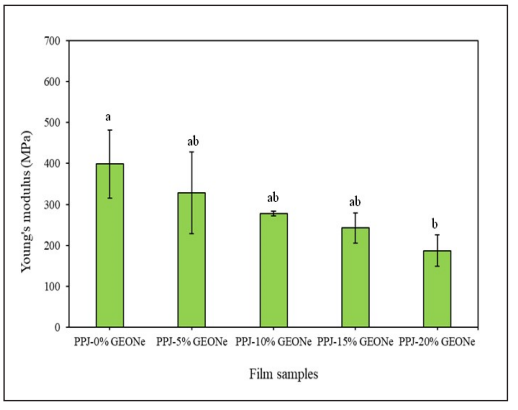

(b)

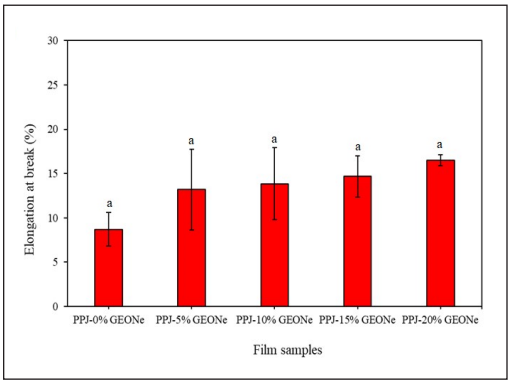

(c)

Figure 2. The tensile strength (a), Young's modulus (b), and elongation at break (c) of PPJ-GEONe films. *Note.* Distinct letters (a, b, and c) show significant differences between means ($p \leq 0.05$) when comparing different percentages of GEONe addition

unaffected by the addition of GEONe (up to 20%). It should be noted that the TS and YM values reported in the current study are higher than those reported by Almasi et al. (2020), most likely due to the use of a higher loading range of GEONe (up to 20%) in the PPJ films. The GEONe droplets in PPJ films provided a plasticising effect, disrupting the hydrogen bonding in the pectin-based films, leading to reduced rigidity and resistance, while increasing the flexibility and segmental mobility of the polymer (Almasi et al., 2020; Otoni et al., 2016). According to Gahruie et al. (2017), the small droplet size of an emulsion can potentially reinforce the biopolymer network by promoting extensive hydrogen bonding (dipole-dipole interaction) between the polar (particularly hydroxyl) groups present along the polymer backbone and the polar head groups of surfactants located at the interface of dispersed nanodroplets in the film-forming solution. Recent studies have shown that adding essential oil-loaded nanoemulsions can reduce the TS of biopolymer-based films, such as pullulan-gelatin films (Shen et al., 2021), chitosan films (Chen et al., 2016), isolated soy protein films (Otoni et al., 2016), and whey protein isolate films (Ghadetaj et al., 2018). The reduced TS was attributed to the plasticising effect of the nanoemulsion droplets, which weakened intermolecular interactions between polymeric chains. In a separate study, Kowalonek et al. (2023) found that adding Tansy EO did not affect the EAB.

Differential Scanning Calorimetric (DSC) Curves

Figure 3 illustrates the DSC curves of pectin-pineapple juice (PPJ) films varied from 0% to 20% loadings of GEONe. These curves represent the thermally induced endothermic changes in the PPJ-GEONe films acquired at a temperature range of -25°C to 200°C. Adding the nanoemulsified ginger essential oil (GEONe) to the PPJ film reduced the enthalpy change (ΔH) values compared to the control film. Among the PPJ-GEONe films, the PPJ-5% GEONe film exhibited the highest ΔH, compared to the control film and PPJ film blended with 10%, 15%, and 20% GEONe. The ΔH of PPJ-GEONe film decreased from 143.01 J/g (PPJ-5% GEONe) to 125.80, 101.79, and 79.60 J/g with the increasing addition of GEONe, respectively. The decrease in the ΔH value of PPJ-GEONe film is also associated with a decrease in the percentage of moisture loss calculated by integrating the area under the endothermic peak in the DSC curves. The existence of hydrophobic ginger essential oil droplets with a high molecular weight disrupted intermolecular interactions within the molecular structure of the PPJ film. Consequently, the heat absorbed softens the structure of the PPJ films combined with GEONe was reduced, improving the film's capable of being extended or shaped below the melting temperature (Nisar et al., 2018; Tongnuanchan et al., 2015). Similar observations were reported by Jahromi et al. (2022) when clove essential oil, both emulsified and non-emulsified, was incorporated into high methoxyl pectin films, resulting in a general reduction in ΔH value.

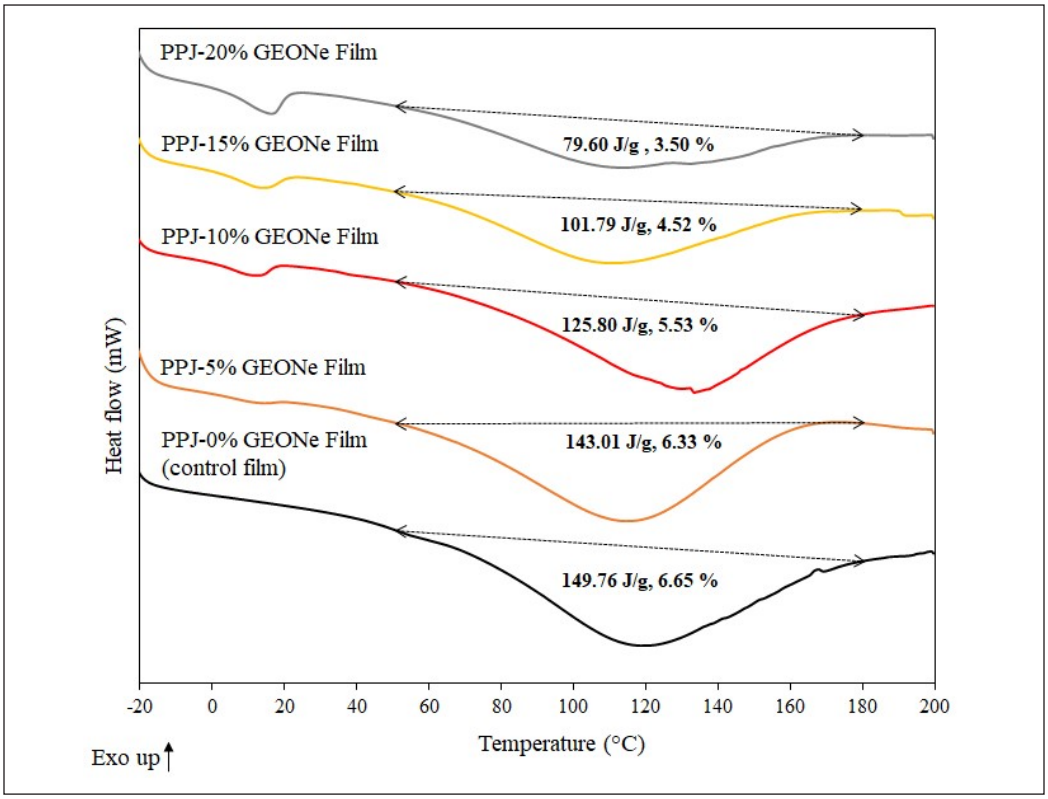

Figure 3. The differential scanning calorimetric (DSC) curves of PPJ-GEONe films
Note. Enthalpy of crystallisation, ΔH (J/g); Moisture loss (%)

CONCLUSION

A stable nanoemulsion of ginger essential oil (GEONe) was successfully produced and incorporated at various loadings to pectin-pineapple juice (PPJ)-based films for improving the PPJ film's physical, mechanical, and thermal properties. The film's formulation consisting of 5 mL ginger essential oil, 3 mL virgin coconut oil, and 1.5 mL polysorbate 80, prepared by sonication at 50% amplitude for 9 min, yields the smallest droplet size with good stability as a nanoemulsion at day 7 (26.00 nm). As the loading of GEONe incorporated into the PPJ film increased, the film thickness significantly increased ($p \leq 0.05$) by 18.75% (PPJ-20% GEONe) compared to the control PPJ film (thickness = 91.0 μm). The moisture content decreased insignificantly ($p > 0.05$) from 11.57% to 10.33%, and the water solubility decreased significantly ($p \leq 0.05$) from 93.77% to 83.16% as the GEONe loading increased from 0% GEONe (control film) to 15% GEONe. The reduction in both moisture content and water solubility can be attributed to the cross-linking of pectin with essential oil, reducing the affinity of the pectin-based film towards water. All PPJ films blended with GEONe exhibited good flexibility, ease of peeling, and a

smooth surface appearance. The incorporation of GEONe resulted in decreased ($p \leq 0.05$) lightness but increased ($p \leq 0.05$) in the yellowness index and total colour differences ($p \leq 0.05$). Incorporating 20% GEONe into the PPJ film led to a significant decrease ($p \leq 0.05$) in the TS and YM to 9.54 ± 2.60 MPa and 187 ± 38.58 MPa, respectively. However, the elongation at break (EAB) of the PPJ-20%GEONe films did not show a statistically significant change ($p > 0.05$) compared to the control film. In terms of thermal properties, there is a decrease in the enthalpy change as the GEONe loading in the PPJ films increases from 5% to 20% (with a range of ΔH = 143.01 J/g to 79.60 J/g). The PPJ-GEONe films have better physical, mechanical and thermal properties compared to the control film. In conclusion, the addition of GEONe alters the physical properties of the PPJ films, enhancing their flexibility and shaping ability, thereby making them potentially suitable for edible food packaging applications.

ACKNOWLEDGEMENTS

The authors acknowledge the financial support provided by the Ministry of Higher Education (MOHE), Malaysia and Universiti Putra Malaysia (UPM) granted with the Fundamental Research Grant Scheme (project code: FRGS/1/2020/TK0/UPM/02/26). Mazween Mohamad Mazlan gratefully thanks the UPM for sponsoring her financial aid under the Graduate Research Fellowship (GRF) program.

REFERENCES

Abraham, R. A., Joshi, J., & Abdullah, S. (2023). A comprehensive review of pineapple processing and its by-product valorization in India. *Food Chemistry Advances*, *3*, Article 100416. https://doi.org/10.1016/j.focha.2023.100416

Adetunji, L. R., Adekunle, A., Orsat, V., & Raghavan, V. (2017). Advances in the pectin production process using novel extraction techniques: A review. *Food Hydrocolloids*, *62*, 239–250. https://doi.org/10.1016/j.foodhyd.2016.08.015

Ali, M. M., Hashim, N., Abd Aziz, S., & Lasekan, O. (2020). Pineapple (Ananas comosus): A comprehensive review of nutritional values, volatile compounds, health benefits, and potential food products. *Food Research International*, *137*, Article 109675. https://doi.org/10.1016/j.foodres.2020.109675

Almasi, H., Azizi, S., & Amjadi, S. (2020). Development and characterization of pectin films activated by nanoemulsion and Pickering emulsion stabilized marjoram (*Origanum majorana L.*) essential oil. *Food Hydrocolloids, 99*, Article 105338. https://doi.org/10.1016/j.foodhyd.2019.105338

AOAC International. (1995). *Official Methods of Analysis of AOAC International* (16th ed.). Association of Official Analytical Chemists.

ASTM D882-18. (2018). *Standard test method for tensile properties of thin plastic sheeting.* American Society for Testing Materials. https://www.astm.org/d0882-18.html

Atarés, L., Bonilla, J., & Chiralt, A. (2010). Characterization of sodium caseinate-based edible films incorporated with cinnamon or ginger essential oils. *Journal of Food Engineering*, *100*(4), 678-687. https://doi.org/10.1016/j.jfoodeng.2010.05.018

Azeredo, H. M., Morrugares-Carmona, R., Wellner, N., Cross, K., Bajka, B., & Waldron, K. W. (2016). Development of pectin films with pomegranate juice and citric acid. *Food Chemistry*, *198*, 101-106. https://doi.org/10.1016/j.foodchem.2015.10.117

Bashiri, S., Ghanbarzadeh, B., Ayaseh, A., Dehghannya, J., Ehsani, A., & Ozyurt, H. (2020). Essential oil-loaded nanostructured lipid carriers: The effects of liquid lipid type on the physicochemical properties in beverage models. *Food Bioscience, 35*, Article 100526. https://doi.org/10.1016/j.fbio.2020.100526

Blanco-Pérez, F., Steigerwald, H., Schülke, S., Vieths, S., Toda, M., & Scheurer, S. (2021). The dietary fiber pectin: Health benefits and potential for the treatment of allergies by modulation of gut microbiota. *Current Allergy and Asthma Reports*, *21*, Article 43. https://doi.org/10.1007/s11882-021-01020-z

Candido, G. S., Natarelli, C. V. L., Carvalho, E. E. N., & Oliveira, J. E. (2022). Bionanocomposites of pectin and pracaxi oil nanoemulsion as active packaging for butter. *Food Packaging and Shelf Life*, *32*, Article 100862. https://doi.org/10.1016/j.fpsl.2022.100862

Chambi, H. N. M., Costa, B. S. D., Lima, W. C. D., & Kassardjian, D. C. (2020). Fruit juices in polysaccharides edible films. *African Journal of Food Science*, *14*(3), 53-62. https://doi.org/10.5897/AJFS2020.1916

Chen, H., Hu, X., Chen, E., Wu, S., McClements, D. J., Liu, S., Li, B., & Li, Y. (2016). Preparation, characterization, and properties of chitosan films with cinnamaldehyde nanoemulsions. *Food Hydrocolloids*, *61*, 662-671. https://doi.org/10.1016/j.foodhyd.2016.06.034

Chen, Q., You, N., Liang, C., Xu, Y., Wang, F., Zhang, B., & Zhang, P. (2023). Effect of cellulose nanocrystals-loaded ginger essential oil emulsions on the physicochemical properties of mung bean starch composite film. *Industrial Crops and Products*, *191,* Article 116003. https://doi.org/10.1016/j.indcrop.2022.116003

DOA. (2022). *Fruit Crop Statistic 2022*. Department of Agriculture

Dranca, F., Talón, E., Vargas, M., & Oroian, M. (2021). Microwave vs. conventional extraction of pectin from Malus domestica '*Fălticeni*' pomace and its potential use in hydrocolloid-based films. *Food Hydrocolloids*, *121*, Article 107026. https://doi.org/10.1016/j.foodhyd.2021.107026

Fasihi, H., Noshirvani, N., & Hashemi, M. (2023). Novel bioactive films integrated with Pickering emulsion of ginger essential oil for food packaging application. *Food Bioscience*, *51*, Article 102269. https://doi.org/10.1016/j.fbio.2022.102269

Fernandes, R. V. D. B., Borges, S. V., Silva, E. K., Silva, Y. F. D., Souza, H. J. B. D., Carmo, E. L. D., Oliveira, C. R. D., Yoshida, M. I., & Botrel, D. A. (2016). Study of ultrasound-assisted emulsions on microencapsulation of ginger essential oil by spray drying. *Industrial Crops and Products*, *94,* 413-423. https://doi.org/10.1016/j.indcrop.2016.09.010

Foodprint. (2020). *The foodprint of food packaging*. Foodprint. https://foodprint.org/reports/the-foodprint-of-food-packaging/

Gahruie, H. H., Ziaee, E., Eskandari, M. H., & Hosseini, S. M. H. (2017). Characterization of basil seed gum-based edible films incorporated with Zataria multiflora essential oil nanoemulsion. *Carbohydrate polymers*, *166,* 93-103. https://doi.org/10.1016/j.carbpol.2017.02.103

Ghadetaj, A., Almasi, H., & Mehryar, L. (2018). Development and characterization of whey protein isolate active films containing nanoemulsions of *Grammosciadium ptrocarpum Bioss*. essential oil. *Food Packaging and Shelf Life*, *16,* 31-40. https://doi.org/10.1016/j.fpsl.2018.01.012

Ghani, N. A. A., Channip, A. A., Hwa, P. C. H., Ja'afar, F., Yasin, H. M., & Usman, A. (2018). Physicochemical properties, antioxidant capacities, and metal contents of virgin coconut oil produced by wet and dry processes. *Food Science & Nutrition*, *6*(5), 1298-1306. https://doi.org/10.1002/fsn3.671

Ghani, S., Barzegar, H., Noshad, M., & Hojjati, M. (2018). The preparation, characterization and in vitro application evaluation of soluble soybean polysaccharide films incorporated with cinnamon essential oil nanoemulsions. *International Journal of Biological Macromolecules*, *112,* 197-202. https://doi.org/10.1016/j.ijbiomac.2018.01.145

Ghoshal, G. (2022). Thyme essential oil nano-emulsion/tamarind starch/whey protein concentrate novel edible films for tomato packaging. *Food Control*, *138*, Article 108990. https://doi.org/10.1016/j.foodcont.2022.108990

Jahromi, M., Niakousari, M., & Golmakani, M. T. (2022). Fabrication and characterization of pectin films incorporated with clove essential oil emulsions stabilized by modified sodium caseinate. *Food Packaging and Shelf Life*, *32*, Article 100835. https://doi.org/10.1016/j.fpsl.2022.100835

Japanese Industrial Standard. (1975). *Japanese Standards Association Z 1707: Plastic Films for Food Packaging.* Japanese Standard Association.

Jiang, T., & Charcosset, C. (2022). Encapsulation of curcumin within oil-in-water emulsions prepared by premix membrane emulsification: Impact of droplet size and carrier oil on the chemical stability of curcumin. *Food Research International*, *157*, Article 111475. https://doi.org/10.1016/j.foodres.2022.111475

Kabasakalis, V. (2000). Ascorbic acid content of commercial fruit juices and its rate of loss upon storage. *Food Chemistry, 70*(3), 325–328. https://doi.org/10.1016/S0308- 8146(00)00093-5

Kong, I., Degraeve, P., & Pui, L. P. (2022). Polysaccharide-based edible films incorporated with essential oil nanoemulsions: Physico-chemical, mechanical properties and its application in food preservation−A review. *Foods*, *11*(4), Article 555. https://doi.org/10.3390/foods11040555

Kumar, S., Reddy, A. R. L., Basumatary, I. B., Nayak, A., Dutta, D., Konwar, J., M. D. Purkayastha, M. D., & Mukherjee, A. (2023). Recent progress in pectin extraction and their applications in developing films and coatings for sustainable food packaging: A review. *International Journal of Biological Macromolecules, 239*, Article 124281. https://doi.org/10.1016/j.ijbiomac.2023.124281

Kowalonek, J., Stachowiak, N., Bolczak, K., & Richert, A. (2023). Physicochemical and antibacterial properties of alginate films containing tansy (*Tanacetum vulgare L.*) essential oil. *Polymers*, *15*(2), Article 260. https://doi.org/10.3390/polym15020260

Kute, A. B., Mohapatra, D., Kotwaliwale, N., Giri, S. K., & Sawant, B. P. (2020). Characterization of pectin extracted from orange peel powder using microwave-assisted and acid extraction methods. *Agricultural Research*, *9*, 241-248. https://doi.org/10.1007/s40003-019-00419-5

Li, X., Tu, Z. C., Sha, X. M., Ye, Y. H., & Li, Z. Y. (2022). Flavor, antimicrobial activity and physical properties of gelatin film incorporated with of ginger essential oil. *Journal of Food Science and Technology*, *59,* 815–824. https://doi.org/10.1007/s13197-021-05080-x

Man, Y. B. C., & Marina, A. M. (2006). Medium chain triacylglycerol. In F. Shahidi (Ed.) *Nutraceutical and Specialty Lipids and their Co-products* (pp. 27–56). Taylor & Francis Group. https://doi.org/10.1201/9781420015911

Marić, M., Grassino, A. N., Zhu, Z., Barba, F. J., Brnčić, M., & Brnčić, S. R. (2018). An overview of the traditional and innovative approaches for pectin extraction from plant food wastes and by-products: Ultrasound-, microwaves-, and enzyme-assisted extraction. *Trends in Food Science & Technology*, *76*, 28–37. https://doi.org/10.1016/j.tifs.2018.03.022

Nastasi, J. R., Kontogiorgos, V., Daygon, V. D., & Fitzgerald, M. A. (2022). Pectin-based films and coatings with plant extracts as natural preservatives: A systematic review. *Trends in Food Science & Technology*, *120*, 193-211. https://doi.org/10.1016/j.tifs.2022.01.014

Nguyen, V., & Diep, T. T. (2022). Efficacy of enriched medium-chain fatty acids in virgin coconut oil in their antibacterial activity against food pathogens. *Philippine Journal of Science*, *151*(3), 813-821. https://doi.org/10.56899/151.03.02

Nisar, T., Wang, Z. C., Yang, X., Tian, Y., Iqbal, M., & Guo, Y. (2018). Characterization of citrus pectin films integrated with clove bud essential oil: Physical, thermal, barrier, antioxidant and antibacterial properties. *International Journal of Biological Macromolecules*, *106*, 670-680. https://doi.org/10.1016/j.ijbiomac.2017.08.068

Noori, S., Zeynali, F., & Almasi, H. (2018). Antimicrobial and antioxidant efficiency of nanoemulsion-based edible coating containing ginger (*Zingiber officinale*) essential oil and its effect on safety and quality attributes of chicken breast fillets. *Food Control*, *84*, 312-320. https://doi.org/10.1016/j.foodcont.2017.08.015

Norcino, L. B., Mendes, J. F., Natarelli, C. V. L., Manrich, A., Oliveira, J. E., & Mattoso, L. H. C. (2020). Pectin films loaded with copaiba oil nanoemulsions for potential use as bio-based active packaging. *Food Hydrocolloids*, *106*, Article 105862. https://doi.org/10.1016/j.foodhyd.2020.105862

Otoni, C. G., Avena-Bustillos, R. J., Olsen, C. W., Bilbao-Sáinz, C., & McHugh, T. H. (2016). Mechanical and water barrier properties of isolated soy protein composite edible films as affected by carvacrol and cinnamaldehyde micro and nanoemulsions. *Food Hydrocolloids*, *57*, 72-79. https://doi.org/10.1016/j.foodhyd.2016.01.012

Pimiento, C. R. Q., Fernández, P. V., Ciancia, M., López-Córdoba, A., Goyanes, S., Bertuzzi, M. A., & Foresti, M. L. (2023). Antioxidant edible films based on pear juice and pregelatinized cassava starch: Effect of the carbohydrate profile at different degrees of pear ripeness. *Polymers*, *15*(21), Article 4263. https://doi.org/10.3390/polym15214263

Ranjbaryan, S., Pourfathi, B., & Almasi, H. (2019). Reinforcing and release controlling effect of cellulose nanofiber in sodium caseinate films activated by nanoemulsified cinnamon essential oil. *Food Packaging and Shelf Life*, *21*, Article 100341. https://doi.org/10.1016/j.fpsl.2019.100341

Rosli, N. A., Islan, G. A., Hasham, R., Castro, G. R., & Aziz, A. A. (2022). Incorporation of nanoparticles based on *Zingiber Officinale* essential oil into alginate films for sustained release. *Journal of Physical Science*, *33*(2), 107–124. https://doi.org/10.21315/jps2022.33.2.7

Roy, S., Priyadarshi, R., Łopusiewicz, Ł., Biswas, D., Chandel, V., & Rhim, J. W. (2023). Recent progress in pectin extraction, characterization, and pectin-based films for active food packaging applications: A review. *International Journal of Biological Macromolecules, 239*, Article 124248. https://doi.org/10.1016/j.ijbiomac.2023.124248

Salehi, F. (2020). Physicochemical characteristics and rheological behaviour of some fruit juices and their concentrates. *Journal of Food Measurement and Characterization*, *14*(5), 2472-2488. https://doi.org/10.1007/s11694-020-00495-0

Sampaio, C. I., Bourbon, A. I., Gonçalves, C., Pastrana, L. M., Dias, A. M., & Cerqueira, M. A. (2022). Low energy nanoemulsions as carriers of thyme and lemon balm essential oils. *Lwt-Food Science Technology*, *154*, Article 112748. https://doi.org/10.1016/j.lwt.2021.112748

Shaaban, H. A., Mahmoud, K. F., Amer, M. M., Amin, A. A., & Mohamed, S. S. (2016). Preparation of antibacterial food active package nano-biocomposite edible film containing pectin and cinnamon essential oil nano-emulsion. *Research Journal of Pharmaceutical, Biological and Chemical Sciences*, *7*(5), 2665–2672.

Shen, Y., Ni, Z. J., Thakur, K., Zhang, J. G., Hu, F., & Wei, Z. J. (2021). Preparation and characterization of clove essential oil loaded nanoemulsion and pickering emulsion activated pullulan-gelatin based edible film. *International Journal of Biological Macromolecules*, *181*, 528-539. https://doi.org/10.1016/j.ijbiomac.2021.03.133

Statistica (2024). *Pineapple Juice - Malaysia*. Statistica. https://www.statista.com/outlook/cmo/non-alcoholic-drinks/juices/pineapple-juice/malaysia

Susmitha, A., Sasikumar, K., Rajan, D., & Nampoothiri, K. M. (2021). Development and characterization of corn starch-gelatin based edible films incorporated with mango and pineapple for active packaging. *Food Bioscience*, *41*, Article 100977. https://doi.org/10.1016/j.fbio.2021.100977

Tongnuanchan, P., Benjakul, S., Prodpran, T., & Nilsuwan, K. (2015). Emulsion film based on fish skin gelatin and palm oil: Physical, structural and thermal properties. *Food Hydrocolloids*, *48*, 248-259. https://doi.org/10.1016/j.foodhyd.2015.02.025

Tulamandi, S., Rangarajan, V., Rizvi, S. S., Singhal, R. S., Chattopadhyay, S. K., & Saha, N. C. (2016). A biodegradable and edible packaging film based on papaya puree, gelatin, and defatted soy protein. *Food Packaging and Shelf Life*, *10*, 60-71. https://doi.org/10.1016/j.fpsl.2016.10.007

Walker, R. M., Gumus, C. E., Decker, E. A., & McClements, D. J. (2017). Improvements in the formation and stability of fish oil-in-water nanoemulsions using carrier oils: MCT, thyme oil, & lemon oil. *Journal of Food Engineering*, *211*, 60-68. https://doi.org/10.1016/j.jfoodeng.2017.05.004

Wu, J., Sun, X., Guo, X., Ge, S., & Zhang, Q. (2017). Physicochemical properties, antimicrobial activity and oil release of fish gelatin films incorporated with cinnamon essential oil. *Aquaculture and Fisheries*, *2*(4), 185-192. https://doi.org/10.1016/j.aaf.2017.06.004

Yıldırım-Yalçın, M., Sadıkoğlu, H., & Şeker, M. (2021). Characterization of edible film based on grape juice and cross-linked maize starch and its effects on the storage quality of chicken breast fillets. *LWT - Food Science and Technology*, *142*, Article 111012. https://doi.org/10.1016/j.lwt.2021.111012

Zainal, F., Gimino, G., Hilmy, I., & Yun, Y. X. (2023, March 6). Eliminating single-use plastics by 2030 seen as an uphill battle. *The Star*. https://www.thestar.com.my/news/nation/2023/03/06/eliminating-single-use-plastics-by-2030-seen-as-an-uphill-battle

Zhang, W., Jiang, H., Rhim, J. W., Cao, J., & Jiang, W. (2022). Effective strategies of sustained release and retention enhancement of essential oils in active food packaging films/coatings. *Food Chemistry*, *367*, Article 130671. https://doi.org/10.1016/j.foodchem.2021.130671

Pertanika J. Sci. & Technol. 33 (S1): 65 - 81 (2025)

PERTANIKA JOURNALS

SCIENCE & TECHNOLOGY

Journal homepage: http://www.pertanika.upm.edu.my/

Effect of Hydrogen Peroxide and Sodium Alcohol Ether Sulphate on the Properties of Porous Rice Husk Ash-based Geopolymer Foam

Nurul Husna Mohd Azib[1], Mohd Salahuddin Mohd Basri[1,2,3]*, Mohd Zuhair Mohd Nor[1], Faiqa Shazeaa Mohd. Salleh[1], Siti Hajar Othman[1,5], Mohd Afandi P Mohammed[1], Norkhairunnisa Mazlan[4,5], Siti Hasnah Kamarudin[6] and Muhammad Hazwan Hamzah[7,8]

[1]Department of Process and Food Engineering, Faculty of Engineering, University Putra Malaysia, 43400 UPM Serdang, Selangor, Malaysia
[2]Laboratory of Halal Science Research, Halal Products Research Institute, Universiti Putra Malaysia (UPM), 43400 Serdang, Malaysia
[3]Laboratory of Biopolymer and Derivatives, Institute of Tropical Forestry and Forest Products (INTROP), Universiti Putra Malaysia, Serdang 43400, Selangor, Malaysia
[4]Department of Aerospace Engineering, Faculty of Engineering, University Putra Malaysia, 43400 UPM Serdang, Selangor, Malaysia
[5]institute of Nanoscience and Nanotechnology (ION2), Institute of Nanoscience and Nanotechnology, Universiti Putra Malaysia, 43400 Serdang, Selangor, Malaysia
[6]School of Industrial Technology, Faculty of Applied Sciences, Universiti Teknologi MARA (UiTM), 40450, Shah Alam, Selangor, Malaysia
[7]Department of Biological and Agricultural Engineering, Faculty of Engineering, Universiti Putra Malaysia, Serdang 43400, Selangor, Malaysia
[8]SMART Farming Technology Research Centre, Faculty of Engineering, Universiti Putra Malaysia, Serdang 43400, Selangor, Malaysia

ABSTRACT

Rice husk is a typical solid waste generated during rice processing, typically disposed of by combustion or landfills. One promising method for repurposing rice husk ash is as a pozzolan in geopolymer foam. This study explores additives like hydrogen peroxide and sodium alcohol ether sulfate (SAES) to enhance the properties of porous geopolymer foam made from rice husk ash. Hydrogen peroxide is utilized as a foaming agent to enhance porosity, while SAES acts as a stabilizer to influence the structure of the foam. The foam was prepared by mixing sodium silicate, sodium hydroxide, rice husk ash, genioperl, hydrogen peroxide, and stabilizer in specific ratios. Two variables are hydrogen peroxide (0.0, 0.1, 0.2, 0.3, and 0.4 wt.%) and

ARTICLE INFO

Article history:
Received: 8 November 2023
Accepted: 5 November 2024
Published: 31 January 2025

DOI: https://doi.org/10.47836/pjst.33.S1.04

E-mail addresses:
husnaazib16@gmail.com (Nurul Husna Mohd Azib)
salahuddin@upm.edu.my (Mohd Salahuddin Mohd Basri)
zuhair@upm.edu.my (Mohd Zuhair Mohd Nor)
faiqazea@upm.edu.my (Faiqa Shazeaa Mohd. Salleh)
s.hajar@upm.edu.my (Siti Hajar Othman)
afandi@upm.edu.my (Mohd Afandi P Mohammed)
norkhairunnisa@upm.edu.my (Norkhairunnisa Mazlan)
sitihasnahkam@uitm.edu.my (Siti Hasnah Kamarudin)
hazwanhamzah@upm.edu.my (Muhammad Hazwan Hamzah)
*Corresponding author

ISSN: 0128-7680
e-ISSN: 2231-8526

SAES (0.0, 0.5, 1.0, 1.5, and 2.0 wt.%). The compressive strength and total porosity tests are conducted according to standards. The results show that increased hydrogen peroxide increased total porosity but decreased compressive strength. On the other hand, SAES improved the foam's structural integrity and maintained the compressive strength without significantly increasing porosity at 1.0 wt.% concentrations. The optimal total porosity and compressive strength were achieved with 0.40 wt.% hydrogen peroxide and 1.0 wt.% SAES. This study contributes to agriculture science and technology by exploring the potential use of rice husk ash-based geopolymer foam and determining the optimum formulation for its production. The findings also suggest that this foam can be utilized in various agricultural applications such as buildings, pipelines, and agriculture fields.

Keywords: Compressive strength, geopolymer foam, hydrogen peroxide, rice husk ash, sodium alcohol ether sulfate

INTRODUCTION

Rice, a fundamental global food, contributes 21% of the world's per capita human energy and 15% of per capita protein. Rice protein, highly nutritious among cereals, contains minerals, vitamins, and fiber. Milling reduces all components except carbohydrates. Rice processing starts with pre-planting activities, including field preparation, transplanting, and harvesting (Kumar et al., 2021). Post-production involves pre-cleaning, dehusking, paddy separation, whitening, grading, weighing, and bagging. The husk separation process removes husk and bran, producing head white rice grains that are well-milled and impurity-free, containing minimal broken grains.

Rice husks, removed during milling, are protective solid coverings. In all rice-producing countries, rice husk, comprising 30% –50% organic carbon, is a readily available waste material. Rice husk composition includes cellulose (50%), lignin (25% –30%), silica (15% –20%), and moisture (10% –15%). The low bulk density of rice husk ranges from 90 kg/m^3 to 150 kg/m^3 (Singh, 2018).

Rice husk ash (RHA) is the product of rice husk incineration. Most evaporative components of rice husk are lost during burning, leaving silicates as primary residues. Ash characteristics depend on rice husk composition, temperature, and burning time. Combustion conditions significantly influence RHA chemical composition, and controlled burning is essential to retain silica in its amorphous state (Dizaji et al., 2022). Uncontrolled combustion at temperatures exceeding 700°C – 800°C produces non-reactive silica minerals like cristobalite and tridymite, making ash pulverization for pozzolanic activity economically unviable. In the construction industry, RHA applications include its use as pozzolan, filler, additive, abrasive agent, oil adsorbent, sweeping part, and suspension agent for porcelain enamels. RHA may partially substitute cement in the building industry (Pacho et al., 2024; Singh, 2018).

Geopolymers are amorphous aluminosilicate ceramic-like materials that are formed and reinforced at room temperature. It was produced using aluminosilicate sources commonly used as geopolymer binders. Alkali hydroxide and silicate solution reactions give a highly alkaline state that contributes to the polymerization process. Because of its excellent strength and environmental impact, geopolymer compounds have arisen and replaced conventional cement compounds (Komnitsas & Zaharaki, 2007; Singh & Middendorf, 2020). Production of geopolymer involves chemical reactions that convert amorphous aluminosilicates (partially or completely) into three-dimensional polymer networks. The response to geopolymerisation is exothermic. The aluminosilicate sources dissolve under a strongly alkaline medium into SiO_4 and AlO_4 tetrahedral units, which are subsequently involved in the polycondensation process (Celik et al., 2018). Geopolymer materials offer numerous advantages, including high resilience, fire resistance, thermal stability, excellent mechanical properties, and acid resistance (Amran et al., 2022). Low-density geopolymers find applications in thermal insulation, fire resistance, and high-temperature applications, making them potential materials (Hassan et al., 2023).

With remarkable properties, low cost, and green synthesis protocols, porous geopolymer foams have emerged as highly promising materials for various high-added-value applications (Li et al., 2023). Chemical foaming agents can prepare the cellular structure of geopolymer foam. The rice husk ash-based geopolymer foam's enhanced compressive strength and porosity make it an excellent candidate for building materials where improved thermal insulation and fire resistance are essential. For example, recent studies have demonstrated using geopolymer foams as insulation panels in energy-efficient buildings, contributing to significant reductions in heating and cooling costs (Tarek et al., 2022). In the pipeline industry, the foam's durability and resistance to chemical corrosion can extend the lifespan of pipeline coatings, reducing maintenance costs and improving safety. Additionally, its application in agriculture as a soil amendment or lightweight aggregate for green roofs can promote sustainability by reducing the environmental impact of construction activities and enhancing soil properties for better plant growth (Fatehi et al., 2021). These case studies underscore the transformative potential of our research in delivering practical, sustainable solutions across multiple sectors.

Hydrogen peroxide is a well-known alternative blowing method that creates a more uniform foam by generating gas at the molecular level. In primary media, it is thermodynamically unstable, decomposing into water and oxygen gas. The trapped gas bubbles expand within the paste, forming voids (macropores). Stabilizers, unlike catalysts, work to slow down chemical reactions. While catalysts and enzymes speed up chemical reactions, stabilizers slow them down (Yan et al., 2024). Stabilizers prevent or alter reactions like corrosion, oxidation, and separation on a molecular and chemical level. Many of these stabilizers prevent a catalyst or enzyme from performing its function. Adding a stabilizer

to the slurry improves the wet foam's stability and aids in the control of the amount of interconnected (open) porosity generated in geopolymer foam (Negri et al., 2020).

The reaction between the aluminum powder and the alkali activator or hydrogen peroxide decomposition in geopolymers allows porous structures to develop. Geopolymer foams can also be produced by gel-casting, using the geopolymerization reaction to stabilize the gas bubbles introduced by rotational mixing in the liquid slurry. Geopolymer foams have excellent physical-chemical and mechanical properties, low density, high strength, thermal stability, and good fire and chemical resistance (Coman et al., 2020; Zhao et al., 2023). The study on foam as concrete using waste materials has long been conducted. However, the study on porous geopolymer foam using rice husk ash is rather limited. Even though geopolymer material has outstanding thermal properties, limited research has been conducted on the optimum formulation for RHA-based geopolymer foam. Due to air pollution from burning rice husks in an open area, rice husks have shown great potential as waste material in producing geopolymer foam.

This study elucidates the effects of hydrogen peroxide and sodium alcohol ether sulfate (SAES) on rice husk ash-based geopolymer foam. By doing so, specific formulations that optimize compressive strength and porosity can be identified, which are crucial for expanding the applications of this material. Unlike previous studies, this study provides a comprehensive analysis of the dual role of these additives, which reveal their potential to enhance material properties for innovative uses in construction and agriculture. The optimal ratio between RHA and activated alkaline solution (AA), the amount of hydrogen peroxide, and the amount of stabilizer (sodium alcohol ether sulfate, or SAES) need to be investigated. Adding hydrogen peroxide is a blowing agent that produces a gas bubble, producing a geopolymer foam cellular structure. The purpose of adding a stabilizer is to influence the compressive strength and total porosity of the porous geopolymer foam.

Despite the promising properties of rice husk ash and its potential in geopolymer applications, research on porous geopolymer foam using rice husk ash remains limited. Most existing studies focus on single-additive systems, leaving a gap in understanding how multiple additives can enhance the material's properties. This study addresses this gap by investigating the combined effects of hydrogen peroxide and sodium alcohol ether sulfate (SAES) on the compressive strength and porosity of rice husk ash-based geopolymer foam. This dual-additive approach offers a novel strategy for optimizing material performance, providing potential for innovative construction and agriculture applications. By identifying specific formulations that optimize compressive strength and porosity, this research contributes to expanding the application scope of geopolymer foam, offering sustainable alternatives to traditional materials.

MATERIALS AND METHODS

Materials

Rice husk ash (RHA) was acquired from Maero Tech Sdn. Bhd., situated in Nilai 3, Negeri Sembilan. The ash underwent size reduction using a blender (MX-SM1031SSL, Panasonic, Malaysia). Sodium hydroxide (NaOH), Sodium silicates, Hydrogen peroxide (H_2O_2), and Sodium alcohol ether sulfate (SAES) were procured from R&M Chemicals at Ever Gainful Enterprise Sdn. Bhd. in Malaysia. NaoH is available in pellet, flake, and powder formulations. This study utilized high-purity commercial-grade sodium hydroxide (NaOH) in flake form, boasting a purity level between 97% and 100%. Sodium silicates were in solution form with a purity of 98%. Sodium alcohol ether sulfate (SAES) was the hydrogen peroxide type. The SAES concentration investigated in this research ranges from 0.0 to 2.0 wt%. Genioperl P52 core-shell rubber (CSR) was acquired from Wacker Chemie AG, Germany. The synthesis process was carefully controlled to ensure the uniform distribution of hydrogen peroxide and sodium alcohol ether sulfate (SAES) within the rice husk ash-based geopolymer matrix. Preliminary trials optimized key parameters such as mixing speed, temperature, and curing time. Specifically, the stirring speed was maintained at 1100 rpm for 15 minutes to achieve a homogenous mixture, while the curing was conducted at a constant temperature of 70°C for 24 hours to ensure consistent foam structure.

Sample Preparation

Compressive strength test samples were prepared by grinding the rice husk ash using a blender MX-SM1031SSL Panasonic, producing fine ground rice husk ash. Next, the test samples were prepared by producing the geopolymer slurry and activated alkaline (AA) solution. The AA was initially synthesized using a sodium hydroxide solution (10 M) and sodium silicate solutions in a 3.5 ratio. Subsequently, the AA solution was blended with rice husk ash (RHA) at a ratio of 0.25 to create a geopolymer slurry. The binder was introduced, along with the addition of genioperl. The geopolymer mixture was stirred gently for 15 minutes using a mechanical stirrer (Wisd WiseStir Overhead Stirrer HS-30D, Witeg Labortechnik GmbH, Germany) at 1100 rpm until the solution became homogenous. After the geopolymer slurry was formed, a blowing agent (hydrogen peroxide) and stabilizing agent (SAES) were added to the mixture based on the designated composition. Amounts of hydrogen peroxide used were 0, 0.1, 0.2, 0.3, and 0.4 wt.%, while SAES were 0, 0.5, 1.0, 1.5, and 2.0 wt.%. The mixture was stirred vigorously. The samples were sealed into a mold according to the standard for the compression test (2.5 x 2.5 x 2.5 cm) and cured in an oven (Memmert Oven ULE400, MEMMERT GmbH + Co. KG, Germany) at 70°C for 24 hours. Then, the geopolymer foam (GPF) samples were stored before testing.

Experiment Procedure

The compressive test was performed following ASTM D695 using the Instron 3382 Floor Model Universal Testing System (INSTRON ® HQ, Norwood, MA). The quantitative analysis of the total porosity of geopolymer foam was performed by calculating the value of true density and the bulk density. Density is calculated by dividing volume by weight. True density was calculated by randomly selecting the weight and volume of one sample from each group (formulation). Bulk density was calculated by the weight and volume for all samples (total 26 runs). During the experimentation, several challenges were encountered, including ensuring the stability of the foam structure, which posed a challenge, especially with varying concentrations of hydrogen peroxide. Mitigation involved optimizing sodium alcohol ether sulfate (SAES) as a stabilizing agent through iterative testing, ensuring the foam maintained its integrity throughout the curing process.

Experimental Design

This study uses a response surface methodology (RSM) and analyzes it using MINITAB software (Minitab Statistical Software, Minitab, LLC, Pennsylvania State University). It involves two factors (hydrogen peroxide and stabilizer) and two replications for 26 runs. The design of the experiment (DOE) is shown in Table 1.

Table 1
Design of experiment

Sample	Coded Factor		Uncoded Factor	
	V_1	V_2	V_1	V_2
S1	2	0	0.4	1.0
S2	0	0	0.2	1.0
S3	2	0	0.4	1.0
S4	0	0	0.2	1.0
S5	0	0	0.2	1.0
S6	0	0	0.2	1.0
S7	-1	1	0.1	1.5
S8	1	1	0.3	1.5
S9	0	0	0.2	1.0
S10	-1	-1	0.1	0.5
S11	-2	0	0.0	1.0
S12	0	0	0.2	1.0
S13	0	-2	0.2	0.0
S14	0	0	0.2	1.0
S15	-1	-1	0.1	0.5
S16	1	-1	0.3	0.5

Table 1 (*continue*)

Sample	Coded Factor		Uncoded Factor	
	V_1	V_2	V_1	V_2
S17	0	2	0.2	2.0
S18	0	-2	0.2	0.0
S19	-2	0	0.0	1.0
S20	1	-1	0.3	0.5
S21	0	0	0.2	1.0
S22	0	0	0.2	1.0
S23	0	0	0.2	1.0
S24	1	1	0.3	1.5
S25	-1	1	0.1	1.5
S26	0	2	0.2	2.0

RESULTS AND DISCUSSION

Statistical Analysis of Total Porosity and Compressive Strength Properties

Results in Table 2 show the estimated effects for total porosity, which indicates that hydrogen peroxide (V_1) was the highly significant factor where $P < 0.000$. In contrast, the stabilizer factor (V_2) was highly insignificant, with $P > 0.050$. The combination of V_1*V_1 showed significant values ($P < 0.000$) and affected the responses. The combination of V_2*V_2 and V1*V2 showed insignificant values ($P > 0.050$) and did not affect the responses. Significant values were observed for R^2 (coefficient of determination) and R^2 (adjusted), standing at 0.8958 and 0.8697, respectively. These results denote a substantial influence, signifying that 89.58% of the variance in the response can be attributed to the pertinent factors within the sample.

Table 2
Estimated effects and coefficient for total porosity

Term	Notation	Coefficient	Std. error of the coefficient	P
Constant		40.1040	0.9256	0.000
Hydrogen Peroxide	V_1	7.5667	0.6435	0.000
Stabilizer	V_2	0.7958	0.6435	0.231
Hydrogen Peroxide * Hydrogen Peroxide	V_1*V_1	-2.5335	0.4657	0.000
Stabilizer * Stabilizer	V_2*V_2	-0.8004	0.4657	0.101
Hydrogen Peroxide * Stabilizer	V_1*V_2	1.7500	1.1146	0.132
R^2 = 89.58 percent		R^2(adj) = 86.97 percent		

Regarding compressive strength, the significance of factors and their interactions was assessed with a confidence level set at 95 percent (P-value of 0.050). Notably, most

interaction effects were deemed highly insignificant when $P > 0.050$. The results presented in Table 3 indicate the insignificance of several factors and interaction effects, including V_2, V_2*V_2, and V_1*V_2, as their corresponding P-values exceed 0.050. Individual factors exhibited high significance ($P < 0.000$) for V_1 and V_1*V_1, while insignificance was observed for V_2 (P= 0.869), V_2*V_2 (P= 0.973), and V_1*V_2 (P= 0.949). The obtained values for R^2 and R^2 (adjusted), namely 0.7823 and 0.7279, respectively, were considered high. It suggests that a substantial portion, specifically 78.23%, of the variance in the response within the sample can be ascribed to the independent variables.

Table 3
Estimated effects and coefficient for compressive strength

Term	Notation	Coefficient	Std. error of coefficient	P
Constant		-0.0343	0.1139	0.766
Hydrogen Peroxide	V_1	0.4518	0.0792	0.000
Stabilizer	V_2	-0.0132	0.0792	0.869
Hydrogen Peroxide * Hydrogen Peroxide	V_1*V_1	0.3452	0.0573	0.000
Stabilizer * Stabilizer	V_2*V_2	0.0020	0.0573	0.973
Hydrogen Peroxide * Stabilizer	V_1*V_2	-0.0088	0.1372	0.949
R^2 = 78.23 percent		R^2(adj) = 72.79 percent		

Equations 1 and 2 represent the regression models for the total porosity and compressive strength.

$$Y_{TP} = 40.104 + 7.5667\ (V_1) + 0.7958\ (V_2) - 2.5335\ (V_1^2) - 0.8004\ (V_2^2) + 1.75\ (V_1*V_2) \quad [1]$$

$$Y_{CS} = -0.0343 + 0.4518\ (V_1) - 0.0132\ (V_2) + 0.3452\ (V_1^2) + 0.002\ (V_2^2) - 0.0088\ (V_1*V_2) \quad [2]$$

where Y_{TP} and Y_{CS} denote the responses, representing total porosity and compressive strength, respectively. V_1 and V_2 correspond to the decoded values of hydrogen peroxide and stabilizer, respectively. Utilizing regression models allows for the calculation and analysis of the influence of these factors on both total porosity and compressive strength in the context of core-shell rubber/rice husk ash-based geopolymer foam.

Effect of Factors on Total Porosity and Compressive Strength Properties

ANOVA and regression models were employed to assess the impact of various factors on the properties of total porosity and compressive strength. Contour plots were employed for enhanced visualization, as demonstrated in Figures 1 and 2. These figures depict the influence of hydrogen peroxide (V_1) and stabilizer (V_2) on the responses. Both figures

indicate that higher V_1 led to an increase in total porosity by up to 50 percent and an increase in compressive strength by up to 2.00 MPa. Simultaneously, elevated V_2 levels resulted in a consistent total porosity of up to 50 percent and a steady compressive strength of up to 2 MPa, as depicted in both figures.

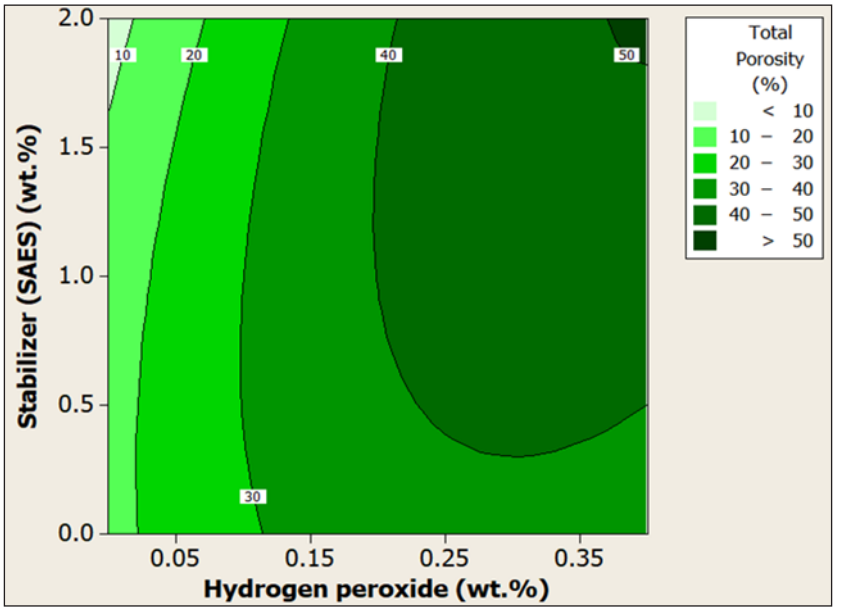

Figure 1. Contour plot for the effect of hydrogen peroxide and stabilizer on the total porosity

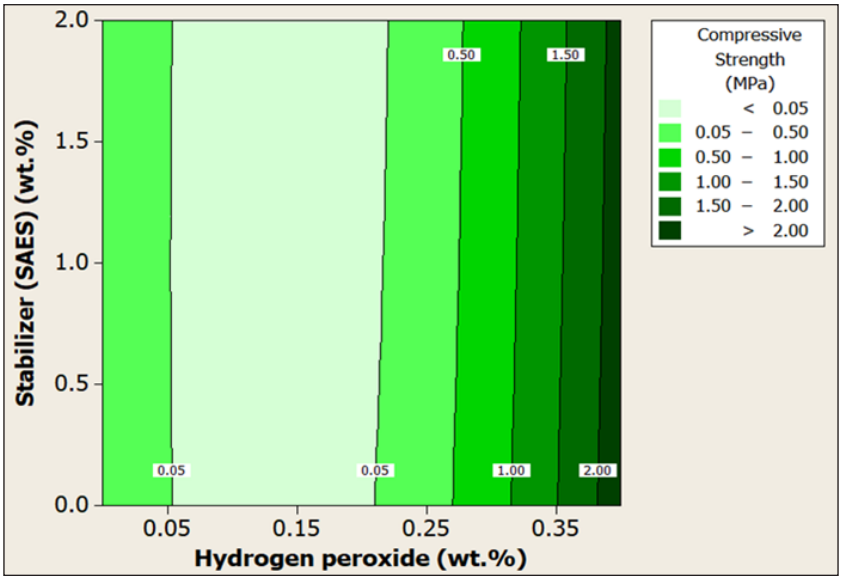

Figure 2. Contour plot for the effect of hydrogen peroxide and stabilizer on the compressive strength

From Figure 1, the total porosity of the geopolymer foam (GPF) significantly increases with increasing amounts of added hydrogen peroxide (V_1). Adding V_1 content in GPF from 0 to 0.4 wt.% at a stabilizer of 1.0 wt.% increases the total porosity from 20% to 50% region. This increment shows that V_1 was significant as the pore-foaming or blowing agent (Bai et al., 2018). Increasing H_2O_2 promotes endogenous gas production during preparation, resulting in larger pores and open-cell structures. It aligns with the findings of Zhang et al. (2022), who reported similar effects in polymeric foams. Unlike previous studies, the results indicate a linear increase in porosity with hydrogen peroxide concentration, suggesting a unique interaction mechanism in this composite (Posuvailo et al., 2022). Besides decreasing the total porosity when the stabilizer increases, the total porosity can be increased with the increase of the stabilizer from 0 to 0.5 wt.% at the H_2O_2 of 0.25 wt.%. At the same time, the total porosity was constant with the increase of stabilizer from 0.5 to 2.0 wt.% at the H_2O_2 of 0.25 wt.%.

Figures 1 and 2 illustrate the noteworthy impact of increasing hydrogen peroxide or stabilizer on porous RHA-based geopolymer foam's total porosity and compressive strength properties. It leads to a simultaneous reduction in total porosity and an enhancement in compressive strength. In Figure 2, it is evident that the compressive strength experiences a decrease as the H_2O_2 content increases from 0 to 0.15 wt.%. Subsequently, compressive strength increases when the H_2O_2 content is further raised from 0.15 to 0.4 wt.%. The augmentation of H_2O_2 results in the formation of more air bubbles in the porous geopolymer, creating pores within the geopolymer matrix (Yan et al., 2024). This behavior is consistent with studies on foam structures where increased porosity reduces density and affects mechanical properties (Zhao et al., 2023). Hydrogen peroxide acts as a blowing agent, decomposing into oxygen and water to form pores within the material, as shown by Bhuyan et al. (2023). Adding stabilizing agents beyond 1.5 wt.% causes the air bubbles to persist and expand through coalescence, resulting in thinner walls and diminished geopolymer strengths. Notably, an increase in H_2O_2 content is associated with a significant decrease in compressive strength (Ji et al., 2020). Conversely, Figure 2 indicates a consistent compressive strength of the geopolymer foam with increasing amounts of added stabilizer (SAES). It suggests that stabilizer (SAES) is an insignificant factor, and the compressive strength remains constant within the specified range of stabilizer (SAES) from 0 to 2.0 wt.% at an H_2O_2 level of 0.15 wt.%.

Optimization and Validation

Figure 3 illustrates the optimization plot showcasing the impact of different combinations of factor settings on the response. The optimization was conducted under specified parameters (hydrogen peroxide: 0.4 wt%; stabilizer: 1.0 wt%). The software predicts the optimal values for total porosity and compressive strength as 45.10 percent and 2.25 MPa, respectively,

achievable with the combination of hydrogen peroxide (V_1) = 0.40 and stabilizer (V_2) = 1.0. The calculated desirability of optimization is 0.83565, indicating that all parameters align with the target for achieving maximum total porosity and compressive strength properties. These optimized materials have potential applications in lightweight construction, as demonstrated by recent industrial applications (Haller et al., 2024).

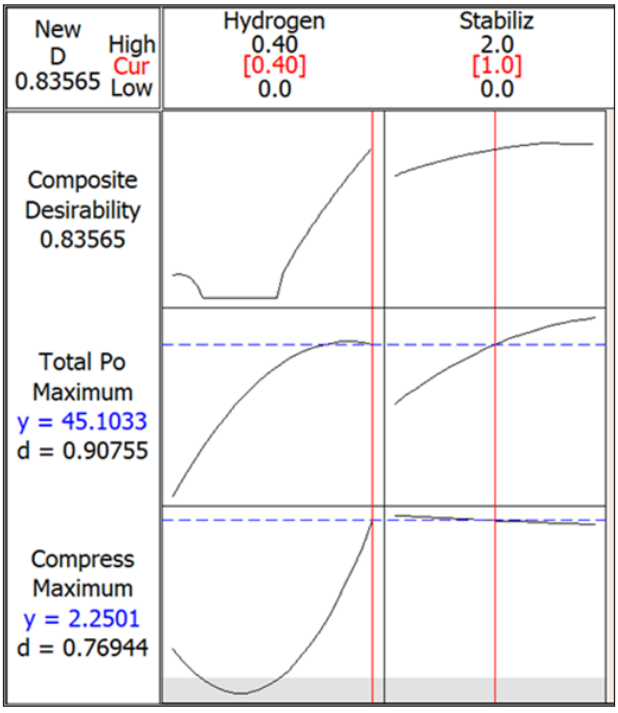

Figure 3. Optimization plot for maximum total porosity and compressive strength

Table 4
Experimental validation for the total porosity and compressive strength properties

Sample no.	Total porosity (%)			Compressive Strength (MPa)		
	Experimental value	Predicted value	Error (%)	Experimental value	Predicted value	Error (%)
SV1	45.09	45.10	0.02	2.29	2.25	1.78
SV2	44.54	45.10	1.24	2.43	2.25	8.00
	$\bar{x}$ Error		**0.63**	$\bar{x}$ Error		**4.89**

Analysis from Table 4 reveals that the average errors for total porosity and compressive strength were notably low, at 0.63% and 4.89%, respectively—well below the 15% threshold. It suggests that the regression model developed through this methodology effectively optimized the responses. In comparison to the control sample lacking hydrogen

peroxide (S19), the control sample exhibited reduced total porosity (13.31%) and increased compressive strength (0.1273 MPa).

Material Behaviour of Sample After Compressive Strength Test

Figure 4 shows the slopes of samples S1, S9, S19 (control sample), S20 and SV2 (optimized) with brittle and ductile behavior. The samples were chosen based on best compressive strength (S1), median compressive strength (S9), sample without the addition of hydrogen peroxide (S19: control sample), poor compressive strength (S20), and optimized sample (SV2).

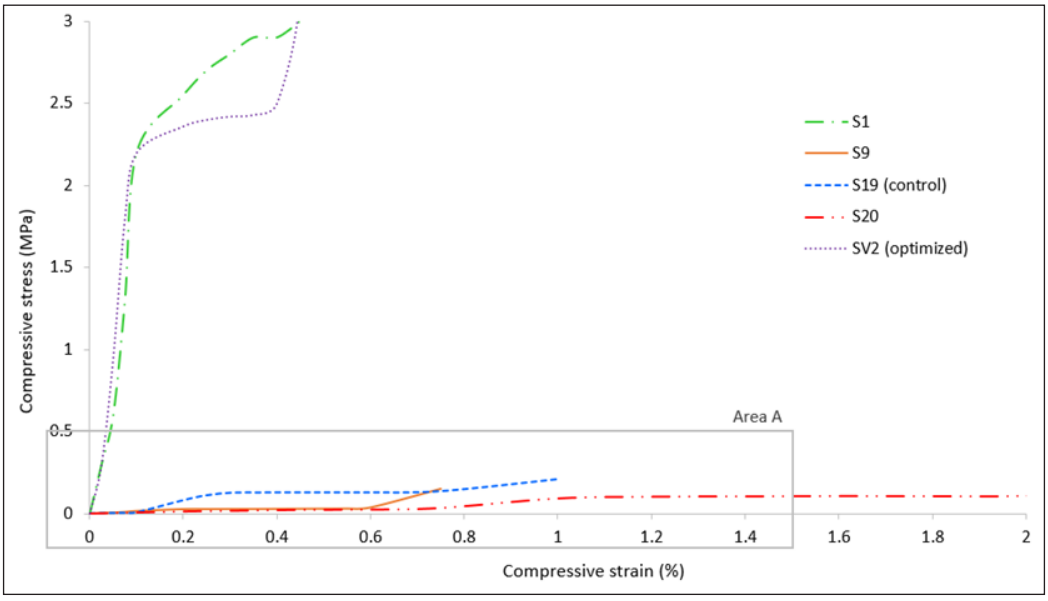

Figure 4. Stress-strain curve of samples S1, S9, S19 (control), S20, SV2 (optimized)

Figure 5 shows the enlarged area A from Figure 4. A steeper slope in a graph indicates that the material is more resilient and less prone to deformation than a gentler slope. Figure 4 shows that SV2 (optimized) (hydrogen peroxide = 0.40, stabilizer = 1.0) exhibited the steepest slope, signifying that it was the most resilient and brittle among the tested ductile samples in resisting deformation. In contrast, S20 (hydrogen peroxide = 0.30, stabilizer = 0.5) was the opposite. This result was probably due to lower hydrogen peroxide content and stabilizer. Lower hydrogen peroxide and stabilizer content lead to a gentler slope (ductile properties). This composition will cause the sample to be highly porous (a function of void content- 40.63%), so it has low compressive strength. The observed increase in brittleness with higher peroxide content has been similarly reported in recent studies by (Ransy et al., 2020).

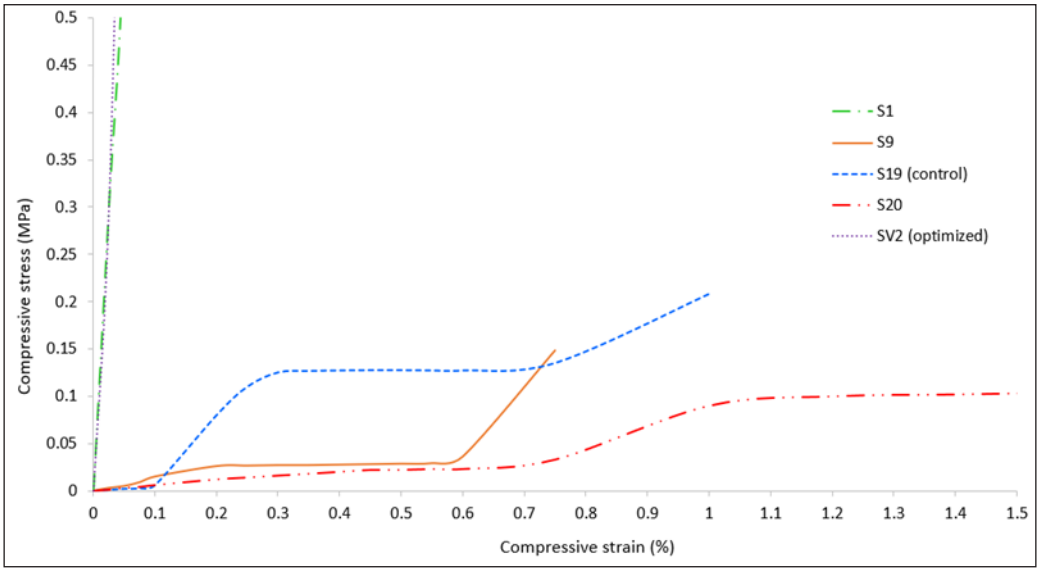

Figure 5. Enlarged area A

Although the sample without hydrogen peroxide (S19) recorded higher compressive strength (0.1273 MPa) than sample S9 (0.0253 MPa), sample S9 showed a shallower slope, which indicates that this sample was easily deformed due to lesser resilience (Funk & Dinger, 2013). This slope was due to the hydrogen peroxide and stabilizer content being at the median content (0.2% of hydrogen peroxide and 0.1% of stabilizer). It has high total porosity but low compressive strength, which leads to ductile behavior.

Contour Plots Superimposition

The methodology employed in generating overlaid graphs for diverse response surfaces involves the integration of contour plots. This approach surpasses the conventional one-factor-at-a-time (OFAT) method, criticized for neglecting variable interactions and involvement in laborious experimental runs (Jampala et al., 2017). Figure 6 illustrates this technique, visually depicting geopolymer foam's optimal processing conditions and formulation range. The contour plot is overlaid by combining the contour plots of total porosity and compressive strength from Figures 1 and 2, respectively. The light green region signifies the total porosity and compressive strength contour area. A thorough analysis of the overlaid contour plots reveals that the optimal range for achieving the highest total porosity and compressive strength, indicated by the dark green region, falls within the ranges of 0.35–0.40 wt.% for hydrogen peroxide and 0.5–2.0 wt.% for stabilizer.

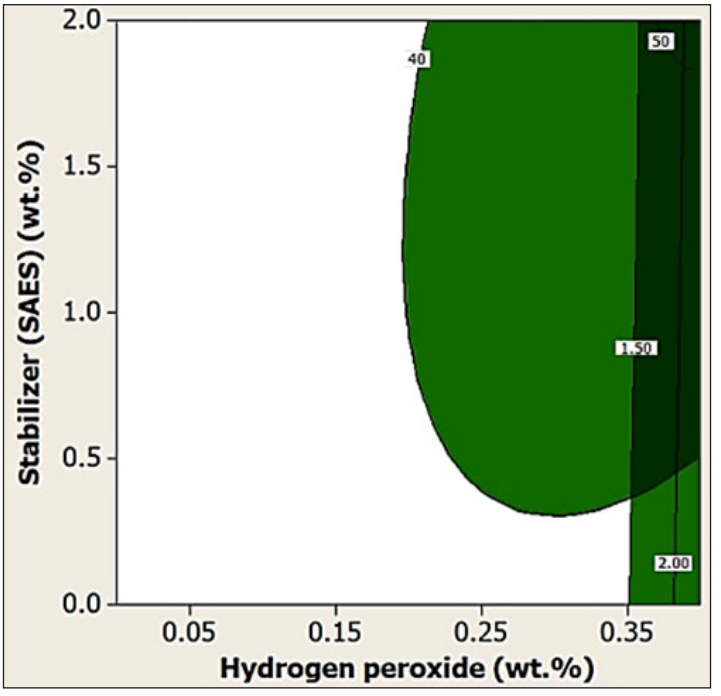

Figure 6. Optimum conditions are a function of the independent variables after the superimposition of the contour plots

CONCLUSION

Examining the effects of hydrogen peroxide and sodium alcohol ether sulfate on the properties of porous rice husk ash-based geopolymer foam involves investigating several factors. These include determining the optimal ratio between RHA and activated alkaline solution (AA) and hydrogen peroxide and stabilizer (SAES) amounts. The results demonstrated that increasing hydrogen peroxide led to increased total porosity and decreased compressive strength due to introducing more voids. Conversely, increasing SAES reduced total porosity by stabilizing the foam structure, but higher concentrations also decreased compressive strength. The optimal balance between porosity and compressive strength was achieved with 0.4 wt.% hydrogen peroxide and 1.0 wt.% SAES. The optimal RHA-based geopolymer foam exhibits 13.3% better total porosity and foam structure when compared to the control sample. The compressive strength showed no significant changes. Due to this improvement, hydrogen peroxide and sodium alcohol ether sulfate (SAES) should be added at optimum percentages to improve the porous rice husk ash-based geopolymer foam. Additional variables such as curing time and temperature could provide further insights and should be considered. This environmentally friendly and cost-effective composite applies to agriculture, food, and construction building sectors.

ACKNOWLEDGEMENT

The authors are grateful to the Department of Process and Food Engineering in the Faculty of Engineering, UPM, Malaysia, for the facilities to carry out the project and the NAGASE (MALAYSIA) SDN. BHD. in providing the genioperl sample.

REFERENCES

Amran, M., Huang, S. S., Debbarma, S., & Rashid, R. S. (2022). Fire resistance of geopolymer concrete: A critical review. *Construction and Building Materials*, *324*, Article 126722. https://doi.org/10.1016/j.conbuildmat.2022.126722

Bai, T., Song, Z. G., Wu, Y. G., Hu, X. D., & Bai, H. (2018). Influence of steel slag on the mechanical properties and curing time of metakaolin geopolymer. *Ceramics International*, *44*(13), 15706-15713. https://doi.org/10.1016/j.ceramint.2018.05.243

Bhuyan, M., Kurtulus, C., Heponiemi, A., & Luukkonen, T. (2023). Peracetic acid as a novel blowing agent in the direct foaming of alkali-activated materials. *Applied Clay Science*, *231*, Article 106727. https://doi.org/10.1016/j.clay.2022.106727

Celik, A., Yilmaz, K., Canpolat, O., Al-Mashhadani, M. M., Aygörmez, Y., & Uysal, M. (2018). High-temperature behavior and mechanical characteristics of boron waste additive metakaolin based geopolymer composites reinforced with synthetic fibers. *Construction and Building Materials*, *187*, 1190-1203. https://doi.org/10.1016/j.conbuildmat.2018.08.062

Coman, V., Teleky, B. E., Mitrea, L., Martău, G. A., Szabo, K., Călinoiu, L. F., & Vodnar, D. C. (2020). Bioactive potential of fruit and vegetable wastes. *Advances in Food and Nutrition Research, 91*, 157-225. https://doi.org/10.1016/bs.afnr.2019.07.001

Dizaji, H. B., Zeng, T., Hölzig, H., Bauer, J., Klöß, G., & Enke, D. (2022). Ash transformation mechanism during combustion of rice husk and rice straw. *Fuel*, *307*, Article 121768. https://doi.org/10.1016/j.fuel.2021.121768

Fatehi, H., Ong, D. E., Yu, J., & Chang, I. (2021). Biopolymers as green binders for soil improvement in geotechnical applications: A review. *Geosciences*, *11*(7), Article 291. https://doi.org/10.3390/geosciences11070291

Funk, J. E., & Dinger, D. R. (2013). *Predictive process control of crowded particulate suspensions: Applied to ceramic manufacturing*. Springer.

Haller, T., Beuntner, N., & Thienel, K. C. (2024). Optimized building envelope: Lightweight concrete with integrated steel framework. *Materials*, *17*(6), Article 1278. https://doi.org/10.3390/ma17061278

Hassan, A., Arif, M., Shariq, M., Alomayri, T., & Pereira, S. (2023). Fire resistance characteristics of geopolymer concrete for environmental sustainability: A review of thermal, mechanical and microstructure properties. *Environment, Development and Sustainability*, *25*(9), 8975-9010. https://doi.org/10.1007/s10668-022-02495-0

Jampala, P., Tadikamalla, S., Preethi, M., Ramanujam, S., & Uppuluri, K. B. (2017). Concurrent production of cellulase and xylanase from Trichoderma reesei NCIM 1186: Enhancement of production by desirability-based multi-objective method. *3 Biotech*, *7*(1), Article 14. https://doi.org/10.1007/s13205-017-0607-y

Ji, Z., Li, M., Su, L., & Pei, Y. (2020). Porosity, mechanical strength and structure of waste-based geopolymer foams by different stabilizing agents. *Construction and Building Materials*, *258*, Article 119555. https://doi.org/10.1016/j.conbuildmat.2020.119555

Komnitsas, K., & Zaharaki, D. (2007). Geopolymerisation: A review and prospects for the minerals industry. *Minerals Engineering*, *20*(14), 1261-1277. https://doi.org/10.1016/j.mineng.2007.07.011

Kumar, N., Chhokar, R., Meena, R., Kharub, A., Gill, S., Tripathi, S., Gupta, O., Mangrauthia, S., Sundaram, R., & Sawant, C. (2021). Challenges and opportunities in productivity and sustainability of rice cultivation system: a critical review in Indian perspective. *Cereal Research Communications*, *50*, 573–601. https://doi.org/10.1007/s42976-021-00214-5

Li, X., Shao, J., Zheng, J., Bai, C., Zhang, X., Qiao, Y., & Colombo, P. (2023). Fabrication and application of porous materials made from coal gangue: A review. *International Journal of Applied Ceramic Technology*, *20*(4), 2099-2124. https://doi.org/10.1111/ijac.14359

Negri, C., Ricci, M., Zilio, M., D'Imporzano, G., Qiao, W., Dong, R., & Adani, F. (2020). Anaerobic digestion of food waste for bio-energy production in China and Southeast Asia: A review. *Renewable and Sustainable Energy Reviews*, *133*, Article 110138. https://doi.org/10.1016/j.rser.2020.110138

Pacho, J. K. M., Florencondia, N., & Aduna, E. J. R. (2024). Evaluating the optical properties of philippine rice hull ash as a potential alternative to calcium carbonate filler for paints. *Iconic Research and Engineering Journals, 7*(11), 477-483.

Posuvailo, V., Kovalchuk, I., & Ivasenko, I. (2022). Influence of hydrogen peroxide on the composition and porosity of oxide-ceramic coatings on alloys of the Al–Si–Cu and Al–Cu–Mg systems. *Materials Science*, *57*(6), 894-899. https://doi.org/10.1007/s11003-022-00619-5

Ransy, C., Vaz, C., Lombès, A., & Bouillaud, F. (2020). Use of H2O2 to cause oxidative stress, the catalase issue. *International journal of molecular sciences*, *21*(23), Article 9149. https://doi.org/10.3390/ijms21239149

Singh, B. (2018). Rice husk ash. In R. Siddique & P. Cachim (Eds.) *Waste and supplementary cementitious materials in concrete* (pp. 417-460). Woodhead Publishing. https://doi.org/10.1016/B978-0-08-102156-9.00013-4

Singh, N. B., & Middendorf, B. (2020). Geopolymers as an alternative to Portland cement: An overview. *Construction and Building Materials*, *237*, Article 117455. https://doi.org/10.1016/j.conbuildmat.2019.117455

Tarek, D., Ahmed, M., Hussein, H. S., Zeyad, A. M., Al-Enizi, A. M., Yousef, A., & Ragab, A. (2022). Building envelope optimization using geopolymer bricks to improve the energy efficiency of residential buildings in hot arid regions. *Case Studies in Construction Materials*, *17*, Article e01657. https://doi.org/10.1016/j.cscm.2022.e01657

Yan, D., Shi, Y., Zhang, Y., Wang, W., Qian, H., Chen, S., Liu, Y., & Ruan, S. (2024). A comparative study of porous geopolymers synthesized by pre-foaming and H2O2 foaming methods: Strength and pore structure characteristics. *Ceramics International*, *50*(10), 17807-17817. https://doi.org/10.1016/j.ceramint.2024.02.270

Zhang, X., Zhang, X., Li, X., Tian, D., Ma, M., & Wang, T. (2022). Optimized pore structure and high permeability of metakaolin/fly-ash-based geopolymer foams from Al–and H2O2–sodium oleate foaming systems. *Ceramics International*, *48*(13), 18348-18360. https://doi.org/10.1016/j.ceramint.2022.03.094

Zhao, J., Trindade, A. C. C., Liebscher, M., de Andrade Silva, F., & Mechtcherine, V. (2023). A review of the role of elevated temperatures on the mechanical properties of fiber-reinforced geopolymer (FRG) composites. *Cement and Concrete Composites*, *137*, Article 104885. https://doi.org/10.1016/j.cemconcomp.2022.104885

Pertanika J. Sci. & Technol. 33 (S1): 83 - 107 (2025)

PERTANIKA JOURNALS

SCIENCE & TECHNOLOGY

Journal homepage: http://www.pertanika.upm.edu.my/

Evaluation of Suitability of the Taguibo River Irrigation System Diversion Dam, Philippines

James Villamor Ariston[2], Christian Dave Domingo Ungab[2], Aljon Ente Bocobo[1,2]*, Arnold Gemida Apdohan[1,2] and Antonietto Ortega Cacayan Jr.[1]

[1]Department of Agricultural & Biosystems Engineering, College of Engineering and Geosciences, Caraga State University, Ampayon, Butuan City, 8600, Philippines
[2]Center for Resource Assessment Analytics and Emerging Technologies (CREATE), Caraga State University, Ampayon, Butuan City, 8600, Philippines
[3]Caraga State University,Ampayon, Butuan City, 8600, Philippines

ABSTRACT

The Taguibo River Watershed and Forest Reserve (TRWFR) is the main source of water consumption and irrigation supply in Butuan City, but the irrigation supply is often insufficient, particularly during dry seasons. Competing demands for water further exacerbate the problem, leading to a reduction in water available for irrigation. This study aims to assess the Taguibo River irrigation system diversion dam using the Analytical Hierarchy Process (AHP) and Geographic Information System (GIS) tools. The dependable flow of the diversion dam was investigated to assess the sustainability of water, which resulted in 466.94 lps, and the AHP analysis identified river discharge as the most important factor in suitability assessment. The generated suitability map shows the specific sites suitable for dam construction within the river, covering approximately 88,599.17 m^2 or 0.16% of the study area. The existing suitability map, in contrast, focused on the entire study area and disregarded the river network as a criterion, resulting in a much larger proportion (68%) of the area being deemed suitable. Overall, the study found that the Taguibo River irrigation system diversion dam is highly suitable based on the selected criteria, and the current suitability map provides valuable information for site selection and construction.

Keywords: Analytical hierarchy process, dependable flow, gis, suitability map, Taguibo river, diversion dam

ARTICLE INFO

Article history:
Received: 8 November 2023
Accepted: 5 November 2024
Published: 31 January 2025

DOI: https://doi.org/10.47836/pjst.33.S1.05

E-mail addresses:
james.ariston@carsu.edu.ph (James Villamor Ariston)
christiandave.ungab@carsu.edu.ph (Christian Dave Domingo Ungab)
aebocobo@carsu.edu.ph (Aljon Ente Bocobo)
agapdohan@carsu.edu.ph (Arnold Gemida Apdohan)
antoncacayan@gmail.com (Antonietto Ortega Cacayan Jr.)
*Corresponding author

INTRODUCTION

The Philippines has natural resources and abundant water bodies. According to Lapong and Fujihara (2008), it has 130 km^3/year of internal water resources. In Region

ISSN: 0128-7680
e-ISSN: 2231-8526

13 (Caraga Region), there are 30 classified rivers, including the Taguibo River, which is known as a Water Quality Management Area (WQMA), six marine water, one lake, and 19 unclassified water bodies, according to the Department of Environment and Natural Resources (EMB, 2019). Due to these vast water resources, dams for domestic and irrigation water supply are essential for economic development. However, the government gave less priority to the water governance sector and institutional framework, such as supporting building structures (Lapong & Fujihara, 2008). The Taguibo River watershed forest reserve (TRWFR) is a major source of potable water that supplies over 40,000 concessionaries or more than 200,000 individuals. In addition, it supplies water for irrigation purposes to 762 hectares of rice lands and is a source of livelihood for occupants of the watershed (BCWD, 2015; EMB, 2019). However, providing adequate water through the service area is currently a problem for the Taguibo River irrigation system diversion dam, especially in the dry season. So, this study focused on site suitability assessment of the Taguibo River irrigation system diversion dam using the analytical hierarchy process (AHP) and provided a suitability map of the study area using geographic information system (GIS) tools.

The use of GIS for accurate decision-making, modern technology is useful as this involves the implementation of complex matters that give the users the ability to understand the problems through analyzing the spatial, producing digital maps, and thus saving time, effort, and cost to reach an optimized solution. A geographic Information System (GIS) is a system of computer software, hardware, and data personnel that input, manipulate, analyze, and present the data and information related to a specific location on the earth's surface (Ali, 2020). AHP is a tool for multi-criteria decision analysis (MCDA) used to logically evaluate and compare several frequently conflicting factors to make the best possible solution (Alpagut et al., 2021). The analytical hierarchy process is a structured technique for organizing and analyzing multiple criterion decisions (Shukla et al., 2013). The process is to decompose a decision problem into a hierarchy of simpler sub-problems and analyze it independently (Bataineh et al., 2018), and it is one of the most common multi-criteria decision analysis (MCDA) methods used in site selection (Midatana et al., 2018). The result was compared to the existing suitability study to find the difference between the two methods used.

MATERIALS AND METHODS

Study Area

The study area was at the Taguibo River Watershed Forest Reserve in Butuan City, Agusan del Norte (Figure 1). The Taguibo River is a vital water source for irrigation and drinking purposes for the residents of Butuan City. The watershed is geographically situated at 125°31'00" to 125°43'16" N latitude and 8°158'00" to 9°05'34"E longitude. It has a total land area of 4,367.44 hectares, covering four barangays: Barangay Anticala in Butuan

City, Barangay San Antonio in Remedios Trinidad Romualdez (RTR), Barangay Mahaba in Cabadbaran City, and a portion of Barangay Kulambugan, Sibagat, and Agusan del Sur. The area continues towards the coastal areas of Magallanes, making a total land area of 12,438 hectares. BCWD, NIA, Taguibo Aquatec Solutions, DENR and LGU Butuan manage the area.

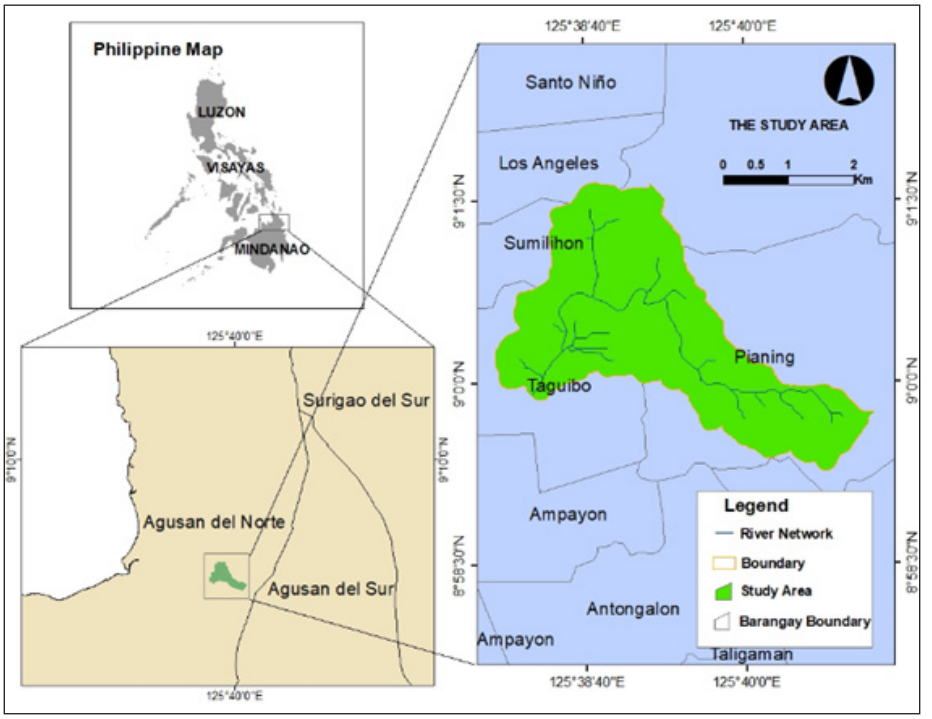

Figure 1. Study area

The watershed's minimum and maximum surface elevations range from 93.0351 m to 1883.9800 m. Based on the Digital Elevation Model (DEM), it possessed a hilly, mountainous surface with soil mostly belonging to the hydrologic soil group B, with loamy and silty loam soils. Moreover, the watershed has a Type II climate, with rainfall spreading evenly throughout the year.

Methodological Framework

Figure 2 shows the methodological framework of this study. Several data were collected from different sources to assess the location suitability of existing diversion dams. These data were then subjected to pre-processing, processing, and aggregation to extract the needed information, using ArcGIS 10.4 and HEC-RAS 6.3.1 to produce and extract maps from the datasets.

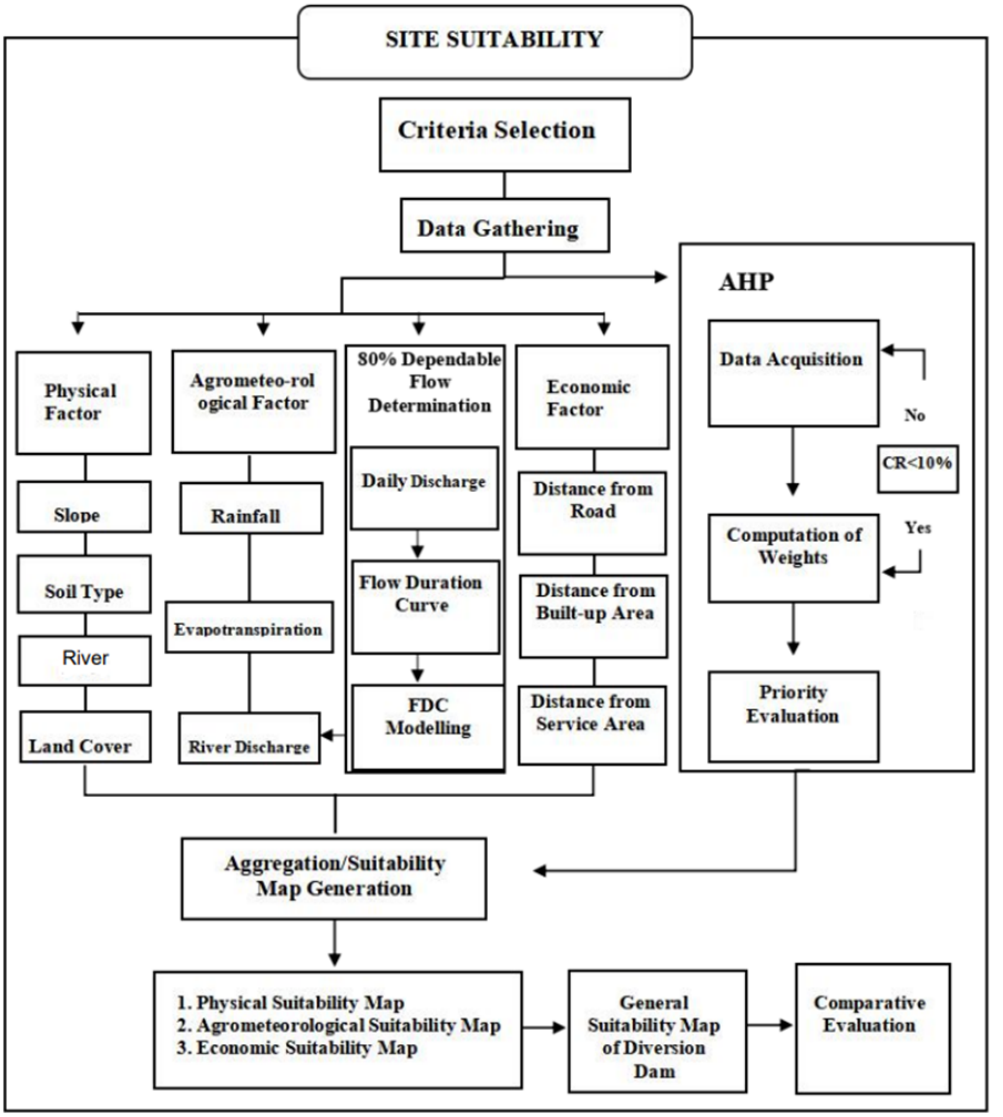

Figure 2. The methodological framework of the study

To be specific, the physical (slope, soil type, river width, and land cover), agrometeorological (rainfall, evapotranspiration, and river discharge) and economic (distance from road, distance from built-up areas, and distance from service area) factors were selected as the main and sub-criteria. On the other hand, the analytical hierarchy process was used to determine the important factors in the selection of site suitability by surveying to collect information from selected experts in different government agencies, private institutions, and individual experts.

Criteria Selection

Site Suitability Analysis (SSA) of a diversion dam needs to determine and select the important criteria that could affect the suitability of the dam on the site (Karakuz & Yildiz, 2022). In this study, 10 criteria were adopted, namely the river network and protected areas. In contrast, the criteria that were used include rainfall, slope, river discharge, soil type, land cover, river width, evapotranspiration, distance from road, distance from built-up areas, and distance from service area (Baltazar et al., 2019) Table 1 lists the adopted criteria with their corresponding description of site suitability for diversion dams.

Table 1
Selected criteria for location suitability

Criteria	:	Description
Slope	:	It is the main factor that influences the safety of a dam.
Soil type	:	It influences diversion dam function in term of runoff amount and seepage.
River Width	:	It affects the foundation of diversion dam construction and how much material will be needed.
Land Cover	:	It affects sediment loads on diversion dams as well as water losses due to evapotranspiration.
River Discharge	:	River flow ensures that there is available water in an irrigation canal.
Rainfall	:	It is an additional source of water for storage.
Evapotranspiration	:	It reduces water storage for irrigation.
Distance from Road	:	It should be located with a multi-ring buffer at 100-meter intervals for repair and maintenance activities.
Distance from Built-up Areas	:	It should be far from built-up areas (residential, commercial) to avoid contamination and pollution.
Distance from Service Area	:	It should have a multi-ring buffer at 0.5 km intervals from its service area to minimize the construction cost.

The selected criteria were organized and grouped into three main criteria. The slope, soil type, river width, and land cover were represented as sub-criteria under the physical main criteria since all the sub-criteria can affect the physical aspects and stability of the diversion dam. Meanwhile, the rainfall, evapotranspiration, and river discharge were kept under agrometeorological main criteria, considering all the selected sub-criteria can greatly affect all the related agrometeorological factors and the water availability of the diversion dam. Lastly, the road, distance from built-up areas, and distance from the service area, represented as sub-criteria, were under the main economic criteria since they mainly affect all the factors related to the economy and the cost of constructing the diversion dam.

Data Collection

Two types of data are GIS data, which was used in map generation, and data for the analytical hierarchy process, AHP, for decision-making analysis (Canco et al., 2021; Chen, 2006). The GIS data were gathered from different sources, including government agencies and institutions, field validation, and through surveys (Table 2).

Table 2
List of collected GIS data and their sources

Data	Source
Digital Elevation Model (DEM)	National and Resource Mapping Information Authority (https://www.namria.gov.ph), 2022
Soil Type	Bureau of Soil and Water Management (https://www.bswm.da.gov.ph/), 2022
Land Cover	CSU-CReATe (Center for Resource Assessment Analytics and Emerging Technologies), 2022
Rainfall	TerraClimate (https://www.climatologylab.org/terraclimate.html), 2023
Evapotranspiration	TerraClimate (https://www.climatologylab.org/terraclimate.html), 2023
River Discharge	CSU-CReATe (Center for Resource Assessment Analytics and Emerging Technologies), 2022
Road Network	CSU-CReATe (Center for Resource and Assessment Analytics and Emerging Technologies), 2022
Service Area	National Irrigation Administration (https://nia.gov.ph), 2023

Specifically, the GIS data, such as DEM, soil type, land cover, river discharge, and road network, were obtained from the Carage State University Center for Resource Assessment, Analytics and Emerging Technologies (CSU-CReATe). On the other hand, the rainfall and evapotranspiration data were gathered from the TerraClimate website. Lastly, the service area was obtained from the National Irrigation Administration (NIA) ASDI-IMO.

Physical Data

The use of thematic maps is a common approach to organizing and visualizing physical data. In this study, thematic maps were used to generate a suitability map of the diversion dam, with a focus on its physical factors. The thematic maps used in this study include the slope, soil map, river width, and land use/land cover map.

Slope Map

The slope was represented as one of the sub-criteria under the physical main criteria. A digital elevation map gathered from the Caraga State University Center for Resource Assessment, Analytics and Emerging Technologies (CSU-CReATe) was used to generate a slope map. It was processed using ArcGIS 10.4 software. The generated slope map was

then used to generate a physical suitability map. The processing includes gathering DEM, using the slope tool and clip tool in ArcGIS 10.4 to clip the boundary of the study area, and reclassifying the slope map for the final output.

Soil Map

Soil type was processed by extracting soil type data from the dataset acquired from BSWM through the office of CSU-CReATe. It was then processed using ArcGIS 10.4 to generate the soil-type thematic map. The generated soil-type map was also used to generate the physical suitability map. The process processing includes gathering soil-type GIS data, applying clip tools to clip the study area boundary using ArcGIS 10.4, and reclassifying the boundary soil-type map for the final output of the soil-type thematic map.

River Width

River width is typically obtained through bathymetry, which requires actual data from the site. However, due to the unavailability of bathymetric data on the site and the critical weather conditions during the data gathering period, HEC-RAS 6.3.1 software was used to acquire the river width using the slope and elevation of the terrain and Arcmap 10.4 was used for mapping. The process includes processing gathered DEM, identification of the river, bank lines, flow paths, and river cross-section. The cross-section of the river was then interpolated and reclassified for the river width final thematic output map.

Land Use/Land Cover Map

The Land Use/Land Cover (LULC) map was generated by utilizing the available data of the Butuan and Taguibo watershed (upstream) LULC for the year 2021 gathered from Caraga State University-Center for Resource Assessment, Analytics and Emerging Technologies (CSU-CReATe). It was then processed using ArcGIS 10.4 tools, and the output LULC thematic map was used to generate a physical suitability map. This process includes merging the land use and land cover of Butuan City with the land cover of the Taguibo River watershed forest reserve, clipping the merged LULC using the boundary map of the study area, and reclassifying for generating the LULC map final output.

Agrometeorological Data

This study used publicly available data and actual data acquired through field activity to acquire the agrometeorological data, including rainfall, river discharge, and evapotranspiration maps. Agrometeorological data were used to generate the suitability map, as it is one of the main criteria of the suitability map. The ArcGIS 10.4 tools were used to generate the maps.

Rainfall Map

A rainfall map was generated using the downloaded dataset from TerraClimate. This study used the 2021 annual precipitation in ".nc" format. The downloaded annual precipitation for the year 2021 was processed using ArcGIS 10.4 tools. The generated rainfall thematic map was then used to generate an agrometeorological suitability map. The process includes making a NetCDF raster layer, resampling, raster to point, interpolation, and clipping using the boundary using the clipping tools of the GIS tools. The clip rainfall map boundary was then reclassified to finalize the rainfall thematic map output.

Evapotranspiration

The evapotranspiration map was generated using actual evapotranspiration (AET) data from the year 2021, which was also acquired from TerraClimate. The file was also in the ".nc" format. Hence, the process of precipitation and evapotranspiration was quite similar. By loading the data and creating a netCDF raster layer, resampling was done to create lower pixel size and higher resolution. The dataset was also projected to WGS 1984 UTM Zone 51N. The resampled data was clipped to the downstream boundary to extract the evapotranspiration data within the boundary. The process includes first downloading the annual evapotranspiration from the TerraClimate website, next making the NetCDF raster layer, resampling, raster to point, interpolation, and clipping the output using the boundary map of the study area through ArcGIS 10.4 tools. The clipped AET map was then reclassified for the final evapotranspiration thematic map output.

River Discharge

A river discharge map was created using the actual daily discharge during the monitoring of streamflow from May to October. It was generated using ArcGIS 10.4, where the base map was used to locate the data collection station. The process includes utilizing cross-section points, adding dependable flow data attributes, interpolation, and reclassifying the output for the final river discharge map.

Economic Data

A variety of factors impacting an area's suitability were systematically assessed and prioritized using a multi-criteria decision analysis (MCDA) technique. With this methodology, each criterion is evaluated according to its relative significance and influence on the decision-making process as a whole. Several economic considerations were taken into account in this analysis, including distance from roads, built-up areas and service areas. The MCDA approach ranks and weighs these variables to provide a comprehensive suitability map that shows places according to their development potential and economic feasibility (Romano et al., 2015).

The design and implementation of a diversion dam project heavily rely on integrating spatial data using ArcGIS 10.4 technologies. Making educated decisions in complicated projects requires the ability to visualize, analyze, and interpret geographical data, made possible by the robust geographic information system (GIS) platform ArcGIS (Goncalvez, 2021).

Overall, using ArcGIS 10.4 tools in this context improves the analysis's efficiency and accuracy (Charles et al., 2024) while also helping to design and carry out the diversion dam project more successfully by ensuring that economic concerns are sufficiently considered.

Distance from Road

The distance from the road was created by using the Mindanao roadmap dataset. It was narrowed down by clipping the road map layer with the downstream boundary, leaving the road network inside the boundary. The generated distance from the road thematic map was used to generate the economic suitability map. The process includes the gathering of GIS Mindanao roadmap data from Caraga State University-Center for Resource Assessment, Analytics and Emerging Technologies (CSU-CReATe), clipping the roadmap using ArcGIS 10.4 tools, applying multi-ring buffer at 100-m intervals, and reclassifying for distance from road map final output.

Distance from Built-up Areas

Distance from built-up areas was generated by utilizing the extracted land use/land cover LULC map. The ArcGIS 10.4 tools were used to generate the thematic maps. The generated distance from the built-up area thematic map was then used for economic suitability map generation. The process includes gathering the LULC thematic map, extracting the built-up area, and assigning multi-ring buffers to measure the distance from built-up areas at 100-m intervals. The map was also clipped using the boundary map of the study area and then reclassified for the distance from the built-up area, which is the thematic map's final output.

Distance from Service Areas Map

Distance from the service area was created using the service area dataset from the National Irrigation Administration (NIA) ASDI-IMO. The dataset was loaded to the ArcMap as a reference in generating its distances through the multiple-ring buffer tool. The generated distance from the service area thematic map was then used for economic suitability map generation. The process includes generating a service area thematic map from the National Irrigation Administration (NIA-ASDI IMO), applying polygon-to-point tools using ArcGIS 10.4 tools, and a multi-ring buffer at 0.5 mm intervals. Lastly, the specified boundary of the study area was clipped and reclassified for the distance from the service area thematic map final output.

Dependable Flow Determination

The dependable flow in irrigation networks was calculated by considering the availability of irrigation data (Zukhrufiyati et al., 2019). Dependable flow calculation can also be done through SNI No. 6738: 2015 concerning the calculation of dependable flow with a discharge–duration curve if the data is available. Equation 1 was used to calculate the reliable flow using the frequency approach. The process includes the daily discharge data acquisition, flow duration curve calculation, and modeling of the flow duration curve using the dplot.

$$Probability\ of\ occurrence = \frac{m}{n+1}100\% \quad [1]$$

Where P(X≥x) = probability of the occurrence of variable X (flow of discharge_≥) that is greater than x(m^3/s)

m = data rank
n = the amount of data
X = a discharge data series
x = the dependable flow if the probability matches the designation

Daily Discharge Data Acquisition

The daily discharge data of the Taguibo River was acquired from the CSU-Center for Resource and Assessment Analytics and Emerging Technologies (CReAte) through the project entitled Water Resource Assessment and Modeling of the Selected Watershed in the Caraga Region for Sustainable Domestic and Irrigation Supply. The available daily discharge data for 2022 was from the project gathered only from one station located near the Taguibo River diversion dam. Since 1-year data was unavailable, the available daily discharge data and selected data from the unpronounced season from May to October 2022 were utilized.

Flow Duration Curve

The flow duration curve (FDC) represents the daily discharge of water against the percentage of time that a particular discharge was equaled or exceeded (Longobardi & Villani, 2013). Microsoft Excel was used to calculate the dependable flow of the river. The daily discharge data was first enumerated with the corresponding date to perform the calculation. Next, the streamflow was sorted from highest to lowest and provided rank in the next column, with rank 1 as the highest discharge and rank 178 as the lowest rank. The next column was the probability of recurrence, which was calculated using Eq. 1, while Eq. 2 was used to determine the return period on the last column**.** The summary of statistics was calculated, and the sum, mean, and standard deviation were also provided.

$$Return\ Period = \frac{\text{rank}}{n^{th}\ rank} \qquad Return\ Period = \frac{\text{rank}}{n^{th}\ rank} \qquad [2]$$

FDC Modeling

Dplot software was used to plot the calculated flow duration curve to show that data falls with an 80% probability of recurrence. In plotting the calculated dependable flow, the table generated in Excel was copied and pasted with the corresponding table in dplot software. Lognormal distribution was used to model the distribution of the different probabilities of recurrence. The modeling exhibited two lines: (1) the actual data calculated using the flow duration curve and (2) the frequency line.

AHP Data Acquisition

An interview was conducted with selected experts related to the topic. The experts were chosen from different government institutions, private offices and individual experts. There were five engineers from the National Irrigation Administration (NIA) regional office, Bancasi, Butuan City, Philippines, and five individuals from different agencies: one expert from the NIA ASDI-IMO office, Brgy. Ambago, Butuan City, Philippines, one from City Agriculturist Office, Brgy. Tiniwisan Butuan City, Philippines, one from the water district, Agusan del Sur, Philippines, one from the Department of Social Worker and Development (DSWD), Philippines, and one private civil engineer individual expert.

Computation of Weights

The pairwise comparison accuracy was calculated using the Consistency Ratio (CR) (Equation 3), which is equivalent to the ratio of the Consistency Index (CI) (Equation 4) and Random Index (RI) to identify the accuracy of the respondents' answers. When the CR is less than 10%, the comparison between criteria is acceptable; otherwise, the CR allows for re-evaluation.

$$Consistency\ Ratio = \frac{\text{CI}}{\text{RI}} \qquad [3]$$

CI can be calculated by,

$$Consistency\ Index = \frac{\lambda max - n}{\text{n} - 1} \qquad [4]$$

Where λmax = (Weight1*S1 + Weight2*S2 + Weight3*S3+……), and n = number of criteria. For random index (RI), a 1.49-constant value was used from Table 3 since it has an overall 10 criteria. The geometric mean was calculated using the (Equation 5) (Dong et al., 2010):

$$Geometric\ Mean\ (G.M) = \sqrt[n]{X_1 * X_2 * X_3 \dots X_n} \quad [5]$$

Where n is the number of returns in the series, and X_i is the variable.

Table 3
Average random consistency index (RI)

Number of criteria	1	2	3	4	5	6	7	8	9	10
Random Index	0.00	0.00	0.58	0.90	1.12	1.24	1.32	1.41	1.45	1.49

Priority Evaluation

The selected 10 criteria were grouped into three main factors: physical factors (slope, soil type, river width, and land use/land cover), agrometeorological factors (rainfall, rover discharge, and evapotranspiration), and economic factors (distance from road, distance from built-up area, and distance from service area). Based on the experts' feedback, the three main factors were evaluated according to their importance. All the graded main criteria were then compared.

Suitability Map Generation

The data acquired were compiled and analyzed in one manner, such as the computed weights from the selected criteria, the generated thematic layers, namely, the rainfall, slope, river discharge, soil type, land cover, river width, evapotranspiration, distance from road, distance from built-up areas, and distance from service area maps. All the thematic layers were loaded to ArcGIS 10.4, and the weighted criteria were used as a reference in performing weighted overlay to generate the suitability maps.

Physical Suitability Map

The weighted overlay tool, a GIS tool that allows users to combine multiple layers of data into a single map layer, was used to generate the suitability map for physical conditions. In this case, the tool measured the suitability of each location based on the physical factors considered.

Agrometeorological Suitability Map

The weighted overlay tool was applied to generate the agrometeorological map. The weighted overlay tool is a GIS tool that allows users to combine multiple layers of data into a single map layer. In this case, the tool was used to measure the suitability of each location based on the agrometeorological factors considered. The thematic maps were overlaid: the evapotranspiration, river discharge, and rainfall maps. The process includes the generation of rainfall, evapotranspiration, and river discharge thematic maps. All the thematic maps

were then overlaid using ArcGIS 10.4 tools. Lastly, the scale value of weight in specific sub-criteria was applied to produce the agrometeorological suitability map.

Economic Suitability Map

The available maps generated using the multi-ring buffer tool were utilized to create the suitability map for economic factors. The multi-ring buffer tool is a GIS tool that creates concentric buffers around a feature or set of features. In this case, the tool created maps showing the distances from the road, built-up areas, and service areas. The process economic suitability map includes generating thematic maps, namely, distance from the road, distance from the built-up area, and distance from the service area. All the generated thematic maps were then overlaid using ArcGIS 10.4 tools and the assigned scale value of weights to generate the economic suitability maps.

General Suitability Map of Diversion Dam

The three main criteria, physical, agrometeorological, and economic, are the factors in determining the suitable sites for the diversion dam. Therefore, the three suitability maps for each aspect were used to create the suitability map for the diversion dam. The three suitability maps were overlaid using the weighted overlay tool and configured with their corresponding weightage value based on the AHP results. The process includes the generation of physical, agrometeorological, and economic suitability maps. Then, I overlaid all the suitability using ArcGIS 10.4 tools and applied weighted criteria gathered from the experts to generate the final AHP suitability map.

RESULTS AND DISCUSSION

Dependable Flow Analysis

Figure 3 shows the flow–duration curve of the stream of the Taguibo River irrigation system diversion dam derived using dplot software. The actual flow was also aligned with the frequency line ($\log10(y) = 3.053-0.4564s(x)$) using a lognormal distribution.

The results of this analysis revealed that the stream's flow follows a lognormal distribution pattern, which is a commonly observed distribution pattern in hydrology, particularly in subtropical and temperate climates. This finding is important because it allows water resource managers and planners to more accurately predict the frequency and probability of different flow rates, which can help them make informed decisions about water allocation and irrigation planning.

Overall, the analysis shows that the Taguibo River irrigation system diversion dam has a dependable flow of 466.94 lps with an 80% probability of recurrence. This means that the stream discharge occurs or is exceeded 80% of the time. These findings provide important information for water resource management and irrigation planners in the area

and highlight the value of using flow duration curves and lognormal distribution to analyze water flow data.

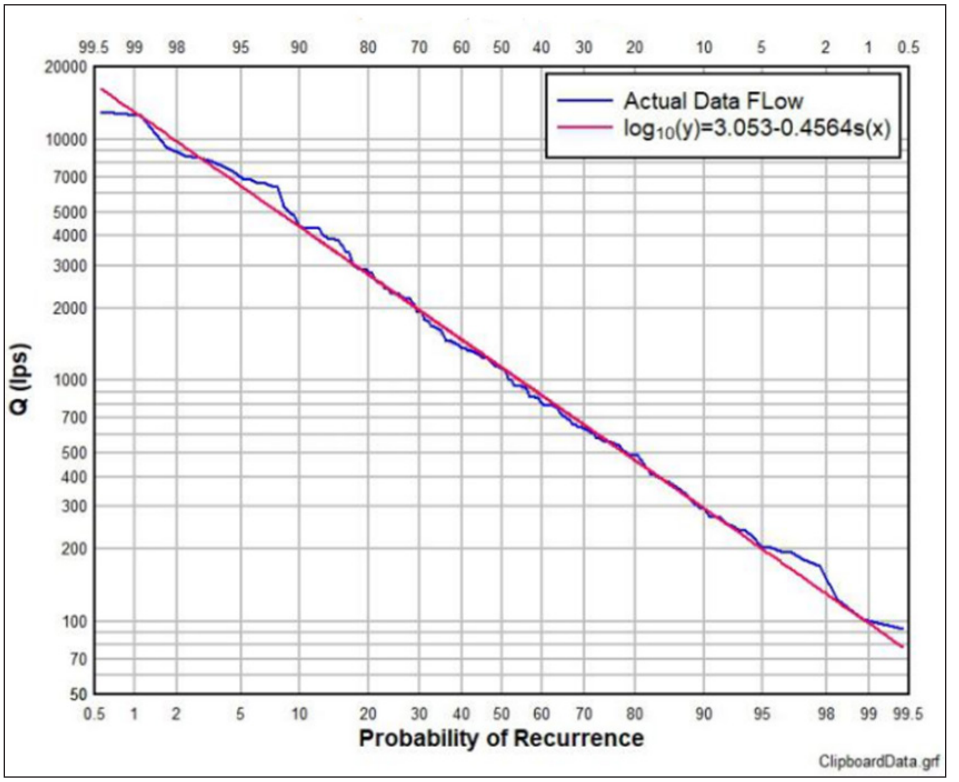

Figure 3. Flow–duration curve of Taguibo River irrigation system diversion dam using dplot

Weighted Criteria Analysis

The study used an analytical hierarchy process to assess the site suitability of the Taguibo River irrigation diversion dam for decision-making. Ten criteria were developed and grouped into three major aspects. These are physical (slope, soil type, land cover, and river width), agrometeorological (rainfall, river discharge, and evapotranspiration), and Economic aspects (distance from service areas, distance from road, distance from built-up areas). Table 4 shows the results of the ten respondents who were experts in their chosen field to determine the relative importance of the criteria and graded each main criterion and sub-criteria. This study normalized and calculated the graded criteria and sub-criteria provided by the experts using the geometric mean method to determine the weight.

The agrometeorological factor was the most important aspect, with 0.41 weight, followed by the physical factor, which had 0.38 weight. Lastly, the least important was the economic factor, with 0.21 weight. The agrometeorological aspect was the most important

factor, according to a few experts, since it involves the availability and sufficiency of the water supply, which is the main issue considered for water diversion (Bacci et al., 2020). Although physical factors could determine the effectiveness of the dam, safety, and foundation (Baltazar et al., 2019), it has resulted as the second most important. Lastly, the expert respondents from the City Agriculture Office of Butuan City and the National Irrigation Administration Office-Regional Field Office considered the economic factor as the least priority due to its dependence on the transportation of materials needed for construction and funding issues, which can be resolved by increasing the funds (Baltazar et al., 2019).

Table 4
Weights of main criteria and sub-criteria from 10 experts

Main criteria	Weight	Sub-criteria	Weight
		Slope	0.169
Physical	0.38	Soil Type	0.317
		River Width	0.265
		Land Cover	0.249
		Rainfall	0.354
Agrometeorological	0.41	Evapotranspiration	0.162
		River Discharge	0.484
		Distance from Road	0.280
Economic	0.21	Distance from Built-up Area	0.290
		Distance from Service Area	0.430

Moreover, the river discharge from agrometeorological aspects was the most important criterion weighted with 0.484, followed by rainfall with a weight of 0.354, and evapotranspiration with 0.162 weight. Meanwhile, soil type from physical aspects was the most important, weighted at 0.317, followed by river width at 0.265, land cover at 0.249, and slope at 0.169 weight. Lastly, distance from the service area was the most important criterion from economic aspects, weighted with 0.430, followed by distance from a built-up area with 0.290 weight, and distance from the road with 0.280 weight.

Furthermore, Table 5 displayed the weight of each sub-criterion. Among the 10 sub-criteria based on the results, river discharge and rainfall from agrometeorological aspects were the highest and second most important criteria, weighted 0.198 and 0.145, respectively. On the other hand, soil type, river width, and land cover under physical aspects were the third, fourth, and fifth important, weighted 0.121, 0.101, and 0.095, respectively. At the same time, the distance from the service area was the sixth most important, weighted at 0.090. Lastly, the three least important criteria were the evapotranspiration, slope, and distance from the built-up area, which have an individual weightage of 0.066, 0.064, and 0.061, respectively.

Table 5
Weights of each sub-criterion applying 10 × 10 matrix

Sub-criteria	Weight
Slope	0.064
Soil Type	0.121
River Width	0.101
Land Cover	0.095
Rainfall	0.145
Evapotranspiration	0.066
River Discharge	0.198
Distance from Road	0.059
Distance from Built-up Area	0.061
Distance from Service Area	0.090
Total	1.000

The expert respondent's result among the three significant aspects (agrometeorological, physical and economic) gave the agrometeorological consideration for the highest weight, which directly impacts the area's suitability for a diversion dam.

Physical Suitability Map

The four thematic layers, slope, soil type, river width, land cover maps, and their physical weights scale, were used to generate a physical suitability map using ArcGIS 10.4 tools. The result given in Figure 4 shows that the physical suitability map has five suitability levels: not suitable, low suitability, moderately suitable, suitable, and highly suitable, which are represented in red, orange, green, violet, and blue, respectively.

Generally, the physical suitability map has found only approximately 1% of the total area along the river due to the selected river width sub-criteria. The majority of the labeled sites were found moderately suitable, represented in green color with 40.74% out of 124,162 m^2 or approximately 50,583.6 m^2, followed by highly suitable, suitable, and low suitable sites, with 26.17%, 20.99%, and 9.38%, respectively out of 124,162 m^2. On the other hand, sites that are not suitable are represented in red and have the lowest area, with 2.72% out of 124,162 m^2 or approximately 3,402.03 m^2. Meanwhile, the location of the Taguibo River irrigation system was moderately suitable. In addition, the area not aligned with the river was also considered unsuitable, specifically in Barangay Anticala, Barangay Los Angeles, Barangay Sumilihon and some parts of Barangay Pianing.

Agrometeorological Suitability Map

As shown in Figure 5, the suitability map of agrometeorological aspects labels two levels of suitability: moderately suitable, represented in green and highly suitable, represented in blue.

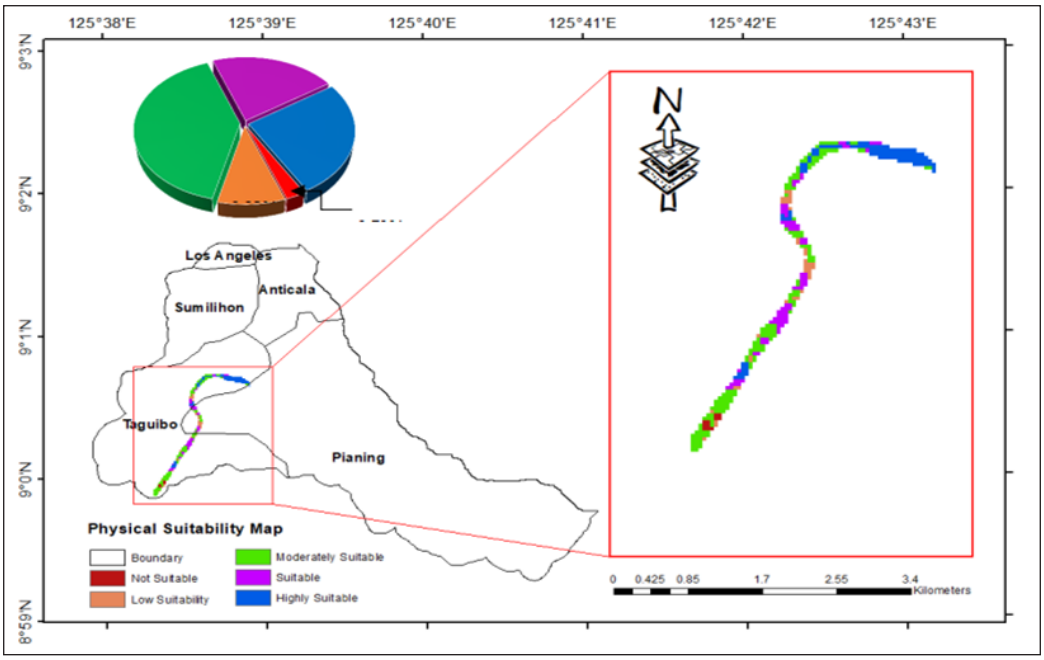

Figure 4. Physical suitability map

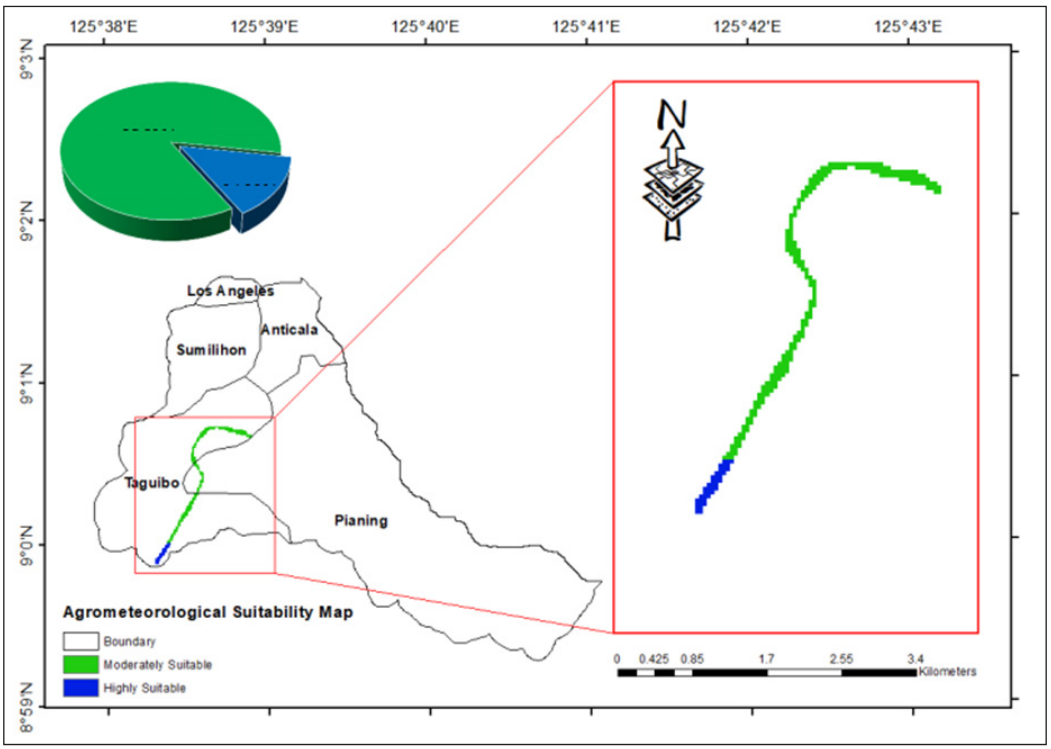

Figure 5. Agrometeorological suitability map

In addition, it was found that there are two labeled sites along the river due to the river discharge criteria. In summary, the majority of the identified sites were moderately suitable and found upstream of the Taguibo River irrigation system diversion dam's location with 85.81% area out of 88,599.17 m^2 or approximately 76,026.95 m^2. On the other hand, the highly suitable sites have an area of 14.19% out of 88,599.17 m^2 total area or approximately 12,572.22 m^2, including the location within the Taguibo River irrigation system diversion dam classified as highly suitable. Moreover, the areas not aligned with the river were also considered suitable, specifically in Barangay Anticala, Barangay Los Angeles, Barangay Sumilihon and some parts of Barangay Pianing.

Economic Suitability Map

Figure 6 labels five suitability levels: not suitable, low suitability, moderately suitable, suitable, and highly suitable, represented in red, yellow, green, sky blue, and blue, respectively. Based on the results, most maps were moderately suitable, while the unsuitable area was the lowest.

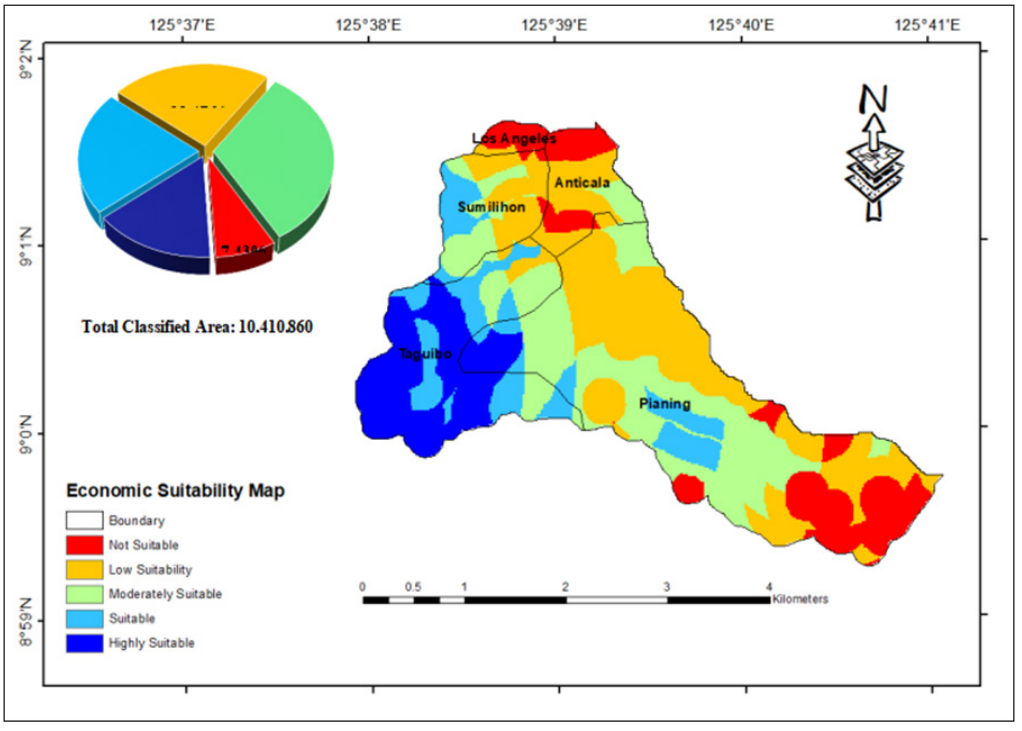

Figure 6. Economic suitability map

In addition, the moderately suitable site was the highest covered area with 32.24% out of 10,410,860 m^2 or approximately 3,356,461.26 m^2, followed by the low suitability site,

suitable, and highly suitable sites, with 23.47%, 21.91%, and 14.95% area, respectively out of 10,410,860 m^2 of the total area covered. At the same time, the site that was not suitable was the lowest area covered, with 7.43% out of 10,410,860 m^2 total area or approximately 773,526.898 m^2. In terms of economic aspects, the Taguibo River irrigation system diversion dam was classified as a highly suitable site.

Final Suitability Map

As displayed in Figure 7, the AHP model suitability map shows five suitability levels of identified sites, namely not suitable, low suitable, suitable, moderately suitable, and highly suitable, represented with five different colors, including red, orange, green, purple, and blue. It was found that the majority of the sites were moderately suitable, with 45.67% out of 88,599.17 m^2 or approximately 40,463.24 m^2 area, followed by the low suitable, highly suitable, and not suitable sites with 30.45%, 10.73%, and 9.69% area covered, respectively out of 88,599.17 m^2 total area. On the other hand, the suitable sites identified as the lowest area covered with 3.46% out of 88,599.17 m^2 or approximately 3,065.53 m^2.

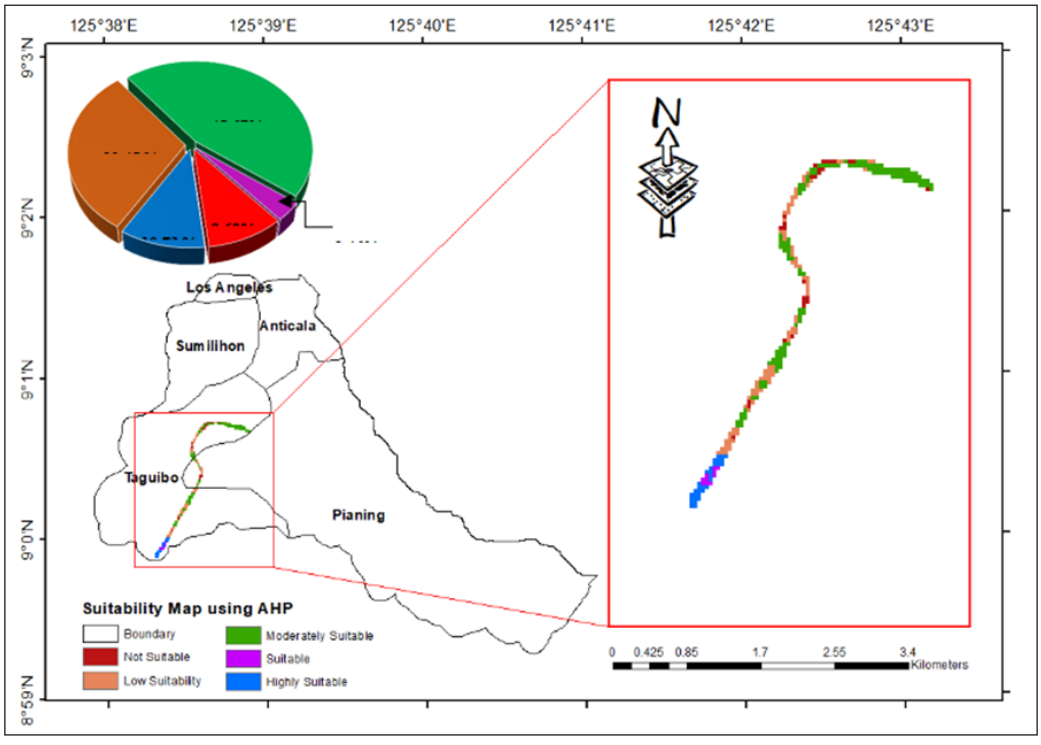

Figure 7. AHP model suitability map

Generally, as observed from the suitability map, all sites identified were located along the river since the diversion dam site selection considered river discharge and river width.

Specifically, the identified sites were located within the major part of Barangay Taguibo, where the Taguibo River irrigation system diversion dam was located, and the last part of Barangay Pianing. The location of the Taguibo River irrigation system diversion dam was identified as a highly suitable site. The results indicate that the criteria selected greatly influence the site suitability selection for the diversion dam. Thus, selecting appropriate criteria that ideally fit with the study area significantly improves the site suitability assessment specifically for the diversion dam.

In addition, Figure 8 shows the summary of the areas identified from the AHP suitability map. Among the Barangays, only two have been classified in the suitability map, Barangay Taguibo and Barangay Pianing, due to the river network classified within their boundary. Barangay Taguibo consists of 8.43% not suitable with an area of 0.64 ha, 28.92% low suitable with an area of 2.21 ha, 46.18% moderately suitable with an area of 3.53 ha, 4.02% suitable with an area of 0.31 ha and 12.45% highly suitable area covering 0.95 ha. Barangay Pianing was classified only into three suitability classes: not suitable, low suitable, and moderately suitable, covering 17.5% (0.21 ha), 40% (0.49 ha), and 42.5% (0.52 ha), respectively. Barangay Taguibo and Barangay Pianing were dominantly classified as moderately suitable in terms of physical and agrometeorological features, which have 38% and 41% influence, respectively, compared to their economic feature for which dominant classification was highly suitable with 21% influence during the overlaying process.

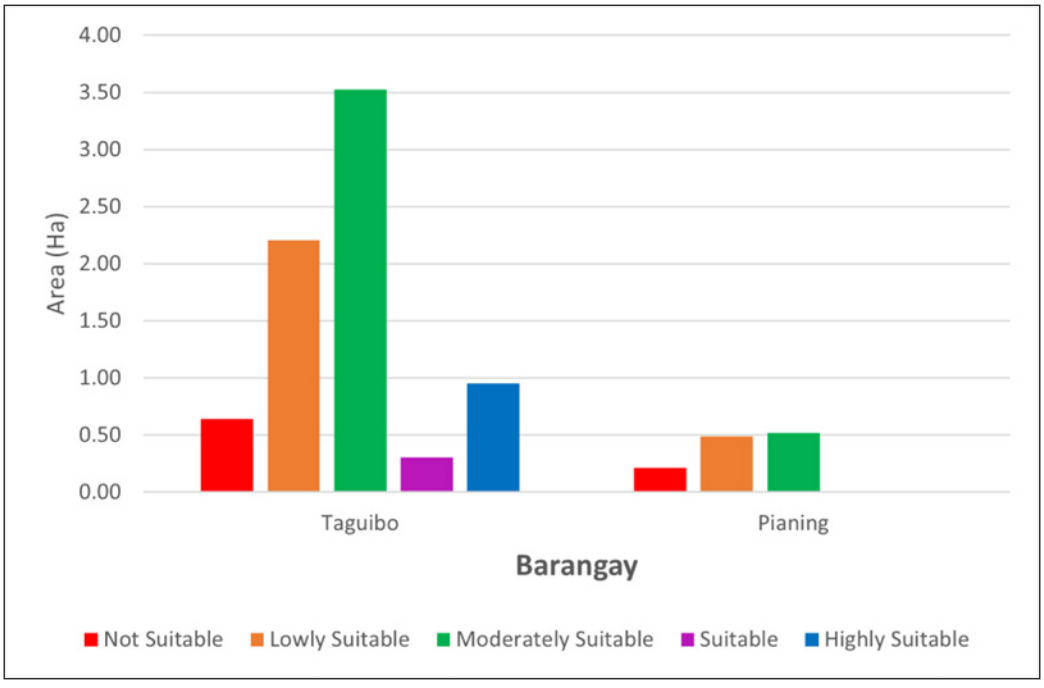

Figure 8. Suitable areas in hectare

Existing (SSIP) Suitability Map

The existing suitability map (Figure 9) was obtained from the CSU-CReAte (Center for Resource and Assessment Analytics and Emerging Technologies) and clipped using ArcGIS 10.4 tools to specify only the study area. The existing map shows two identified sites: highly suitable (purple) and marginally suitable (green).

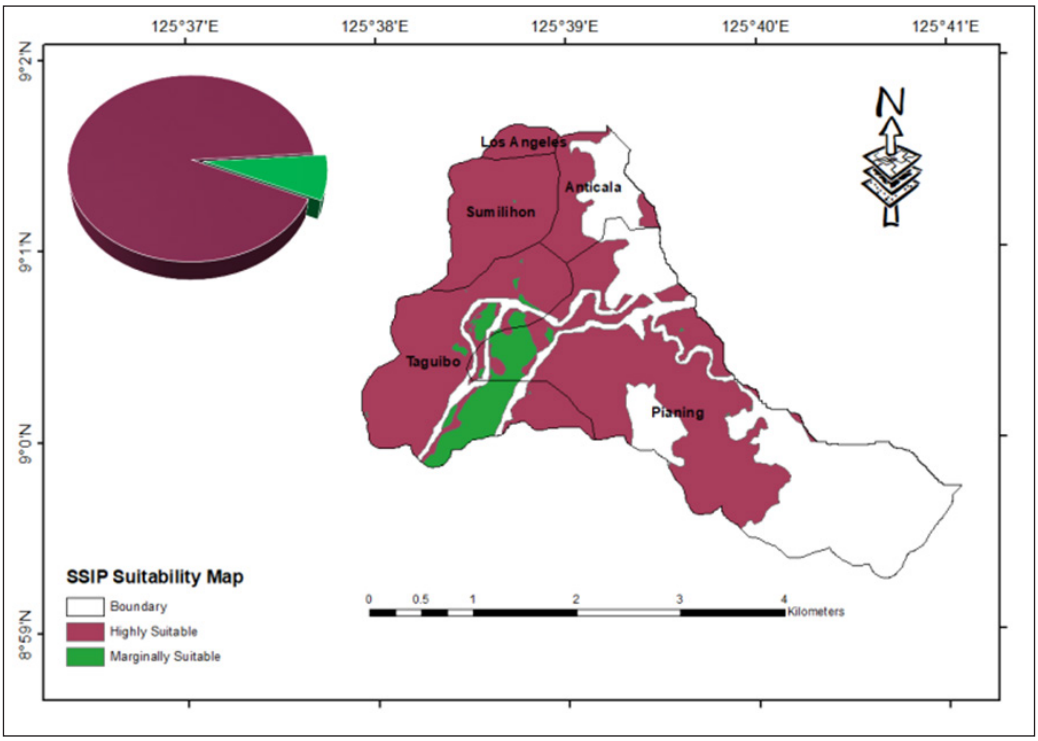

Figure 9. Existing suitability map

Specifically, it was observed that 92.22% (6,765,086 m^2) of the total area of 7,335,812 m^2 were highly suitable sites. On the other hand, the remaining 7.78% (570,726 m^2) of the total area was identified as marginally suitable. However, the map shows that the part of Barangay Pianing was not included as a suitable site since it was a steep slope area, including the upper part of the study area located near the boundary of Barangay Anticala and Barangay Pianing.

Comparative Evaluation

Two methods were used to generate the two different final suitability maps. Both methods used GIS tools in suitability maps. However, in the current suitability map, an analytical hierarchy process, AHP, was used to identify the most important criteria selected to

improve the decision-making assessment. The existing suitability map used a standardized protocol to generate suitability maps according to the standard set by the BSWM, National Water Resources Board, and all 13 participating state universities and colleges around the Philippines. In addition, the result of the AHP model suitability map shows more on the specific location as it followed the feedback from the experts. In terms of physical aspects, the Taguibo River irrigation system diversion dam was classified as moderately suitable due to the river width and slope as well as the soil type composition of the location area. In addition, the Taguibo River irrigation system, in terms of agrometeorology, was classified as highly suitable, which is also due to the river discharge and rainfall sub-criteria. Lastly, the Taguibo River irrigation system diversion dam was classified in terms of economic factors as highly suitable since the location of the diversion dam was near the access road and the service area. The result also indicates that the criteria selected significantly influence the generated AHP model suitability map. The existing map generally considers the whole study area, disregarding the river and steep slope areas. In addition, the location of the Taguibo River irrigation system diversion dam was classified as highly suitable based only on the AHP model suitability map since the existing suitability map disregarded the river network as a criterion for site suitability assessment.

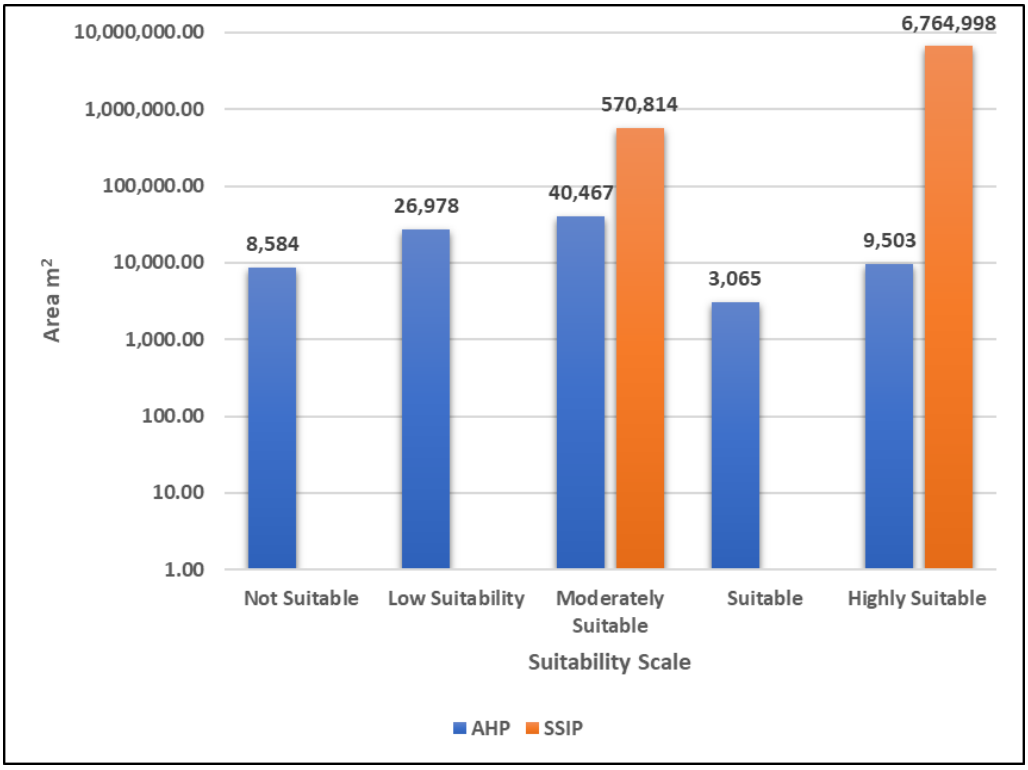

Figure 10. Comparative data (area)

To compare the two generated maps, the AHP model (Figure 7) and the existing model (Figure 9) suitability maps show differences in the area covered with suitability classification levels. Figure 10 shows that the highly suitable sites in the AHP model suitability map have 9,503 m^2, while the SSIP model has 6,764,998 m^2. On the other hand, by comparing the marginally suitable sites of both models, the AHP model has 40,467 m^2, while the SSIP model has 570,814 m^2. The graph shows that the SSIP model has the highest value of both highly suitable and marginally suitable sites since it generated the model considering the whole study area. In contrast, the AHP model only covered the river networks.

CONCLUSION

The final AHP suitability map of the study area found along the river, with 10.73% out of 88,599.17 m^2 total area of the river was highly suitable or approximately 9,506.69 m^2, and not suitable sites found 9.69% out of 88,599.17 m^2 or approximately 8,585.26 m^2 area covered. Meanwhile, the researchers found that the total area comprising marginally suitable and highly suitable sites in the existing suitability map was approximately 7,335,812.72 m^2 or 733.58 ha out of the total area. 92.22% (6,765,086.49 m^2) out of 7,335,812.72 m^2 were highly suitable, while the remaining 7.78% (570,726.23 m^2) were identified as marginally suitable sites. The comparison for both suitability maps generally differs due to the methods used. The AHP model suitability map shows the specific sites that were suitable and not suitable for diversion dam, which indicates along the river due to the river discharge as part of the criteria, whereas the existing suitability map disregarded the river network as part of the criteria, including the steep slope areas. Thus, selected criteria were generally the main factors in assessing suitability sites.

The study suggested that using GIS tools combined with the AHP approach in decision-making shows significant results based on the suitability map output. However, further knowledge about the AHP methods, such as criteria selection, experts, and technical aspects in terms of how to convey the questionnaire to the experts, was essential to execute the analytical hierarchy process (AHP) and provide accurate results in decision-making. The researchers also suggest conducting field validation to identify the accuracy of the generated AHP model suitability map. In addition, the researchers suggest evaluating the capacity of the Taguibo River irrigation system diversion dam. Moreover, the percentage of reoccurrence of water volume should be evaluated to identify the highest volume of water that affects the diversion dam's capacity.

ACKNOWLEDGEMENT

The authors are thankful to the Department of Agricultural and Biosystems Engineering (DABE), College of Engineering and Geosciences, Caraga State University (CSU),

Ampayon Butuan City 8600, Philippines, for the facilities provided during the conduct of this study and also to the Center for Resource Assessment, Analytics and Emerging Technologies (CReATe) under the project entitled "Water resource assessment and modeling of the selected watershed in the Caraga Region for sustainable domestic and irrigation supply."

REFERENCES

Ali, E. (2020). Geographic information system (GIS): Defination, development applications & components. In *Urbanisation in India: Causes, Growth, Trends, Patterns, Consequences & Remedial Measures* (pp. 1-13). Department of Geography, Ananda Chandra College.

Alpagut, B., Romo, A. L., Hernández, P., Tabanoğlu, O., & Martinez, N. H. (2021). A GIS-based multicriteria assessment for identification of Positive Energy Districts boundary in cities. *Energies, 14*(22), Article 7517. https://doi.org/10.3390/en14227517

Bacci, M., Ousman Baoua, Y., & Tarchiani, V. (2020). Agrometeorological forecast for smallholder farmers: A powerful tool for weather-informed crops management in the Sahel. *Sustainability, 12*(8), 3246. https://doi.org/10.3390/su12083246

Baltazar, B. M., Saludes, R. B., Dorado, M. A., Cruz, P. C. S. (2019, October 14-18). *Site suitability analysis of diversion dams in Quezon, Philippines using multi-criteria decision analysis and GIS.* [Paper presentation]. The 40th Asian Conference on Remote, Daejeon, South Korea.

Bataineh, O., Hjeelah, D. A., & Arabiat, S. (2018). Multi-criteria decision making using AHP to select the best CAD software. In A. Abraham, S. Kovalev, V. Tarassov, V. Snasel, M. Vasileva & A. Sukhavov (Eds.) *Proceedings of the Second International Scientific Conference "Intelligent Information Technologies for Industry*" (pp. 106-115). Springer. https://doi.org/10.1007/978-3-319-68324-9_12

BCWD. (2015). *Social development program implemented within Taguibo River watershed forest reserve*. Butuan City Water District. https://bcwd.gov.ph//

Canco, I., Kruja, D., Lancu, T., (2021). AHP, A reliable method for quality decision making: A case study in business. *Sustainability*, *13*(24), Article 13932. https://doi.org/10.3390/su132413932

Charles, A. C., Armstrong, A., Nnamdi, O. C., Innocent, M. T., Obiageri, N. J., Begianpuye, A. F., & Timothy, E. E. (2024). Review of spatial analysis as a geographic information management tool. *American Journal of Engineering and Technology Management, 9*(1), 8-20. https://doi.org/10.11648/j.ajetm.20240901.12

Chen, C. F. (2006). Applying Analytical Hierarchy Process (AHP) approach to convention site. *Journal of Travel Research, 45*(2), 167-174. https://doi.org/10.1177/0047287506291593

Dong, Y., Zhang, G., Hong, W. C., & Xu, Y. (2010). Consensus models for AHP group decision making under row geometric mean prioritization method. *Decision Support Systems, 49*(3), 281–289. https://doi.org/10.1016/j.dss.2010.03.003

EMB. (2019). *Taguibo river water quality: Annual report for CY 2019* (Report CY 2019). Environmental Management Bureau. chrome-extension://efaidnbmnnnibpcajpcglclefindmkaj/https://emb.gov.ph/wp-content/uploads/2020/11/FINAL-EMB-ANNUAL-REPORT-FOR-CY-2019.pdf

Goncalvez, A. B. (2021). Spatial analysis and geographic information systems as tools for sustainability research. *Sustainability, 13*(2), Article 612. https://doi.org/10.3390/su13020612

Karakuz, C. B., & Yildiz, S. (2022). GIS-Multi criteria decision analysis-based land suitability for dam site selection. *International Journal of Environmental Science and Technology, 19*(12), 12561-12580. https://doi.org/10.1007/s13762-022-04323-4

Lapong, E., & Fujihara, M. A. (2008). Water resources in the Philippines: An overview of its uses, management, problems and prospects. *Journal of Rainwater Catchment Systems, 14*(1), 57-67. https://doi.org/10.7132/jrcsa.KJ00004978343

Longobardi, A., & Villani. P. (2013). A Statistical, parsimonious, empirical framework for regional flow duration curve shape prediction in high permeability Mediterranean region. *Journal of Hydrology, 507*, 174-185. https://doi.org/10.1016/j.jhydrol.2013.10.019s

Midatana, S., Saran, S., & Ramana, K. V. (2018). Site suitability analysis for industries using GIS and multi criteria decision making. *ISPRS Annals of the Photogrammetry, Remote Sensing and Spatial Information Sciences, 4*, 447-454. https://doi.org/10.5194/isprs-annals-IV-5-447-2018

Romano, G., Sasso, P. D., Liuzzi, G. T., & Gentile, F. (2015). Multi-criteria decision analysis for land suitability mapping in a rural area of Southern Italy. *Land Use Policy, 48*, 131-143. https://doi.org/10.1016/j.landusepol.2015.05.013

Shukla, O., Upadhayay, L., & Dhamija, A. (2013, November 20-22). *Multi criteria decision analysis using AHP technique to improve quality in service industry: An empirical study*. [Paper presentation]. International Conference on Industrial Engineering (ICIE-2013), Surat, India, https://doi.org/10.13140/RG.2.1.2747.0881

Zukhrufiyati, A., Triyono, J., Ginting, S., & Irianto, E. W. (2019, September 1-7). *Determination of dependable flow for microhydro power plant in irrigation network*. [Paper presentation]. 3rd World Irrigation Forum (WIF3), Bali, Indonesia.

Pertanika J. Sci. & Technol. 33 (S1): 109 - 136 (2025)

PERTANIKA JOURNALS

SCIENCE & TECHNOLOGY

Journal homepage: http://www.pertanika.upm.edu.my/

Application of GIS and SWAT Model for Assessing Water Yield at Taguibo River Watershed Forest Reserve (TRWFR), Butuan City, Philippines

Aljon Ente Bocobo[1,2]*, Arnold Gemida Apdohan[1,2], Antonietto Ortega Cacayan Jr.[1], Kenneth John Peña Lajera[2] and Febe Hyacinth Andoy Simbolas[2]

[1]Department of Agricultural & Biosystems Engineering, College of Engineering and Geosciences, Caraga State University, Ampayon, Butuan City, 8600, Philippines
[2]Center for Resource Assessment Analytics and Emerging Technologies (CREATE), Caraga State University, Ampayon, Butuan City, 8600, Philippines
[3]Caraga State University,Ampayon, Butuan City, 8600, Philippines

ABSTRACT

As urban development has progressed, the demand for reliable water supply in Butuan City has increased significantly. However, due to limited water suppliers, the availability of sanitary water could be more inconsistent. Furthermore, the region has experienced heightened occurrences and intensified magnitudes of floods and droughts because of the influence of climate change. Consequently, ensuring an adequate water supply to augment the needs of the growing population has become a pressing concern. Thus, this study developed a hydrological model utilizing the Geographic Information System (GIS) and the Soil and Water Assessment Tool (SWAT) to assess the water yield of the Taguibo River Watershed Forest Reserve. The model was calibrated and validated using monthly average observed discharge data from 2012 to 2013 and 2010 to 2011. The validation phase demonstrated a strong correlation between the model-simulated and actual values, with R2 = 0.87, NSI = 0.73, and PBIAS= –19%, which revealed the satisfactory performance of the model. These findings underscore the effectiveness of integrating the GIS environment and SWAT model for evaluating watershed hydrology and estimating water yield. Overall, this study showcases the potential of GIS and the SWAT model in comprehensively examining the hydrological aspects of watersheds and providing valuable insights into water yield calculations.

Keywords: Hydrological Model, GIS, SWAT, Taguibo River Watershed Forest Reserve (TRWFR), Water Yield

ARTICLE INFO

Article history:
Received: 8 November 2023
Accepted: 5 November 2024
Published: 31 January 2025

DOI: https://doi.org/10.47836/pjst.33.S1.06

E-mail addresses:
aljunwarriorb@gmail.com (Aljon Ente Bocobo)
agapdohan@carsu.edu.ph (Arnold Gemida Apdohan)
antoncacayan@gmail.com (Antonietto Ortega Cacayan Jr.)
kennethjohnlajera123@gmail.com (Kenneth John Peña Lajera)
simbolashyacinth@gmail.com (Febe Hyacinth Andoy Simbolas)
*Corresponding author

ISSN: 0128-7680
e-ISSN: 2231-8526

INTRODUCTION

Butuan City in the Philippines relies heavily on the Taguibo Watershed for essential ecosystem services, the most significant being its role as a dependable supplier of clean and fresh drinking water to the surrounding communities. In the Caraga Region, this surface catchment also acts as an environmental buffer against harsh or inclement weather (Santillan et al., 2011; Sanguila et al., 2016). Indeed, a reliable water supply is crucial to all living and non-living organisms. According to Kodoatie and Sjarief (2010), water availability refers to the anticipated quantity of water within a designated period existing at a particular site that encompasses various water bodies such as rivers, dams, lakes, reservoirs, and other related water structures. However, as the global population increases, there is a corresponding increase in demand for water to fulfill various needs such as household, municipal, agricultural, and industrial. Undoubtedly, the assessment of water resources serves as an essential prerequisite for fostering sustainable development and effective management of water resources on a global scale (Kodoatie & Sjarief, 2010).

Hydrologic models have turned out to be crucial tools in assessing water resources. Understanding hydrological responses to Land Use and Land Cover (LULC) change becomes essential for the sustainable utilization of water resources and local ecological preservation of any catchment area. Hydrological modeling is carried out to understand this complex interaction and conceptualize and investigate the relationships among human activities, climate, and water resources. A river basin-scale model called the Soil and Water Assessment Tool (SWAT) that integrates GIS technology was established to measure the effects of land management techniques in substantial, intricate watersheds. Moreover, it improves the accuracy of generated results for water discharge from rainfall and basin physical characteristics. Input data like soil, land use, and slope of the study area were input into the model to simulate various physical processes in the basin. A graphical user interface is created via GIS and SWAT (Young et al., 1994). This study aims to develop a hydrological model using GIS and SWAT to assess the water yield of the Taguibo River Watershed.

METHODS

Study Area

The Taguibo River Watershed Forest Reserve (TRWFR) is located at Barangay Anticala, Butuan City (Figure 1). It encompasses approximately 4,367.44 hectares of public land in Butuan, RTR and Cabadbaran in the province of Agusan del Norte, with most of the land located in the city of Butuan (Moriarty et al., 2005). The watershed has a Type II climate, with rainfall spreading evenly throughout the year. This study was conducted within the TRWFR near the Taguibo Aquatic Solutions Corporation (TASC) reservoir as a sampling site for the study.

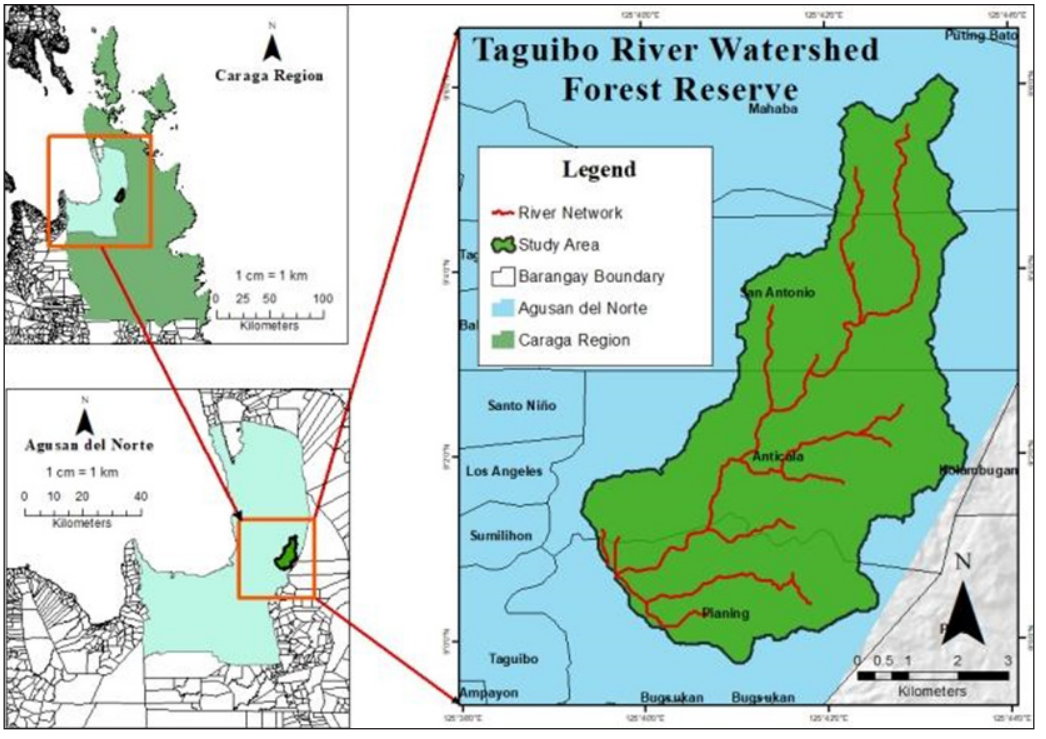

Figure 1. Map of the study area

Methodological Framework of the Study

Several methods were employed to set up the SWAT model, including data gathering, data processing, Hydrologic Response Unit (HRU) analysis, inputting the data into the SWAT model, running the model, and calibrating and validating the model. Figure 2 provides a visual representation of the methodology to simulate the hydrological processes of the Taguibo River Watershed Forest Reserve.

Data Collection

This study collected the following types of datasets, which were vital to processing and conducting the study's approaches. These were secondary data from different institutions. The datasets used for simulation in the SWAT model are presented in Table 1.

Digital Elevation Model

SWAT's automated watershed delineation feature produced the watershed's boundary. This feature employs the DEM data to recognize the flow direction and accumulation and establish a flow accumulation grid. After selecting an outlet point, the tool traces the upstream flow paths, creating the watershed boundary.

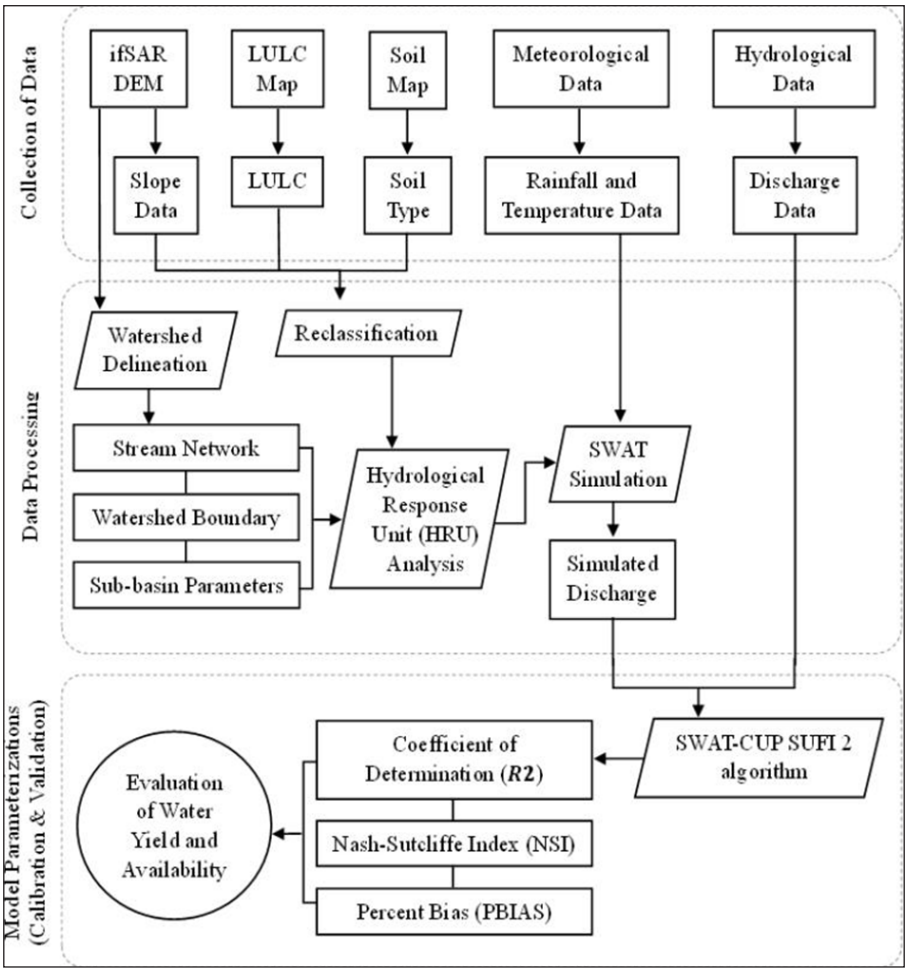

Figure 2. Flow diagram of the methodology

Table 1
Datasets used for simulation in the SWAT Model

DATASETS	SOURCE
Digital Elevation Model (DEM)	Mines and Geosciences Bureau
Land Use Land Cover (LULC) Map	CSU-CReATe (Center for Resource Assessment, Analytics and Emerging Technologies) generated using the Landsat OLI images
Soil Map	Bureau of Soil and Water Management (BSWM)
Weather Data (precipitation and minimum/ maximum temperatures)	NASA Power | Data Access Viewer (power.larc.nasa.gov/ data-access-viewer)
Discharge Data (Observed)	Butuan City Water District (BCWD) through CSU-CReATe (Center for Resource Assessment, Analytics and Emerging Technologies)

Slope Map

A slope map was derived from the DEM to define the Hydrological Response Unit, HRU. The slope map was generated by calculating the slope angle of the terrain using the DEM data.

Land Use Land Cover Map

The map was generated using Landsat 8 OLI images, which have a resolution of 30 meters and a supervised Support Vector Machine (SVM) classifier. The overall accuracy of the map was determined to be 96.6%. The map was used to identify and classify the different types of land cover in the study area. The land use land cover classification was based on the different spectral signatures obtained from the satellite images.

Soil Map

The soil map classified the soil into different types and contained information about the soil characteristics of the study area. This map was used as input while defining land use, soil, and slope for the HRU analysis in the SWAT modeling. This step was essential in identifying the different HRUs based on the soil type and slope of the land, which ultimately helped stimulate the study area's hydrological processes.

Meteorological Data

Weather Data

The historical daily weather data for the temperature and precipitation of the study area from 2012 to 2021 (a 10-year duration) were downloaded from NASA Power Data Access Viewer (power.larc.nasa.gov/data-access—viewer), as presented in Table 2. The data can also be acquired through government weather stations like the Philippine Atmospheric and Geophysical Service Administration (PAGASA).

SWAT needed daily climate and weather information gleaned from measurable data sets or produced by a weather generator model. The model needs precipitation, temperatures, relative humidity, wind speed, and solar radiation data.

Table 2
Monthly weather data for 2021

Months	WEATHER DATA		
	Minimum Temperature (°C)	Maximum Temperature (°C)	Precipitation (mm)
January	19.37	30.08	659.18
February	20.30	32.01	432.42
March	20.10	31.81	348.05

Table 2 (*continue*)

Months	WEATHER DATA		
	Minimum Temperature (°C)	Maximum Temperature (°C)	Precipitation (mm)
April	21.05	32.73	213.06
May	22.14	32.89	396.48
June	21.76	32.94	187.50
July	22.00	32.95	267.74
August	22.01	32.80	212.17
September	21.79	33.76	282.91
October	21.14	32.94	435.15
November	21.68	31.66	567.30
December	21.12	30.37	664.57

Hydrological Data (Observed Discharged Data)

The observed discharge data was collected from a stream located at 8.9786° N, 125.6287° E, situated 150 meters upstream of the TASC Hydro Dam outlet. It is positioned before the dam's outlet along the water flow path. This location is commonly used to measure discharge (water flow rate) and monitor the inflow into the dam. The observed discharge data for the years 2010, 2011, 2012, and 2013 were acquired from Butuan City Water District (BCWD) through CSU-CReATe. These data were used to calibrate and validate the model using the SWAT-CUP - SUFI-2 optimization algorithm.

Data Processing

The first step was to process the DEM using ArcMap 10.3 software. The study area's watershed boundary was extracted by clipping the DEM data using the clip command tool within the ArcMap interface, which had the same coordinate system. The slope map was then generated by using the slope command tool in the ArcMap 10.3 interface. The land use map, soil map, weather data (precipitation and minimum/maximum temperatures), and discharge data (observed) were used as inputs to generate the model, and different maps were created that were essential for the study. The data processing was necessary to convert raw data into usable input formats for the model.

Hydrological Response Unit Analysis

HRU analysis combined three categorical variables- soil type, slope, and land- to create HRUs. The slope spatial analysis tool in Arc Map 10.3 software was used to determine the slope of a watershed from a DEM. The tool converts the elevation into a slope projection using the percent slope using the DEM file as the input raster. The subsurface lateral water movement, flow buildup and routing, as well as the sediment yield for each sub-basin,

were filled in by this parameter for SWAT (Arnold et al., 1998). The unique combinations of land use, soil type, and slope were used to develop the HRUs.

SWAT Input

A scale model of a river basin or watershed is called SWAT, or Soil and Water Assessment Tool. Dr. Jeff Arnold created it for the USDA Agricultural Research Service (ARS). It was created to predict how land management methods in sizable, complicated watersheds with a range of soil types would affect water, sediment, and agricultural chemical outputs. A watershed is divided into multiplex sub-watersheds in SWAT, and these are then further divided into hydrologic response units, HRUs, which are made up of homogeneous topographical, soil, and management characteristics. Water balance is said to be the driving force behind all SWAT activities because it influences plant growth and the flow of sediments, nutrients, pesticides, and pathogens (Arnold et al., 2012). This model can mimic several important hydrologic processes, such as evapotranspiration, surface runoff, infiltration, percolation, shallow and deep aquifer flow, and channel path (Arnold et al., 1998). SWAT can simulate various hydrologic processes, including canopy storage, surface runoff, infiltration, evapotranspiration, lateral flow, tile drainage, and water redistribution within the soil profile (Abbaspour et al., 2015). The hydrologic cycle in the SWAT model is simulated by utilizing the water balance as expressed in Equation 1.

$$SW_t = SW_o + \sum_{i=1}^{n} \left(R_{day} - Q_{surf} - ET - W_{seep} - Q_{gw}\right) \quad [1]$$

where SW*t* is the final soil water content (mm), SW*o* is the initial soil water content on day i (mm), t is the time (days), R*day* is the amount of precipitation on day i (mm), Q*surf* is the amount of surface runoff on day *i* (mm), E*a* is the amount of evapotranspiration on day *i* (mm), W*seep* is the amount of water entering the vadose zone from the soil profile on day i (mm). Qgw is the amount of return flow on the day *i* (mm).

Watershed Delineation

In constructing the model, the generated DEM was first used to delineate the watershed by generating sub-watersheds using the ArcSWAT automatic watershed delineator toolkit. The output includes calculating the stream network, determining the watershed boundary, and calculating the sub-basin parameters.

SWAT Simulation

Given that the raw input data are complete, the setup and running of the model simulation were completed. SWAT may then instantly check for any issues after that. Using SWAT Output Viewer or ArcMap 10.3, the output data from the SWAT project was viewed and

displayed on time series graphs or themed maps. One may view daily, monthly, and yearly output parameters broken down by watershed, HRU, sub-basin, and reservoir.

Water Yield

In the output of the SWAT model, the total water yield can be viewed and presented in daily, monthly, yearly, or average values for each sub-basin or the whole watershed. Equation 2 is used to represent water yield in the SWAT model:

$$WYLD = SURQ + LATQ + GWQ - TLOSS - pond\ abstractions \quad [2]$$

where WYLD is the water yield in millimeters; SURQ is the contribution of surface runoff to streamflow in millimeters; LATQ is the contribution of lateral flow to streamflow in the watershed on a given day, month, or year in millimeters; GWQ is the contribution of groundwater to stream in the watershed on a given day, month, or year in millimeter; and TLOSS is the transmission loss, or the amount of water lost from tributary channels in the HRU. The entire HRU Land Use Soils Report drainage area was multiplied by the Water Yield to calculate the volume. Given that the Butuan City Water District taps and distributes surface water from this area of the watershed, the water yield was computed for this study (Ayivi & Jha, 2018).

Calibration and Validation of the Model

Calibration is estimating model parameters that cannot be measured directly. It can be an automated process, a manual procedure, or a combination of these. The goal of calibration is to determine the model's performance potential. Refsgaard and Storm (1996) provided a methodical approach for model calibration and validation. The method for calibrating the SWAT was outlined from 2003 to 2013 (11 years); however, in this study, calibration was done from 2003 to 2008. The same validation procedures were used for the watershed from 2009 to 2013. Three performance indicators were employed in this study: percent bias (PBIAS), Nash-Sutcliffe Index (NSI), and coefficient of determination (R^2).

SWAT -CUP SUFI 2 Algorithm

The streamflow, used as a reference to calculate other water flows indirectly, was the primary measurable metric of water flow in the watersheds (Farzana et al., 2019). Streamflow is one of the measurements used for calibration and validation in hydrology modeling (Saleh et al., 2000). Other factors like evapotranspiration, groundwater recharge, and surface runoff, among others, are challenging to assess and have data only available at specific periods in time and space (Bracmort et al., 2006).

The algorithm for Sequential Uncertainty Fitting (SUFI-2) is an approach that uses the chosen parameter ranges during an iteration process consisting of 300–1000 simulations to attempt to capture most of the measured data within the model's 95% prediction uncertainty (95PPU) (Abbaspour et al., 2015). Through trial runs, automatic calibration procedures were carried out using a prior parameter analysis (10–100 simulations). The sensitivity analysis of stream flow-related variables throughout this trial helped to identify the final values chosen for calibration and validation. For both processes, homogeneous flow time series durations were selected to offer consistent statistical samples and to evaluate the more recently available data. Nevertheless, due to cumulative model input uncertainties, a good correlation during validation may provide an inconsistent output (Bracmort et al., 2006).

Coefficient of Determination (R^2)

The coefficient of determination (R^2) indicates the percentage of variance in derived data that the model experiences. R^2, as expressed in Equation 3, is the most used criterion for evaluating a model's performance.

$$R^2 = \left(\frac{\sum_{i=1}^{n}(O_i - \bar{O})(P_i - P)}{\sqrt{\sum_{i=1}^{n}(O_i - \bar{O})^2}\sqrt{\sum_{i=1}^{n}(P_i - P)^2}} \right) \quad [3]$$

where O_i is the observed flow discharge at the time I, $\bar{O}$ is the average observed flow discharge, P_i is simulated flow discharge at time I, P¯, P is the average simulated flow discharge, and n is the number of registered flow discharge data. Table 3 lists the general performance rating criteria for the calibration and validation of this model (Farzana et al., 2019).

Table 3
Performance rating for R^2

Performance Rating	R^2
Very Good	$R^2 > 0.70$
Good	$0.60 < R^2 \leq 0.70$
Satisfactory	$0.50 < R^2 \leq 0.60$
Unsatisfactory	$R^2 > 0.50$

Nash-Sutcliffe Index

The Nash-Sutcliffe Index, NSI, value represents how well the 1:1 line fits the observed versus simulated data. Equation 4 calculates NSI.

$$NSI = 1 - \frac{\sum_{i=1}^{n}(O_i - P_i)^2}{\sum_{i=1}^{n}(O_i - \bar{O})^2} \quad [4]$$

Where the notations indicate the same meaning as described before, Table 4 provides the performance ratings for this model's NSI, which are classified at various levels (Bracmort et al., 2006; Saleh et al., 2000).

Table 4
Performance rating for NSI

Performance Rating	***NSI***
Very Well	*NSI* > 0.65
Adequate	0.54 < *NSI* < 0.65
Satisfactory	*NSI* > 0.50

Percent Bias

The percent bias, PBIAS, measures whether the simulated data is greater or smaller than the observed data (Gupta et al., 1999). A PBIAS score of 0 implies accurate model simulation. Positive values suggest that the model was underestimated, whilst negative values indicate that the model was overestimated (Gupta et al., 1999). Equation 5 is used to determine PBIAS:

$$PBIAS = \frac{\sum_{i=1}^{n}(O_i - P_i)}{\sum_{i=1}^{n} O_i} \times 100 \quad [5]$$

where the notations indicate the same meaning as described before.

RESULTS AND DISCUSSION

Watershed Delineation

Watershed delineation divided the project area into 26 sub-basins, each with a topographic report containing information such as the maximum, minimum, mean, and standard deviation of elevation. The total project area has a maximum elevation of 1883.98 m and a minimum of 93.0351 m above mean sea level. The mean elevation for the area is 890.33 m, and the standard deviation is 395.865 m. The output from the watershed delineation process also included the reach, sub-watershed, and sub-basin boundaries. The map in Figure 3 shows the delineated upstream watershed, including the watershed boundary, basins, longest path, and its reach. The generated sub-basin boundaries provided an understanding of the hydrological system of the study area, which is critical in the simulation of water resources in the SWAT model. Overall, the delineation of the watershed and sub-basins provides

essential information for water resource management and conservation in the study area (Li et al., 2021; Shivhare et al., 2018).

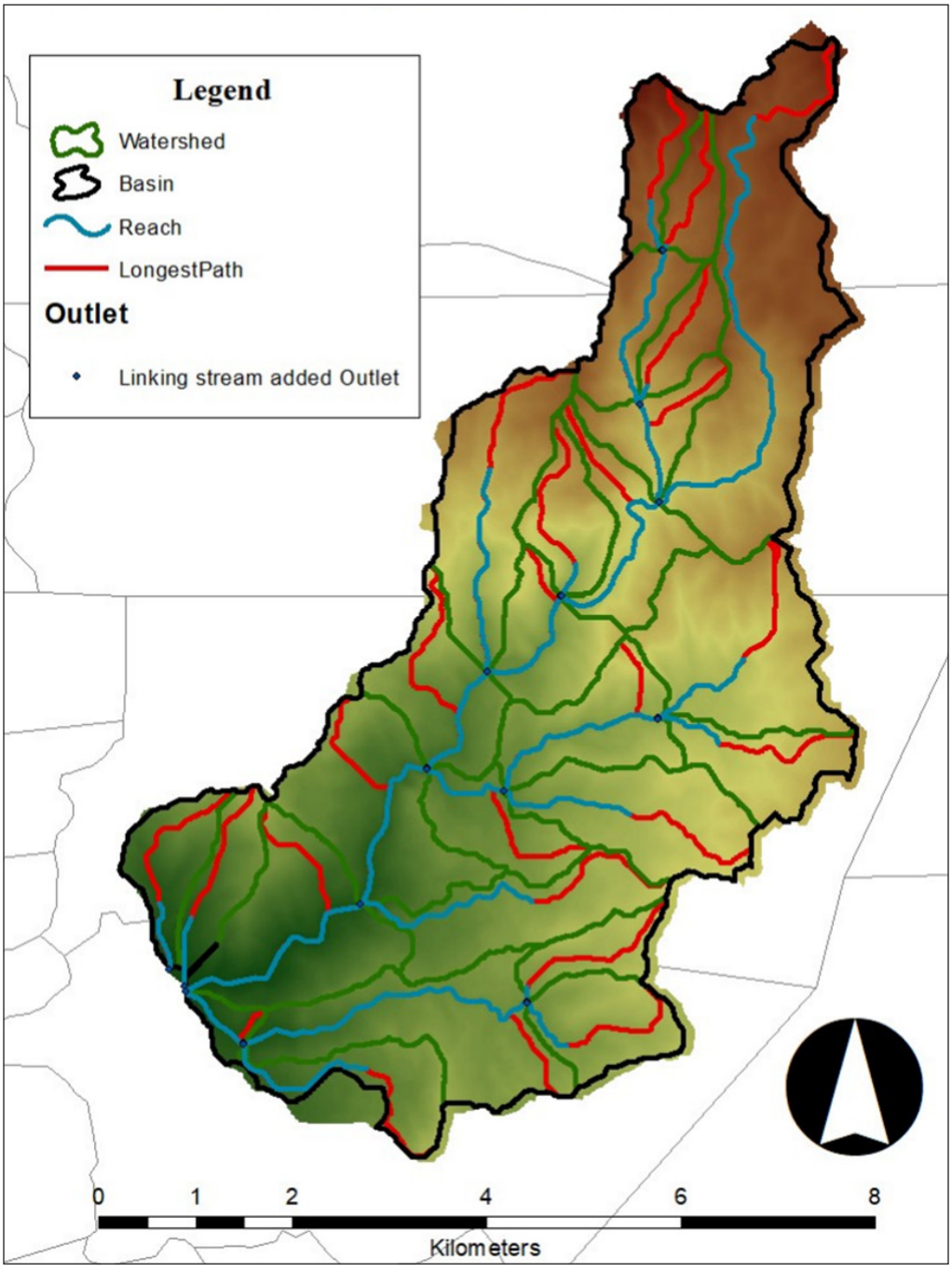

Figure 3. Delineated upstream watershed

Hydrological Response Unit Results

The hydrological response unit, HRU, included the region for the study area's upstream watershed, 4105.43 hectares (10144.7303 acres). Table 5 contains the reclassified land use, soils, and slope statistics during the HRU process.

Table 5
Hydrological response unit (HRU) results

	Land Cover Classes	SWAT Classes	Area (ha)	Watershed Area (%)
Land Use	Agricultural Area	AGRL	65.17	1.59
	Palm	OILP	333.25	8.12
	Grassland	FRSE	247.98	6.04
	Mixed Vegetations	PAST	30.71	0.75
	Forest	FRST	3398.61	82.78
	Urban	URBN	25.05	0.61
	Barren	BARR	0.51	0.01
	Water	WATR	4.15	0.10
Soil	Mountain Soil (undifferentiated)	MTSOILUND	2065.33	50.31
	Malalag Silt Loam	MALALAGSL	2025.38	49.33
	Camansa Clay	CAMANSAC	14.72	0.36
Slope (%)		50–9999	1670.79	40.70
		30–50	1396.72	34.02
		20–30	610.33	14.87
		10–20	368.67	8.98
		0–10	58.93	1.44

Figure 4 visually represents various land use classes in the watershed. The study utilized a land LULC map to identify and classify different land cover types in the watershed area. The LULC map was generated using satellite images and a supervised SVM classifier. Eight land use classes were identified and mapped out in this area. The percentage of the total area covered by each land use class is also in the figure. Agricultural land covers 1.59% of the entire watershed area, palm covers 8.12%, and grassland covers 6.04%. Pasture, on the other hand, covers only 0.75% of the site. The residential land use class covers only 0.61% of the watershed area, while barren land covers only 0.01%. Water covers 0.10% of the total area. Notably, the forest land use class dominates the entire area of the watershed, covering 82.78%. It implies that a mix of different forest types covers most of the land in the watershed; this can have important implications for the local ecosystem, such as providing habitat for wildlife, contributing to local climate regulation, and protecting soil from erosion.

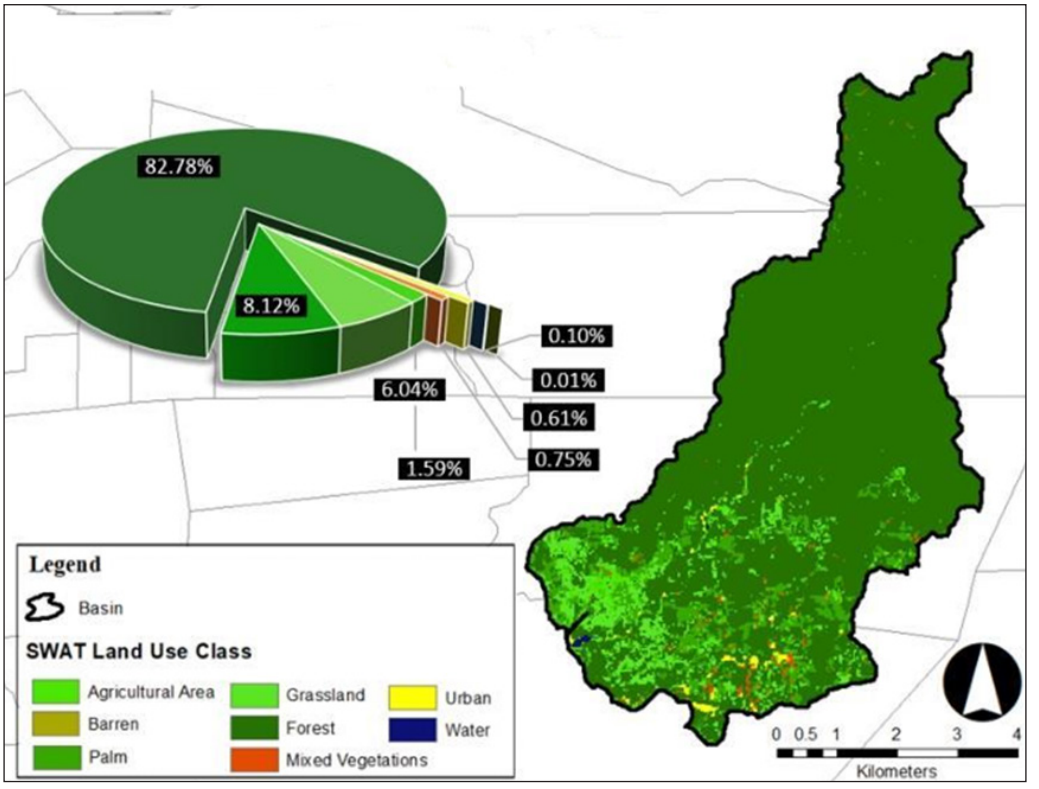

Figure 4. Reclassified land use map

Figure 5 depicts the characteristics of different types of soils found in a mountainous region, along with the corresponding watershed area. The three soil types mentioned in this figure are Mountain Soil (undifferentiated), Malalag Silt Loam, and Camansa Clay. The Mountain soil covers 50.31% of the watershed, while Malalag silt loam covers 49.33% of it. The remaining 0.36% of the watershed comprises Camansa clay.

Figure 5 also suggests that most of the soil in the watershed belongs to hydrologic soil group B, characterized by loamy and silty loamy soils (Galintao & Santillan, 2020). This soil group has moderate infiltration rates, water storage capacity, and runoff potential. These characteristics can influence how water moves through the soil, affecting factors such as erosion, groundwater recharge, and water availability for plants and animals. This information can help understand the region's hydrology and ecology and make wise land use decisions.

Figure 6 displays the essential information about the classes of the slope and their respective watershed area. The data are presented into five distinct categories. The first category, which covers the range of slopes between 50 and 9999, has the highest percentage, 40.70%; this suggests that a significant portion of the watershed area has a steep slope, which could impact water flow and lead to erosion. The second category, which covers the

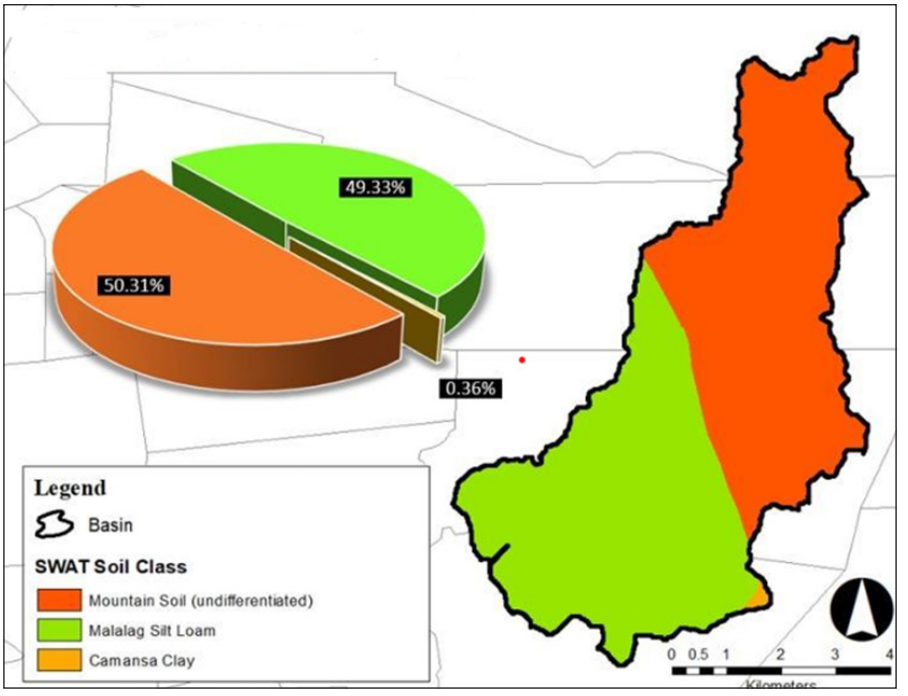

Figure 5. Reclassified soil map

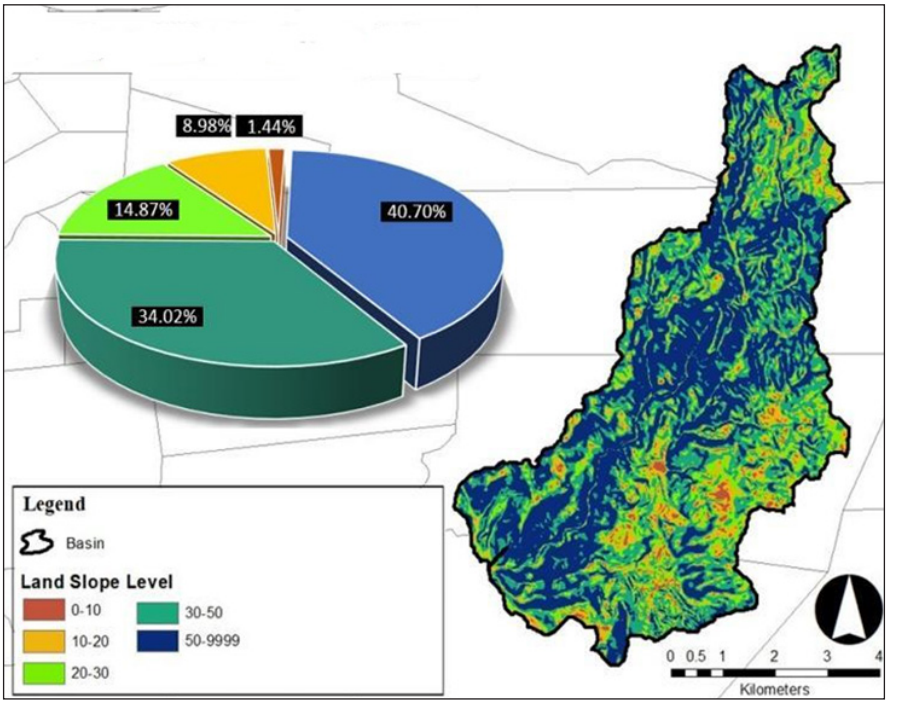

Figure 6. Reclassified land slope map

range of slopes between 30 and 50, has a percentage of 34.02%; this is also a significant percentage and indicates that a large portion of the watershed area has a moderate slope. The third category, which covers the range of slopes between 20 and 30, has a percentage of 14.87%; this indicates that a smaller portion of the watershed area has a moderately low slope. The fourth category, which covers the range of slopes between 10 and 20, has a percentage of 8.98%; this is a relatively small percentage and suggests that a small portion of the watershed area has a low slope. Finally, the fifth category, which covers the range of slopes between 0 and 10, has the smallest percentage of 1.44%; this suggests that only a tiny portion of the watershed area has a nearly flat slope. The information on the distribution of slopes (Figure 6) can be used to understand the potential impact of water flow and erosion on the landscape. It can help inform decisions about land use and conservation efforts.

The map shown in Figure 7 shows the full HRU result, basin, and its reach. The HRU is a combination of the soil data, land use land cover data, and slope data that was derived from the DEM of the study area. The forest dominated the entire watershed with about 82.78%. Moreover, it has loamy and silty loamy soils that have moderate infiltration rate, water storage capacity, and runoff potential. Also, with 40.70%, a significant portion of the watershed area has a steep slope that can affect water flow and lead to erosion.

SWAT Output Data

The SWAT simulation generates various output files, including reach, sub-basin, and HRU outputs, which could be displayed as daily, monthly, annual, or average yearly values. For each area of the watershed that it is assigned to, each output file comprises a summary of the data. The output is important for this study because it provides an overview of the water resources of the watershed and includes simulations of water yield, evapotranspiration (ET), surface runoff, percolation, lateral flow, groundwater flow (return flow), transmission losses, ponds, and other hydrological components Khoury et al. (2023). Additionally, only the water yield from sub-basins 1 through 26, encompassing the Taguibo River Watershed, was used in this analysis from 2010 to 2021 because the watershed was separated into sub-basins.

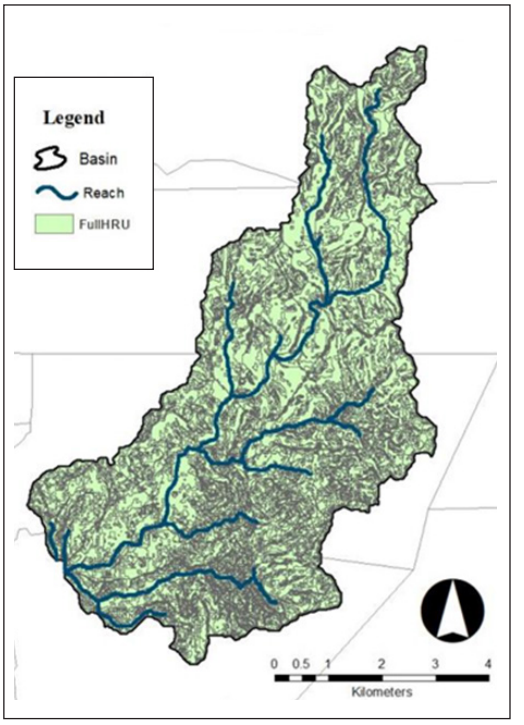

Figure 7. Hydrological response unit result

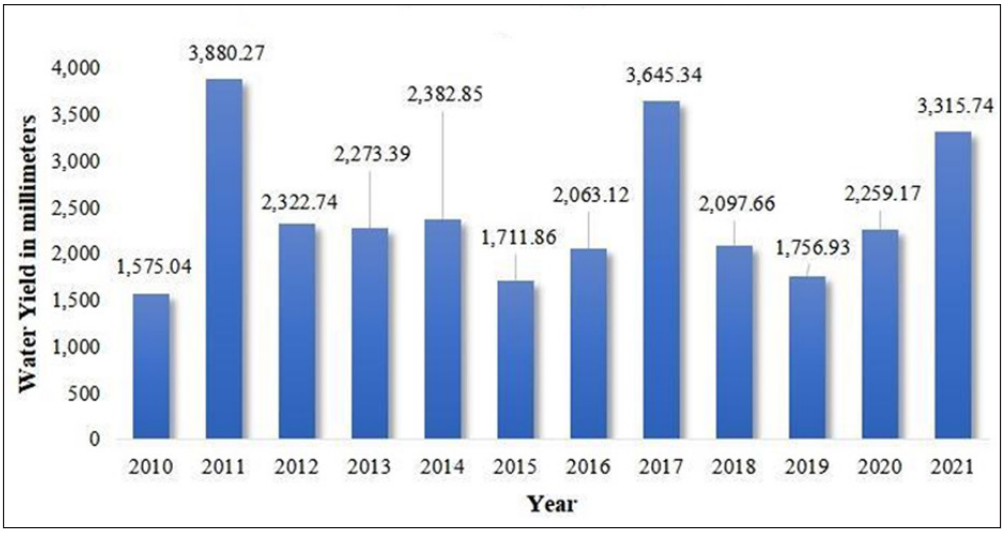

Figure 8. Water yield of the TRWFR at different years

Figure 8 displays the water yield graph for the upstream watershed from 2010 to 2021; this graph provides an important visual representation of the trend of water yield values over time to understand the changes in the watershed. Upon close examination, it becomes clear that the trend of the water yield values has changed significantly annually, meaning that the water produced yearly by the watershed was inconsistent. One factor that contributed to these alterations was precipitation. Changes in precipitation patterns can significantly impact the amount of water produced by the watershed Guo et al. (2023). For example, if there is a drought, the amount of water produced will likely be lower than if there is a period of heavy rain. Other factors such as changes in land use, temperature fluctuations, and natural events like wildfires may also play roles in these alterations. It is crucial to study these factors to understand the watershed's dynamics better and to develop effective strategies for managing its resources.

Figure 9 presents the spatial distribution of water yield levels in an upstream watershed for the years 2010, 2013, 2015, and 2018, illustrating the variability in water availability over time. Between 2010 and 2013, the watershed experienced an overall increase in water yield, indicating higher precipitation or changes in watershed conditions that enhanced water retention. However, a notable decrease in water yield occurred in 2015, likely due to a slight reduction in precipitation across the watershed area. By 2018, water yield levels had increased again, indicating a recovery that may be linked to improved precipitation rates or other hydrological factors. In contrast, Figure 10 highlights a significant rise in water yield in 2021, which can be attributed to a marked increase in precipitation patterns within the watershed, as shown in Figure 11.

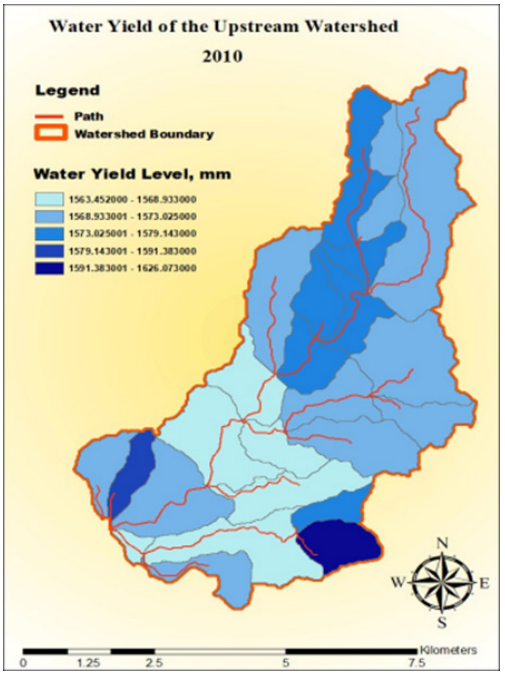

(a)

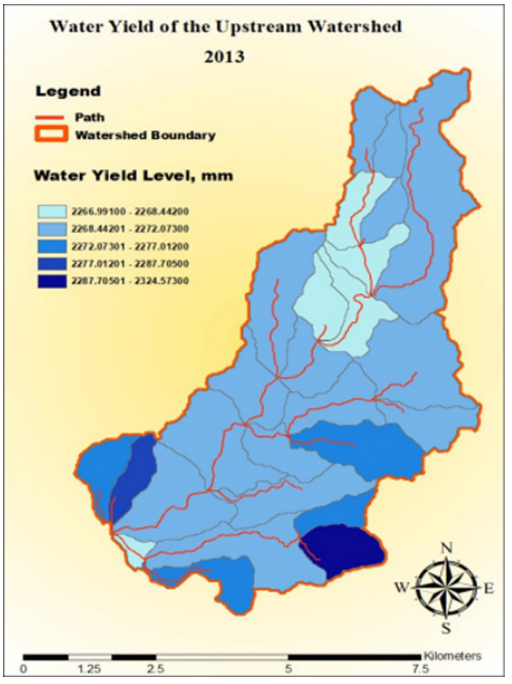

(b)

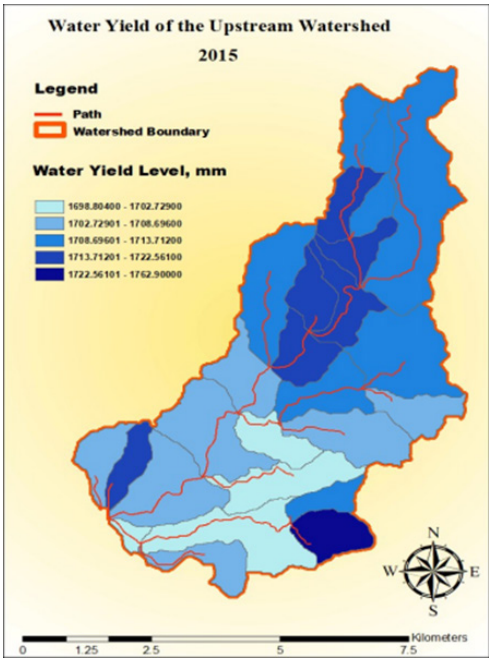

(c)

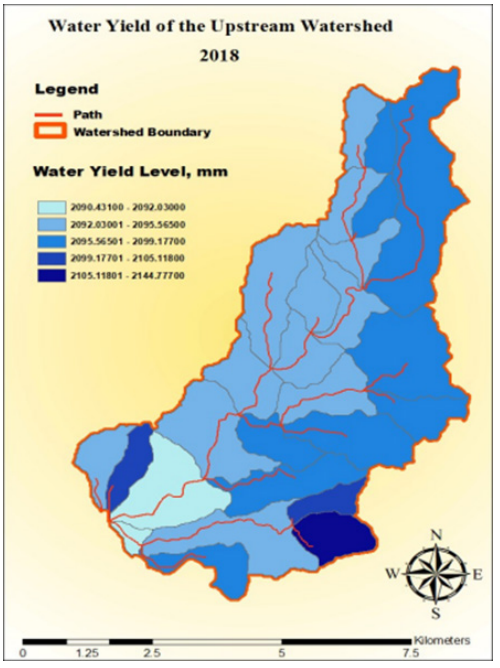

(d)

Figure 9. Upstream water yield: (a) 2010; (b) 2013; (c) 2015; (d) 2018

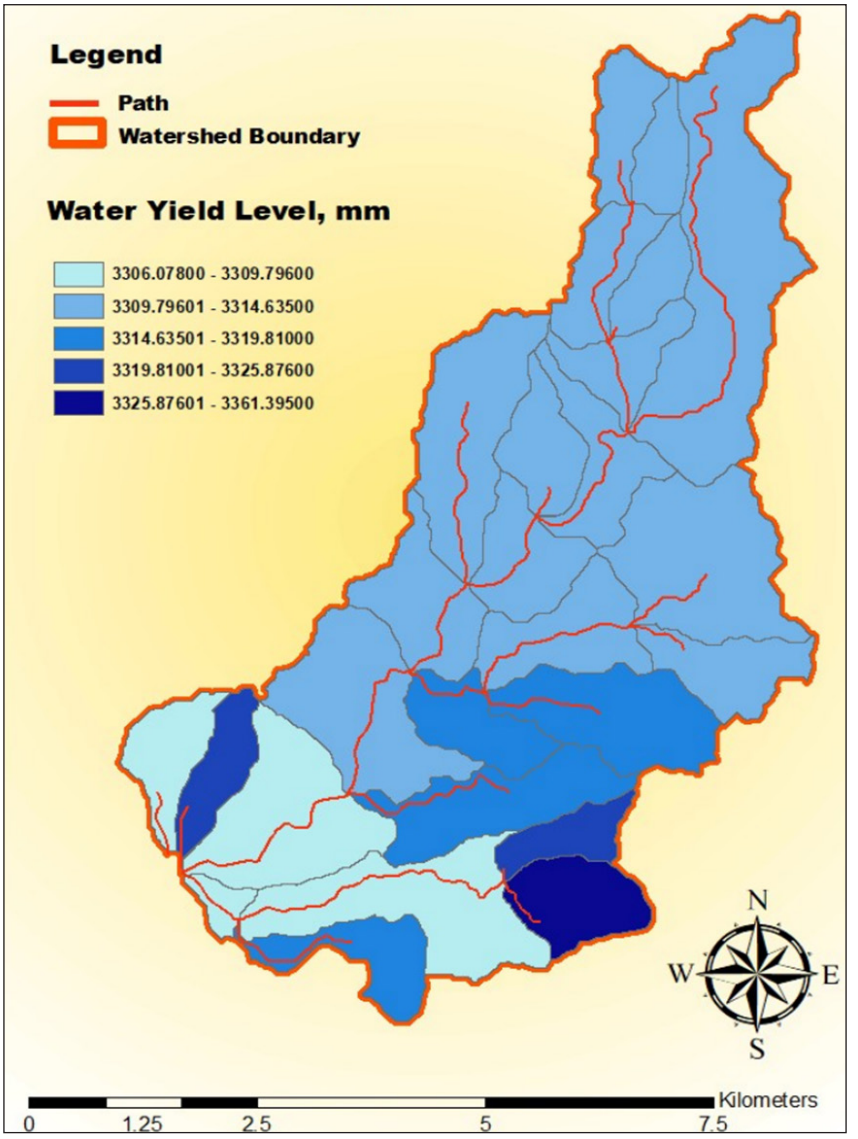

Figure 10. Upstream water yield 2021

Relationship Between Water Yield and Precipitation

Figure 11 illustrates the total annual water yield and precipitation from the year 2010 to 2021. The changes in flow in the catchment area rely on the variations of the precipitation Oda et al. (2024). The first year shows decreased water yield and precipitation, with almost 2000 mm of average water yield and annual precipitation between 2,000 mm and 4,000 mm. The following year, 2011, shows that the average water yield almost reached 4,000 mm, and its annual precipitation reached between 4,000 mm and 6,000 mm, the highest

reach in the past years. The years 2012–2016 have the least significant changes based on their average water yield and precipitation. There is a significant difference between 2016 and 2021.

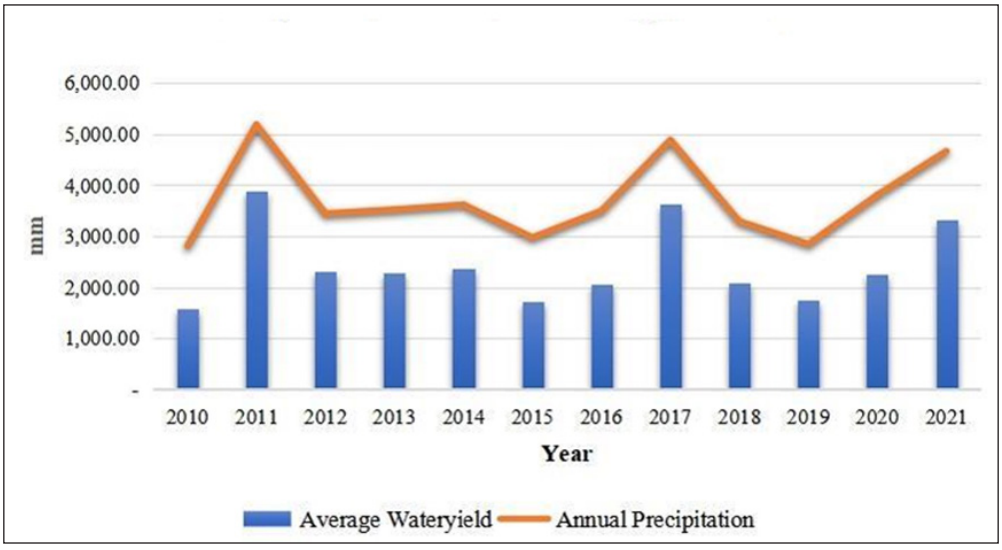

Figure 11. Relationship of water yield and precipitation

Comparison between Runoff Volume and Land Use Land Covers

Figure 12 illustrates the average monthly streamflow data for the years 2013, 2015, 2018, and 2021 based on simulations from the SWAT model. The study area experiences a tropical Type II climate, as classified by the Philippine Atmospheric, Geophysical and Astronomical Services Administration (PAGASA), characterized by a generally even distribution of rainfall throughout the year, with no distinct dry season. This climate features wet and very wet periods rather than clear wet-dry seasonal divisions. However, the region does undergo a phase of high precipitation from November to February, often accompanied by heavy rain showers. From March to October, the remaining months receive relatively lower precipitation levels. When comparing across years, there are notable differences. In 2013, streamflow starts high but sharply drops from March to May, with a moderate peak in November; however, its peak values are lower compared to other years. The year 2015 has the lowest overall streamflow, especially from May through August, reflecting possibly drier conditions. The year 2018 follows a similar trend to 2013 but maintains relatively higher values from March to June without any extreme peaks. Meanwhile, 2021 stands out with significantly higher streamflow throughout the year. It suggests an unusually high influx of water in late 2021, possibly due to heavy rainfall or other hydrological factors.

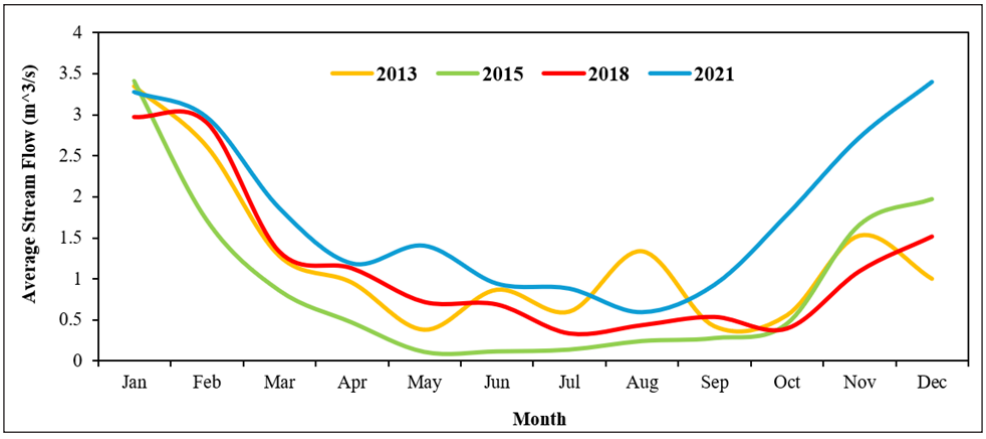

Figure 12. Simulated streamflow of the model for the years 2013, 2015, 2018 and 2021

Figure 13 illustrates the relationship between forest area and streamflow in 2013, 2015, 2018, and 2021. In 2013, the forest area was 2,483 ha, with a 1.24 m3/s streamflow representing the lowest forest area and a relatively high streamflow in the observed period. By 2015, the forest area had expanded to 3,039 ha, while streamflow decreased to 0.95 m^3/s, possibly due to increased water retention as forest cover grew and lower precipitation received that year (Figure 11). In 2018, forest area continued to increase, reaching 3,143 ha, with a slight rise in streamflow to 1.17 m^3/s. By 2021, the forest area reached 3,658 ha, and streamflow showed a substantial increase to 1,83 m^3/s. Despite the large forest area, this notable increase in streamflow suggests that other factors, such as higher precipitation or changes in hydrological conditions, may have contributed to the fluctuations in streamflow, particularly the significant increase observed in 2021.

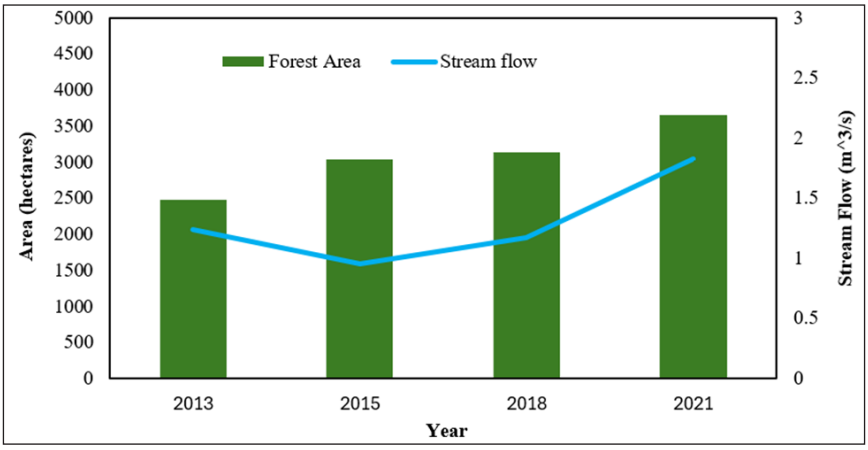

Figure 13. Forest area and its estimated streamflow Estimated streamflow in the watershed for the years 2013, 2015, 2018, and 2021

Model Calibration of LULC Year 2021

The result in Figure 14 compares the discharge of observed and predicted flows throughout the calibration period for two years (2010–2011). This study only used 2010 and 2011 as input years during calibration due to the insufficiency of the data acquired. These data served as the basis for the succeeding years that should be included in the calibration process. Figure 14 indicates the actual and simulated flow, denoted by blue and orange colors. The actual flow coincides with the simulated values. Moreover, the observed and simulated points intersect in April of 2010, July of 2010, December of 2010, March of 2011, and December of 2011.

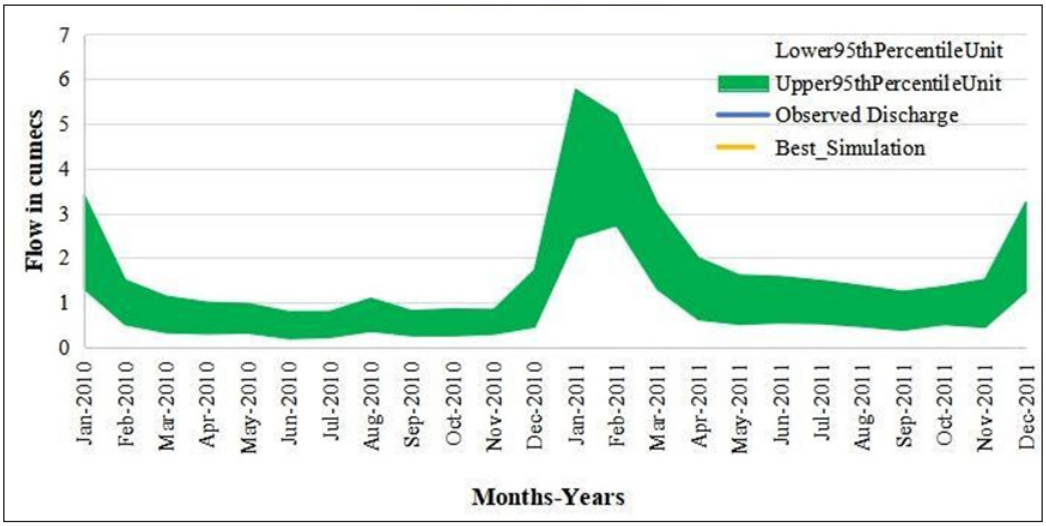

Figure 14. Comparison of the observed and simulated discharges during model calibration for two years (2010–2011)

Figure 15 illustrates the link between the observed and simulated discharges with R^2= 0.63, NSI = 0.33, and PBIAS = –29.9%. The observed and simulated flows have a good linear relationship. According to the NSI value of 0.33, the simulation results were adequate. A negative PBIAS value of -29.9% indicates a correct model simulation. The difference between the simulated and observed discharge data should be evaluated to see if the model is effective and how well it forecasts the actual water flows in a river or stream. The model's capacity to simulate water flows under various conditions can be trusted if the simulated discharge data agrees with the observed data.

Figure 16 compares observed and simulated discharges throughout the validation period from 2012 to 2013, represented by blue and orange lines. Due to the inadequacy of the collected data, the model was validated using only the input years of 2012 and 2013. The following years were expected to be incorporated into the validation procedure based on

these data. The observed and simulated values of the model during validation meet in most of the months throughout the years 2012 and 2013. It started to link together in January 2012 and started to disconnect in February 2012, and continues to correlate in April 2012, August to October 2012, early December 2012, late December 2012 to February 2013, July to August 2013, and late October 2013 to December 2013.

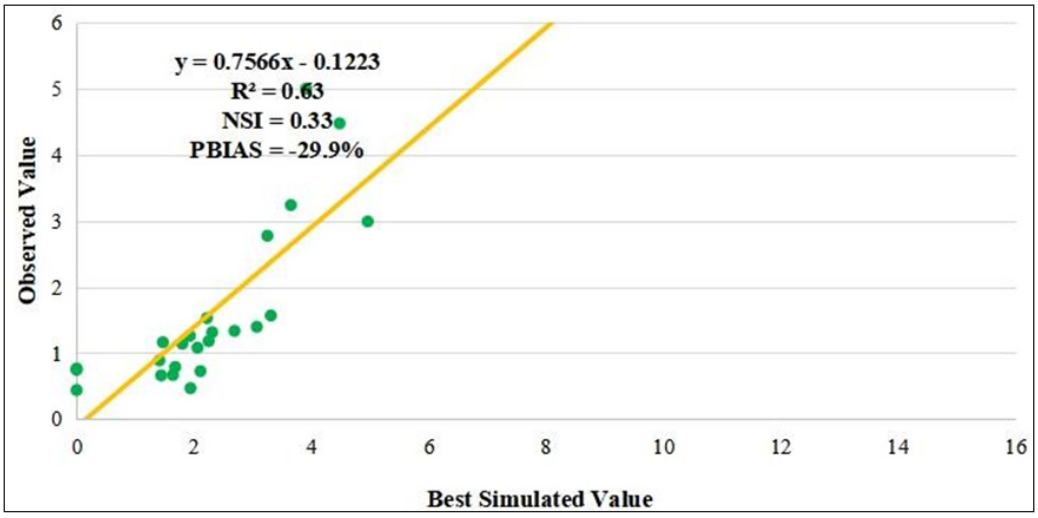

Figure 15. Relationship between the simulated and observed discharges during the calibration period

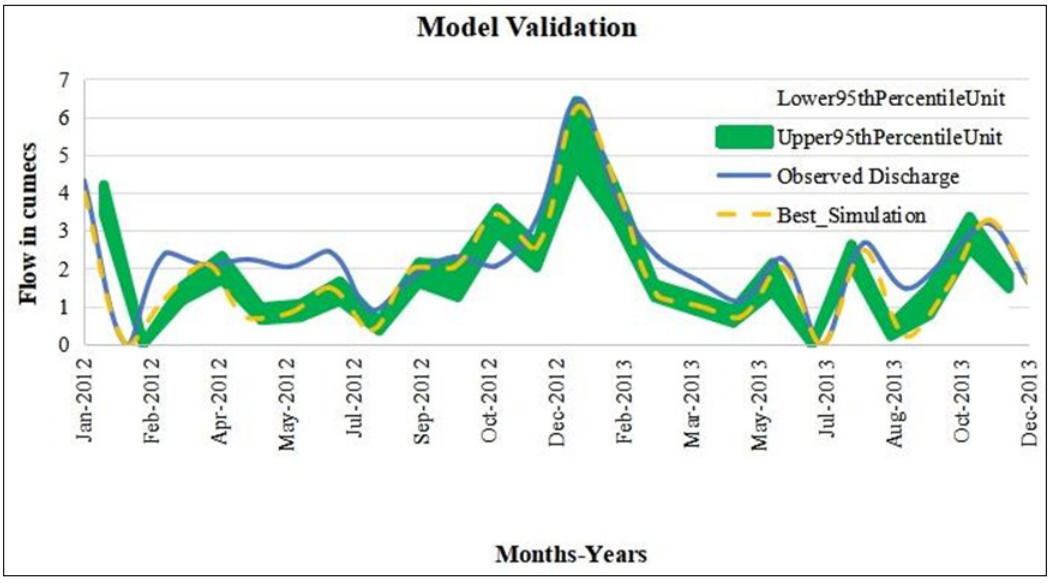

Figure 16. Comparison of the observed and simulated discharges during model validation for two years (2012–2013)

Model Validation of LULC Year 2021

In general, validation is a crucial stage in the creation of hydrological models in ArcSWAT. It improves water management decision-making, identifies model constraints, and increases the model's credibility by establishing trust in its capability to simulate water flows under various conditions (Koltsida et al., 2023).

The scatter graph in Figure 17 demonstrates the relationship between the simulated and observed discharges of the model during the validation period. Compared to the calibration period, validation acquired better results. In addition, it indicates that the observed and simulated flows have a good linear relationship with R^2 of 0.87 and NSI of 0.73, which means that the findings were satisfactory. A negative PBIAS value of –19% indicated a correct model simulation. It is essential to validate the relationship between the observed and simulated discharge data to guarantee that the hydrological model correctly predicts water flows in a river or stream. In addition to that, it also aids in evaluating model correctness, refines the model, gives decision-makers better data for managing water resources, and boosts trust in the model's dependability.

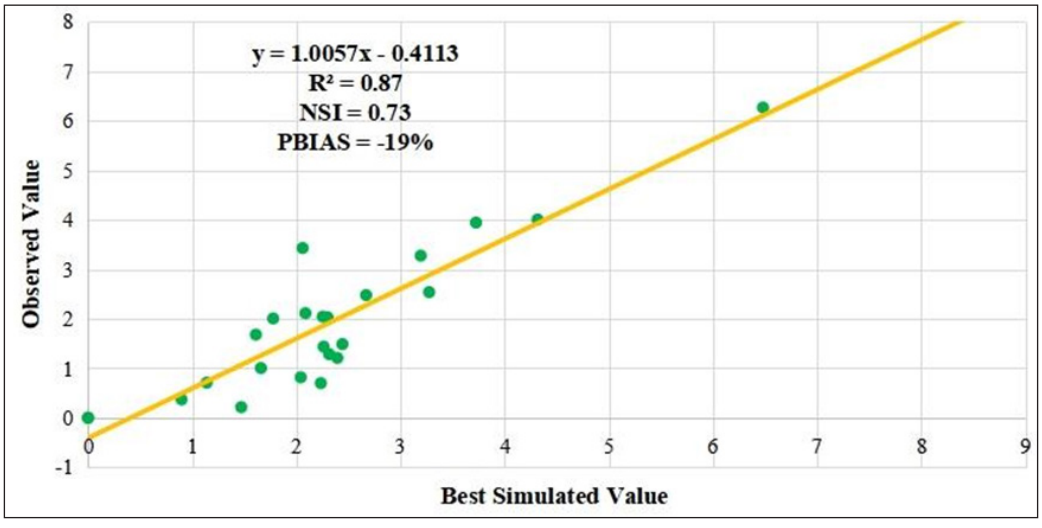

Figure 17. Relationship between simulated and observed discharges during the validation period

Comparison of calibrated and validated stream flows using different land covers for the years 2013, 2015 and 2018.

Figure 18 presents the calibration and validation results for streamflow simulations across three land use and land cover (LULC) years: 2013, 2015, and 2018. Each sub-figure represents stream flow simulation results for a specific LULC year, with the green shaded area showing the 95% uncertainty range, bounded by lower and upper confidence limits. The blue line indicates the observed discharge, representing actual recorded stream flow

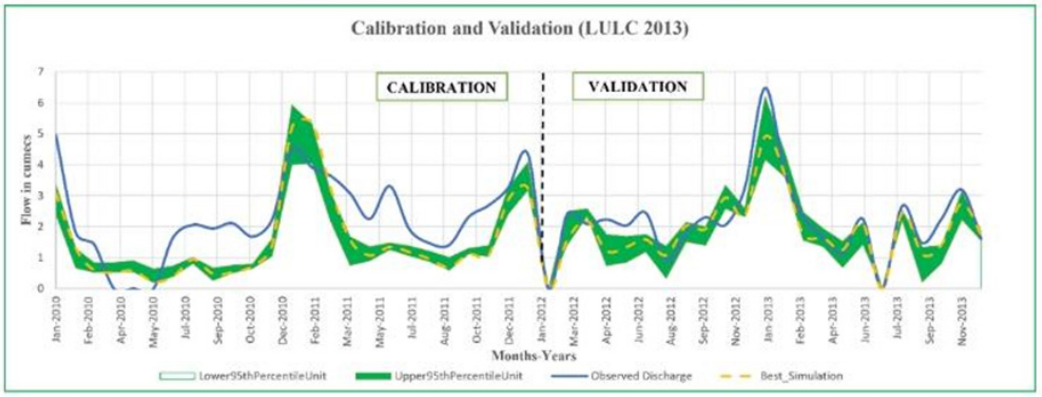

(a)

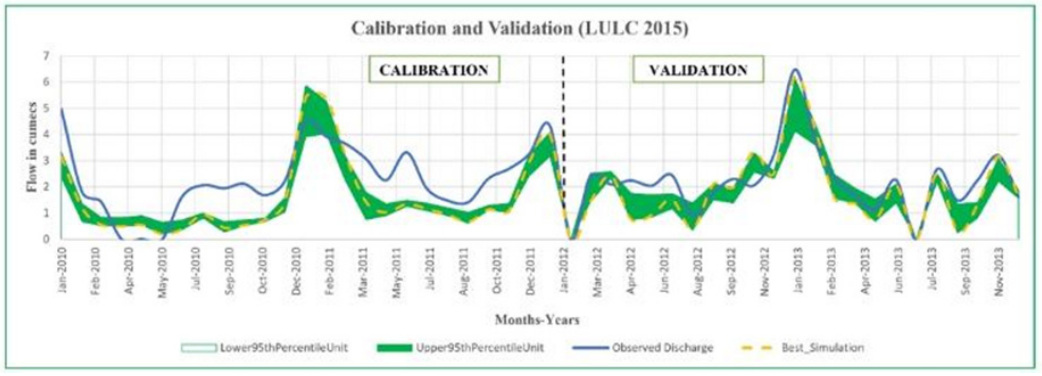

(b)

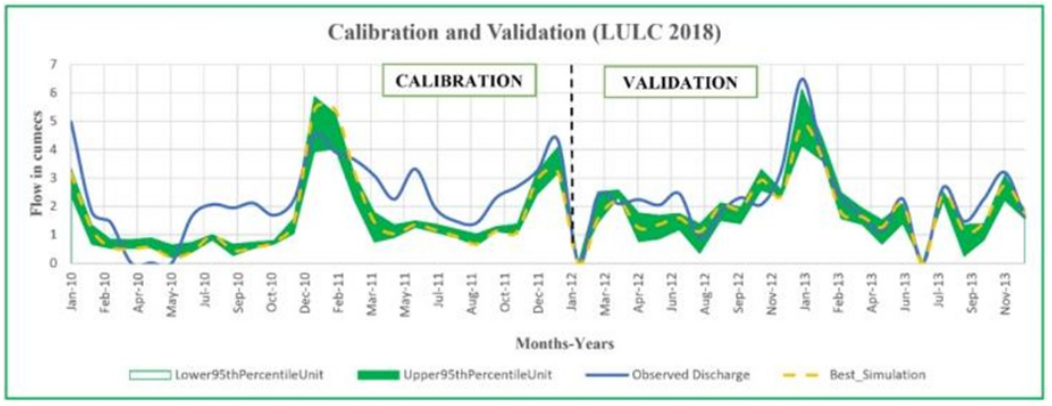

(c)

Figure 18. Calibration and validation of different land covers for the years (a) 2013, (b) 2015, and (c) 2018

data, while the yellow line shows the model's best simulation output. The time series is divided into two main segments: calibration (left of the vertical dashed line) and validation (right of the vertical dashed line). Calibration involves adjusting model parameters to fit observed data, while validation tests the model's performance on separate data to evaluate its predictive capability.

Across all three LULC scenarios, the model demonstrates a reasonable fit to the observed discharge data, with the best simulation line closely following the observed discharge line for both calibration and validation periods. It suggests that the model calibration process was successful for each LULC year, showcasing the ability of the model to simulate stream flow under different land cover conditions. The observed data generally falls within the uncertainty range, indicating that the model captures the variability in stream flow reasonably well. However, some observed peaks and valleys fall outside the uncertainty bounds, suggesting periods of less accurate simulation during high or low flow conditions. Comparing the three LULC years, there is consistency in model performance, though slight differences may reflect the impact of land cover changes on stream flow.

On the other hand, Table 7 shows the statistical measures used to evaluate the accuracy of the calibrated and validated values, including R^2, NSI, and PBIAS. The values obtained for these measures were promising, indicating that the calibrated and validated values were accurate and reliable. Overall, the study suggests that the calibrated and validated values for land use in 2021 were reliable and consistent with the historical trends. It was important for making informed decisions about land use and resource management (Santhi et al., 2001).

Table 8
Values of parameters for different land covers for the years 2013, 2015 and 2018

YEARS	Calibration			Validation		
	R^2	NSI	PBIAS	R^2	NSI	PBIAS
2013	0.63	0.21	–32.1	0.88	0.76	–19
2015	0.63	0.20	–32.1	0.87	0.76	–16.4
2018	0.63	0.20	–32.1	0.89	0.78	–17

CONCLUSION

The study conducted within the Taguibo River Watershed Forest Reserve (TRWFR) in Butuan City, Philippines, highlights the role of hydrological modeling in effectively managing water resources amidst the challenges posed by rapid urban development and climate change and utilizing the Geographic Information System (GIS) and the Soil and Water Assessment Tool (SWAT), the researchers successfully calibrated and validated a hydrological model that demonstrated a strong correlation between simulated and observed discharge data, affirming its effectiveness in simulating watershed hydrology. Key findings

from the study revealed that the watershed, characterized by a predominance of forest land and steep slopes, exhibits significant annual variability in water yield, influenced by precipitation patterns and land use changes. The outputs of the model provide valuable insights into the dynamics of water yield across the sub-basins. The research emphasizes the necessity of integrating advanced modeling tools like SWAT and GIS in water resource assessments, particularly in areas facing environmental pressures. By addressing the interplay between land cover, hydrology, and climate factors, this study contributes to a deeper understanding of watershed dynamics. It offers a foundation for informed decision-making in water resource management and conservation efforts in the Taguibo River Watershed Forest Reserve. The findings encourage continued research and collaboration among stakeholders to enhance water supply management and mitigate the impacts of climate change, ensuring the sustainability of water resources in the future.ng population.

ACKNOWLEDGEMENT

The authors are thankful to the Center for Resource Assessment, Analytics and Emerging Technologies (CReATe), one of the RDI Centers of Caraga State University, through the Water Resource Project team and Taguibo Aquatech Solutions Inc. (TASC) team for providing the data and materials and assisting the researchers during data collection and processing.

REFERENCES

Abbaspour, K. C., Rouholahnejad, E., Vaghefi, S., Sirinivasan, R., Yang, H., & Klove, B. (2015). A continental-scale hydrology and water quality model for Europe: Calibration and uncertainty of a high-resolution large-scale SWAT model. *Journal of Hydrology*, *524,* 733–752. https://doi.org/10.1016/j.jhydrol.2015.03.027

Arnold, J. G., Moriasi, D. N., Gassman, P. W., Abbaspour, K. C., & White, M. J. (2012). SWAT: Model use, calibration, and validation. *Transactions of the ASABE*, *55*(4), 1491-1508.

Arnold, J. G., Srinivasan, R., Muttiah, R. S., & Williams, J. R. (1998). Large area hydrologic modeling and assessment part I: Model development. *Journal of the American Water Resource Association*, *34*(1), 73-89. https://doi.org/10.1111/j.1752-1688.1998.tb05961.x

Ayivi, F., & Jha, M. K. (2018). Estimation of water balance and water yield in the reedy fork-buffalo creek watershed in North Carolina using SWAT. *International Soil and Water Conservation Research, 6*(3), 203-213. https://doi.org/10.1016/j.iswcr.2018.03.007

Bracmort, K. S., Arabi, M., Frankenberger, J. R., Engel, B. A., & Arnold, J. G. (2006). Modelling long-term water quality impact of structural BMPs. *Transactions of the ASABE, 49*(2), 367-374.

Farzana, S. Z., Zafor, M. A., & Shahariar, J. A. (2019). Application of SWAT model for assessing water availability in Surma River Basin. *Journal of the Civil Engineering Forum, 5*(1), 29-38. https://doi.org/10.22146/jcef.39191

Galintao, R. O., & Santillan, M. M. (2020, November 16-19). Using remote sensing and GIS to identify alternative water sources for Butuan City, Philippines. [Paper presentation]. IEEE Region 10 Conference (TENCON), Osaka, Japan. https://doi.org/10.1109/TENCON50793.2020.9293724

Guo, Q., Yu, C., Xu, Y., Yang, Y., & Wang, X. (2023). Impacts of climate and land-use changes on water yields: Similarities and differences among typical watersheds distributed throughout China. *Journal of Hydrology: Regional Studies*, *45,* Article 101294. https://doi.org/10.1016/j.ejrh.2022.101294

Gupta, H. V., Sorooshian, S., & Yapo, P. O. (1999). Status of automatic calibration for hydrologic models: Comparison with multilevel expert calibration. *Journal of Hydrologic Engineering, 4*(2), 135-143. https://doi.org/10.1061/(ASCE)1084-0699(1999)4:2(135)

Khoury, I. A., Boithias, L., & Labat, D. (2023). A review of the application of the soil and water assessment tool (SWAT) in karst watersheds. *Water, 15*(5), Article 954. https://doi.org/10.3390/w15050954.

Kodoatie, R. J., & Sjarief, R. (2010). *Tata ruang air*. Penerbit Andi.

Koltsida, E., Mamassis, N., & Kallioras, A. (2023). Hydrological modeling using the soil and water assessment tool in urban and peri-urban environments: The case of Kifisos experimental subbasin (Athens, Greece). *Hydrology and Eart Science System, 27*(4), 917–931. https://doi.org/10.5194/hess-27-917-2023

Li, X., Sun, W., Zhang, D., Huang, J., Li, D., Ding, N., Zhu, J., Xie, Y., & Wang, X. (2021). Evaluating water provision service at the sub-watershed scale by combining supply, demand, and spatial flow. *Ecological Indicators, 127,* Article 107745. https://doi.org/10.1016/j.ecolind.2021.107745

Moriarty, P., Batchelor, C., & Laban, P. (2005). *Using water resources assessments within the empower planning cycle for IWRM* (Working Paper No. 4). Empowers Partnership. https://www.researchgate.net/publication/265432676_Using_Visions_Scenarios_and_Strategies_within_the_EMPOWERS_Planning_Cycle_for_IWRM

Oda, T., Iwasaki, K., Egusa, T., Kubota, T., Iwagami, S., Iida, S. I., Momiyama, H., & Shimizu, T. (2024). Scale-dependent inter-catchment groundwater flow in forested catchments: Analysis of multi-catchment water balance observations in Japan. *Water Resources Research, 60*(7), Article e2024WR037161. https://doi.org/10.1029/2024WR037161

Refsgaard, J. C., & Storm, B. (1996). Construction, calibration, and validation of hydrological models. In M. B. Abbott & J. C. Refsgaard (Eds.) *Distributed Hydrologic Modeling* (pp. 41–54). Springer. https://doi.org/10.1007/978-94-009-0257-2_3

Saleh, A., Arnold, J. G., Gassman, P. W. A., Hauck, L. M., Rosenthal, W. D., Williams, J. R., & McFarland, A. M. S. (2000). Application of SWAT for the upper North Bosque River watershed. *Transactions of the ASAE, 43*(5), 1077-1087.

Sanguila, M. B., Cobb, K. A., Siler, C. D., Diesmos, A. C., Alcala, A. C., & Brown, R. M. (2016). The amphibians and reptiles of Mindanao Island, southern Philippines, II: The herpetofauna of northeast Mindanao and adjacent islands. *ZooKeys*, *624*, Article 1–132. https://doi.org/10.3897/zookeys.624.9814

Santhi, C., Arnold, J. G., Williams, J. R., Dugas, W. A., Srinivasan, R., & Hauck, L. M. (2001). Validation of the SWAT model on a large river basin with point and nonpoint sources. *JAWRA Journal of the American Water Resources Association, 37(5), 1169-1188*. https://doi.org/10.1111/j.1752-1688.2001.tb03630.x

Santillan, J., Makinano, M., & Paringit, E. (2011). Integrated Landsat image analysis and hydrologic modeling to detect impacts of 25-year land-cover change on surface runoff in a Philippine watershed. *Remote Sensing, 3*(6), 1067-1087. https://doi.org/10.3390/rs3061067

Shivhare, N., Rahul, A. K., Omar, P. J., Chauhan, M. S., Gaur, S., Dikshit, P. K. S., & Dwivedi, S. B. (2018). Identification of critical soil erosion prone areas and prioritization of micro-watersheds using geoinformatics techniques. *Ecological engineering, 121*, 26-34. https://doi.org/10.1016/j.ecoleng.2017.09.004

Young, G. J., Dooge, J. I., & Rodda, J. C. (1994). *Global water resource issues*. Cambridge University Press.

Pertanika J. Sci. & Technol. 33 (S1): 137 - 155 (2025)

PERTANIKA JOURNALS

SCIENCE & TECHNOLOGY

Journal homepage: http://www.pertanika.upm.edu.my/

Development of a Testing Rig for the Ram Pump

Ma. Grace Curay Sumaria[1,2]*, Roberto Carino. Guarte[2], Jaysonh Lua[1] and Marjorie Eralino Timbal[1,2]

[1]Department of Agricultural and Biosystems Engineering, College of Engineering and Technology, Visayas State University, ViSCA, Baybay City, Leyte, Philippines
[2]Renewable Energy Research Center, College of Engineering and Technology, Visayas State University, ViSCA, Baybay City, Leyte, Philippines

ABSTRACT

A testing rig for a hydraulic ram pump (HRP) is crucial as it allows for the precise assessment of pump performance, identification of potential issues, and optimization of design for maximum efficiency and reliability. This study aims to develop a testing rig for HRP and evaluate the technical performance of an HRP prototype using a three-factor factorial experiment in a completely randomized design (CRD) with drive pipe angle, waste valve angle and output pipe sizes as the factors having 27 treatments with three replications each. A testing rig was designed and constructed. It consists of a testing rig frame, water supply tank, water header tank, drive pipe, hydraulic ram pump assembly, and hydraulic ram pump support assembly. The rig was used in the evaluation of an HRP prototype. Results showed that at a combination of 10° drive pipe angle, 34° waste valve angle, and 1.0″[A1] diameter output pipe, the highest mean HRP volumetric efficiency of 92.46 % was obtained with mean output discharge of 6.446 L/min, mean pressure of 55.16 kPa and mean water delivery head/height of 6.31 m. The highest mean output discharge of 15.440 L/min was obtained at treatment combinations of 10° drive pipe angle, 46° waste valve angle and 1.0″ diameter output pipe with mean HRP volumetric efficiency of 55.17%, mean pressure of 62.05 kPa and mean water delivery head of 6.34 m. The highest mean pressure of 68.95 kPa was obtained at the treatment combination of 10° drive pipe angle, 46° waste valve angle, and 0.5″ and 0.75″ diameter output pipes. The developed testing rig for a hydraulic ram pump would help ensure optimal performance, reliability, and efficiency by enabling precise assessment and issue identification.

ARTICLE INFO

Article history:
Received: 8 November 2023
Accepted: 5 November 2024
Published: 31 January 2025

DOI: https://doi.org/10.47836/pjst.33.S1.07

E-mail addresses:
grace.sumaria@vsu.edu.ph (Ma. Grace C. Sumaria)
roberto.guarte@vsu.edu.ph (Roberto C. Guarte)
jaysonhlua@gmail.com (Jaysonh B. Lua)
marjorie.timbal@vsu.edu.ph (Marjorie Eralino Timbal)
*Corresponding author

Keywords: Design and development, hydraulic ram pump, technical performance, testing rig

INTRODUCTION

Effective irrigation and efficient water use are crucial factors in achieving good

ISSN: 0128-7680
e-ISSN: 2231-8526

productivity, profitability, and high economic quality of the agriculture industry. In developing countries, water resources are predominantly rationed and used up in agriculture, particularly irrigation. In the Philippines, irrigation research and development are primarily directed towards large or small-scale pumps and tube well irrigation systems for rice production. There are still limited advancements in farmer-led irrigation development, small-scale irrigation systems, and technologies supporting farming systems in the elevated farmlands of the country. This is contrary to the context that most water resources, such as springs, small-scale diversion dams, micro-irrigation systems, and irrigation distribution systems, such as drip and sprinkler irrigation, are starting to gain traction as an initiative by local farmer groups in highland vegetable farming systems (Sheikh et al., 2014).

Hydraulic Ram Pump

Hydraulic ram pump (HRP) is one of the renewable energy technologies. It has been used to provide water needed for irrigation and domestic purposes, particularly in areas with limited water resources. This mechanical hydro-power device is well established for domestic and farm water pumping at remote sites, with a steady water flow at a low level. The momentum of the stream flow is used to pump some of the water from lower to higher elevations. Due to technological advancement, most technologies rely on sources of power derived from fossil fuels, thus neglecting the HRP (Nederstigt, 2014). Over the last two centuries, the designs of HRP have been stabilized, and many variations of the basic configuration (drive pipe, pump, pump house, and delivery pipe) have been tried. It is clearly a useful way of filling a header tank for piped water, especially in rural areas (Twidell & Weir, 2006). With many HRP designs, it is difficult to establish which is the most efficient and effective. Water flow rate, pipe size, elevations, and ram pump designs are the basic factors that affect the pumping rate of the HRP. This study aims to test and evaluate the efficiency of an HRP prototype to guide users, technologists, and developers interested in using ram pumps for economic development. The study's general objective is to develop a testing rig for HRP. Specifically, this study aims to (1) design and fabricate a testing rig for HRPs and (2) evaluate the performance of an HRP prototype using the testing rig in terms of water output discharge, pressure build-up in the air chamber, height of water discharge/delivery head, and volumetric efficiency as affected by the drive pipe angle, waste valve angle, and output pipe sizes.

METHODOLOGY

Basic Components of the Testing Rig for HRP

The testing rig for HRP is intended to provide a facility in the College of Engineering that could evaluate the technical performance of any HRP under different conditions, including

but not limited to the volume of the water source, elevation of the water header source, size of the drive pipe, angle of inclination of the delivery pipe, design of the HRP, and size of the delivery pipe, among others. The testing rig comprises seven major parts: the water supply tank, testing rig frame, water header tank, drive pipe (input pipe), HRP assembly, HRP support assembly, and the water delivery pipe (output pipe). Figure 1 shows the proposed testing rig with its components.

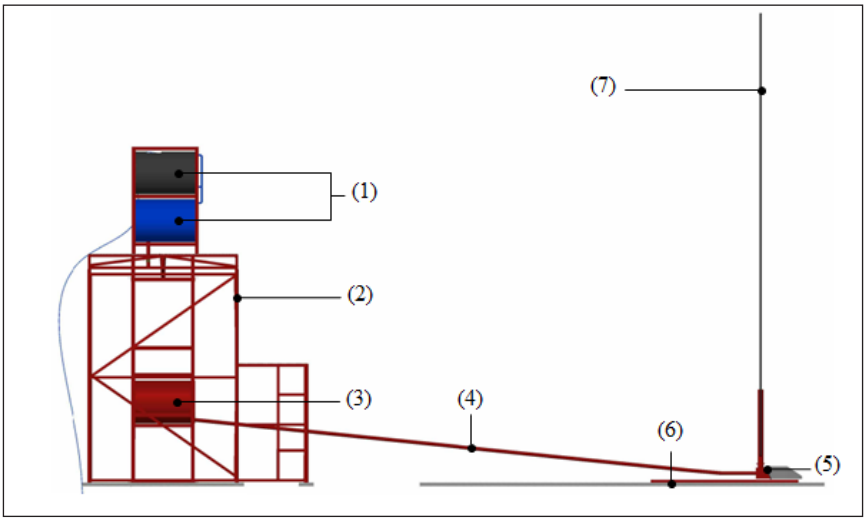

Figure 1. The proposed testing rig for the hydraulic ram pump showing the water supply tank (1), testing rig frame (2), water header tank (3), drive pipe (4), hydraulic ram pump assembly (5), ram pump support assembly (6), and the water delivery pipe (7)

Design and Fabrication of Different Components of the Testing Rig

Testing Rig Frame

The testing rig frame is mainly composed of two parts: the support for the water supply tank and the support for the water header tank. The design of these two main parts of the testing rig frame and the materials used in their fabrication are described below.

Water Supply Tank Support. The water supply tank is constructed on a plain concrete foundation with four main pillars. The pillars are 5.10-cm (2″) diameter G.I. pipe 3.1-m (122″) high and supported by welded 5.10-cm (2″) angle bars. A 16-mm diameter plain round bar flooring is constructed at the top of the pillars.

Water Header Tank Support. The water header tank support is constructed within the pillars. The support is vertically welded and made of 5.10-cm (2″) angle bars forming a rectangular shape. The water header tank can be adjusted to any elevation through a frame

of 5.10-cm (2″) angle bars. The support and the frame are pinned through a 16-mm hole with a 16-mm diameter plain round bar.

Water Supply Tank

The water supply tank is made of two petrol oil barrels that can hold approximately 232 liters of water each. One barrel is placed atop the other with the required metal support of 5.10 cm (2″) angle bars. The top barrel receives water supplied by a 1.27-cm (0.5″) diameter water-blue pipe connected to a constant source through a 2.54-cm (1.0″) diameter hole bored on the top side of the barrel. At the bottom of the top barrel is a hole of 0.5-in in diameter welded to a 0.75-in G.I. pipe that channels the water directly to the second barrel. Like the top barrel, the water header tank is the water that receives water supplied by a 5.10-cm (2″) diameter G.I. pipe connected on the bottom side of the second barrel. The water supplied to the water header tank is controlled by a gate valve.

Water Header Tank

The water header tank is made of one petrol oil barrel, similar to the water supply tank arrangement. The barrel is cut fully open at the top side and placed below the second barrel with the required metal support frame made of 2″ (5.10 cm) angle bars. It receives the water supplied by a 2″ (5.10 cm) diameter G.I. pipe connected from the second barrel above.

Drive Pipe

The drive pipe is directly connected at the bottom of the water header tank. It is made of 2″ (5.10 cm) diameter and 8 meters long G.I. pipe. The length of the drive pipe was computed using the formula:

$$150 < L/D < 1000$$

Using a 2″ or 5.08 cm Ø drive pipe,

$150 < L/D$	$1000 > L/D$
$150(5.08\text{ cm}) < L$	$1000(5.08\text{ cm}) > L$
$L > 762$ cm or 7.62 meters	$L < 5080$ cm or 50.80 meters

Thus, for a 2″ (5.10-cm) diameter G.I. pipe, a drive pipe greater than 7.62 meters and shorter than 50.80 meters should be used. It is connected to the HRP through an angled 2″ (5.10-cm) diameter G.I. pipe and G.I. union.

The Hydraulic Ram Pump Assembly

An HRP is composed of eight parts: (1) the drive pipe, (2) the HRP body, (3) the waste valve, (4) the check valve (delivery valve), (5) the air chamber, (6) snifter, (7) water delivery

pipe, and (8) the wastewater catcher. The source water is directed to the pump through the drive pipe. When water enters the HRP, the waste valve closes due to pressure, which creates high pressure in the HRP body. This high pressure opens the check valve, and water rushes to the air chamber. It compresses the air inside the chamber, and the compressed air forces the water downward, causing the check valve to close. Then, water in the air chamber is diverted to the delivery pipe. The pressure in the HRP body drops and opens the waste valve, allowing water to flow outside. The cycle repeats, and the HRP operates continuously. Design considerations of different components of the HRP and the material used in their fabrication are described below.

HRP Body

The whole HRP body is made up of 1/4″ (0.635 cm) thick stainless-steel plates. It is rectangular in shape with an inclined frontal face. The walls of the HRP body are fully welded with each other, and a flange in the front is made for the waste valve. A 3″ (7.65-cm) diameter hole is made at the upper side of the HRP body, and a 5-cm long and 3″ (7.65-cm) diameter G.I. pipe is connected and welded fully. A flange is also connected to the upper edge of the 3″ diameter G.I. pipe.

Waste Valve

The waste valve comprises welded 1/4″ (0.635-cm) thick stainless-steel plates and is fabricated with a rectangular flange. The cross-sectional area of the waste valve opening is 24.93 cm^2. The swing valve or door is attached to a fixed fabricated door hinged to swing in an inward direction. A bolt is fitted at the middle of the swinging valve to hold the rubber gasket attached to the front side of the swing valve together with the additional weight for the swing valve. The edges of the opening, which the swing valve closes, are sealed with a rubber gasket. A stopper is made inside the HRP body to prevent the swing valve from totally opening and to adjust the opening of the swing valve. It is made up of a horizontal stainless steel welded in two 1/4″ x 2 1/2″ stainless steel bolts. It is bolted beside the opening of the waste valve for easy adjustments. The swing valve is attached to the rectangular flange, which is removable and sealed with a rubber gasket to prevent leakage. The rubber gasket and flange are fastened by 3/8″ x 1″ bolts in the HRP body. The rectangular flange will be removed when adjustments to the ram body are made.

Check Valve

The check valve is made of a 1/4″ (0.635 cm) thick circular steel plate welded at the top of the HRP body. The steel plate is bored with eight holes, each 10 mm in diameter. The total cross-sectional area of the holes is equivalent to the cross-sectional area of the drive

pipe. The moving part of the check valve uses circular rubber from used car tires, adopting the design from the AIDFI and adding a washer that presses the car tire rubber, following the mechanism of Watt's design.

Air Chamber

The air chamber is made up of a 3″ (7.65 cm) diameter and 1-m long G.I. pipe. A flange is made at the end of the pipe, and eight holes are bored for bolt fitting in connecting to the HRP body. The other end of the chamber is closed by a welded steel plate. A rubber gasket is used between flanges to prevent leakage. A 1″ (2.55 cm) hole is bored outside the air chamber and connected with a G.I. nipple 3″ (7.65 cm) long. It is connected to the delivery pipe. A pressure gauge is installed at the top side of the air chamber through a bored hole connected with a 12-mm diameter pipe.

Delivery Pipe

The delivery pipe is made of a G.I. pipe. It is parallel to the air chamber and connected to the bottom side through an elbow. The elbow facilitates the water coming out of the delivery pipe.

Snifter

The snifter is a small hole less than 1 mm in the HRP body. It is bored 2 cm below the check valve on the left side of the cylinder.

Wastewater Catcher

The wastewater catcher is made of stainless steel and designed to catch wastewater coming out of the check valve.

HRP Support Assembly

The HRP support assembly is made of plain concrete. It includes a welded HRP holder that is 2.44 m long and made of 1″ (2.55 cm) angle bars and a 16-mm diameter plain round bar. The holder is fastened in the assembly to hold the ram pump.

Technical Performance Evaluation of the Fabricated HRP

A preliminary evaluation of the fabricated HRP was done to determine whether it meets the standard and considerations intended for the study. It was also a way to identify issues that still needed improvement. The final evaluation of the system was implemented after a series of improvements involving precise data gathering and analysis.

Experimental Design and Treatments

In order to achieve the objectives of the study, the technical performance of the HRP was evaluated using a three-factor-factorial experiment in a completely randomized design (CRD) with the angle of elevation of the drive pipe or drive head (H), angle of inclination of the waste valve or waste valve clearance (Θ_w) and delivery pipe size diameter (Ø) as the factors (variables). Each factor comprised three treatments, which were replicated thrice. So, there were 3x3x3 = 27 treatment combinations ($T_1 – T_{27}$; Table 1). Three treatments for the angles of elevation of the drive pipe used were $H_1 = 5°$, $H_2 = 10°$, and $H_3 = 15°$. The treatments for the angles of elevation of the drive pipe were: $\Theta_{w1} = 34°$, $\Theta_{w2} = 46°$, and $\Theta_{w3} = 59°$. The treatments for delivery pipe diameter sizes were: $Ø_1 = 1″$, $Ø_2 = 3/4″$, and $Ø_3 = ½″$.

Table 1
Variables evaluated in each treatment

Treatment Combination	Variable		
	The angle of Elevation of Drive Head (H)	Angle of Inclination of the Waste Valve (Θ_w)	Delivery Pipe Diameter Size (Ø)
T_1	5°	34°	1/2″
T_2	5°	34°	3/4″
T_3	5°	34°	1″
T_4	5°	46°	1/2″
T_5	5°	46°	3/4″
T_6	5°	46°	1″
T_7	5°	59°	1/2″
T_8	5°	59°	3/4″
T_9	5°	59°	1″
T_{10}	10°	34°	1/2″
T_{11}	10°	34°	3/4″
T_{12}	10°	34°	1″
T_{13}	10°	46°	1/2″
T_{14}	10°	46°	3/4″
T_{15}	10°	46°	1″
T_{16}	10°	59°	1/2″
T_{17}	10°	59°	3/4″
T_{18}	10°	59°	1″
T_{19}	15°	34°	1/2″
T_{20}	15°	34°	3/4″
T_{21}	15°	34°	1″
T_{22}	15°	46°	1/2″
T_{23}	15°	46°	3/4″
T_{24}	15°	46°	1″
T_{25}	15°	59°	1/2″
T_{26}	15°	59°	3/4″
T_{27}	15°	59°	1″

Data Collection

Pressure

Pressure is determined by reading a pressure gauge connected to the air chamber.

Delivery Water Discharge (Q)

The water discharged by the delivery pipe is determined by a volumetric method using a bucket. An elbow is inserted at the tip of the delivery pipe to direct the flow to the bucket. The water discharge is measured in volume per unit time (liters per minute).

Height of Water in each Pump

The height of water delivered by the HRP (delivery head) through the delivery pipe for each treatment/treatment combination was determined using the same pipe without the elbow at the tip. A measuring tape was installed at the tip of the delivery pipe to determine the height of the pump.

Ram Pump Efficiency

Four variables measured in the HRP efficiency (%) computation are mentioned below.

Height of Source or Drive Head (H)

Three heights are established based on the angle of elevation of the header tank. These were measured from the waste valve to the header tank.

Height of Delivery Water Discharge or Delivery Head (h)

The height of the delivery pipe was measured from the header tank to the tip of the delivery pipe.

Waste Valve Water Discharge (Q_w)

The flow rate of the water discharged by the waste valve or the wastewater is measured using the volumetric method. The bucket was placed at the tip of the wastewater catcher to measure the wastewater. It was expressed in volume per unit time (liters per minute).

Statistical Analysis

The effect of the drive head, waste valve clearance, and the diameter of the delivery pipe on the discharge and efficiency of the pump were analyzed using analysis of variance (ANOVA) for a three-factor factorial experiment in a completely randomized design. Treatment means were compared using Tukey's Honestly Significant Difference (HSD)

method whenever the null hypothesis on the equality of treatment mean was rejected at a 5% level of significance.

RESULTS AND DISCUSSION

Technical Performance of HRP

Figure 2 shows the completed and functional Testing Rig with its components. The technical performance of the HRP prototype using the Testing Rig was evaluated following a 3 x 3 x 3 factor-factorial experiment in a Completely Randomized Design (CRD) with the angle of elevation of the drive pipe, angle of inclination of the waste valve, and delivery pipe size/diameter. These three variables/factors were evaluated for their effect on the water output discharge, Q; the water height at the delivery pipes, H); and pressure developed inside the air chamber, P. The results of the technical evaluation are presented in the following sections.

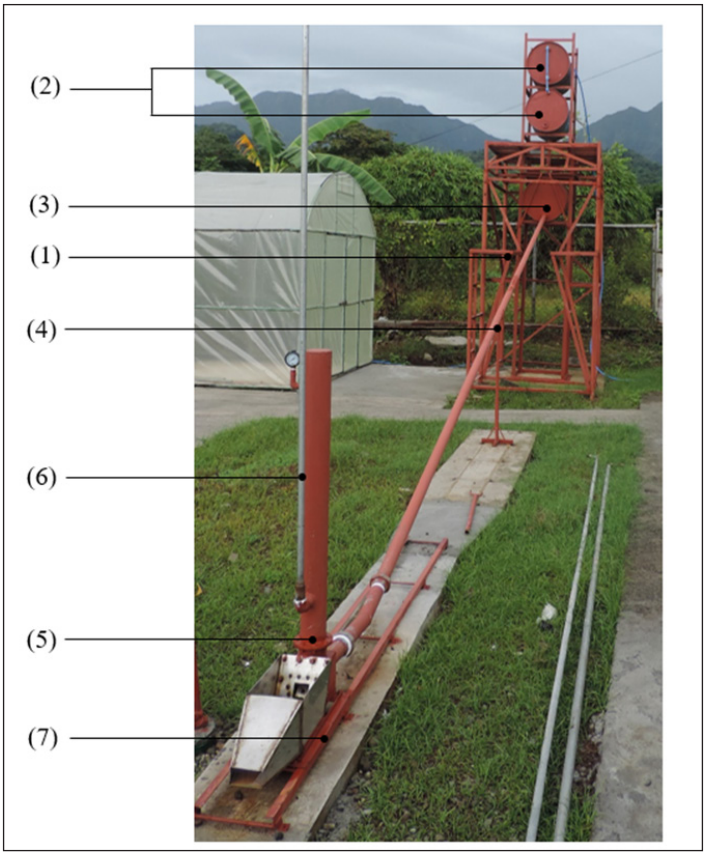

Figure 2. The components of the constructed testing rig for the hydraulic ram pump: (1) testing rig frame, (2) water supply tank, (3) water header tank, (4) drive pipe, (5) hydraulic ram pump, (6) delivery pipe, and (7) HRP support assembly

Water Output Discharge

The raw data on the water output discharge of the HRP as affected by the different factors are presented in Table 2. The HRP had the highest water output discharge when operated at T_{15} (H = 10°, Θ_w = 46°, Ø = 1″) with a mean output discharge of 15.440 L/min and lowest at T_{19} (H = 15°, Θ_w = 34°, Ø = 1/2″) with a mean output discharge of 2.101 L/min. Table 3 contains ANOVA results on the three factors affecting the water output discharge.

Table 2
Water output discharge (L/min) at each treatment combination in three replications

Treatment (H, Θ_w, Ø)	**Replication**			**Mean**
	1	**2**	**3**	
T_1 (5°, 34°, 1/2″)	0	0	0	0
T_2 (5°, 34°, 3/4″)	0	0	0	0
T_3 (5°, 34°, 1″)	0	0	0	0
T_4 (5°, 46°, 1/2″)	7.84	8.43	8.04	8.10
T_5 (5°, 46°,3/4″)	8.24	8.02	8.81	8.36
T_6 (5°,46°,1″)	7.16	8.08	7.07	7.44
T_7 (5°, 59°, 1/2″)	7.58	7.00	6.87	7.15
T_8 (5°, 59°, 3/4″)	7.40	7.05	7.18	7.21
T_9 (5°, 59°, 1″)	6.72	6.90	6.70	6.77
T_{10} (10°, 34°, 1/2″)	6.04	5.56	5.74	5.78
T_{11} (10°, 34°, 3/4″)	5.72	6.00	6.02	5.91
T_{12} (10°, 34°, 1″)	6.40	6.38	6.56	6.45
T_{13} (10°, 46°, 1/2″)	14.62	14.31	14.87	14.60
T_{14} (10°, 46°, 3/4″)	14.64	13.80	14.84	14.43
T_{15} (10°, 46°, 1″)	15.29	15.63	15.40	15.44
T_{16} (10°, 59°, 1/2″)	0	0	0	0
T_{17} (10°, 59°, 3/4″)	0	0	0	0
T_{18} (10°, 59°, 1″)	0	0	0	0
T_{19} (15°, 34°, 1/2″)	2.15	1.86	2.29	2.10
T_{20} (15°, 34°, 3/4″)	2.22	2.24	2.13	2.20
T_{21} (15°, 34°, 1″)	2.39	2.96	2.28	2.54
T_{22} (15°, 46°, 1/2″)	0	0	0	0
T_{23} (15°, 46°, 3/4″)	0	0	0	0
T_{24} (15°, 46°, 1″)	0	0	0	0
T_{25} (15°, 59°, 1/2″)	0	0	0	0
T_{26} (15°, 59°, 3/4″)	0	0	0	0
T_{27} (15°, 59°, 1″)	0	0	0	0

Note : A 0 value means the HRP is not operating
H : Drive pipe angle or angle of elevation of the drive pipe
Θ_w : Waste valve angle or angle of inclination of the waste valve
Ø : Delivery or output pipe diameter size

Table 3
Analysis of variance (ANOVA) on the water output discharge (L/min) of the hydraulic ram pump as affected by drive pipe angle, waste valve angle, and output pipe size for three replications

Source of Variation	Degrees of Freedom	Sum of Squares	Mean Square	F Statistic Value	p-value
Drive Pipe Angle (A)	2	541.82	270.91	5044.06***	0.00
Waste Valve Angle (B)	2	458.67	229.34	4269.96***	0.00
Output Pipe Size (C)	2	0.14	0.07	1.29^{ns}	0.28
A x B	4	914.03	228.51	4254.52***	0.00
A x C	4	2.53	0.63	11.79***	0.00
B x C	4	0.67	0.17	3.14*	0.02
A x B x C	8	1.18	0.15	2.74**	0.01
Error	54	2.90	0.05		
Total	80	1921.94			

ns - not significant; * - significant; ** - highly significant; *** - very highly significant

The analysis of variance indicates that the interaction among drive pipe angle, waste valve angle, and output pipe size has a highly significant effect on the water output discharge. However, the interaction effect between drive pipe angle and waste valve angle contributes the most to the differences in water output discharge, accounting for almost 48% of the total variation. Table 4 presents the results of the comparison of the treatments with nonzero water output discharge.

Table 4
Comparison of the mean water output discharge at different combinations of (A) drive pipe angle, (B) waste valve angle, and (C) output pipe size

Treatment (A,B,C)	Mean	Treatment (A,B,C)	Mean	Treatment (A,B,C)	Mean
T_{15} (10°, 46°, 1″)	15.44^{a}	T_{6} (5°, 46°, 1″)	7.44^{cde}	T_{11} (10°, 34°, 3/4″)	5.91^{gh}
T_{13} (10°, 46°, 1/2″)	14.60^{ab}	T_{8} (5°, 59°, 3/4″)	7.21^{def}	T_{10} (10°, 34°, 1/2″)	5.78^{h}
T_{14} (10°, 46°, 3/4″)	14.43^{b}	T_{7} (5°, 59°, 1/2″)	7.15^{ef}	T_{21} (15°, 34°, 1″)	2.54^{i}
T_{5} (5°, 46°, 3/4″)	8.36^{c}	T_{9} (5°, 59°, 1″)	6.77^{efg}	T_{20} (15°, 34°, 3/4″)	2.20^{i}
T_{4} (5°, 46°, 1/2″)	8.10^{cd}	T_{12} (10°, 34°, 1″)	6.45^{fgh}	T_{19} (15°, 34°, 1/2″)	2.10^{i}

*Means with the same letters are not significantly different at the 5% level of significance using Tukey's Honestly Significant Difference (HSD) Method

Results of Tukey's test (Table 4) show that treatments T_{15}, T_{13}, and T_{14} produced output discharge of 15.44, 14.60, and 14.43 L/min, respectively. The three lowest water output discharges come from T_{21}, T_{20}, and T_{19} at 2.54, 2.20, and 2.10 L/min, respectively. The interaction effect between drive pipe angle and waste valve angle using an output pipe of 1″ diameter is compared in Figure 3. The waste valve angle of 46°, 50°, and 34° provided the highest water output discharge at the 10°, 5°, and 10° drive pipe angle, respectively. However, the 34° waste valve angle produced the same amount of water output discharge at the 15° drive pipe angle, unlike the 46° and 59° waste valve angles.

The interaction effect between the drive pipe angle and waste valve angle using an output pipe of 3/4″ diameter is presented in Figure 4. The waste valve angles of 46°, 59°, and 34° provided the highest water output discharge at 10°, 5°, and 10° drive pipe angles, respectively. However, the 34° waste valve angle produced the same amount of water output discharge at the 15° drive pipe angle, unlike the 46° and 59° waste valve angles. This result is the same as obtained with the 1″ diameter output pipe.

Figure 5 illustrates the interaction effect between the drive pipe angle and waste valve angle using an output pipe of 1/2″ diameter. Again, the 46° waste valve angle delivered the highest water output discharge at the 10° drive pipe angle, similar to its behavior in the larger diameters. The 59° and 34° waste valve angles also remained consistent in their water output discharge at the different angles of elevation of the drive pipe.

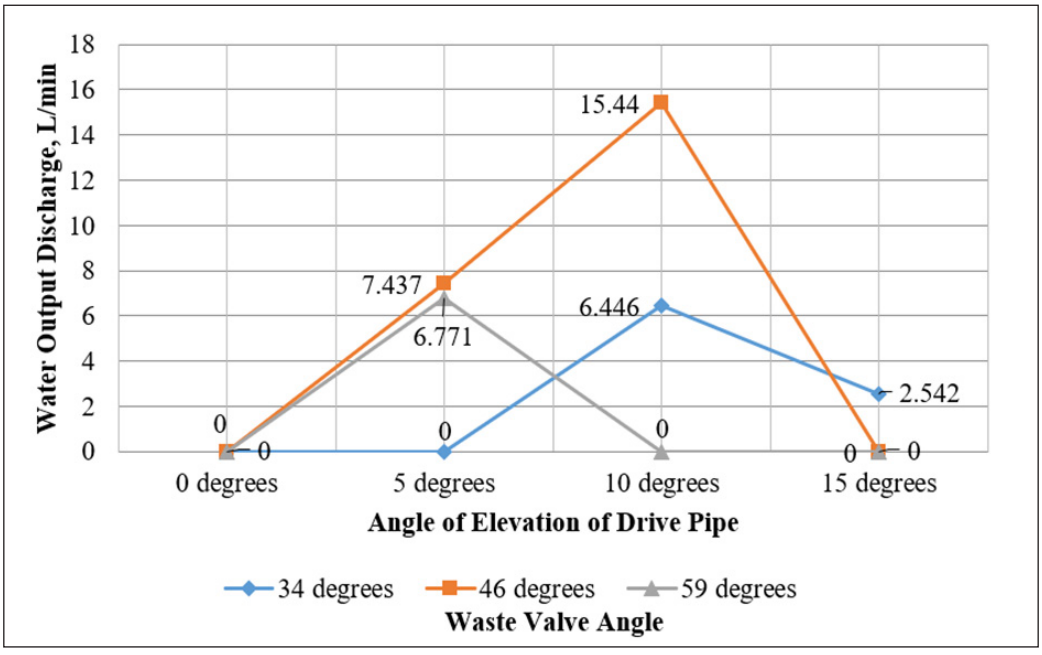

Figure 3. Water output discharge (L/min) of HRP as affected by drive pipe angle and waste valve angle using an output pipe of 1″ diameter

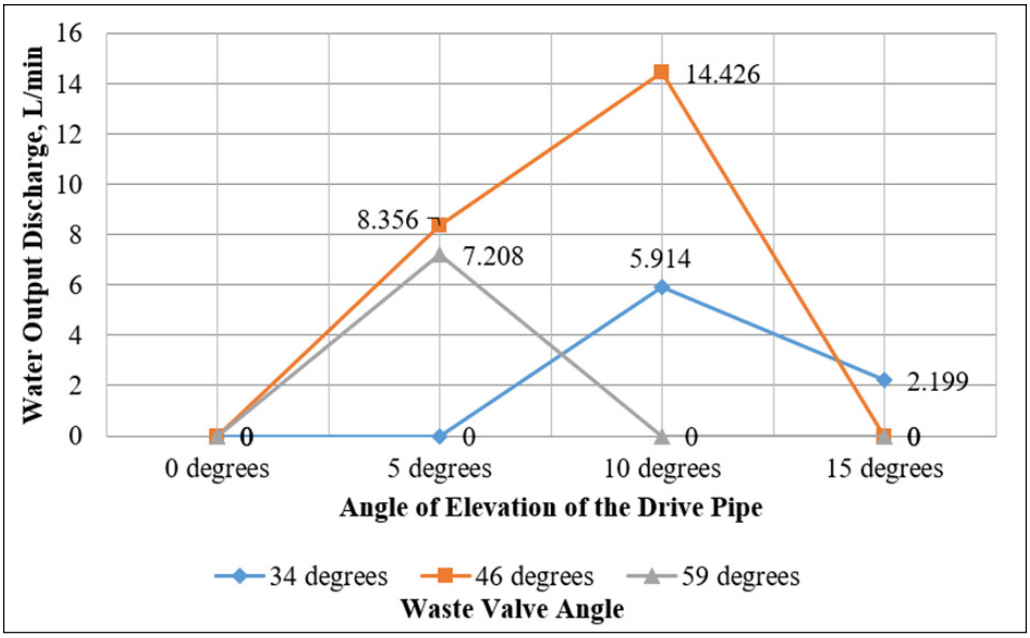

Figure 4. Water output discharge (L/min) of HRP as affected by drive pipe angle and waste valve angle using output pipe of 3/4″ diameter

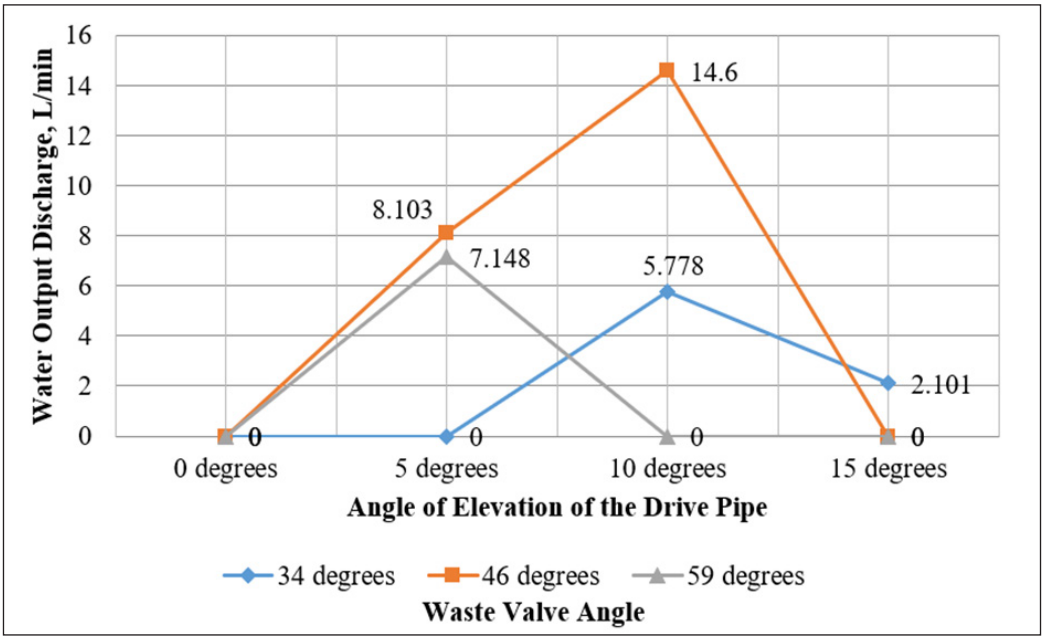

Figure 5. Water output discharge (L/min) of HRP as affected by drive pipe angle and waste valve angle using output pipe of 1/2″ diameter

Height of the Water Discharge

The data on the height of the water discharge of the HRP as affected by the different factors are presented in Table 5. The highest height was 6.38 m for T_{13} (H = 10°, Θ_w = 46°, Ø = 1/2″) and the lowest was 6.31 m for T_{11} (H = 10°, Θ_w = 34°, Ø = 3/4″) and T_{12} (H = 10°, Θ_w = 34°, Ø = 3/4″). Table 6 compares the ANOVA on the water discharge height affected by the three factors.

Table 5
Height (m) of water discharge at each treatment combination in three replications

Treatment (H, Θ_w, Ø)	Replication			Mean
	1	2	3	
T_1 (5°, 34°, 1/2″)	0	0	0	0
T_2 (5°, 34°, 3/4″)	0	0	0	0
T_3 (5°, 34°, 1″)	0	0	0	0
T_4 (5°, 46°, 1/2″)	7.84	8.43	8.04	8.10
T_5 (5°, 46°,3/4″)	8.24	8.02	8.81	8.36
T_6 (5°,46°,1″)	7.16	8.08	7.07	7.44
T_7 (5°, 59°, 1/2″)	7.58	7.00	6.87	7.15
T_8 (5°, 59°, 3/4″)	7.40	7.05	7.18	7.21
T_9 (5°, 59°, 1″)	6.72	6.90	6.70	6.77
T_{10} (10°, 34°, 1/2″)	6.04	5.56	5.74	5.78
T_{11} (10°, 34°, 3/4″)	5.72	6.00	6.02	5.91
T_{12} (10°, 34°, 1″)	6.40	6.38	6.56	6.45
T_{13} (10°, 46°, 1/2″)	14.62	14.31	14.87	14.60
T_{14} (10°, 46°, 3/4″)	14.64	13.80	14.84	14.43
T_{15} (10°, 46°, 1″)	15.29	15.63	15.40	15.44
T_{16} (10°, 59°, 1/2″)	0	0	0	0
T_{17} (10°, 59°, 3/4″)	0	0	0	0
T_{18} (10°, 59°, 1″)	0	0	0	0
T_{19} (15°, 34°, 1/2″)	2.15	1.86	2.29	2.10
T_{20} (15°, 34°, 3/4″)	2.22	2.24	2.13	2.20
T_{21} (15°, 34°, 1″)	2.39	2.96	2.28	2.54
T_{22} (15°, 46°, 1/2″)	0	0	0	0
T_{23} (15°, 46°, 3/4″)	0	0	0	0
T_{24} (15°, 46°, 1″)	0	0	0	0
T_{25} (15°, 59°, 1/2″)	0	0	0	0
T_{26} (15°, 59°, 3/4″)	0	0	0	0
T_{27} (15°, 59°, 1″)	0	0	0	0

Note : A 0 value means the HRP is not operating
H : Drive pipe angle or angle of elevation of the drive pipe
Θ_w : Waste valve angle or angle of inclination of the waste valve
Ø : Delivery or output pipe diameter size

Table 6
Analysis of variance (ANOVA) on the height (m) of the water discharge of the hydraulic ram pump as affected by drive pipe angle, waste valve angle, and output pipe size for three replications

Source of Variation	Degrees of Freedom	Sum of Squares	Mean Square	F Statistic Value	p-value
Drive Pipe Angle (A)	2	80.62	40.31	4081254.88***	0.00
Waste Valve Angle (B)	2	79.57	39.78	4027974.13***	0.00
Output Pipe Size (C)	2	0.001	0.000	39.13***	0.00
A x B	4	643.46	160.87	16287631.63***	0.00
A x C	4	0.001	0.000	34.48***	0.00
B x C	4	0.003	0.001	65.75***	0.00
A x B x C	8	0.002	0.000	24.50***	0.00
Error	54	0.001	9.87E-6		
Total	80	803.65			

*** - very highly significant

The ANOVA indicates that the interaction among the drive pipe angle, waste valve angle, and output pipe size has a highly significant effect on the height of water discharge. However, the interaction effect between drive pipe angle and waste valve angle has the highest contribution to the differences in water discharge height. It accounts for 80.07% of the variation in water discharge height. Results of the comparison of the treatments with nonzero height of water discharge are presented in Table 7.

Table 7
Comparison of the mean height (m) of water discharge at different combinations of drive pipe angle (A), waste valve angle (B), and output pipe size (C)

Treatment (A,B,C)	Mean	Treatment (A,B,C)	Mean	Treatment (A,B,C)	Mean
T_{13} (10°, 46°, 1/2″)	6.3867^{a}	T_{4} (5°, 46°, 1/2″)	6.3433^{bc}	T_{5} (5°, 46°, 3/4″)	6.3300^{de}
T_{9} (5°, 59°, 1″)	6.3800^{a}	T_{15} (10°, 46°, 1″)	6.3400^{bcd}	T_{10} (10°, 34°, 1/2″)	6.3200^{ef}
T_{8} (5°, 59°, 3/4″)	6.3500^{b}	T_{20} (15°, 34°, 3/4″)	6.3333^{cd}	T_{6} (5°, 46°, 1″)	6.3200^{ef}
T_{7} (5°, 59°, 1/2″)	6.3500^{b}	T_{19} (15°, 34°, 1/2″)	6.3333^{cd}	T_{12} (10°, 34°, 1″)	6.3100^{f}
T_{14} (10°, 46°, 3/4″)	6.3467^{b}	T_{21} (15°, 34°, 1″)	6.3300^{de}	T_{11} (10°, 34°, 3/4″)	6.3100^{f}

*Means with the same letters are not significantly different at the 5% level of significance.

The results of Tukey's test (Table 7) show that treatment combinations T_{13} and T_9 produced the two highest heights, 6.3867 m and 6.38 m, respectively. The second three highest heights were 6.35 m, 6.35 m and 6.3467 m for T_8, T_7, and T_{14}, respectively. The shortest heights were 6.32 m, 6.32 m, 6.31 m, and 6.31 m, produced by T_{10}, T_6, T_{12}, and T_{11}, respectively.

The Pressure Developed Inside the Air Chamber

Table 8 presents the pressures developed inside the HRP's air chamber as affected by the different factors. The highest pressure of 68.95 kPa was recorded for T_6, T_7, T_8, T_9, T_{13}, and T_{14}, while the lowest pressure of 51.71 kPa was produced for T_{19}.

Table 8
Pressure (kPa) in the air chamber of the hydraulic ram pump at each treatment combination in three replications

Treatment (H, Θ_w, Ø)	**Replication**			**Mean**
	1	**2**	**3**	
T_1 (5°, 34°, 1/2″)	0	0	0	0
T_2 (5°, 34°, 3/4″)	0	0	0	0
T_3 (5°, 34°, 1″)	0	0	0	0
T_4 (5°, 46°, 1/2″)	65.50	65.50	65.50	65.50
T_5 (5°, 46°,3/4″)	62.05	62.05	62.05	62.05
T_6 (5°,46°,1″)	68.95	68.95	68.95	68.95
T_7 (5°, 59°, 1/2″)	68.95	68.95	68.95	68.95
T_8 (5°, 59°, 3/4″)	68.95	68.95	68.95	68.95
T_9 (5°, 59°, 1″)	68.95	68.95	68.95	68.95
T_{10} (10°, 34°, 1/2″)	60.33	60.33	60.33	60.33
T_{11} (10°, 34°, 3/4″)	60.33	60.33	60.33	60.33
T_{12} (10°, 34°, 1″)	55.16	55.16	55.16	55.16
T_{13} (10°, 46°, 1/2″)	68.95	68.95	68.95	68.95
T_{14} (10°, 46°, 3/4″)	68.95	68.95	68.95	68.95
T_{15} (10°, 46°, 1″)	62.05	62.05	62.05	62.05
T_{16} (10°, 59°, 1/2″)	0	0	0	0
T_{17} (10°, 59°, 3/4″)	0	0	0	0
T_{18} (10°, 59°, 1″)	0	0	0	0
T_{19} (15°, 34°, 1/2″)	51.71	51.71	51.71	51.71
T_{20} (15°, 34°, 3/4″)	60.33	60.33	60.33	60.33
T_{21} (15°, 34°, 1″)	60.33	60.33	60.33	60.33
T_{22} (15°, 46°, 1/2″)	0	0	0	0
T_{23} (15°, 46°, 3/4″)	0	0	0	0
T_{24} (15°, 46°, 1″)	0	0	0	0

Table 8 (*continue*)

Treatment (H, Θ_w, Ø)	Replication			Mean
	1	2	3	
T_{25} (15°, 59°, 1/2″)	0	0	0	0
T_{26} (15°, 59°, 3/4″)	0	0	0	0
T_{27} (15°, 59°, 1″)	0	0	0	0

Note: A 0 value means the HRP is not operating
H: Drive pipe angle or angle of elevation of the drive pipe
Θ_w: Waste valve angle or angle of inclination of the waste valve
Ø: Delivery or output pipe diameter size

Table 9 gives the ANOVA for the pressure build-up in the air chamber. It indicates that the interaction between drive pipe angle, waste valve angle, and output pipe size has a highly significant effect on pressure. However, the interaction effect between the drive pipe angle and waste valve angle is the most important, as it can explain 78.66% of the variation in the pressure readings.

Table 9
Analysis of variance (ANOVA) for the pressure in the air chamber (kPa) of the hydraulic ram pump as affected by drive pipe angle, waste valve angle, and output pipe size for three replications

Source of Variation	Degrees of Freedom	Sum of Squares	Mean Square	F Statistic Value	p-value
Drive Pipe Angle (A)	2	10609.33	5304.665	2.441E + 29***	0.00
Waste Valve Angle (B)	2	6472.69	3236.34	1.49 E + 29***	0.00
Output Pipe Size (C)	2	5.94	2.97	1.37E + 26***	0.00
A x B	4	64328.67	16082.17	7.40E + 29***	0.00
A x C	4	164.52	41.13	1.89E + 27***	0.00
B x C	4	39.64	9.91	4.56E + 26***	0.00
A x B x C	8	158.60	19.83	9.12E + 26***	0.00
Error	54	1.17E-24	2.17E-26		
Total	80	81779.39			

*** - very highly significant

Hrp Volumetric Efficiency

Table 10 presents the HRP's volumetric efficiencies as affected by the different factors. The combination of 10° drive pipe angle and 34° waste valve angle using 1″ diameter output pipe produced the highest HRP volumetric efficiency of 92.46%, while the combination of 15° drive pipe angle and 34° waste valve angle using 1″ diameter output pipe gave the lowest HRP volumetric efficiency of 45.63%.

Table 10
Volumetric efficiency of the Hydraulic Ram Pump (HRP) at each treatment combination in three replications

Treatment (H, Θ_w, Ø)	Replication			Mean
	1	2	3	
T_1 (5°, 34°, 1/2″)	0	0	0	0
T_2 (5°, 34°, 3/4″)	0	0	0	0
T_3 (5°, 34°, 1″)	0	0	0	0
T_4 (5°, 46°, 1/2″)	92.23	90.48	89.06	92.23
T_5 (5°, 46°,3/4″)	84.91	92.73	89.28	84.91
T_6 (5°,46°,1″)	87.78	79.55	82.38	87.78
T_7 (5°, 59°, 1/2″)	57.37	56.93	58.73	57.37
T_8 (5°, 59°, 3/4″)	59.36	60.39	60.27	59.36
T_9 (5°, 59°, 1″)	57.08	54.72	55.94	57.08
T_{10} (10°, 34°, 1/2″)	64.86	69.88	69.21	64.86
T_{11} (10°, 34°, 3/4″)	72.07	68.33	69.93	72.07
T_{12} (10°, 34°, 1″)	92.58	95.56	92.46	92.58
T_{13} (10°, 46°, 1/2″)	60.14	63.75	61.77	60.14
T_{14} (10°, 46°, 3/4″)	53.21	56.44	55.16	53.21
T_{15} (10°, 46°, 1″)	56.08	54.49	55.17	56.08
T_{16} (10°, 59°, 1/2″)	0	0	0	0
T_{17} (10°, 59°, 3/4″)	0	0	0	0
T_{18} (10°, 59°, 1″)	0	0	0	0
T_{19} (15°, 34°, 1/2″)	43.40	50.52	46.84	43.40
T_{20} (15°, 34°, 3/4″)	59.46	52.91	55.43	59.46
T_{21} (15°, 34°, 1″)	49.71	41.87	45.63	49.71
T_{22} (15°, 46°, 1/2″)	0	0	0	0
T_{23} (15°, 46°, 3/4″)	0	0	0	0
T_{24} (15°, 46°, 1″)	0	0	0	0
T_{25} (15°, 59°, 1/2″)	0	0	0	0
T_{26} (15°, 59°, 3/4″)	0	0	0	0
T_{27} (15°, 59°, 1″)	0	0	0	0

Note: A 0 value means the HRP is not operating
H: Drive pipe angle or angle of elevation of the drive pipe
Θ_w: Waste valve angle or angle of inclination of the waste valve
Ø: Delivery or output pipe diameter size

CONCLUSION AND RECOMMENDATIONS

A suitable rig for testing hydraulic ram pumps is essential for confirming the pump's optimal performance. The combination of 10° drive pipe angle, 46° waste valve angle and 1.0″ diameter output pipe provided the highest mean output discharge of 15.440 L/min.

The combination of 10° drive pipe angle, 34° waste valve angle, and 1.0″ diameter output pipe resulted in the highest mean HRP volumetric efficiency of 92.46%. The combination of 10° drive pipe angle, 46° waste valve angle, and 0.5″ diameter output pipe provided the highest mean pressure of 68.95 kPa and the highest mean water delivery head of 6.38 m. The study suggests the provision of a bigger water supply tank and a continuous water source for the operation of the HRP. A waste water tank below the HRP support assembly is recommended to collect the wastewater and pump it again to the water supply tank. Longer drive pipes are recommended when using the testing rig to achieve higher delivery head and output discharge. Also, pipe fittings and elbows need to be eliminated from the design because they cause energy loss, resulting in a decrease in the delivery head and output discharge. Further study using different HRP designs is recommended to come up with an optimum HRP design for promotion in rural areas.

ACKNOWLEDGEMENT

The researchers express their deepest gratitude to the Visayas State University for funding the project through the Office of the Vice President for Research, Extension, and Innovation (OVPREI) and the Regional Climate Change Research and Development Center (RDDRDC).

REFERENCES

Nederstigt, J., & Bom, G. J. (2014). *Renewable Energy for Smallholder Irrigation: A Desk Study on the Current State and Future Potential of using Renewable Energy Sources for Irrigation by Smallholder Farmers*. SNV Netherlands Development Organization

Sheikh, S., Handa, C. C., & Ninawe, A. P. (2014). Design methodology for hydraulic ram pump (Hydram). *International Journal of Mechanical Engineering and Robotics Research, 2*(04), 170–175.

Twidell, J., & Weir, T. (2006). *Renewable energy resources* (2nd ed.). Routledge. https://doi.org/10.4324/9780203478721

REFEREES FOR THE PERTANIKA
JOURNAL OF SCIENCE & TECHNOLOGY

Vol. 33 (S1) 2025

The Editorial Board of the Pertanika Journal of Science and Technology wishes to thank the following:

Badronnisa Yusuf
UPM, Malaysia

Balqis Mohamed Rehan
UPM, Malaysia

Farah Nora Aznieta
UPM, Malaysia

Md Abdul Mojid
BAU, Bangladesh

Mohamed Fikry Mohamed Ahmed
Chulalongkorn University, Thailand

Nasrul Amri Mohd Amin
UniMAP, Malaysia

Nur Hanani Zainal Abedin
UPM, Malaysia

Radhiah Shukri
UPM, Malaysia

Radin Zaid Radin Umar
UTeM, Malaysia

Rahmi Nurdiani
Universitas Brawijaya, Indonesia

Salwa Mahmood
UTHM, Malaysia

BAU – *Bangladesh Agricultural University*
UTHM – *Universiti Tun Hussein Onn Malaysia*
UPM – *Universiti Putra Malaysia*
UniMAP – *Universiti Malaysia Perlis*
UTeM – *Universiti Teknikal Malaysia Melaka*

While every effort has been made to include a complete list of referees for the period stated above, however if any name(s) have been omitted unintentionally or spelt incorrectly, please notify the Chief Executive Editor, *Pertanika* Journals at executive_editor.pertanika@upm.edu.my

Any inclusion or exclusion of name(s) on this page does not commit the *Pertanika* Editorial Office, nor the UPM Press or the university to provide any liability for whatsoever reason.

Pertanika Journal of Science & Technology
Vol. 33 (S1) 2025

Content

Pertanika Editorial Office, Journal Division,
Putra Science Park,
1st Floor, IDEA Tower II,
UPM-MTDC Center,
Universiti Putra Malaysia,
43400 UPM Serdang,
Selangor Darul Ehsan
Malaysia

http://www.pertanika.upm.edu.my
Email: executive_editor.pertanika@upm.edu.my
Tel. No.: +603- 9769 1622

PENERBIT UPM PRESS

http://www.penerbit.upm.edu.my
Email: penerbit@upm.edu.my
Tel. No.: +603- 9769 8851

e-ISSN 2231-8526
9 772231 852000

ISSN 0128-7680
9 770128 768083